

**Biophysically Detailed Modelling of The
Functional Impact Of L-Type Calcium
Channel Gene Mutations Associated with
the ‘Short QT Syndrome’**

A thesis submitted to The University of Manchester
for the degree of Doctor of Philosophy
in the Faculty of Science and Engineering

2018

Sehar Sarfraz

School of Physics and Astronomy

Contents

Abstract	15
Declaration	16
Copyright Statement	17
Acknowledgement.....	18
Dedication	19

CHAPTER 1

Introduction

1.1 Cardiac Anatomy.....	20
1.2 The Cardiac Electrophysiology.....	22
1.3 Cardiac Action Potential	22
1.4 Features of the Action Potential	24
1.4.1 The Transmembrane Potential (TMP).....	25
1.4.2 The Action Potential Duration	25
1.4.3 The Excitation Threshold	25
1.4.4 The Diastolic Interval (DI).....	26
1.4.5 The Basic Cycle Length	26
1.4.6 Resting Membrane Potential (RMP) and Depolarisation.....	26
1.4.7 Refractory Region	27
1.4.8 Synchronous Contraction	27
1.5 Morphology of the Action Potential in Different Parts of the Heart.....	28
1.5.1 Sinoatrial Node.....	29
1.5.2 Atria.....	29
1.5.3 AV Node	29
1.5.4 Purkinje Fibres	30
1.5.5 Ventricle	30
1.6 Ionic Basis of Resting and Action Potential.....	31
1.6.1 The Cell Membrane.....	31
1.6.2 Ion Transportation	33
1.6.3 Passive Transport	34
1.6.4 Active Transportation.....	34
1.6.5 Ion Permeability	35
1.7 Mechanism of Ion Channel Gating	36
1.7.1 Ligands Gated Ion Channels	36
1.7.2 Stretch-Activated Ion Channels	36
1.7.3 Voltage-Gated Channels	37
1.7.4 Leakage Channel.....	37
1.8 Cardiac Ion Channels	37
1.8.1 Sodium Channels	37
1.8.1.1 Nav1.5	38
1.8.2 Calcium channels	38
1.8.2.1 Cav1.2.....	39
1.8.2.2 α 1 Subunit of Cav1.2	40
1.8.2.3 β Subunits of Cav1.2 Channel	40
1.8.2.4 α 2 δ Subunit.....	41

1.8.2.5 γ Subunit.....	41
1.8.2.6 T-Type Calcium Channels	41
1.8.3 Calcium-Induced Calcium Release	41
1.8.4 Sodium-Calcium Exchange.....	45
1.8.5 Potassium Channels	45
1.8.5.1 The Transient Outward ($Kv4.x/I_{to}$) Potassium Channels.....	45
1.8.5.2 The Fast-Delayed Rectifier (hERG1/ I_{Kr}) Potassium Channels	46
1.8.5.3 The Slow Delayed Rectifier ($Kv7.1/I_{Ks}$) Potassium Channels	46
1.8.5.4 The Inward Rectifier ($Kir2.X/I_{K1}$) Potassium Channels.....	46
1.9 Thesis Overview.....	47
1.10 References	48

CHAPTER 2

Cardiac Arrhythmias and Diseases

2.1 Introduction	52
2.1.1 Bradycardia	52
2.1.2 Tachycardia	52
2.1.3 Fibrillation.....	52
2.1.4 Ischemia	53
2.2 Genetic Mutation Induced Cardiac Arrhythmias	53
2.3 SQT Syndrome, QT Intervals and ECGs	53
2.4 Short QT Syndrome	57
2.4.1 SQT1/ KCNH2/hERG/ I_{Kr} Mutation.....	58
2.4.2 SQT2 / KCNQ1/ I_{Ks} Gene Mutation	59
2.4.3 SQT3 /KCNJ2/ I_{Ks} Mutation.....	60
2.4.4 SQT4/ CACNA1C/ G490R/ I_{CaL} Mutation.....	61
2.4.5 SQT4/ CACNA1C/ A39V/ I_{CaL} Mutation.....	62
2.4.6 SQT5/ CACNB2 $\beta 2$ / S481L / I_{CaL} Mutation.....	63
2.4.7 CACNA2D1 $\alpha 2\delta$ -1 S755T/SQT6 I_{CaL} Mutation.....	63
2.5 Discussion	64
2.6 References	67

CHAPTER 3

Mathematical Electrophysiology

3.1 Introduction.....	72
3.2 Cell Equivalent Circuit.....	72
3.2.1 Nernst Equations	74
3.3 The Hodgkin-Huxley Model	76
3.3.1 The Hodgkin-Huxley Cell Model Formulation.....	77
3.4 The Markov Chain Model.....	79
3.5 The O'Hara & Rudy model	80
3.6 Development of the SQT4-6 O'Hara & Rudy Models.	82
3.6.1 The Base I_{CaL} Model	82
3.6.2 The SQT4 O'Hara & Rudy Model.....	83
3.6.3 The SQT 5 O'Hara & Rudy Model	84
3.6.4 The SQT6 O'Hara & Rudy Model.....	85
3.7 Experimental Protocols	86

3.7.1 APD ₉₀	86
3.7.2 Action Potential Duration Restitution	86
3.7.3 Steady State Restitution Curves	87
3.7.4 ERP Restitution Curves	87
3.7.5 The Single Cell Model Simulation	87
3.7.6 1D Heterogeneous Transmural Strand Model	88
3.7.7 AP Propagation in 1D Heterogeneous Transmural Ventricular Tissue Model	89
3.7.8 Computation of Conduction Velocity	89
3.7.9 Evaluation of the Tissue Excitation Threshold (TET)	89
3.7.10 Computing the Pseudo-ECG	90
3.7.11 The Temporal Vulnerable Window Measurement	90
3.7.12 Induction of the Re-entry in the 2D Sheet	91
3.7.13 Tip Trajectories	91
3.9 References	94
Overview of Chapter 4, 5 and 6	98

CHAPTER 4

CACNA1C Linked Short QT4 Syndrome

4.1 Introduction	99
4.2 CACNA1C SQT4/G490R Mutation	100
4.3 CACNA1C SQT4/A39V Mutation	100
4.4 Simulation of Single Cell I _{CaL} for the CACNA1C α 1 WT and SQT4/A39V /G490R Mutation Conditions	100
4.5 Rate Dependent Restitution Properties of WT and SQT4 (A39V and G490R) Conditions	104
4.6 Membrane Potential Heterogeneity	113
4.7 1D Simulations for CACNA1C WT and SQT4/A39V/ G490R Conditions	115
4.7.1 ECG and QT Interval	116
4.7.2 Investigation of the Arrhythmogenic Substrate in CACNA1C WT and SQT4 1D Simulations	119
4.7.3 Computation of the Conduction Velocity across the 1D Strand	121
4.8 Investigation of the Arrhythmogenic Substrate in an Idealised 2D Tissue Sheet	122
4.9 Formation of Spiral Wave and its Behavior in a 2D Idealised Tissue	125
4.10 I _{CaL} Enhancement as a Potential Therapeutic Target in the SQT4	129
4.10.1 Single Cell	130
4.10.2 1D Strand Model	130
4.11 Summary	133
4.12 References	135

CHAPTER 5

CACNB2b S481L SQT5 Syndrome

5.1 Introduction	139
5.2 Simulation of Single Cell I _{CaL} for the CACNB2b β 2 Control and SQT5/S481L Mutation Conditions	140
5.3 Rate Dependent Restitution Properties of the WT and SQT5/S481L	144
5.4 Investigation of the QT Abbreviation and the Elevation of the ST Segment on the	

Electrocardiogram	150
5.4.1 1D Model Simulations	150
5.4.2 ECGs	151
5.5 Investigation of the Unidirectional Block and Arrhythmogenic Substrate in the SQT5	152
5.6 Computation of the Conduction Velocity and Excitation Threshold Across the 1D Strand	154
5.7 Investigation of Arrhythmogenic Substrate in the 2D Idealised Geometry for the WT and SQT5 Variants of CACNB2b β 2 Cav1.2	156
5.8 Phase Mapping and the Trajectory of the Excitation Spiral Wave in 2D Idealised Tissue for CACNB2b β 2 WT and S481L.....	159
5.9 Investigating Enhancement of I_{CaL} as a Potential Therapeutic Target in the SQT5	162
5.10 Summary	164
5.11 References.....	167

CHAPTER 6

S755T CACNA2D1 α 2 δ -1 Linked Short QT 6 Syndrome

6.1 Introduction.....	171
6.2 Simulation of Single Cell I_{CaL} for the CACNA2D1 α 2 δ -1 Control and SQT6/S755T Mutation Conditions	172
6.3 Rate Dependent Restitution Properties of WT and SQT6/S755T.....	175
6.4 1D Tissue Modelling and ECG Computation	181
6.5 Investigation of the Unidirectional Conduction Block and Size of the Arrhythmogenic Substrate in 1D Strand Model of the Left Ventricular Myocyte for the CACNA2D1 α 2 δ -1 WT and S755T	184
6.6 Computation of Conduction Velocity and Excitation Threshold	185
6.7 Investigation of the Arrhythmogenic Substrate in Idealised 2D Geometry for the CACNA2D1 WT and S755T	187
6.8 Phase Mapping of the Re-entrant Excitation Wave	189
6.9 Summary	192
6.10 References	194

CHAPTER 7

Electromechanical Cardiac Myocyte Model

7.1 Introduction.....	197
7.2 Myofilament Model	197
7.2.1 Electromechanical Modelling	197
7.2.2 Stretch-Activated Channel	198
7.2.3 Tissue Mechanics Model.....	199
7.2.4 Mechanical Feedback in the Electrophysiology Tissue Model.....	201
7.3 Single Cell Electromechanical Simulations without Stretch- Activated Current I_{sac}	201
7.3.1 SQT Syndrome 4 \ Cav1.2 CACNA1C α 1 A39V and G490R.....	201
7.3.2 CACNB2b β 2 SQT5/S481L.....	204
7.3.3 CACNA2D1 α 2 δ -1 SQT6/S755T	206
7.4 Single Cell Electromechanical Dynamics with Stretch Activated Channels	208
7.4.1 SQT4	208
7.4.2 SQT5	210

7.4.3 SQT6	212
7.5 Tissue Simulations	214
7.5.1 Re-entrant Excitation Wave Dynamics in a 2D Electromechanical Tissue Model ...	214
7.5.2 3D Electromechanical Consequences of SQT Syndromes	217
7.6 Discussion	221
7.7 References	223

CHAPTER 8

8.1 Discussion	227
8.1.1 SQT4/A39V and G490R	228
8.1.2 CACNB2b β 2 SQT5/ S481L.....	229
8.1.3 CACNA2D1 α 2 δ -1 SQT6/S755T	230
8.2 SQT4, SQT5 and SQT6 Electro-Mechanical Model	231
8.3 Common Mechanisms between the SQT 1-6 Variants.....	232
8.4 Limitations	233
8.5 Future Developments	234
8.6 Closing Words	234
8.7 References	236
Appendix A	239
Appendix B	242
Appendix C	243

59944

List of Tables

Table 2.1: The QT scale based on different studies, illustrating the QT spectrum, extending from extremely short to enormously long in males and females.....	57
Table 2.2: A short summary of all the Short QT Syndromes, the relevant experimental data, mutations and their effects on the relevant channel currents.....	65
Table 3.1: The distribution of ENDO, MCELL and EPI cell types along the 15mm long strand.	88
Table 4.1: Computed APD ₉₀ (ms) values for LVEPI, LVMCELL and LVENDO cell types for WT, A39V and G490R mutation conditions.....	104
Table 4.2: APD ₉₀ shortening in different cell types.....	104
Table 4.3: Comparison of different features of ECGs with different I _{Kr} current densities, while the I _{CaL} ratio is 1:1:1 across LVEPI, MIDDLE and LVENDO cell types.....	118
Table 5.1: Computed APD ₉₀ (ms) of LVEPI, LVMCELL and LVENDO cell types under CACNB2b β 2 Ca _v 1.2 WT and S481L mutation conditions.....	143
Table 5.2: Shortening of APD ₉₀ under the S481L condition.....	144
Table 6.1: Simulated APD ₉₀ (ms) values for LVEPI, LVMCELL and LVENDO cell types under WT and S755T mutation conditions.	175
Table 6.2: Shortening of APD ₉₀ under S755T condition.....	175
Table 7.1: APD ₉₀ values for the LVEPI, LVMCELL and LVENDO cell types obtained from an electrophysiological and electromechanically coupled single cell models.....	203
Table 7.2: Computed minimal contracted SL for WT, A39V, and G490R conditions and the corresponding normalised force associated to WT A39V and G490R.	204
Table 7.3: Computed minimal contracted SL for WT and S481L conditions and the corresponding normalised force of contraction relative to WT	206
Table 7.4: Computed minimal contracted SL for WT and S755T conditions and the corresponding normalised force of contraction relative to WT.....	208
Table 7.5: Changes in the APD ₉₀ (ms) with the incorporation of I _{sac}	210
Table 7.6: Role of I _{sac} on the minimal contracted sarcomere length and the corresponding normalised force.....	210
Table 7.7: Changes in APD ₉₀ due to I _{sac}	212
Table 7.8: Role of I _{sac} on the minimal contracted sarcomere length and the corresponding normalised force.....	212
Table 7.9: Changes in APD ₉₀ due to I _{sac}	213

Table 7.10: Role of I_{sac} on the minimal contracted sarcomere length and the corresponding normalised force.....	214
Table C1: Colour codes representing the change of voltage in Figure 5.1.....	243

List of Figures

Figure 1.1: Schematic representation of the structure and the conduction system of the heart	21
Figure 1.2: Illustration of 5 phases of a typical atrial and ventricular action potential (AP), and the corresponding primary ion currents during these phases.	24
Figure 1.3: Schematic diagram of an action potential (AP) illustrating the key characteristics of an AP.....	25
Figure 1.4: Illustration of a simulated action potential, describing the APD ₉₀ , diastolic interval (DI) and basic cycle length	26
Figure 1.5: Schematic representation of the heart, the action potentials from different regions and the electrocardiogram (ECG).	28
Figure 1.6: Plasma membrane consists of lipid bilayers with embedded proteins	32
Figure 1.7: Illustration of the voltage-gated Na ⁺ channels and selectivity filter	33
Figure 1.8: Active and passive ion channel transport	33
Figure 1.9: The current voltage relationship for the L and T type calcium channels.....	39
Figure 1.10: Predicted topology of L-type calcium channel explaining α_1 , β , and $\alpha_2\delta$ subunits.....	40
Figure 1.11: The schematic diagram of the intracellular Ca ²⁺ cycle.....	43
Figure 1.12: The Actin–myosin cross-bridge cycle.....	44
Figure 2.1: Schematic representation of cardiac electrocardiogram (ECG).....	55
Figure 2.2: Proposed topology of the α subunit of Kv11.1 channels encoded by KCNH2 gene, illustrating the position of the N588K mutation.....	59
Figure 2.3: The proposed topology of the Kir2.1 channel, indicating the location of the D172N mutation in the transmembrane region.....	61
Figure 2.4: The proposed topology of the α and β subunits of Cav1.2 channel.....	62
Figure 2.5: Predicted topology of the $\alpha_2\delta$ -1 subunit of CACNA2D1 gene.....	64
Figure 3.1: Electric Circuit equivalent of a cell membrane.....	74
Figure 3.2: A two-state transition diagram of HH model.....	78
Figure 3.3: Schematic diagram of O’HRd human ventricular myocyte model.....	82
Figure 3.4: Trajectories in phase space from all the elements of a 2D idealised model containing a spiral wave.....	92

Figure 4.1: Voltage clamp protocol, experimental and simulated L-Type calcium current traces for the WT and mutations	101
Figure 4.2: Computed I-V relationship for L-Type calcium channel (CACNA1C α -subunit) for the WT, A39V and G490R conditions	102
Figure 4.3: Simulated action potentials and I_{CaL} time traces	103
Figure 4.4: APD ₉₀ restitution curves for WT and A39V.....	105
Figure 4.5: APD ₉₀ restitution curves for WT and G490R.....	106
Figure 4.6: Maximal slope of the APD ₉₀ restitution curves, WT (blue), A39V (green) and G490R (red)	107
Figure 4.7: Steady-state APD ₉₀ rate dependence curves for WT (blue) and A39V (green) condition.....	108
Figure 4.8: Steady state APD ₉₀ rate dependence curves for WT (blue) and G490R (red) condition.....	109
Figure 4.9: Slope for Steady-state APD ₉₀ restitution curves for WT (blue), A39V (green) and G490R (red)	110
Figure 4.10: ERP restitution curves for WT and A39V.....	111
Figure 4.11: ERP restitution curves for WT and G490R.....	112
Figure 4.12: The maximal slope of ERP-R curve of the LVENDO, LVMCELL and LVEPI cell types. WT (blue), A39V (green) and G490R (red).....	113
Figure 4.13: Membrane potential heterogeneity (δV).....	114
Figure 4.14: Maximum δV during repolarisation between LVMCELL-LVEPI, LVENDO-LVEPI and LVENDO-LVMCELL cells in WT A39V and G490R conditions.....	115
Figure 4.15: Space-time colour-mapping of membrane potential in a 15mm ventricular wall strand during the propagation of an action potential cycle (BCL=1000ms).....	116
Figure 4.16: Spatial distribution of APD ₉₀ along the 15mm long 1D strand for the WT (blue), A39V (green) and G490R (red) models	116
Figure 4.17: Pseudo-electrocardiograms associated with the WT and SQT4 (A39V and G490R) conditions. WT (blue), A39V (green) and G490R(red).....	118
Figure 4.18: Vulnerable window across the transmural 1D strand.....	120
Figure 4.19: Measured Vulnerable Window (VW) widths within the marked region in Figure 4.18. WT (blue), A39V (green) and G490R (red)	121
Figure 4.20: Conduction velocity (CV) restitution curves for WT (blue), A39V (green) and G490R (red) conditions.....	122

Figure 4.21: Excitation threshold plotted against stimulus intervals (SIs) for the WT (blue), A39V (green) and G490R (red) mutation conditions.	122
Figure 4.22: Snapshots of initiation and conduction of the spiral re-entrant excitation wave in a 2D idealised model.	124
Figure 4.23: Minimal spatial length of the premature stimulus S2 that is necessary to initiate re-entrant spiral waves in WT (blue), A39V (green) and G490R (red).	124
Figure 4.24: Computed illustration of the trajectories and the electrical activity of the spiral waves in a 2D model of the human ventricle cells.	127
Figure 4.25: Life Span of the re-entrant spiral waves in the 2D tissue model and the dominant frequency obtained from the power spectral density analysis of the WT, A39V and G490R conditions.	128
Figure 4.26: Phase mapping and the identification of the Phase Singularity (PS) points for the WT and the mutations in space over time.	129
Figure 4.27: Current enhancement/blockade to normalise the AP durations under the A39V and the G490R conditions.	132
Figure 4.28: Current enhancement/blockade to normalize QT interval.	133
Figure 5.1: Voltage clamp protocol, experimental and simulated L-Type calcium current traces for the WT and S481L (4.1c) conditions.	141
Figure 5.2: Computed I-V relationship for L-Type calcium channel (CACNB2b β 2-subunit) for the WT (blue) and S481L (green) conditions.	142
Figure 5.3: Simulated action potential and I_{CaL} time traces	143
Figure 5.4: APD ₉₀ restitution curves for WT and S481L.	145
Figure 5.5: Maximal slopes of the APD ₉₀ Restitution curves, WT (blue) and S481L (green)	146
Figure 5.6: Steady-state APD ₉₀ rate dependence curves under WT (blue) and S481L (green) condition.	147
Figure 5.7: Maximal Slopes of the steady State restitution curves	148
Figure 5.8: ERP restitution curves for the WT and the S481L.	149
Figure 5.9: Slopes of ERP restitution curves.	150
Figure 5.10: Space-time colour-mapping of membrane potential in a 15mm ventricular wall strand during the propagation of an action potential cycle	151
Figure 5.11: Distribution of APD ₉₀ along the transmural 1D strand model of ventricular cells for the WT (blue) and S481L (green) conditions.	151
Figure 5.12: Pseudo-Electrocardiograms associated with the WT and S481L (S481L) conditions. WT (blue), S481L (green).	152

Figure 5.13: Vulnerable window (VW) for the WT (blue) and S481L (green) models.....	153
Figure 5.14: Measured vulnerable window (VW) width in the marked region in Figure 5.13 for the WT (blue) and S481L (green) models.....	154
Figure 5.15: Conduction velocity (CV) restitution curves. WT (blue) and S481L (green) conditions.....	155
Figure 5.16: The relationship between the excitation threshold potential and stimulus intervals (SI). WT (blue) and S481L (green) mutation conditions.....	155
Figure 5.17: Snapshots of initiation and conduction of re-entrant excitation waves in a 2D idealised tissue model for CACNB2 β 2 Cav 1.2 WT (a) and S481L (b).....	157
Figure 5.18: Minimal spatial length of the premature stimulus S2 that is necessary to initiate a re-entrant excitation wave under the WT and S481L conditions.....	158
Figure 5.19: Total life span of the re-entrant excitation spiral wave in 2D idealised tissue model for WT (blue) and S481L SQT5 (green) conditions.....	158
Figure 5.20: Phase mapping of the spiral wave in a 2D idealised tissue model of the left ventricular myocyte for CACNB2b β 2 CaV1.2 WT (a) and S481L (b) conditions.....	160
Figure 5.21: Behaviour of the re-entrant spiral wave in a 2D idealised tissue for WT and S481L variants of CACNB2b β 2.	161
Figure 5.22: Current enhancement/blockade to normalise the AP duration under the S481L condition.	163
Figure 5.23: Current enhancement/blockade to normalise the QT interval.....	164
Figure 5.24: The effect of an increased I_{Kr} density of the amplitude of T-wave.....	165
Figure 6.1: Computed I-V relationship for the WT and S755T models.....	173
Figure 6.2: Simulated action potentials and I_{Ba} time traces	174
Figure 6.3: APD ₉₀ restitution curves for WT and S755T.....	176
Figure 6.4: Maximal slopes of APD ₉₀ restitution curves. Slopes of APD ₉₀ restitution curve for WT (blue) and S755T (green).....	177
Figure 6.5: Steady-state APD ₉₀ rate dependence curves for WT and S755T condition.....	178
Figure 6.6: Maximal slope of steady-state restitution curves.	179
Figure 6.7: ERP restitution curves.....	180
Figure 6.8: Slope of ERP restitution curve for WT and S755T.	181
Figure 6.9: Space-time colour-mapping of membrane potential in a 15mm ventricular wall strand during the propagation of an action potential cycle	182
Figure 6.10: Spatial distribution of APD ₉₀ along the transmural 1D strand model of the	

ventricular myocyte for the WT (blue) and S755T A(green) conditions.....	182
Figure 6.11: Pseudo-ECGs corresponding to the WT and SQT6 (S755T) conditions. WT (blue), S755T (green).....	183
Figure 6.12: Vulnerable window across the transmural 1D strand plotted as a function of position for the WT and S755T.....	184
Figure 6.13: Measured vulnerable window (VW) width for the WT and S755T.....	185
Figure 6.14: Conduction velocity (CV) restitution under WT (blue) and S755T (green) conditions.....	186
Figure 6.15: Excitation threshold plotted against stimulus intervals (SI) for the WT (blue) and S755T (green) mutation conditions.....	186
Figure 6.16: Snapshots of initiation and conduction of re-entry in a 2D idealised model.	188
Figure 6.17: Minimal spatial lengths of a premature S2 stimulus that is sufficient to initiate re-entrant spiral waves in WT (blue) and S755T (green) conditions.....	189
Figure 6.18: Total life span of excitation re-entrant spiral wave for CANCA2D1 $\alpha 2 \delta$ -1 WT (blue) and S755T (green) SQT6 conditions.	189
Figure 6.19: Phase mapping of the re-entrant excitation wave for WT (a) and S755T (b) conditions.....	190
Figure 6.20: Behaviour of the re-entrant spiral wave in the 2D idealised tissue sheet for the WT and S755T models.....	191
Figure 6.21: Dominant frequency values computed from the power spectral distribution function for WT and S755T.....	192
Figure 7.1: Simulated single cell electromechanical dynamics from the WT, A39V and G490R mutation models	202
Figure 7.2: Simulated single cell electromechanical dynamics from the CANCB2b $\beta 2$ WT and S481L models.....	205
Figure 7.3: Simulated single cell electromechanical dynamics from the WT and S755T models.....	207
Figure 7.4: Role of the I_{sac} on the dynamics of the SQT4 electromechanical single cell model. WT (blue), A39V (green) and G490R (red).	209
Figure 7.5: The role of I_{sac} on the dynamics of the SQT5 electromechanical single cell model. WT (blue) and S481L (green).	211
Figure 7.6: Role of the I_{sac} on the dynamics of WT and S755T variant of CACNA2D1 electromechanical single cell model.....	213
Figure 7.7: Snapshots of initiation and conduction of re-entrant excitation waves in a 2D	

idealised tissue model of the left ventricular myocyte, for WT (a), A39V (b), G490R (c), S481L (d) and S755T (e).....	216
Figure 7.8: Minimal length of S2 stimulus necessary to initiate re-entry in the 2D electromechanical tissue models of the WT, A39V, G490R, S481L and S755T	217
Figure 7.9: Snapshots of the Electrical wave propagation and mechanical contraction at 0ms, 100ms, 200ms, 300ms,400ms and 500ms in WT (a), A39V (b), G490R (c), S481L (d), and S755T (e).....	220
Figure 7.10: Ejection fraction measurement... ..	221
Figure 8.1: Common mechanism between SQT1-6 mutation.....	233
Figure C1: The power spectral distribution of the recorded local electrical activity of the WT, A39V, G490R, S481L and S755T models.....	244

Abstract

The cardiac L-type calcium channel is an oligomeric complex consisting of α_1 , β , and $\alpha_2\delta$ subunits. The $\text{Ca}_v1.2$ α -1C, the pore-forming subunit is encoded by CACNA1C gene, while the Ca_v β_2 and Ca_v $\alpha_2\delta$ -1 subunits encoded by CACNB2b and CACNA2D1 respectively, control the biophysical properties and trafficking of Ca_v channels. In human ventricular cells, $\text{Ca}_v1.2$ channel regulates the inward movement of the calcium ions. The dome profile of the ventricular action potential is the result of inward calcium movement which also triggers Ca^{2+} release from the sarcoplasmic reticulum (SR) that regulates the excitation-contraction coupling. Genetic mutations in Ca_v subunits can be responsible for several phenotypes including the early repolarisation syndrome, the Brugada syndrome and the short QT syndrome. Short QT syndrome associated with L-type calcium channels are relatively new and rare clinical entity, manifested by an elevated ST segment and a shorter than normal QT interval. A short QT interval with an elevated ST segment can contribute to cardiac arrhythmia, ventricular fibrillation and sudden cardiac death (SCD). The work presented in this thesis is the development of a computational model to explain the functional behaviour of gene mutations associated with the SQT syndromes, initiation and maintenance of ventricular arrhythmias, and impairment of ventricular contraction. Three different mathematical models for SQT4, SQT5, and SQT6 were developed by using extant biophysical experimental data. The LTCC Hodgkin-Huxley formulation of the O'Hara & Rudy human ventricular single cell model (ORd) was reformed to integrate the kinetic properties of WT, SQT4 (A39V and G490R), SQT5 (S481L) and SQT6 (S755T) mutations. The validated formulations were then incorporated into the O'Hara & Rudy ventricular single cell and anatomically detailed tissue models (1D and 2D) to demonstrate how these variants advance to ventricular arrhythmias. The ORd electrophysiological short QT models were coupled with the myofilament model to investigate the functional impact of mutation on the mechanical coupling in single cell models. Simulated results showed that each mutation uniquely increased the temporal vulnerability of tissue to arrhythmogenesis in response to the premature excitation stimulus, indicating an increased risk of arrhythmia. Electromechanical single and 3D models illustrate a reduction of contractility in all three short QT models. These results provide better understanding into the mechanisms by which genetic variants of SQT4 (A39V and G490R), SQT5 (S481L) and SQT6 (S755T) mutations are pro-arrhythmic.

Declaration

I declare that this thesis is an original report of my own research and it is solely composed by myself and no part of this thesis has been submitted for any other degree or professional qualification of this or any other university or other institute of learning.

Sehar Sarfraz

Copyright Statement

- a) The author of this thesis (including any appendices and/or schedules to this thesis) owns certain copyright or related rights in it (the “Copyright”) and s/he has given The University of Manchester certain rights to use such Copyright, including for administrative purposes.
- b) Copies of this thesis, either in full or in extracts and whether in hard or electronic copy, may be made only in accordance with the Copyright, Designs and Patents Act 1988 (as amended) and regulations issued under it or, where appropriate, in accordance with licensing agreements which the University has from time to time. This page must form part of any such copies made.
- c) The ownership of certain Copyright, patents, designs, trademarks and other intellectual property (the “Intellectual Property”) and any reproductions of copyright works in the thesis, for example graphs and tables (“Reproductions”), which may be described in this thesis, may not be owned by the author and may be owned by third parties. Such Intellectual Property and Reproductions cannot and must not be made available for use without the prior written permission of the owner(s) of the relevant Intellectual Property and/or Reproductions.
- d) Further information on the conditions under which disclosure, publication and commercialisation of this thesis, the Copyright and any Intellectual Property and/or Reproductions described in it may take place is available in the University IP Policy (see <http://documents.manchester.ac.uk/DocuInfo.aspx?DocID=2442> 0), in any relevant Thesis restriction declarations deposited in the University Library, The University Library’s regulations (see <http://www.library.manchester.ac.uk/about/regulations/>) and in The University’s policy on Presentation of Theses.

Acknowledgement

I would like to take this opportunity to show my utmost gratitude to my supervisor, Professor Henggui Zhang. I would like to thank him for giving me the opportunity to conduct research under his supervision and for his support and guidance throughout my research.

I would also like to thank Ismail Adeniran, Haibo Ni, Kun Jain, Dominic Whittaker and all the other colleagues for their support during my research.

Finally, I would like to take this opportunity to thank my husband, Shahzad Qamar Khan and my son Khizar Shahzad Khan for being the biggest support throughout my studies.

Dedication

To my father, Sheikh Sarfraz Hussain, for his continuous patience and support and my mother, for being the driving force in my life.

CHAPTER 1

Introduction

1.1 Cardiac Anatomy

The heart is a “hollow, muscular” organ. It contracts repeatedly in a rhythmic pattern to supply blood to the entire body through the blood vessels. The term "cardiac" comes from the Greek word Kardia which means “related to the heart”. The Heart is located between the lungs in the thoracic cavity. Structurally it can be defined as a four-chambered, double pump. The cardiac muscle has an ability of self-excitation, which means it has its own conduction system. Although in a healthy heart, contractions occur at regular intervals, any change in the nervous or hormonal system can influence the rhythmic pattern such as exercise or the perception of danger. The heart is enclosed by a thick membranous cavity called pericardium which is divided into two layers, the serous pericardium and the fibrous pericardium. The pericardial cavity is positioned between the two layers of serous pericardium i.e. between the parietal layer and visceral layer (epicardium). The pericardial cavity secretes a fluid that reduces friction as the heart beats [1].

The cardiac system can be divided into two pumps which operate in series i.e. the right atrium, the right ventricle, the left atrium and the left ventricle.

Right atrium: the deoxygenated blood from the body enters the right atrium through the inferior and superior vena cava. The blood then flows to the right ventricle.

Right ventricle: the deoxygenated blood is pumped to the lungs for the oxygenation process via the pulmonary circuit, through the pulmonary artery.

Left atrium: the oxygenated blood from the lungs flows into the left atrium via the pulmonary veins.

Left ventricle: blood from the left atrium is received via the bicuspid valve. The oxygenated blood is pumped to the aorta and supplied to the rest of the organs via the systemic circuit [2].

The muscular walls of the ventricle are thicker than the upper chambers (the atrium walls) as the blood pumps out of this chamber at a greater pressure (the systolic/ diastolic pressure is 25 mmHg/4 mmHg and 120 mmHg/10 mmHg for the right and left ventricles) as

compared to the atrium (0-4 mmHg and 8-10 mmHg for right and left atrium). The thicknesses of the left and right ventricle are not identical [3]. The interventricular septum of the right ventricle is much thinner (3-5 mm) than that of the left ventricle (10 mm). Stronger forces are required to pump blood through the systemic circuit than the pulmonary circuit. The left and right cardiac pumps are divided by a vertical wall known as the septum. The septum inhibits the mixing of oxygenated and deoxygenated blood. The Atrioventricular (AV) valves prevent backward flow of the blood from the ventricles into the atria within the heart [3, 4].

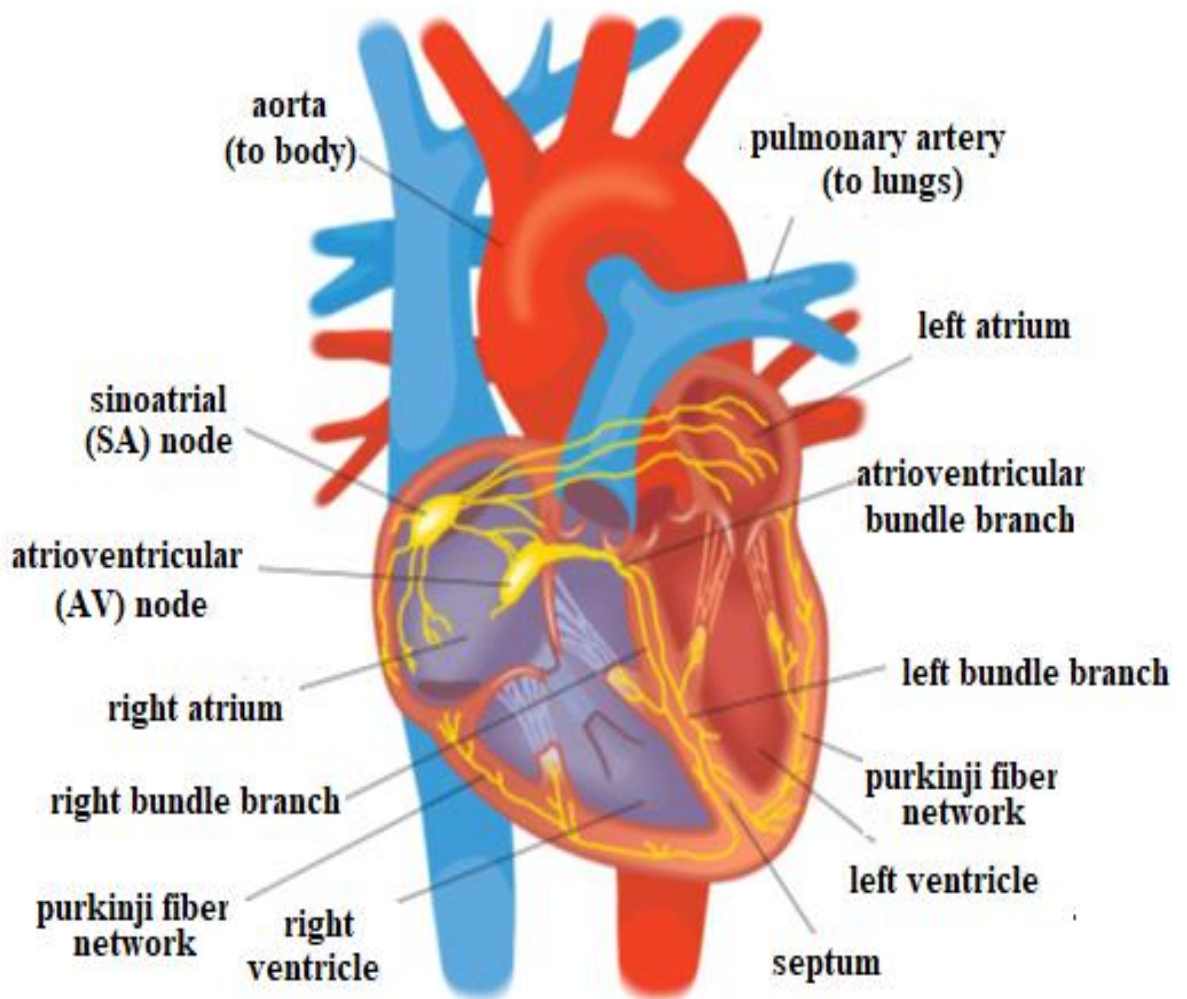


Figure 1.1: Schematic representation of the structure and the conduction system of the heart [Modified from 5]. The electrical conduction is controlled by the pacemaker cells in the sinoatrial node. Electrical impulses initiated in the SA node spread to the atrioventricular node and the bundle of His, through the bundle branches, and then into the ventricles via the cardiac conduction system [6, 7].

1.2 Cardiac Electrophysiology

The origin of the heartbeat is a biological phenomenon that depends on the cardiac conduction system. The detailed study of the fundamentals of the cardiac conduction system is essential to cardiology and clinical cardiac electrophysiology (EP). Clinical electrophysiology serves as a source to understand the electrical disorders of the heart. This particular area of research has been embellished by adopting techniques from different disciplines, including molecular biology, biophysics, molecular biology, genetics, cell biology, biochemistry, and computer modelling. These tools are very beneficial to understand the underlying phenomena of different cardiac diseases.

Each cell in the body including cardiac cells, accommodates ion channels that are specifically permeable to Na^+ , K^+ , Ca^{2+} and Cl^- . These ions move across these channels, thus generating an electric current. Ion channels are coded by proteins implanted in the cardiac membrane and serve as a passage between the extracellular and the intracellular spaces for different ion types [10, 11]. The ion channel defects can lead to life-threatening diseases, for example the Short QT syndromes where patients exhibit an abnormally short QT interval on the electrocardiogram (ECG) or the long QT syndromes (LQTS), where a patient have an abnormally long QT interval on the ECG [10-12]. These protein channel defects can lead to life threatening arrhythmias.

In order to understand the detailed background of cardiac electrophysiology and the Short QT Syndrome, which is the main objective of this thesis, this chapter gives an overview of the action potential, its features and the ion channels, particularly those with gene mutations associated with the SQTs. The present Chapter will give a review of different ion channels which play an important role in the generation of the cardiac action potential, and the following chapter (Chapter 2) further describes the functional consequences of mutations to these channels.

1.3 Cardiac Action Potential

The systematic and rhythmic contraction of cardiac myocytes is initiated by an electrical impulse generated by a sequence of ion movement across the lipid bilayer through specialised ion channels, producing a difference in the membrane potentials between the intra-cellular and the extra-cellular spaces that is called the action potential (AP). The action potential can be measured as an electrical signal and it demonstrates the time dependent changes in the membrane potential of the cardiac myocytes [6].

There are five phases of the cardiac action potential (Figure 1.2) [7]. Phase 4 is known as the resting phase with a resting potential of -90 mV in normal myocardial cells. A leakage of K^+ ions through open K^+ inward rectifying channels, keeps the transmembrane potentials (TMP) stable at resting potentials [18-21]. During the phase 0 (rapid depolarisation phase) a rapid activation of the sodium channel shifts the transmembrane potential (TMP) towards the positive voltage, reaching around -70 mV [20]. Then the Na^+ current rapidly shifts the TMP to 0 mV and slightly above 0 mV for a short period of time called the upstroke. L-type (“long-opening”) Ca^{2+} channels open when the transmembrane potential is greater than -40 mV, and it generates a constant influx of Ca^{2+} ions down its concentration gradient [19, 20]. Potassium channels activate slowly on a later stage [18-20], producing phase 1 of the early repolarisation phase. In this case, TMP is slightly positive, which opens K^+ channels for a brief period producing a transient outward potassium current I_{to} , repolarising the transmembrane potential to nearly 0 mV [18-29]. The plateau phase or the phase 2 of the AP is the longest phase. It describes the refractory period of the cell due to the inward movement of the L-type ions and the efflux of potassium ions [18-24]. Delayed rectifier K^+ channels open later in phase 2 and K^+ ions flow outward, down their concentration gradient. The electrical balance of these two counter-currents maintain the TMP value just below 0 mV during the phase 2 [21-23]. Phase 3 of the action potential is a rapid repolarisation phase. During the phase 3, the inactivation of calcium channels and the efflux of the potassium ion drops the transmembrane potentials back to the resting potential of -90 mV [18-25, 34].

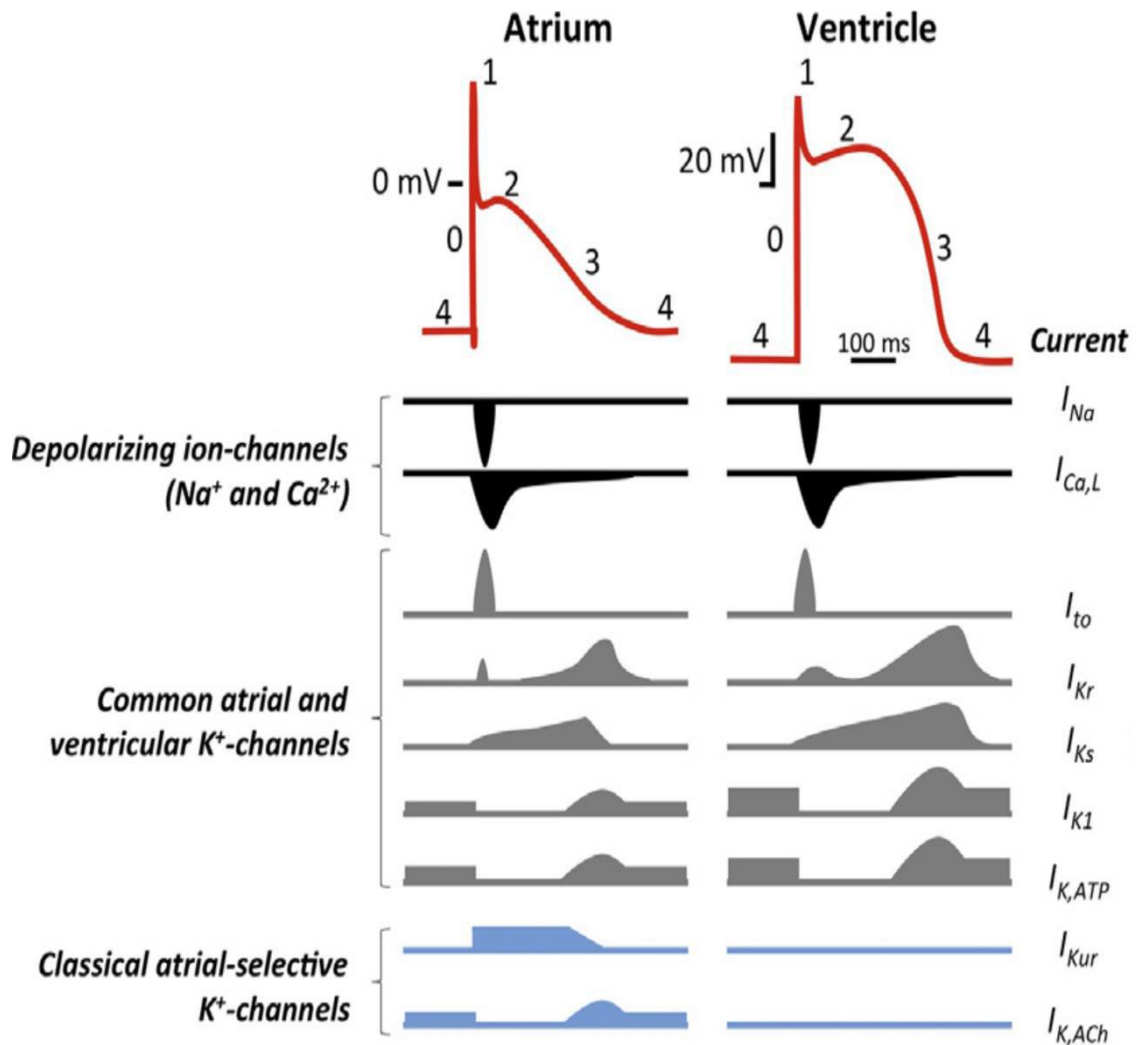


Figure 1.2: Illustration of 5 phases of a typical atrial and ventricular action potential (AP), and the corresponding primary ion currents during these phases. The lower panel describes the schematic diagrams representing the contribution of depolarisation and repolarisation currents during the AP [Modified from 7].

1.4 Features of the Action Potential

The action potential is one of the most important concepts in electrophysiology. To quantify and describe an action potential, different features of the action potential have been proposed and widely used in electrophysiology. Here, the most commonly used biomarkers are introduced.

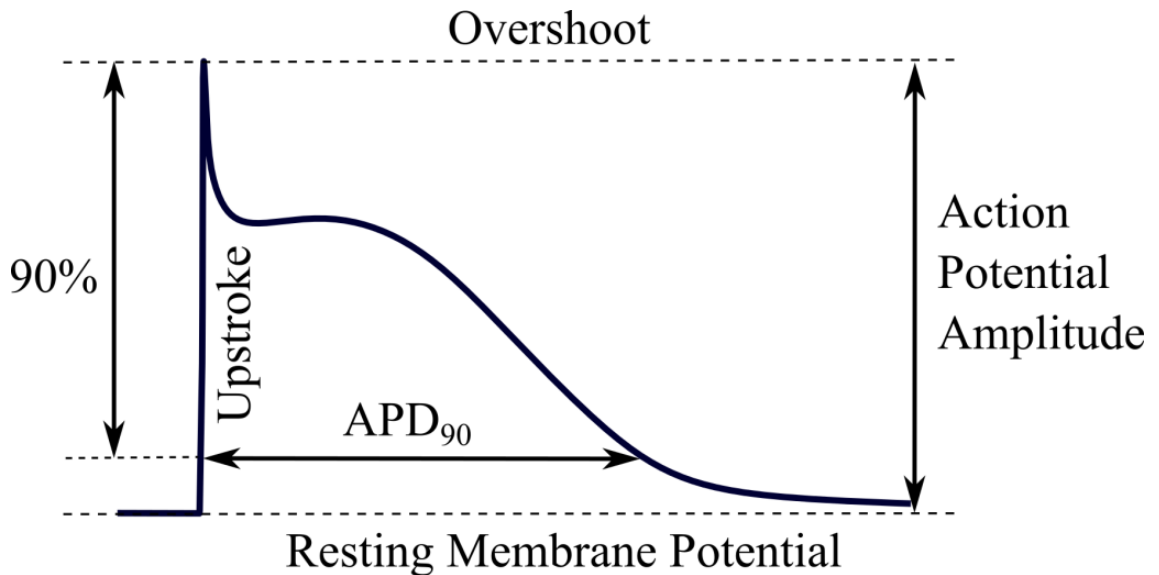


Figure 1.3: Schematic diagram of an action potential (AP) illustrating the key characteristics of an AP. The upstroke velocity (V_{max}) is defined as the maximum change in voltage per unit time during the phase 0 of an AP. The maximum transmembrane voltage a myocyte can achieve during an AP is defined as the overshoot. The difference between the resting membrane potential and the overshoot is defined as an AP amplitude [6, 7].

1.4.1 The Transmembrane Potential (TMP)

TMP can be defined as an electrical potential difference across the plasma membrane of the cell. When the net movement of positive ions is in the outward direction, the TMP becomes more negative, while it is more positive when there is a net movement of positive ions into the cell [4, 8-14].

1.4.2 The Action Potential Duration

Action potential duration is the total time between phase 0 and phase 3 [1]. AP starts with the depolarisation of the cell membrane due to the influx of sodium ions at phase 0 and ends with the rapid repolarisation phase 3 due to the rapid efflux of K^+ ions [1, 2, 18-26, 41]. The duration of the action potential varies in different regions of the heart.

1.4.3 The Excitation Threshold

The minimal excitation energy delivered by an excitation stimulus that triggers a propagating action potential in a cardiac tissue [1] is known as excitation threshold. In a few cases the stimulus does not have enough energy to elicit an AP though, it shows a slight change in

membrane potential, but is not strong enough to generate an AP. That stimulus is known as sub threshold stimulus [1, 2, 3, 4, 15].

1.4.4 The Diastolic Interval (DI)

It can be defined as a time interval between the end of repolarisation and the start of next action potential as explained in Figure 1.4 [1, 16].

1.4.5 The Basic Cycle Length

The basic cycle length can be defined as the combined length of the APD and DI. It is the total time of a single heart beat including all events between two consecutive heartbeats [1, 40].

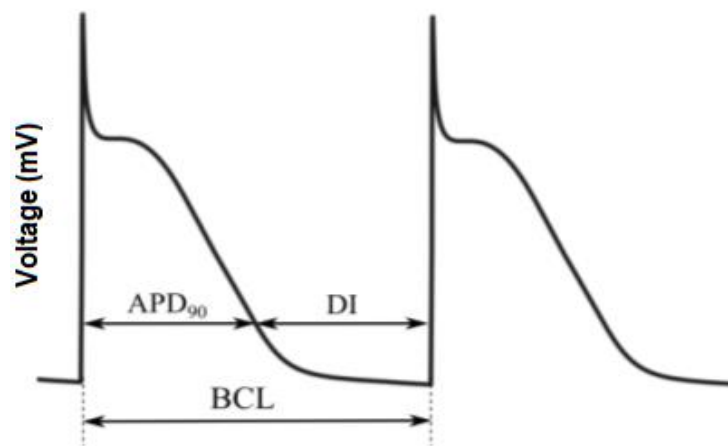


Figure 1.4: Illustration of a simulated action potential, describing the APD₉₀, diastolic interval (DI) and the basic cycle length (BCL) [16].

1.4.6 Resting Membrane Potential (RMP) and Depolarisation

RMP is a constant potential at which a cell shows no current passing through the plasma membrane [17]. It has been predicted that at constant membrane potential the outward ionic concentration gradient is balanced by the inward concentration gradient i.e. the intercellular space of the cell membrane is more negative as compared to the extracellular space. The RMP for a more excitable cell is -60 mV to -80 mV, while for a less excitable cell its value varies between -20 mV and -40 mV [17-19].

An upstroke in the membrane potential can be seen with the depolarisation stimulus, as it opens the Na⁺ channels activation gates rapidly. Phase 2 represents the inactivation of sodium channels, with a drop in potential due to the early repolarisation [1, 41].

1.4.7 Refractory Region

During the refractory phase, an influx of calcium ions and the outward delayed rectifying component of the potassium current, I_{Kr} balances the influx and efflux of ions, which generates the plateau region of the action potential. The plateau region represents the cell in a refractory state during which a 2nd AP cannot be generated. The Na⁺ channels, responsible for the depolarisation of the cell, are closed and remain inactive for a time called the refractory period. Inactivation of Ca²⁺ channels, responsible for the late repolarisation of the cell, and the increase in I_{Kr} ion channels conductance are the ionic changes which can explain the refractory period of a cell [20, 21].

Absolute refractory period: it can be defined as a time interval during which the cell is completely unexcitable to a new stimulus.

Effective refractory period: a 2nd stimulus may cause a minimal depolarisation of the cell membrane during this phase, but it's not strong enough to propagate a conducting wave.

Relative refractory period (RRP): the cell can be depolarised, and an action potential can be propagated if a greater than normal stimulus is applied during this period.

Super-normal period: it is considered as a hyper-excitable period. A relatively weaker than normal stimulus can depolarise the cell membrane and initiate a propagating action potential during the super-normal phase of the refractory region [21].

1.4.8 Synchronous Contraction

All cardiac myocytes are coupled electronically through the gap junctions. The periodic action potential generated in the pacemaker cells is conducted through the cardiac conduction system and to the whole heart via the gap junctions. The cell to cell communication of the cardiac action potential is essential for the rapid and uniform contraction of the heart [20, 21].

1.5 Morphology of the Action Potential in Different Parts of the Heart

The heart functions properly if a group of atrial and ventricular cardiac cells activate rapidly. The ionic channels in the heart enable the electrical activity and generate an action potential which initiates from the sinoatrial node, located at the junction of the superior vena cava and the right atrium. It is responsible for the initiation of the heart's spontaneous activity (Figure 1.5) [4, 8, 12, 13]. The spontaneous electrical activity initiated in the SA node spreads to the surrounding atrial tissue via the gap junctions which couple cardiac cells electrotonically. It then spreads to the atrioventricular node (AVN) from which it excites the His Bundle Purkinje system, which in turn conducts the electrical activity to the ventricular myocardium (Figure 1.5) [4, 8, 12, 13].

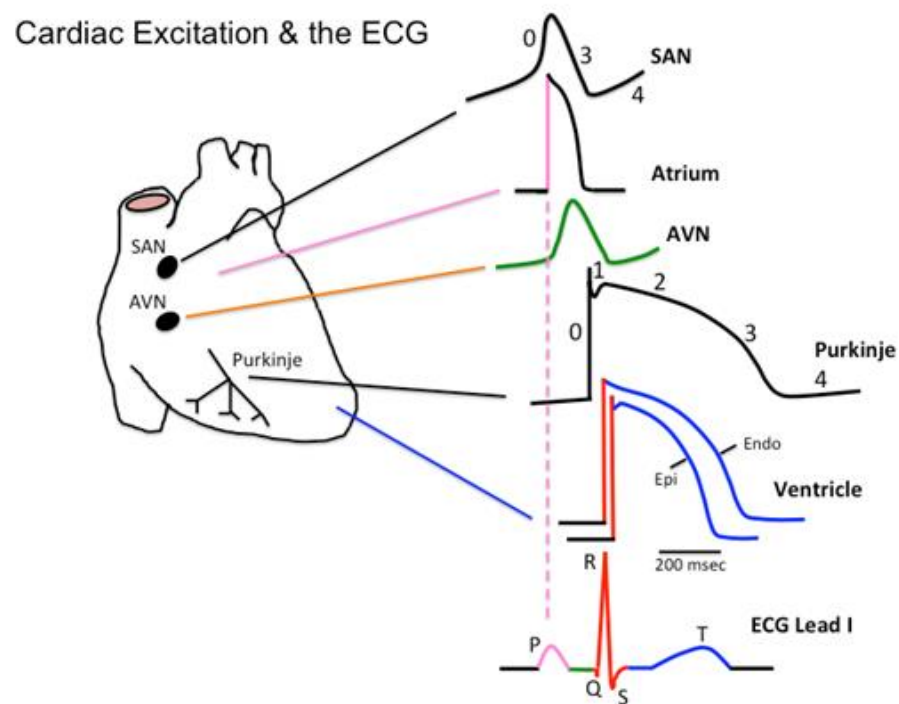


Figure 1.5: Schematic representation of the heart, the action potentials from different regions and the electrocardiogram (ECG). It illustrates the regional difference of action potentials based on their upstroke velocity and the AP duration. The differences in action potential configuration in different regions of the heart are caused by the variability of ion channel expressions in different regions. The different components of the body surface ECG reflect different events in the cardiac cycle (as indicated by the colour coding) [22].

Based on the depolarisation rate during the upstroke (Phase 0), cells in different regions of the heart can be divided into two groups. This difference is mainly due to the inward current during the depolarisation phase; Ca^{2+} for slow response cells and Na^+ for fast response cells. The atria, His Bundle, Purkinje and ventricular myocardial have rapid depolarisation phases, and are thus considered to be fast response cells, while the SAN and AVN cells are classified as slow response cells due to the slow depolarisation phase (phase 0) [23].

1.5.1 Sinoatrial Node

The sinoatrial node generally known as the SA node is a complex band of spontaneously depolarising cells (pacemaker cells) having a diameter of about 5-10 μm . The action potential duration (APD) range is between 100-200 ms with a propagation velocity that is less than 0.5 m/s and demonstrates the fastest rate of generating action potentials in the heart. The SAN contains slow response cells with a low upstroke velocity of about 5 V/s in human. Its diastolic potential ranges from -60 mV to -50 mV. SAN cells located peripherally have more negative diastolic potentials due to their electrical coupling with the atrial cells (atrial cells have more negative resting electrical impulses potentials than the SAN). It controls the pace of the heartbeat and thus this mechanism is considered as a normal pacemaker of the heart [24]. The signal generated in SA node is instantaneously transmitted to the rest of the heart through cardiac conduction system [23, 24].

1.5.2 Atria

Atrial cells have a diameter of about 10-15 μm and a propagation velocity between 0.3-0.4 m/s. The resting membrane potential of the atrial cells is more negative than the SAN (-80 mV as compared to -60 mV in SAN), which suggests atrial cells have a more stable resting potential with no spontaneous activity [12, 13, 25, 26]. In mammalian hearts, the APD is different in left and right atria (between 100-300 ms). It is longer in the right atrium than in the left atrium. Atrial cells are classified as fast response cells, with a rapid upstroke (the upstroke velocity is between 100-200 V/s) followed by a plateau phase (phase 2) in the mammalian hearts. The atrial cells show a gradual repolarisation with no clear distinction between the plateau phase (phase 2) and a final repolarisation phase (phase 3) [8, 13, 14].

1.5.3 AV Node

The atrioventricular node (AV node), is a group of self-exciting cells having a diameter of about 5-10 μm . The group of AV nodal cells is situated within the atrial septum, between the

right ventricle and atrium. These cells have a resting potential of -60 mV to -70 mV with a depolarisation rate of 5-15 V/s. The action potential propagates at a velocity of 0.1 m/s. The AVN cells have an action potential duration of 100-300 ms in mammalian hearts. The AV Node transmits the electrical signal from the atria to the ventricles through the bundle of His [24-27]. The AV node has a slow conduction pattern and delays impulses for 0.1 seconds before transmitting them to the ventricular tissue cells through the His bundle. This delay ensures that the atria contracts and empty its contents before it transmits electrical impulses to the His bundle [26, 27].

1.5.4 Purkinje Fibres

Purkinje fibres are myocardial fibre cells positioned in the interior of the ventricular walls of the heart [8, 9, 10]. The diameter of the Purkinje fibre cells is 100 μm [19, 24, 26]. These cells are classified as fast response cells with the fast depolarisation rate of 500-700 V/s and the resting potential of -90 mV to -95 mV. The APD is about 319 ± 23 ms in the human heart [35] depending on the frequency of stimulation. The AP has a propagation velocity of 2 m/s to 5 m/s. During a ventricular contraction, the Purkinje fibres conduct a contraction impulse from the right and left bundle branches to the ventricular myocardium [9], which results in the contraction of the ventricular tissues and the blood is forced out of the heart either to the pulmonary circulation or to the systemic circulation. A network composed of Purkinje fibres, AV node and SA node controls the heart rate [9, 10].

1.5.5 Ventricle

Transmurally, the ventricular myocardium has divided into three cell types; the endocardium (ENDO), the midmyocardium (MCELL) and the epicardium (EPI) cells with a diameter of 10-20 μm [19, 24, 38, 39]. The innermost layer of the ventricular wall is composed of ENDO cells, the EPI cells composed the outermost layer while between these two layers are the MCELL region. In a ventricle tissue MCELL has the longest APD, while the EPI cells demonstrate the shortest APD in all species. However, experimental evidence has been found where ENDO has exhibited a shorter APD as compared to the EPI in human ventricular cells [37-39]. The ventricular myocardial cells show different features in different regions of the ventricles. The APD is shorter in the right ventricle than in the left ventricle and has a more marked phase 1 repolarisation [19, 24]. The EPI and the MCELL cells have a marked phase 1 repolarisation as compared to ENDO which results in a prominent notch, giving the AP a spike-dome appearance [24, 25]. The resting potential of the ventricular cells is about -80

mV to -90 mV, with an upstroke velocity of 100-200 V/s [24-26] in the mammalian heart. The AP propagates at about 0.3-1.0 m/s [19, 24, 25, 26] and spreads from the endocardium near the apex to the epicardial wall at the base [26].

1.6 Ionic Basis of Resting and Action Potential

Each body cell including cardiac cells, accommodates ion channels. Ions are constantly moving across these channels, thus generating an electric current. These ion channels are coded by proteins implanted in the cardiac membrane and serve as a passage between the extracellular and intracellular spaces for different ion types [10, 11].

1.6.1 The Cell Membrane

The plasma membrane is the most important feature of a cardiac cell to understand ionic excitation. Its insight helps to understand the ion exchange, the action potential and eventually the whole heart. It consists of lipid bilayers with embedded proteins. Some of these proteins are involved in an exchange of different ions between extracellular and intracellular fluids [12, 35]. They act as ion permeation pathways, the lipid bilayer separates the extracellular lipids from the intracellular lipids, and it acts as a dielectric with a capacitance of about 1.0 $\mu\text{F}/\text{cm}$ [12, 35]. It serves as a barrier in a cell which selectively restricts and controls the movement of organic molecules and ions to enter or to leave the cell [12, 13, 14, 35] and thus acts like a protective shield. The cell membrane can be considered as a “leaky” capacitor and not as an ideal isolator between the extracellular and intracellular lipids. A resistor in parallel with a capacitor can then be considered as the electrical equivalent of the cell membrane [14]. The thickness of the cell membrane is between 7-8 nm, while the resistance varies with membrane potential i.e. it is a measure of ion flow through the lipid bilayer. A change in membrane potential can be calculated by using Ohm’s law ($V=IR$, where V is the voltage in Volts, I is the current in Amperes and R is the resistance in Ohms) [14]. A detailed discussion of cell equivalent circuits is given in Chapter 3.

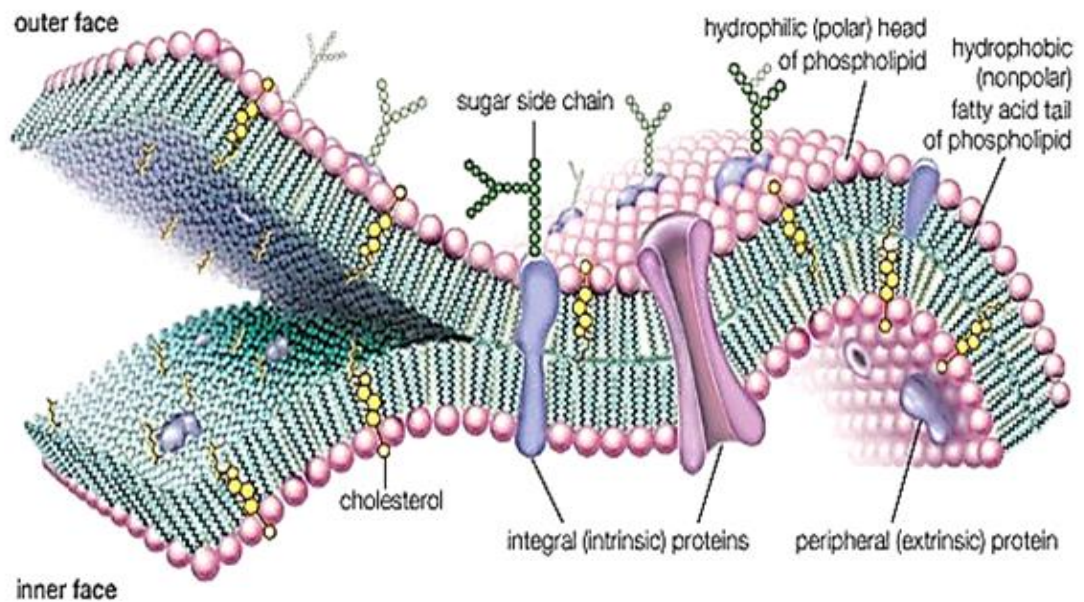


Figure 1.6: A plasma membrane consists of lipid bilayers with embedded proteins [14]. Some of these proteins are involved in an exchange of different ions between extracellular and intracellular fluids. They act as ion permeation pathways. The lipid bilayer separates the extracellular lipids from the intracellular lipids, and it acts as a dielectric with the capacitance of about $1.0 \mu\text{F}/\text{cm}$ [37].

The phenomenon of ion channel gating can be considered as a change in protein anatomy, that permit or prevent ion exchange. The gating mechanism is a complex phenomenon which still requires an additional research. For a basic understanding, ion channels can be considered to remain in one of three states: open, inactive and closed. A channel is considered at rest (closed channel) when ions do not transmit through the pore. The channel is open and ion exchange can be possible with an appropriate stimulus. The channel is also closed while it is in an inactivated state which restricts any ion movement through the channel [15, 16]. The ion movements across the cell membrane through ion channels generate an action potential. Ion permeation and gating [15] are the two fundamental properties of an ion channel which are necessary to understand the contribution of a specific ion channel during the action potential. The gating mechanism explains the kinetics of the opening and closing of the channel, where permeation illustrates the selectivity of the channel for a specific ion [15, 16]. The selectivity of the ion channel depends upon the pore formed by the protein of the channel. The selectivity filter can be defined as the narrowest conduction passage through the pore of different channels [15, 16].

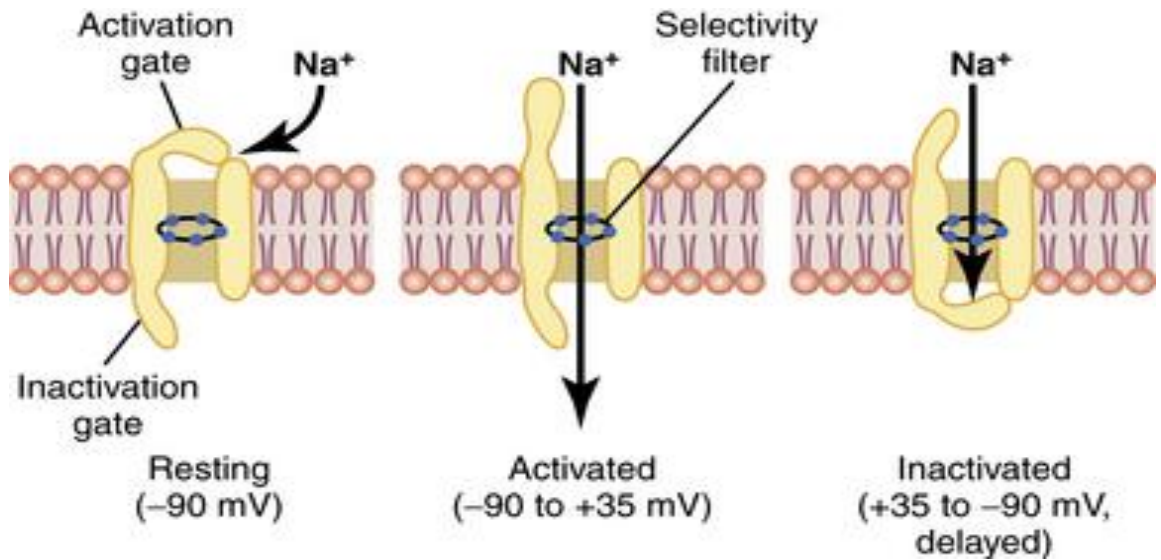


Figure 1.7: Illustration of the voltage-gated Na⁺ channels and selectivity filter. It illustrates activation and inactivation gates and the successive activation and inactivation of the sodium channels with the change in the membrane potential (V_m). The selectivity filter can be defined as the narrowest conduction pathway [4].

1.6.2 Ion Transportation

Ions transported either directly through lipid bilayers or through the protein channels follow two different transport mechanisms, passive and active transport.

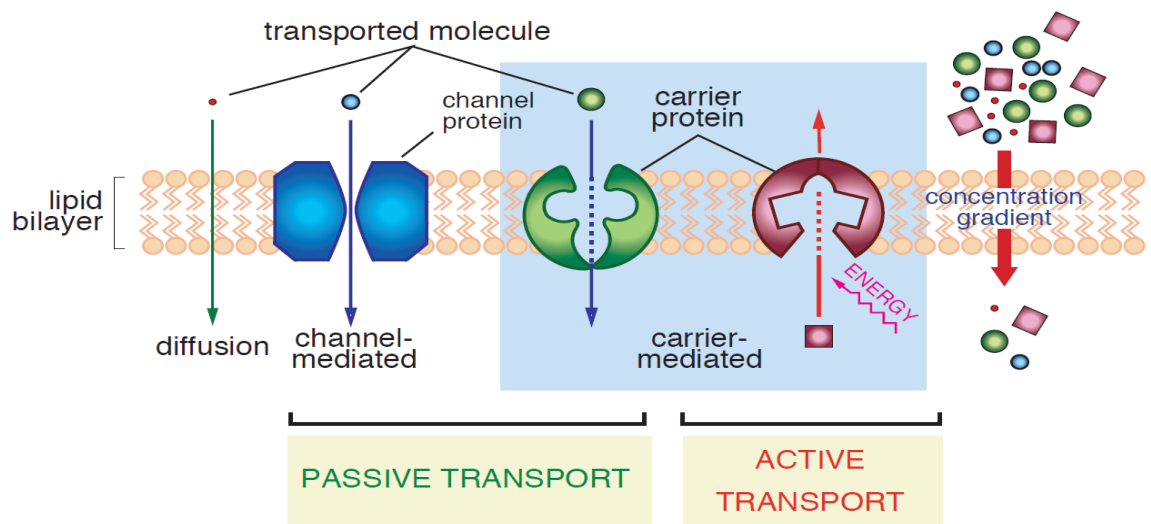


Figure 1.8: Active and Passive ion channel transport. Passive transport can be combined, facilitated (channel mediated, or carrier mediated) and simple diffusion. In active transportation, an additional energy is required to transport an ion against its concentration gradient [17].

Figure 1.8 [17] explains the mechanism of active and passive transportation. Diffusion or passive transport occurs either directly through lipid bilayers or through the protein channels (open channel or voltage-gated channel) [18]. Facilitated diffusion of substances crossing the cell (plasma) membrane takes place with the help of channel proteins and carrier proteins. Channel proteins are less selective than carrier proteins, and usually mildly discriminate between their cargo based on size and charge. The carrier proteins are more selective, often only allowing one particular type of molecule to cross. In the case of active transportation, an additional energy is required to transport an ion against its concentration gradient [17, 18, 22].

1.6.3 Passive Transport

Passive transport can be combined, facilitated (channel mediated, or carrier mediated) or simple diffusion (Figure 1.8). Simple diffusion is the transport of ions either through the space between the lipid bilayer or through a membrane opening without interacting (chemically) with a carrier protein [22]. The rate of diffusion (cm^2/sec) depends on the kinetic motion of the ions, ion concentration in a certain region and the size of the membrane opening [18, 19, 22].

Translocation of ions across a lipid bilayer from a low concentration region to a high concentration region through a carrier protein can be explained as facilitated diffusion [18, 22]. In the case of facilitated diffusion, ions do not require any additional energy for their transportation as they move along the direction of their concentration gradient [18, 19, 22].

1.6.4 Active Transportation

Active transport through a selectively permeable protein is an opposite phenomenon to that of passive transport. It transports ions from a low concentration region to a high concentration region, i.e. it moves the ion against its concentration gradient. An ion moving through the cell membrane against its concentration or electrochemical gradient requires an additional energy. In the case of cardiac cells, this excessive energy is derived by the breakdown of adenosine triphosphate (ATP) molecules directly or by other phosphate compounds [20].

1.6.5 Ion Permeability

As we have discussed earlier that the proteins embedded in the lipid bilayer of a cell membrane control the movement of ions between extracellular and intracellular fluids.

These proteins provide an alternative pathway for ion transportation. Ion channel classification is based on their selective permeability, size, valence and hydration energy [22, 23, 35]. Channel proteins allow free movement of water and selective ions while carrier proteins fasten ions which are to be transported between the lipid bilayers. A configurational change in a protein channel directly affects the movement of the substance that is transported [18-23]. The concentration difference and selective permeability of ions through different protein channels between the inner and outer fluids of plasma membrane creates a potential difference [21].

Sodium (Na^+), calcium (Ca^{2+}) and potassium (K^+) ions play a vital role in cardiac electrophysiology [18, 33, 34, 35]. They have a great contribution to the construction of the cardiac action potential [12, 18]. A patch clamp experiment shows that the intracellular potential of a resting cardiac myocyte is more negative in comparison to its extracellular environment [23]. According to electrophysiological convention, the movement of positively charged ions across the plasma membrane is referred to as the inward current, while the movement of negative current is the outward current [20].

Most inward currents are generated in the heart due to a rapid influx of positively charged ions (sodium Na^+ and calcium Ca^{2+} ions). An outward movement of a negative ion from the interior of a cell is also referred to as an inward current and has the same impact on membrane potential as that of a positive ion [15, 21, 23].

The ion channel's permeability changes for each ion during the AP. The inward or outward movement of an ion is determined by the electrochemical gradient [23, 24]. The inward movement of positive charge (inward current) causes depolarisation of the cell membrane by opening the voltage gated channels. A cardiac action potential is initiated when a depolarisation pulse passes through the resting myocyte [19, 24]. The action potential is propagated along the cells when this depolarisation wave opens the voltage-gated channels, resulting in an additional flow of the inward current. This additional depolarisation causes adjacent cells to similarly depolarise through the gap junctions [24]. The translocation of ions across the cell membrane is influenced by three major forces [25-27]:

Chemical potential: the ion moves down the concentration gradient under the influence of chemical potential (the free energy per particle) [26, 27].

Electrical potential: ions repel the other ions or molecules with same charge under the influence of the electric potential [25-27].

Mechanical forces: these forces are generally associated with stretch-activated channels [26, 27].

1.7 Mechanism of Ion Channel Gating

1.7.1 Ligands Gated Ion Channels

The closing and opening of ion channels as well as the transportation of ions through protein channels is regulated by the membrane potential [26]. However, ion translocation can be modulated in the presence of other factors such as membrane-bound ligands, mechanical forces or chemical signals [26, 27]. The most important of these are ligand gated channels in the nervous system. In the ligand gated channels, the opening of the channel depends on the binding of a ligand to a receptor [26]. For example, in the APT sensitive K^+ ligand-gated channel, the opening probability is proportional to the ratio of the adenosine triphosphate (ATP) ($[ADP] / [ATP]$) to concentration of intracellular adenosine di-phosphate (ADP) [26, 27, 34].

1.7.2 Stretch-Activated Ion Channels

The electrical impulses propagating through the heart cells trigger an excitation-contraction [26-28]. Whereas a mechanical contraction enables the heart to modulate its electrical activity [29, 30]. This is generally known as a mechano-electric feedback [28, 29, 30]. Shortening of the AP, changes in AP morphology, premature excitation and after depolarisation [29-33] are phenomena which are associated with the stretch-related electrical activities [29, 30]. The stretch-activated channels convert stretch into an electric impulse by altering the conductance of the ion channels [31-33].

1.7.3 Voltage-Gated Channels

Ion channels are voltage sensitive, so a distinct range of TMP is obligatory for the opening of a specific ion channel [23]. A specific ion channel will be closed and impermeable if TMP is out of that range [22, 23]. During an action potential different ion channels open and close depending on the TMP changes, allowing the movement of different ions at different times. Once closed, these channels cannot be opened again until the TMP is back to resting values, which control the excessive influx/efflux of ions [18, 40].

1.7.4 Leakage Channel

There is no actual driving force for the opening of leakage channel. They open at random events with an intrinsic rate of switching between the closed and open states [19, 16].

1.8 Cardiac Ion Channels

Ion channels are the key to understanding cardiac rhythmicity and contractility. It is important to understand these fundamental participants and their physiological roles in a cardiac cell [1, 2, 3, 40, 41, 42].

1.8.1 Sodium Channels

The voltage gated Na^+ channels commonly coexist as protein complexes composed of an α subunit with one or two β subunits [42]. Studies have described a total of nine α subunits to date [42]. The additional β subunits ($\beta 1$ – $\beta 4$) are not compulsory to construct the operative channels but can affect the trafficking or the biophysical properties of the channel [42]. The influx of sodium ions through the Na^+ channel is responsible for the rapid depolarisation of the cell membrane (Phase 0, upstroke). The magnitude of the sodium current increases between -60 mV to 10 mV. The sodium current reverses at about 50 mV. The recovery process is very rapid for the sodium channel (1-10 ms) and it increases with the hyperpolarisation [18-20, 42, 43]. Sodium channels are found in the atria, ventricles and Purkinje fibre cells where they play a substantial role during the depolarisation phase (phase 0 shows a sharp upstroke for a duration ≈ 2 -3 ms) of the action potential. In SAN and AVN the depolarisation phase (phase 0) is not very rapid (20-30 ms), which suggests sodium

channels play little or no active role in these cells due to their absence or low diastolic potential in these cells.

1.8.1.1 Nav1.5

The cardiac sodium channel Nav1.5 is encoded by the SCN5A gene. I_{Na} expression is not the same in all excitable and non-excitable cells. Its activation and inactivation are dependent on the membrane potential. It opens and inactivates rapidly in response to the depolarisation stimulus. The basic functionality of this channel is to initiate the action potential and encourage its propagation in the neighbouring cells. The initial influx through the Nav1.5 channels will increase the TMP to a more positive voltage and serves as the depolarisation trigger for the Ca^{2+} and K^+ channels [42]. The activation of calcium is followed by a calcium induced calcium release from the sarcoplasmic reticulum (SR), which leads to the shortening of the sarcomeres. The ventricular depolarisation, the atrial depolarisation and the gap junctions responsible for the conduction between adjacent cardiomyocytes express a high local concentration of Nav1.5. I_{Na} influx through the SCN5A channels is responsible for the phase one (upstroke) of the action potential in the atrial and ventricular myocardium [42].

1.8.2 Calcium Channels

Calcium current influx initiates with the activation of voltage dependent calcium channels [43, 44]. It also regulates the calcium-induced calcium release concentration in the sarcoplasmic reticulum through the ryanodine receptor 2 (RyR2) [43]. The gain in the intracellular calcium concentration leads to the electromechanical (EC) coupling [43, 44]. Ca^{2+} controls the integrity of the cell and is fundamental for the evolution of the heart [43]. Calcium channels are composed of polypeptide complexes, which are composed of $\alpha 1$, $\beta 2$, $\alpha 2/\delta$ subunits. Studies have also revealed the presence of γ subunits in a few tissues i.e. skeletal muscles and brain [44]. These subunits are considered as the functional units of the Ca^{2+} channel complex. In the channel, complex β and $\alpha 2/\delta$ subunits are tightly attached to the $\alpha 1$ subunit without any covalent bonding. Although these additional subunits can manipulate the functionality of the channel, the major changes in electrophysiological and pharmacological properties of calcium channels are controlled by multiple $\alpha 1$ subunits [43, 44]. Based on these pharmacological and electrophysiological properties, voltage-gated calcium channels are divided into different subfamilies and are named after their $\alpha 1$ subunits [44]. These subfamilies are defined as Cav2.2 (N-type), Cav2.1 (P/Q-type), Cav3.1–3.3 (T-type) and Cav2.3 (R-type). Cav1.1, Cav1.2, Cav1.3, and Cav1.4 belongs to the subfamily of

L-type calcium channels [44]. L is used to label these channels due to the long-lasting length of activation process. In the human ventricular cells $\text{Ca}_v1.2$ channel mediates the I_{CaI} flux and it is composed of $\alpha1$, β , and $\alpha2\text{-}\delta1$ subunits [43, 44].

Cardiac myocytes have two different types of calcium channels. In a cardiac cell L-type Ca^{2+} channels are the prime source of Ca^{2+} ions and play the major role in the regulation of the pacemaker activity, and the electromechanical coupling. While the cardiac T-type Ca^{2+} channel expression levels change with different factors i.e. various cardiac disorders, age, heart regions and mammalian species [43, 44].

1.8.2.1 $\text{Ca}_v1.2$

In a normal functional heart, $\text{Ca}_v1.2$ channel is an essential cell membrane protein complex that regulates the inward movement of Ca^{2+} ions. The cardiac ventricular myocytes express only the L-type component of $\text{Ca}_v1.2$ channel [44]. A strong depolarisation (threshold for the activation is approximately -40 mV) is required for the activation of $\text{Ca}_v1.2$ channels. The $\text{Ca}_v1.2$ channels are regarded as high voltage-gated channels [43, 44].

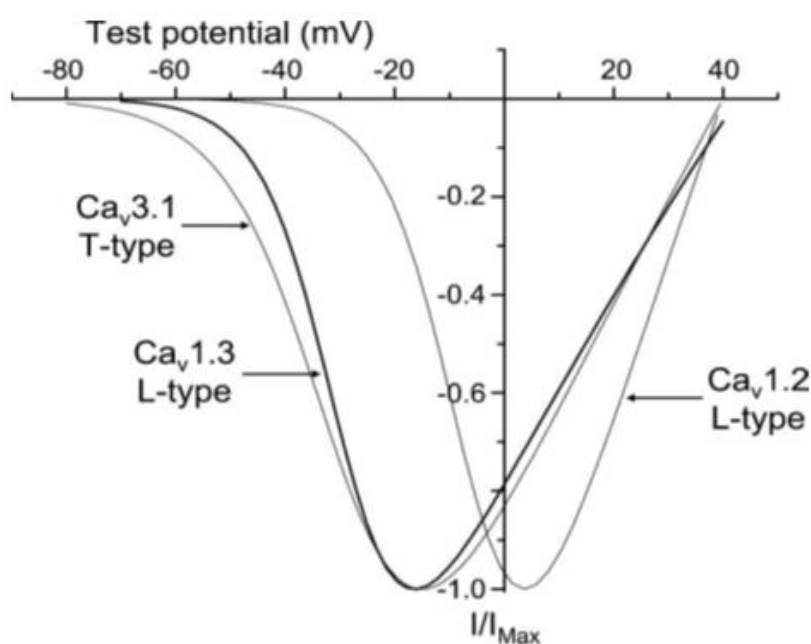


Figure 1.9: The current (I/I_{Max}) voltage (V_m) relationship for the L and T type calcium channels. $\text{Ca}_v1.2$ and $\text{Ca}_v1.3$ belongs to the L-type subfamily, while $\text{Ca}_v3.1$ belongs to the family of T-type calcium channels. $\text{Ca}_v1.2$ channel protein is expressed in human ventricle and classified as a high voltage channel (activates at -40 mV), while the T type channel activates at relatively lower membrane potentials and is regarded as low voltage channels [46].

1.8.2.2 $\alpha 1$ Subunit of $\text{Ca}_v1.2$

The largest subunit $\alpha 1$, is the main modulator in the $\text{Ca}_v1.2$ channel, as it contains the voltage sensor and the conduction pore. It also controls the channel gating mechanism [43, 44]. The systematic arrangement of $\alpha 1$ subunit is a complex of four homologous domains (I-IV), with six transmembrane segments (S1-S6) in each domain [43, 44, 45].

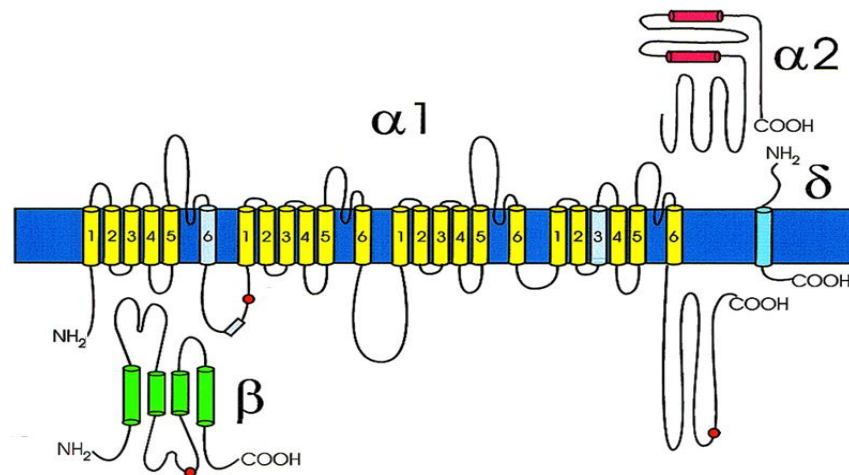


Figure 1.10: Predicted topology of the L-type calcium channel showing $\alpha 1$, β , and $\alpha 2\delta$ subunits [47]. S4 segment is the voltage sensor. S5 and S6 segments are the pore loops in each domain and regulate ion conductance and selectivity. S1–S6 segments are linked through the intracellular loops and connected to the cytosolic N- and C-termini. C-terminus plays a vital role in channel trafficking to the cell surface. It is an important location in the channel complex for the interaction of signalling proteins that either decode local Ca^{2+} signals or regulate LTCCs [43-45].

1.8.2.3 β Subunits of $\text{Ca}_v1.2$ Channel

The $\text{Ca}_v1.2, \beta$ subunit has four distinct subfamilies ($\beta 1$ – $\beta 4$), encoded by four different genes, each subunit has different extending variants [45]. The I–II intracellular loop of $\alpha 1$ subunits, the known $\alpha 1$ interaction domain has a high-affinity site and acts as a link between $\alpha 1$ and β subunits. The β subunit controls several properties of $\text{Ca}_v1.2$ channel physiology that includes surface expression, degradation, and gating [44].

1.8.2.4 $\alpha 2\delta$ Subunit

The $\alpha 2\delta$ subunit has four isoforms ($\alpha 2\delta$ -1– $\alpha 2\delta$ -4), which are produced from the transcription of a single gene [44]. The $\alpha 2$ protein is situated in the extracellular region, and the δ subunit serves as a link to connect it to the plasma membrane [44, 45]. The $\alpha 2\delta$ subunits play a vital role to regulate the voltage-dependence and the kinetics of the channel. In a heterologous system, these subunits are able to increase the amplitude of L-type calcium channel currents by approximately two to three-fold [44, 45].

1.8.2.5 γ Subunit

The γ subunits are membrane proteins and have eight specific isoforms (γ 1– γ 8) [44, 45]. They have four transmembrane segments and intracellular N- and C-termini. γ 4, γ 6, γ 7, and γ 8 isoforms of γ subunits have been demonstrated in human cardiac myocytes [44].

1.8.2.6 T-Type Calcium Channels

The voltage dependent Ca^{2+} channels are classified as either high voltage-activated or low voltage-activated Ca^{2+} channels [43, 44]. T-type calcium channels fall in the category of low voltage-activated channels, Figure 1.9 [46] (its threshold of activation is about -75 mV to -50 mV), as they activate at low membrane potentials (as compared to I_{CaL}) and have fast inactivation. Both the T-type and L-type Ca^{2+} channels have been identified in cardiac myocytes [44]. As discussed earlier L-type Ca^{2+} channels have four subunits, α 1, γ , β and $\alpha 2\delta$. Only the pore-forming subunit α 1 is identified for T-type channels [44, 45]. $\text{Cav}3.1$ ($\alpha_1\text{G}$), $\text{Cav}3.2$ ($\alpha_1\text{H}$) and $\text{Cav}3.3$ ($\alpha_1\text{I}$) isoforms are considered to compose the T-type Ca^{2+} channel complex [44].

Two isoforms, $\text{Cav}3.1$ and $\text{Cav}3.2$, of the T-type Ca^{2+} channel, are identified in embryonic hearts [45]. Their expression is insignificant in an adult's ventricular myocyte as it visibly declines during the development of an embryonic heart. However, its expression is more dominant in the conduction system. In the SA node, it facilitates the pacemaker depolarisation. L-type and T-type Ca^{2+} channels can be distinguished based on their conductance properties and gating mechanisms, as described in Figure 1.9 [44, 45].

1.8.3 Calcium-Induced Calcium Release

Cardiac tissue has an ability to perform synchronised contractions [44], APs spread by the

gap junctions of intercalated discs to regulate the coordinated contraction of the cardiac muscle [46, 47]. The phenomena of excitation-contraction coupling involve the conversion of an electrical impulse into a mechanical response that facilitates muscle contraction [47]. In a cardiac muscle, action potentials serve as an electrical impulse that triggers the mechanical response through the sliding of filaments [47]. The phenomena of the mechanical contraction require calcium induced calcium release (CICR) from intracellular spaces. CICR is the fundamental tool for the activation of SR calcium (depolarisation of sarcolemma), which is essential for the electromechanical coupling in the cardiac tissue. The L-type calcium channels are activated during the action potential [47, 48], calcium ions flow into the cell, the influx of Ca^{2+} stimulates ryanodine receptors (RyR) to release calcium ions from the sarcoplasmic reticulum which increase the cytosolic Ca^{2+} [47]. The mechanism of contraction is not fully understood, researchers are still trying to find out what causes the ryanodine receptor to open. It can be linked to the physical opening of the L-type calcium channels or the presence of calcium [47, 48].

The mechanical contraction in a cardiac muscle involves the myofilament model of contraction, the myosin filaments slide over the actin filaments, which helps the muscle fibre to contract and relax with a change in the fibre length [47, 48]. The entire process can be described: an action potential, generated by the pacemaker cells, is propagated to initiate the contraction through the gap junctions [48]. After the rapid depolarisation phase, calcium enters the cell through L-type calcium channel. The influx of Ca^{2+} ions then triggers the depolarisation of RyR, that will initiate the release of calcium through the SR into the cardiomyocyte. The intracellular calcium returns to the SR with the end of the contraction [48].

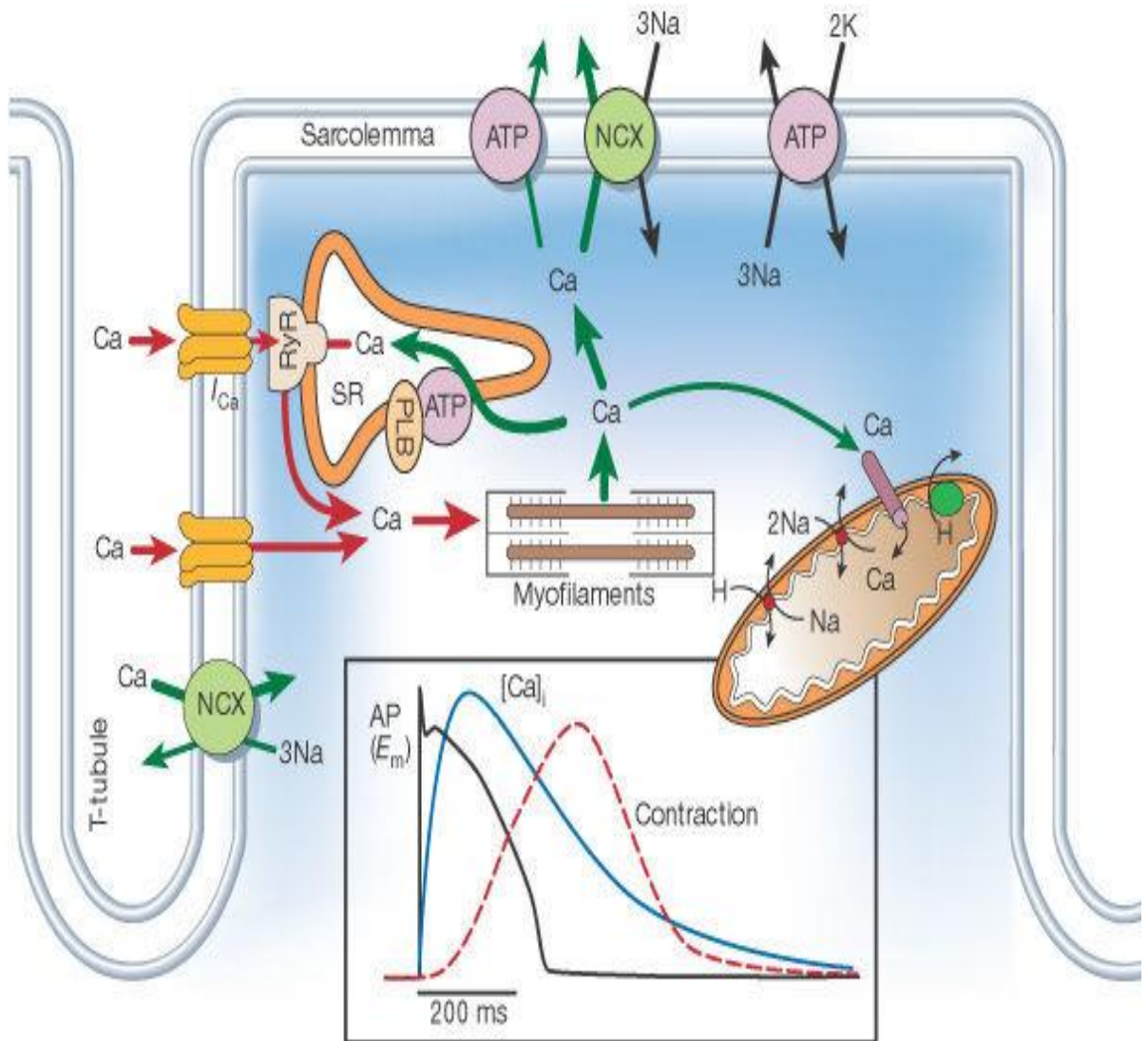


Figure 1.11: The schematic diagram of the intracellular Ca²⁺ cycle. The red arrows illustrate the direction of Ca²⁺ influx, while the green arrows explain the behaviour of the Na⁺/Ca²⁺ exchanger, ATPase (ATP), phospholamban (PLB), sarcoplasmic reticulum (SR), ryanodine receptor (RyR). Insert: time course of the intracellular Ca²⁺ concentration and the contraction initiated by the action potential. The calcium that enters through the L-type Ca²⁺ channels stimulates the SR to release Ca²⁺ into the cytoplasm. This process produces a rise in intracellular Ca²⁺ concentration from a diastolic level of less than 0.1 μM to systolic levels of 1-10 μM [51].

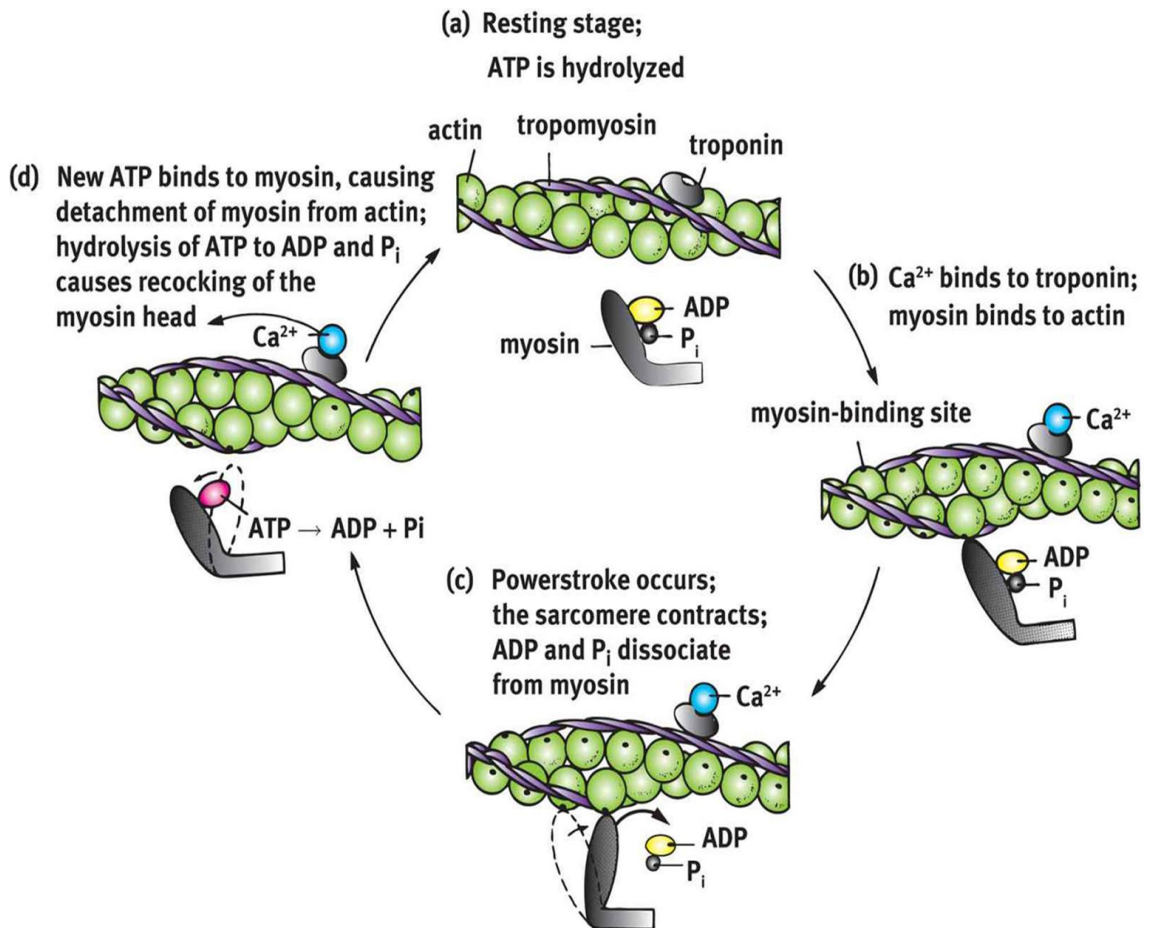


Figure 1.12: The Actin–Myosin cross-bridge cycle. a) The resting stage, b) the calcium binding to the troponin exposes the myosin-binding sites on the actin filament. The free myosin heads bind with the exposed sites on the actin and forms the cross bridges. c) These actin–myosin cross bridges then allow myosin to drag the actin towards the middle of the sarcomere, resulting in a shortening of the sarcomere, d) ATP attachment to myosin head weakens the bond between the myosin head and the actin. Hydrolysis of ATP to ADP and phosphate (P_i) detach the myosin from the actin which effectively ends the contraction [50].

Calcium in the cytoplasm binds to troponin and exposes the binding site on the actin filament. This will allow the myosin head to be bound to an actin filament to initiate contraction. The myosin head changes the conformation and drags the actin filaments toward the centre of the sarcomere. The ATP activates the myosin head, which weakens the bonding between the myosin head and the actin. The troponin complex returns to its initial position on the binding site of the actin filament, with a drop in the intracellular calcium concentration from the sarcoplasmic reticulum, which effectively ends the contraction [44, 46, 47, 48].

1.8.4 Sodium-Calcium Exchange

Specific transport proteins play a very important integral part in the exchange of ions across the cell membranes. These proteins can be classified as ATP-driven transporters and secondary active transporters. Secondary active transporters are the second largest group of transporter proteins after the G-protein coupled receptors [47].

The participation of $\text{Na}^+/\text{Ca}^{2+}$ exchanger systems in the regulation of intracellular Ca^{2+} draws a lot of attention. It is now quite clear that $\text{Na}^+/\text{Ca}^{2+}$ exchange has a significant physiological effect in cardiac myocytes. In the cardiac cell, the $\text{Na}^+/\text{Ca}^{2+}$ exchanger is the dominant Ca^{2+} efflux pathway [1, 44, 48].

1.8.5 Potassium Channels

Potassium ions play an important role in the construction of cardiac action potentials. In the heart, several different potassium channels conduct potassium in a single action potential at different TMPs [1, 2, 8].

The impulse generated by the depolarisation of sodium channels will activate the transient outward potassium current (I_{to}) during the start of phase 1. I_{to} plays a very important part in the atria and in sub epicardial ventricular myocytes. I_{Kr} and I_{Ks} , the rapid and slow delayed rectifier potassium currents, respectively, along with I_{K1} the inward rectifier currents, are responsible for the repolarising phase of the cardiac myocyte. I_{Kr} , I_{Ks} and I_{K1} currents are responsible for the phases 3 and 4 in both atria and the ventricular APs [1, 2, 25].

1.8.5.1 The Transient Outward ($\text{Kv}4.x/I_{\text{to}}$) Potassium Channels

The ionic current I_{to} is involved in early repolarisation phase of the cardiac action potential. A visible decrease of TMP can be observed with the activation of I_{to} channels. I_{to} , the transient outward current, can be divided into two groups, I_{tof} , rapidly activating and inactivating current and I_{tos} , a current with slow recovery kinetics [7, 8]. $\text{Kv}1.4$ channels regulate I_{tos} [8]. Although $\text{Kv}1.4$ channels are expressed throughout the ventricular and atrial wall, their expression is not very strong. The faster component of transient outward potassium current, I_{tof} activates rapidly while the inactivation is a slow process [7, 8]. I_{tof} is responsible for the characteristic notch (phase 1 repolarisation) in the cardiac action potential, which is more dominant in atria. The I_{tof} expression is not heterogeneous across

the ventricular wall, the amplitude of current is substantial in epicardial and mid-myocardial layers but it's not very prominent in the endocardial layer. As a result, a notch can only be seen in epicardial and midmyocardial ventricular action potentials [1, 3, 4, 7, 8].

1.8.5.2 The Fast-Delayed Rectifier (hERG1/I_{Kr}) Potassium Channels

The hERG1 gene, encoding K_V11.1 channel is responsible for I_{Kr}. It plays a substantial role in the repolarisation process of the nodal tissue, atria, Purkinje fibres and ventricular cells [8, 53]. These channels have very distinctive biophysical properties. They inactivate rapidly followed by a slow deactivation, allowing a relatively large potassium current to be conducted through these channels, which will slowly accelerate the membrane potential towards the resting membrane potential [1, 3, 4, 7, 8].

1.8.5.3 The Slow Delayed Rectifier (K_v7.1/I_{Ks}) Potassium Channels

The voltage-gated K_V7.1 channel is encoded by KCNQ1 genes. These genes activate the voltage-gated potassium channels during the repolarisation phase of the cardiac action potential with a progressive change in the TMP. The I_{Ks} channel has slow activation and deactivation kinetics, which allows the KCNQ1 channels to inactivate over longer depolarisation periods. I_{Ks} channels are expressed in various body tissues and modulate important physiological functions [1, 3, 7, 8, 28]. The most important role of cardiac I_{Ks} is the slow repolarisation phase of the cardiac action potential. Mutations in I_{Ks} channels are associated with long QT syndromes, Jervell and Lange-Nielsen syndrome, and familial atrial fibrillation [8, 25].

1.8.5.4 The Inward Rectifier (Kir2.X/I_{K1}) Potassium Channels

The inward rectifier K⁺ channels Kir2.X (Kir2.1, Kir2.2 and Kir2.3) regulate cardiac I_{K1}. I_{K1}, the inward rectification current, can be described as a novel current that rectifies in the inward direction [25, 53]. It plays an important role to stabilise the membrane potential in the heart [25].

The structure of the I_{K1} channel is composed of four subunits. Unlike the other voltage gated channels each subunit of Kir2.X contains only two transmembrane domains, M1 and M2 [7, 8, 53]. The density of I_{K1} in ventricular myocytes is generally greater than that in atrial myocytes, where it illustrates a substantial and complete inward rectification, with a marked negative conductance slope at depolarised potentials when compared to atrial myocytes. This may cause a different morphology of action potentials in atrial and ventricular myocytes [7, 8, 25].

1.9 Thesis Overview

Chapter 1 gives a brief background of the fundamental elements involved in cardiac electrophysiology. Chapter 2 will explain the gene mutations involved in the SQT syndromes and its consequences on the QT interval. Chapter 3 contains the methodology and Short QT model developments while Chapter 4-7 presents results computed from the single cell, transmural 1D, 2D and 3D models of WT, SQT4, SQT5 and SQT6 mutations. The main objective of the current study was to investigate the functional behavior of the SQT mutation and investigate the arrhythmogenic consequences of the Short QT mutations using 1D and 2D tissue models of the human ventricle cell.

1.10 References

- [1] R. R. O’Rahilly, Basic Human Anatomy: Regional study of human structure. Philadelphia: Saunders, 1983.
- [2] W. F. Boron. and E. L. Boulpaep, Medical physiology, 3rd edition. Elsevier - Health Sciences Division, pp. 147-529, Feb 2012.
- [3] R. H. Whitaker, “Anatomy of the heart,” *Medicine (Baltimore)*, vol. 34, no. 5, pp. 163–165, May 2006.
- [4] Guyton and Hall, Medical physiology, 11th edition, Elsevier Inc, pp. 45-75, July 2005.
- [5] M. J. Godman, M. E. De Bakey et.al., heart: electrical impulses from pacemaker, Art, from Encyclopædia Britannica
Online, accessed May 2, 2017,
<http://www.britannica.com/EBchecked/media/64469/Electrical-conduction-in-the-heart-in-healthy-individuals-is-controlled>.
- [6] C. Antzelevitch, “M cells in the human heart,” *Circ. Res.*, vol. 106, no. 5, pp. 815–817, Mar. 2010.
- [7] Pinnell, S. Turner, and S. Howell, “Cardiac muscle physiology,” *Contin. Educ. Anaesth. Crit. Care Pain*, vol. 7, no. 3, pp. 85–88, Jun. 2007.
- [8] B. Alberts, A. Johnson, J. Lewis, M. Raff, K. Roberts, and P. Walter, “Principles of membrane transport,” 4th edition, New York: Garland Science, 2002.
- [9] J. M. Berg, J. L. Tymoczko, and L. Stryer, “The transport of molecules across a membrane may be active or passive,” W.H. Freeman, pp. 530-600, 2002.
- [10] D. U. Silverthorn, Human physiology: An integrated approach, 5th edition, San Francisco: Benjamin Cummings, pp. 250-300, 2009.
- [11] A. O. Grant, “Cardiac ion channels,” *Circ. Arrhythm. Electrophysiol.*, vol. 2, no. 2, pp. 185–194, Apr. 2009.
- [12] R. Plonsey, R.C. Barr, “Bioelectricity: A quantitative approach”, 3rd edition, Springer, 2007.
- [13] R. C. Little, W.C. Little, “Physiology of the heart and circulation,” 4th edition, Chicago: Year book Medical, pp 53-100, 1989.
- [14] Membrane Biology, Encyclopedia Britannica. [Online]. Available: <https://www.britannica.com/science/membrane-biology>. [Accessed: 21-Jun-2017].
- [15] G. Bojanov, “Blood pressure, heart tones, and diagnoses, in handbook of cardiac anatomy, physiology, and devices”, Humana Press, pp. 243–255, 2009.

- [16] B. R. Choi, T. Liu, and G. Salama, "Adaptation of cardiac action potential durations to stimulation history with random diastolic intervals," *J. Cardiovasc. Electrophysiol.*, vol. 15, no. 10, pp. 1188–1197, Oct. 2004.
- [17] Lauralee Sherwood, "Introduction to physiology and homeostasis. From cells to systems," 8th edition, Yolanda cossio, pp. 90-91, 2009.
- [18] N.M. Muthayya," Cell physiology, In: N.M. Muthayya," cell, human physiology", Jaypee brothers' medical publishers, 4th edition, pp.14-15, 2011.
- [19] G. Loussouarn et al., "Physiological and pathophysiological insights of Nav1.4 and Nav1.5 comparison," *Front. Pharmacol.*, vol. 6, pp. 1-20, Jan. 2016.
- [20] D. Bers, "Excitation-contraction coupling and cardiac contractile force". Springer 2nd edition, pp. 1-18, 2001.
- [21] Enno de Lange and J. P .Kucera, " The transfer functions of cardiac tissue during stochastic pacing", *biophysical journal*, vol. 96, pp. 294-311, Jan 2009.
- [22] J. R. Hume and A.O. Grant, "Agents used in cardiac arrhythmias In: basic and clinical pharmacology" (chapter 14), McGraw-Hill, 12th edition, 2012.
- [23] A. M. Katz, *Physiology of the heart*, Lippincott Williams and Wilkins, 5th edition pp. 60- 176, Nov. 2010.
- [24] P. A. Izzo, *Handbook of cardiac anatomy, physiology, and devices*. Springer, pp. 215-233, 2015.
- [25] A. N. Lopatin, C.G. Nichols, "Inward rectifiers in the heart: An update on I(K1) *J Mol Cell Cardiol*, vol 33, pp. 625–638, 2001.
- [26] R. M. Anderson, "The Gross physiology of the cardiovascular system". Tucson, AZ: Racquet Press, 2nd edition, pp.3-15, 2012.
- [27] M. Xin, E. N. Olson, and R. Bassel-Duby, "Mending broken hearts: cardiac development as a basis for adult heart regeneration and repair," *Nat. Rev. Mol. Cell Biol.*, vol. 14, no. 8, pp. 529–541, Aug. 2013.
- [28] A. Mobasher, R. Lewis, J. E. J. Maxwell, C. Hill, M. Womack, and R. Barrett-Jolley, "Characterization of a stretch-activated potassium channel in chondrocytes," *J. Cell. Physiol.*, vol. 223, no. 2, pp. 511–518, May 2010.
- [29] M. J. Lab, "Contraction-excitation feedback in myocardium. Physiological basis and clinical relevance.," *Circ. Res.*, vol. 50, no. 6, pp. 757–766, Jun. 1982.
- [30] M. J. Lab, "Mechanoelectric feedback (transduction) in heart: concepts and implications," *Cardiovasc. Res.*, vol. 32, no. 1, pp. 3–14, Jul. 1996.
- [31] P. Kohl and U. Ravens, "Cardiac mechano-electric feedback: past, present, and prospect," *Prog. Biophys. Mol. Biol.*, vol. 82, no. 1–3, pp. 3–9, May 2003.

- [32] M. R. Franz, D. Burkhoff, D. T. Yue, and K. Sagawa, “Mechanically induced action potential changes and arrhythmia in isolated and in situ canine hearts,” *Cardiovasc. Res.*, vol. 23, no. 3, pp. 213–223, Mar. 1989.
- [33] E. Drouin, F. Charpentier, C. Gauthier, K. Laurent, H. Le Marec, “Electrophysiologic characteristics of cells spanning the left ventricular wall of human heart: evidence for presence of M cells,” *J. Am. Coll. Cardiol.*, vol. 26, pp. 185–192, Jul. 1995.
- [34] J. Jalife, M. Delmar, J. Anumonwo, O. Berenfeld, and J. Kalifa, *Basic cardiac electrophysiology for the clinician*. 2nd edition, John Wiley & Sons, 2011.
- [35] I. Adeniran, M. J. McPate, H. J. Witchel, J. C. Hancox, and H. Zhang, “Increased vulnerability of human ventricle to re-entrant excitation in hERG-linked variant 1 short QT syndrome,” *PLOS Comput. Biol.*, vol. 7, no. 12, p. e1002313, Dec. 2011.
- [36] R. Uauy, P. Mena, and C. Rojas, ‘Essential fatty acids in early life: structural and functional role’, *Proc. Nutr. Soc.*, vol. 59, no. 1, pp. 3–15, Feb. 2000.
- [37] E. K. Schmitt and C. Steinem, “5 Electrochemical analysis of ion channels and Transporters in Pore-Suspending Membranes,” in *Applications of Electrochemistry and Nanotechnology in Biology and Medicine II*, N. Eliaz, Ed. Boston, MA: Springer US, vol. 53, pp. 267–333, 2012.
- [38] C. M. Armstrong and B. Hille, “Voltage-gated ion channels and electrical excitability,” *Neuron*, vol. 20, no. 3, pp. 371–380, Mar. 1998
- [39] F. Lehmann-Horn and K. Jurkat-Rott, Voltage-gated ion channels and hereditary disease, *Physiol. Rev.*, vol. 79, no. 4, pp. 1317–1372, Jan. 1999.
- [40] L. Shen, “Principles of computational modelling in neuroscience, David Sterratt, Bruce Graham, Andrew Gillies and David Willshaw,” *Brief. Bioinform.*, vol. 13, no. 3, pp. 390–392, May 2012.
- [41] Stephan E. Lehnart, *Transport of ions and small molecules across membranes*, University Medical Centre Göttingen Georg August University, Göttingen, Germany Andrew R. Marks Columbia University, New York, NY, 2007.
- [42] Y. Chen-Izu et al., “Na⁺ channel function, regulation, structure, trafficking and sequestration,” *J. Physiol.*, vol. 593, no. 6, pp. 1347–1360, Mar. 2015.
- [43] F.-Y. Lee, J. Wei, J.-J. Wang, H. Liu, T. Shih, and C.-I. Lin, “Electromechanical properties of Purkinje fibre strands isolated from human ventricular endocardium,” *J. Heart Lung Transplant*, vol. 23, no. 6, pp. 737–744, Jun. 2004.
- [44] I. Bodi, G. Mikala, S. E. Koch, S. A. Akhter, and A. Schwartz, “The L-type calcium channel in the heart: The beat goes on,” *J. Clin. Invest.*, vol. 115, no. 12, pp. 3306–3317, Dec. 2005.

- [45] F. Hofmann, V. Flockerzi, S. Kahl, and J. W. Wegener, “L-type Cav1.2 calcium channels: From *In vitro* findings to *In vivo* function,” *Physiol. Rev.*, vol. 94, no. 1, pp. 303–326, Jan. 2014
- [46] D. Lipscombe, “L-type calcium channels highs and new lows”, American Heart Association, pp 981–987, March 2014.
- [47] K. D. Keef, J. R. Hume, and J. Zhong, “Regulation of cardiac and smooth muscle Ca²⁺ channels (Cav1.2a, b) by protein kinases,” *Am. J. Physiol. Cell Physiol.*, vol. 281, no. 6, pp. C1743–C1756, Dec. 2001.
- [48] Z. Buraei and J. Yang, “Structure and function of the β subunit of voltage-gated Ca²⁺ channels,” *Biochim. Biophys. Acta*, vol. 1828, no. 7, pp. 1530–1540, Jul. 2013.
- [49] M. Endo, “Calcium-induced calcium release in skeletal muscle,” *Physiol. Rev.*, vol. 89, no. 4, pp. 1153–1176, Oct. 2009.
- [50] Tim Taylor, “The muscular system - The musculoskeletal system.” [Online]. Available: <http://www.schoolbag.info/biology/mcat/53.html>.
[Accessed: 25-May-2017].
- [51] D.M. Bers. Cardiac excitation–contraction coupling. *Nature*. 2002;415: 198–205. doi:10.1038/415198a.

CHAPTER 2

Cardiac Arrhythmias and Diseases

2.1 Introduction

In general, sinus rhythm refers to the normal rhythm of the heart, where the electrical activity initiated in the SA node further spreads into other parts of the heart through the cardiac conduction system. Normal adult heart rates range between 60 to 100 beats/min. Any abnormality in the sinus rhythm is referred as an arrhythmia, which stands for something ‘without rhythm’. In cardiology, arrhythmia results in an irregular contraction, which reduces the heart’s ability to pump efficiently and, in severe cases, causes death. Many cardiac structural or electrophysiological diseases can lead to arrhythmias. This Chapter will describe a few of the most common of these diseases. It is worth noting that many of the cases described below are often not distinct from each other [1].

2.1.1 Bradycardia

Bradycardia can be described as a slow heart rate. It can be caused by a defect in the parasympathetic regulatory system. Trained athletes often exhibit bradycardia. A very slow heart rate can reduce the amount of oxygen and nutrients delivered to the body, which can put strain on the organs. Bradycardias are also linked with Sinus Exit and AV-nodal block [2, 3].

2.1.2 Tachycardia

Tachycardia is associated with the fast-cardiac activation. Generally, it is linked to a fast-pacing ectopic pacemaker or the presence of re-entrant spiral waves, that can make the heart more susceptible to tachycardia. Dizziness, palpitation and chest pain are the most common symptoms in patients with tachycardia. In severe conditions, it can lead to unconsciousness and cardiac arrest [2, 3].

2.1.3 Fibrillation

Fibrillation also refers to fast and irregular cardiac activation, but it is marked by the presence of multiple re-entrant spiral waves instead of one as in tachycardia [2]. Fibrillation can cause

severe effects on cardiac output by significantly impairing the synchronised contraction of the heart. More irregular conduction patterns and ECG waveforms are found with fibrillation as compared to tachycardia [2, 3]. Atrial fibrillation, which can be sustained for long periods, is the most common form of cardiac fibrillation [4]. While ventricular fibrillation, in most cases, immediately leads to a heart attack and can cause death, it has also been observed that atrial fibrillation can provoke ventricular fibrillation, heart attack, stroke and, in few cases, sudden death [5, 6].

2.1.4 Ischemia

Ischemia is usually caused by a lack of blood flow to a certain region of the heart, which can result in the formation of dead cells. These regions can reduce the heart's ability to contract efficiently. They can also contribute to the break-up of regular propagation waves and lead to re-entry [3].

2.2 Genetic Mutation Induced Cardiac Arrhythmias

For several years, researchers have tried to discover the answers to many unresolved cardiac phenomena which have no links to the cardiac structure [7]. Finding the defects in cardiac genes was a big revolution in cardiology and electrophysiology. Genetic studies have revealed that most of the gene mutations have no significant effects on impairing cardiac functions [7]. However, some gene mutations can alter different properties of the heart. For example, mutations in the SCN5A, encoding I_{Na} , can lead to the reduced excitability of the heart and may lead to Sinus node exit block [7, 8]. Mutation in CACNA1C, encoding α subunit of Cav1.2 can lead to SQT / Brugada syndrome, which can cause AF/VF, palpitation or sudden cardiac death [9].

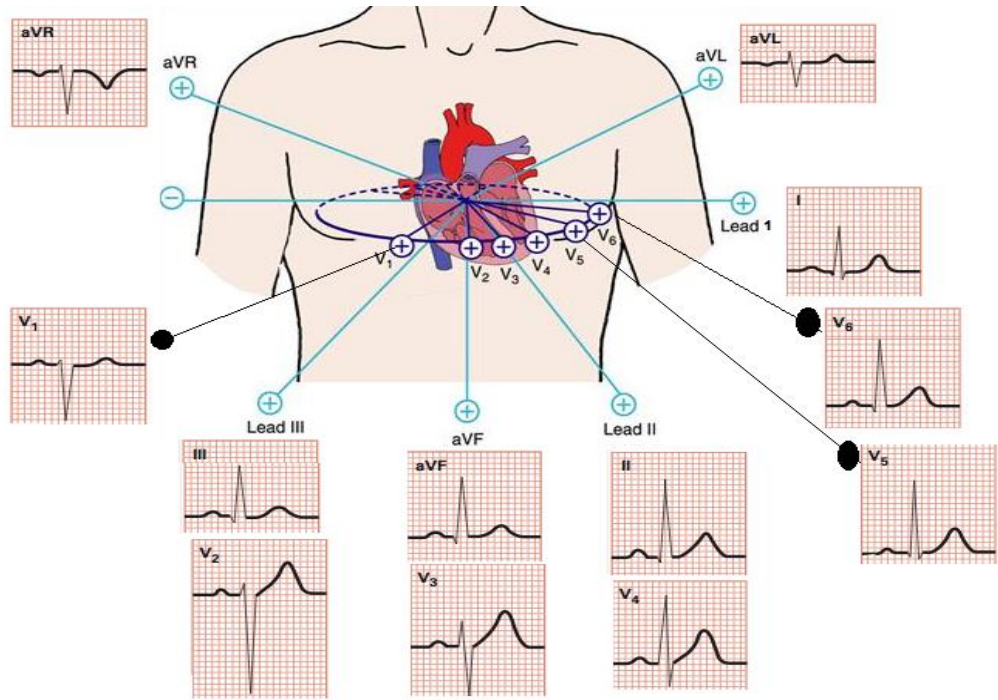
2.3 SQT Syndrome, QT Intervals and ECGs

A syndrome is defined as a condition characterised by a group of symptoms which consistently occur together. The QT syndromes are linked to the abnormal morphology of the QT interval on ECGs. In electrophysiology, ventricular depolarisation and repolarisation are represented by the QT interval on the electrocardiogram. The QT interval is the time between the beginning of the Q and the end of T-wave (Figure 2.1b). An ECG records the electrical activity of the heart; each heart beat can be described as a train of waves, arching away from the baseline [10].

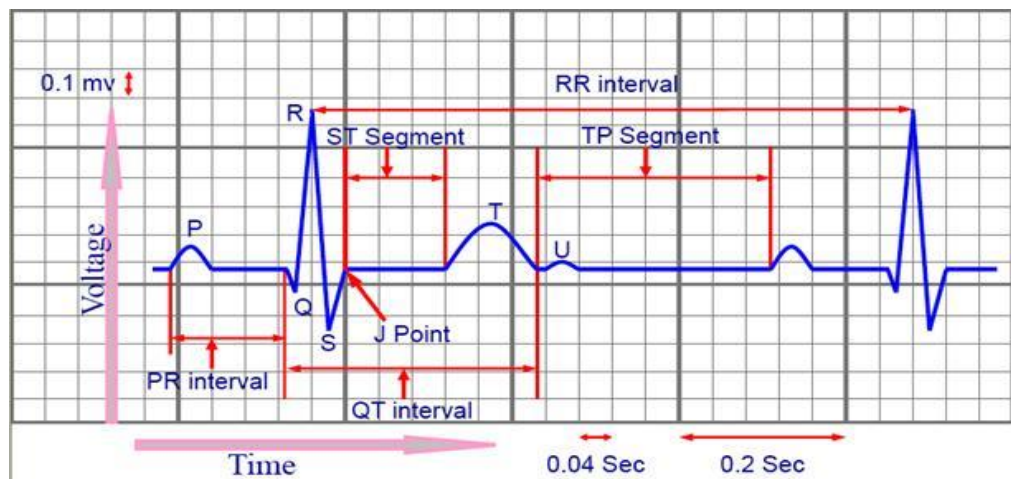
These deflections, labelled as P, Q, R, S and T on each of its deflection points, on an ECG describe the time dependent transformation of electrical activity in the heart [10].

The ECG is divided into the following sections [10]:

- P-wave; a small low voltage deflection on Figure 2.1b, which is caused by the depolarisation of the atria, as the depolarisation impulse propagates from the SA node through the atria [10].
- PQ-interval describes the time between the beginning of the P-wave and the beginning of the QRS complex. It is the time gap between the beginning of atrial depolarisation and the beginning of ventricular depolarisation. The only transmission route of the depolarisation impulse from atria to ventricles is the AV node, because an electrically inert fibrous ring separates the atria from the ventricles in a normal heart. The AV node slows down the cardiac conduction from the atria to the ventricles, allowing the atria to contract and empty their contents before the depolarisation impulse conducts through the bundle of His and the right and left bundle branches into the right and left ventricles [10].
- The QRS complex has the largest-amplitude section of the ECG. It represents the ventricular depolarisation. The downward deflection in figure 2.1b describes the initial depolarisation of the ventricular wall before the depolarisation spreads in the right and left ventricles [10].
- The QT-interval represents the total time between the start of ventricular depolarisation and the end of ventricular repolarisation [10].
- The ST segment is the time between the end of the S-wave (commonly known as the J- point) and the beginning of the T-wave [10].
- The T-wave describes the process of ventricular repolarisation. As the action potential duration of epicardium cells are shorter than the endocardium, a repolarisation process occurs first in the epicardium, followed by the repolarisation of the endocardium cells which causes the T-wave to have an upright structure [10].



(a)



(b)

Figure 2.1: Schematic representation of a cardiac electrocardiogram. a) An ECG is a plot of voltage (mV) on the y-axis against the time on the x-axis. A 12 lead ECG explains the electrical activity of the heart at different positions on the cardiac system. The y-axis of the ECG graph represents the amplitude of the wave deflections i.e. 10 mm equals 1 mV with standard calibration (10 small boxes are equal to 1 mV, as shown in 2.1b). 1 mm (small) horizontal box represents time equals to 40 ms. b) An ECG waveform illustrating the P, Q, R, S and T waves representing the atrial and ventricular depolarisation and repolarisation on the ECG [Modified from 11 and 55].

Based on the duration of the QT interval, QT syndromes are divided into two distinct pathological clinical entities, Long QT and Short QT syndromes [12]. The QT abnormalities can be congenital or acquired. The congenital QT syndromes are linked with the mutations in the regulatory protein coding genes or in the ion channel subunits with an autosomal inheritance or sporadic pattern. Acquired QT abnormalities are more common than the congenital form. Drug induced prolonging of QT intervals are the most common cases of the acquired QT form [23]. Researchers have been working on Long QT Syndrome (LQTS) since 1856 [12]. In contrast to LQTS, SQTs are described by an abnormally short QT interval on the ECG with an increased risk of atrial and ventricular arrhythmias [12, 13]. Short QT syndrome is a rare, inherited genetic disease, associated with ion channel defects. It is a relatively new clinical entity as compared to the LQTS [13]. Genetic studies have concluded that the shortening of the QT interval can be associated with cardiac ion channel defects [14, 15, 16], or in other words, SQT syndrome is caused by a mutation in the proteins that regulate the kinetics of the ion channels [17]. In 2000, Gussak et al. [26] described SQTs as a new clinical entity, associated only with hyperkalaemia, hypercalcaemia, hyperthermia, acidosis and endocrine disorders. The inherited nature and arrhythmogenic probabilities of SQTs were further described by Gaita et al [54].

The inherited long and short QT syndromes are identified by an abnormal QT interval on the ECG. The QT duration changes with the heart rate; the faster the heart rate, the shorter the QT interval. Cardiologists still struggle to assess the upper and the lower boundaries of the normal QT interval. Two different population-based studies have helped to set the upper and the lower limit of the QT interval [14, 26, 54]. These studies have described the distribution of QTc intervals in a large population of healthy individuals, where QTc refers to the corrected QT interval (QTc, using the Bazett formula) [19, 20, 21, 24],

$$QTc = \frac{QT}{\sqrt{RR}} \quad (2.1)$$

The QTc is the corrected QT interval in milliseconds (ms), QT is the measured QT interval for each beat, while RR is the time interval between the two consecutive beats (Figure 2.1b). Based on these studies, the normal QTc values for males are between 350 ms to 450 ms and for females they are between 360 ms to 460 ms [20, 21, 22]. However, the QTc intervals of both healthy population and individuals affected by SQTs or LQTS, overlap considerably in practice [21, 22].

Patients are diagnosed with extremely short QT (QTc < 300 ms) intervals in initial SQT studies [21, 22]. More recent studies have described individuals with QTc intervals of 320 ms and 360 ms. QTc < 330 ms is very rare in a generally healthy population. According to the population-based studies, QTc < 340 ms prevails only in 0.5% of a generally healthy public [22]. Table 2.1 describes the QT scale based on different studies for defining the spectrum of QT intervals, extending from extremely short to tremendously long in males and females [20, 21, 22].

QTc interval for males (ms)	QTc interval for females (ms)	Classification
>470	> 480	LQTS even if not symptomatic
450-470	460-480	LQTS when supported by symptoms, family history or additional test
390-450	400-460	LQTS possible if supported by additional test: repeated ECG, T wave morphology and exercise
360-390	370-400	Normal QT interval
360-300	370-340	SQTS if supported by symptoms and family history
<300	<340	SQTS even if not symptomatic

Table 2.1: The QT scale based on different studies, illustrating the QT spectrum, extending from extremely short to enormously long in males and females. SQTS refers to the Short QT Syndrome and LQTS refers to the Long QT Syndrome [Adopted from 23].

2.4 Short QT Syndrome

The SQT syndrome is a very rare cardiac electrical disorder. SQTS probands have structurally normal hearts, without any evident disease and with extremely short QT intervals, due to abbreviated atrial and ventricular effective refractory periods [26]. The shortening of the effective refractory period in SQTS patients can increase atrial and ventricular susceptibility to premature stimuli, which can lead to the development of atrial and ventricular fibrillation [19, 20, 24, 25]. This irregular atrial rhythm leads to palpitations, shortness of breath, dizziness, chest tightness and fatigue. Clinical data have suggested that the probability of ventricular arrhythmias and sudden cardiac death is also very high in SQT

patients. Sudden cardiac death (40%) and palpitation (30%) are the most common symptoms [24, 25]. Genetic studies of patients suggest, a high risk of SCD over their entire life span, with a peak between their 20s and 40s [26, 27]. Gollob et al. [28] have proposed a more specific criterion for the diagnosis of SQT syndrome patients, and it was based on four different analyses, i.e. ECG, clinical history, family history and genotype [28].

Six different variants of the short QT syndromes have been diagnosed to date, SQT1 to SQT6. The first variant of SQTs was identified in the KCNH2 (hERG) gene, which regulates the rapidly rectifying outward component of potassium current I_{Kr} [15, 30]. SQT2 is associated with the KCNQ1 gene, which regulates the slow-delayed outward rectifier potassium channel I_{Ks} [15, 16, 46]. A mutation in the Kir2.1 channel responsible for the inwardly-rectifying potassium channel current (I_{K1}), encoded by KCNJ2 gene, is mentioned as SQT3 [15, 16, 46]. SQT4, SQT5 and SQT6 are more recently identified variants; these mutations are associated with CACNA1C, CACNB2b and CACNA2D1 genes [29] respectively. The SQT4, SQT5 and SQT6 mutations are associated with a combined short QT/ Brugada syndrome phenotype [29]. An elevated ST-segment on the ECG is observed in these cases along with the QT abbreviations [29, 30]. The sixth variant of short QT syndrome is the newest among all of them and is associated with CACNA2D1 [51].

2.4.1 SQT1/ KCNH2/hERG/ I_{Kr} Mutation

The first variant of short QT syndrome (SQT1) was discovered in two separate families, where members of both families exhibited the hERG mutation. The first family exhibited a C to G substitution, while a C to A substitution was displayed by the other family, which led to an Asparagine to Lysine substitution in hERG/ I_{Kr} channel [31]. In a different study, the same exchange of Asparagine to Lysine at position 588 was discovered in a 3rd family [31, 33]. Affected individuals displayed abbreviated QT (QTc) intervals on ECGs, 225-240 ms over the normal heart range [33, 46].

The KCNH2 gene encodes an α -subunit of the Kv11.1 channel, which regulates the outward component of the potassium current (I_{Kr}) [15, 31, 33, 46]. The human hERG gene N588K is located between S5-P linker in the extracellular region, as shown in Figure 2.2, and inactivation of the Kv11.1 channel is dominated by this region. Data shows the N588K mutation shifts the inactivation of hERG channels towards more positive potentials, which leads to an increase of I_{Kr} function [32, 33, 46].

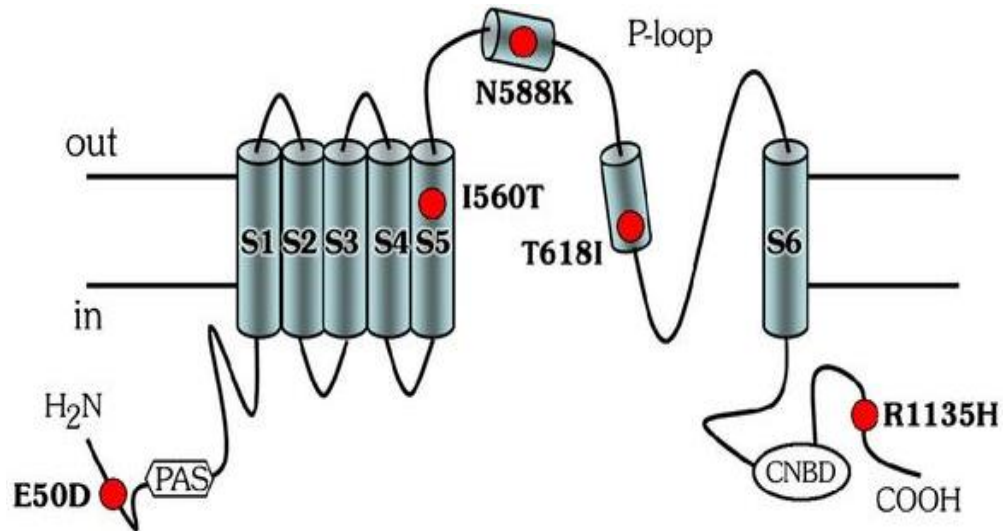


Figure 2.2: The proposed topology of the α subunit of Kv11.1 channel encoded by the KCNH2 gene, illustrating the position of the N588K mutation. The N588K mutation is located in the S5-P-loop linker region of hERG. The S5-P-loop region is known to influence the inactivation process of the hERG channel [33].

2.4.2 SQT2 / KCNQ1/ I_{Ks} Gene Mutation

KCNQ1 protein is co-expressed with KCNE1; it regulates the slow delayed rectifier current I_{Ks} . KCNE1 is the β -subunit of the basic I_{Ks} channel complex that controls trafficking and behaviour of the KCNQ1 α subunit [45]. The second variant of SQTs was identified in a 70-year-old man, who effectively recovered from ventricular fibrillation. The patient's genetic data revealed an amino acid substitution of Valine to Leucine at position 307 (V307L) in the α subunit of KCNQ1 channel protein. A QTc interval of ~ 300 ms was observed on an ECG [32, 45]. *In vitro* electrophysiological studies suggest a shift of the voltage reliance of the activation towards more negative voltages for the V307L mutation. It also accelerates the time duration of activation, by not only impairing the activation, but also by terminating inactivation [31, 46]. Incorporating these changes into a human ventricular model described an enhanced influx of I_{Ks} during the repolarisation phase, which has been believed to reduce the total duration of the action potential, preceding an abbreviated QT interval [31, 45, 46]. However, due to insufficient experimental animal data, the exact mechanisms responsible for the increased risk of arrhythmogenesis in SQTs patients, has not been fully classified [45, 46]. Electrophysiological studies of SQT2 mutation have also shown considerable shortening of effective refractory periods (ERP), and significant changes in the transmural distribution of the AP across the ventricular wall [36]. The second case of SQT syndrome was diagnosed in a baby girl, born at 38 weeks. The patient was diagnosed with bradycardia

and irregular rhythm before birth [35]. Her heart rate was noticeably bradycardic after birth. ECGs revealed atrial fibrillation, slow ventricular response and an abbreviated QT interval of 280 ms [35, 36]. Further investigation revealed a substitution of Valine to Methionine at position 141 (V141M) in the S1 domain of the KCNQ1 protein channel. The baby girl had no family history of SQT syndromes, and therefore, it is defined as a *de novo* mutation in the infant [35].

2.4.3 SQT3 /KCNJ2/ I_{Ks} Mutation

The SQT3 was first reported in 2005 when an asymptomatic 5-year-old child was diagnosed with an irregular ECG during a routine clinical examination; data showed a QTc interval of 315 ms with a tall narrow T-wave [37]. Further investigation revealed her mother showed no complications in her ECG, while her father showed a history of palpitations and pre-syncope episodes [37]; the ECGs revealed a proband and her father had almost identical QT intervals and T-wave morphology. The father's family history had unremarkable ECGs and no reported sudden cardiac deaths [37, 38].

Genetic screening was performed for proband and her father showed no mutations in KCNH2 or KCNQ1; instead they exhibited a G to A substitution at position 514 in KCNJ2 [37]. This resulted in an amino acid substitution of Aspartate (D) to Asparagine (N) at position 172 in the Kir2.1 K protein. Genetic data of the family suggested that the D172N mutation may have developed as a *de novo* in the father, in the transmembrane region of Kir2.1, Figure 2.3. As discussed in Chapter 1, Kir2.1 protein, responsible for the inwardly rectifying current I_{K1} is expressed in both human atrial and ventricular tissue [39]. It contributes during phase 4 of the AP to maintain the negative resting potential of both atrial and ventricular tissue [40]. This property of I_{K1} channel makes its presence very important in ventricular repolarisation. A loss of I_{K1} expression during phase 4 can lead to Andersen's syndrome [41], while a gain of function (V93I mutation) can cause a genetic AF [42, 43, 44].

In Figure 2.3, the D172N mutation is situated in the transmembrane region of the Kir2.1 channel, and studies showed that the region is involved in the binding of polyamines and Mg²⁺ ions, which accelerates the inward rectification of the Kir2.1 channel current [36]. An increase in outward I_{K1} with a rightward voltage shift of peak current cannot be seen experimentally for D172N mutations due to the impairment of that binding [36, 38].

To understand the heterozygous state of the SQT3 mutation, a co-expression of WT and D172N channels were incorporated in computer modelling which resulted in an increase of the outward component of I_{K1} current that is approximately halfway between WT and D172N [38].

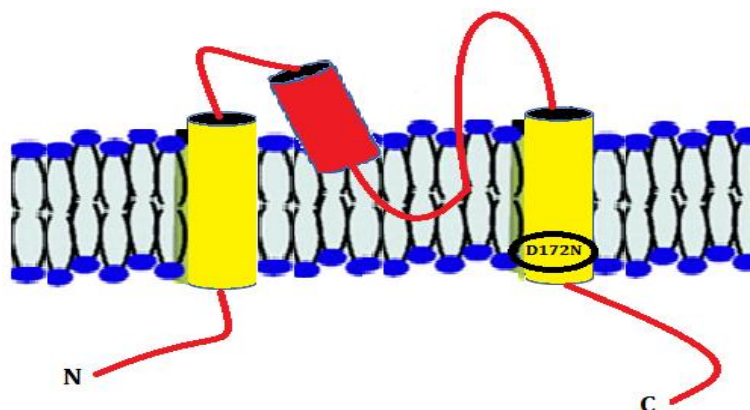


Figure 2.3: The proposed topology of the Kir2.1 channel, indicating the location of the D172N mutation in the transmembrane region of the I_{K1} channel [38].

Unlike the 1st three variants of Short QT syndrome, the 4th, 5th and 6th variants are relatively new, and are associated with the L-type calcium channel [9]. The 4th and the 5th variant of SQTs were diagnosed by Antzelevitch et al. [9] in 2007. They analysed 82 probands for BrS and early repolarisation syndromes. Data revealed that seven probands (8.5%) had mutations in the genes encoding the $\alpha 1$ and beta $\beta 2$ subunits of L-type calcium channels [47, 48]. ECGs showed short QT intervals (<360 ms) associated with an elevated ST segment [9, 49].

2.4.4 SQT4/ CACNA1C/ G490R/ I_{CaL} Mutation

The 1st variant of SQT4 was found in a white Turkish male, diagnosed with atrial fibrillation with a QTc interval < 346 ms. He had a family history of SCD, his brother having died of sudden cardiac arrest. Further analysis showed an elevated ST segment in V1 to V2 leads [9], while the QT interval demonstrated very insignificant rate dependence. Coronary angiography ruled out any structural defects. The study carried out by Antzelevitch et al. [9, 27] described the proband with a mutation in exon 10 of CACNA1C. Genetic data revealed a heterozygous substitution of an Adenine to Guanine, which leads to a substitution of an Arginine to Glycine at position 490, and they named it G490R [9]. Two of his daughters were also diagnosed with G490R mutation, having QTc interval of 360 ms and 373 ms, respectively [9, 27, 49].

2.4.5 SQT4/ CACNA1C/ A39V/ I_{CaL} Mutation

The 2nd variant of SQT4 was found in a 44 years old European male. The ECG exhibited a marked ST segment elevation in lead II and a prominent J-wave in lead III. The family history showed a mother with syncope leading to SCD, while the 75-year-old father showed no significant ECGs. Genetic screening of the proband showed a heterozygous C to T transition at position 116 in exon 2 of CACNA1C protein, which anticipated a Valine to Alanine substitution at position 39, A39V [9, 47, 49].

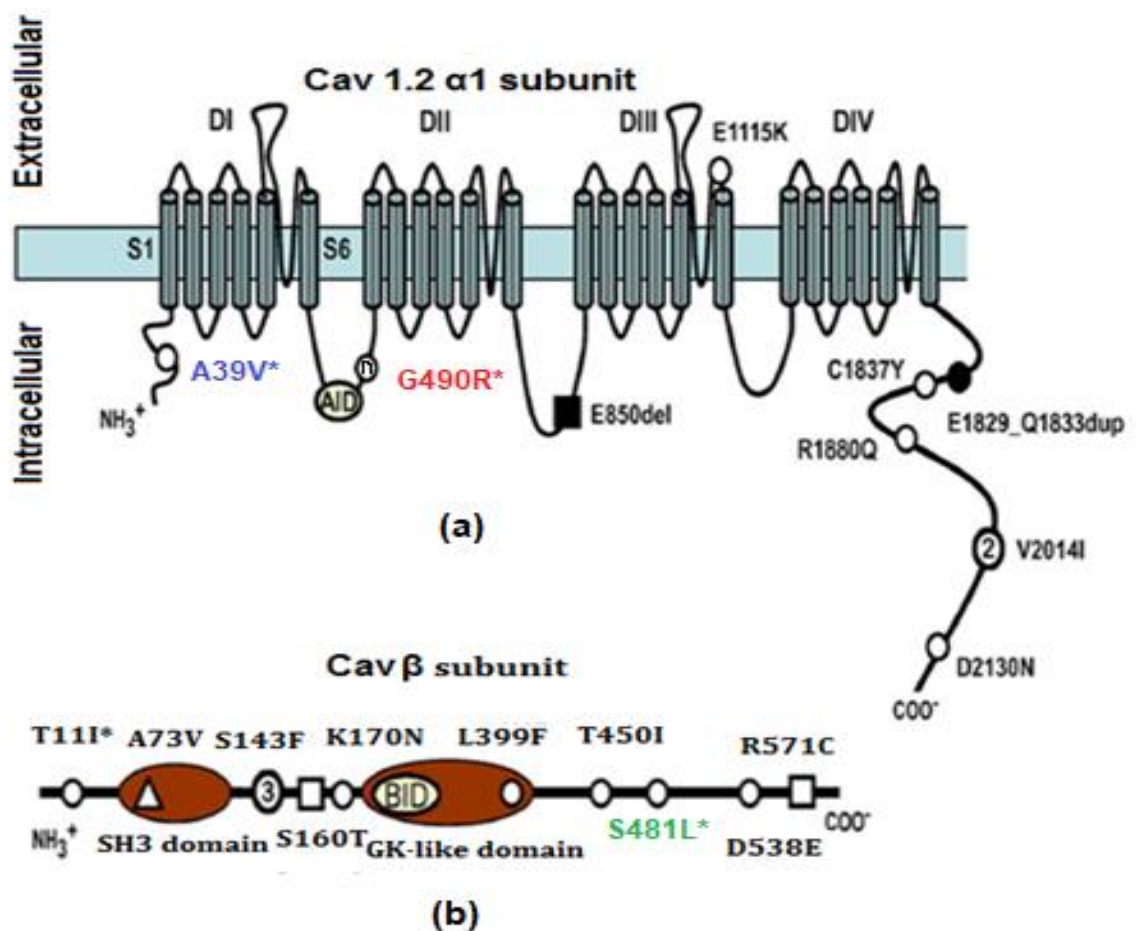


Figure 2.4: The proposed topology of the α and β subunits of Cav1.2 channel [Modified from 9]. (a) α subunit: both mutations are positioned within a highly-preserved region of the Cav1.2 protein. G490R (red) is positioned in the cytoplasmic linker between domains I and II, while A39V (blue) is positioned near the N-terminus, (b) β subunit: the mutation S481L (green) is situated in the C-linker region of the β subunit of Cav1.2 [49].

Studies have suggested that the A39V mutation impairs the trafficking of the Cav1.2 channel, which will result in a loss of current function. In control variants, the channels' surface expression increases vigorously when an α subunit of the Cav1.2 channel is co-expressed with Cav β , as Cav β binds the intracellular I-II linker of the α subunit [47].

Recently, researchers have found mutations in the N-terminus of Nav1.5 [48], which displays trafficking defects similar to A39V. Based on these studies, it can be assumed that, in general the N-terminus structure is associated with trafficking of cardiac voltage-gated channels [47, 48].

G490R, identified by Antzelevitch et al [9], is located in the I-II linker of the Cav1.2 channel. Experimental data showed a reduction of current density to a large extent in the presence of the G490R mutation. The central and peripheral pattern of fluorescence suggests a normal trafficking pattern for the G490R channels [9].

2.4.6 SQT5/ CACNB2b β 2/ S481L / I_{CaL} Mutation

The β -subunit of Cav1.2 channel, encoded by the CACNB2b gene, is involved in the gating and traffic modulation of L-type calcium channels [49]. The first reported case of CACNB2b mutation was that of a 25-year-old European male, diagnosed with ventricular fibrillation (VF) which led to SCD [9, 47, 49]. ECG presented a QTc interval of 330 ms, with a curved shape ST-segment elevation [9]. Genetic data of the proband revealed a heterozygous transition from C to T at position 1442, in exon 13, that anticipates a Leucine to Serine substitution at position 481 (S481L) of CACNB2b [9]. His 23-year-old brother also displayed symptoms of syncope since the age of 21. A further clinical and genetic investigation of the family revealed a positive phenotype in 6 family members based on the elevation of ST-segment (ST segment elevation >2 mm) and a QTc interval < 360 ms and 370 ms in males and females respectively. S481L was present in all six family members with a positive phenotype. A few family members exhibited tall peaked T-waves, with shorter-than-normal QT. The mutation is located in the C-linker region of β subunit of Cav1.2 as shown in Figure 2.4 [9, 49].

2.4.7 CACNA2D1 α 2 δ -1 S755T/SQT6 I_{CaL} Mutation

The 6th variant of SQTS was identified by Templin et al. [51] in a 17-year-old Caucasian female. She suffered a sudden loss of consciousness due to ventricular fibrillation, which

was successfully stopped after two external defibrillation shocks. The ECG explains a QT interval of 317 ms (QTc 329 ms) with tall, narrow T-waves. Genetic screening of the patient diagnosed no mutations in *KCNH2*, *KCNQ1*, *KCNJ2*, *CACNA1C* and *CACNB2b* genes. Genetics revealed a heterozygous transition from G to C at position 2264 in *CACNA2D1* assuming a Threonine to Serine substitution at position 755 (S755T). S755T is positioned at the external C-terminal of $Ca_v \alpha_2$, Figure 2.5 [51]. The S755T mutation leads to a loss of current function with barium as the charge carrier. Surprisingly, surface biotinylation experiments detected no defects in trafficking. However, Templin et al. observed positive shifts in the activation and inactivation curves, consistent with those found in cells lacking $Ca_v \alpha_2\delta_1$ [51].

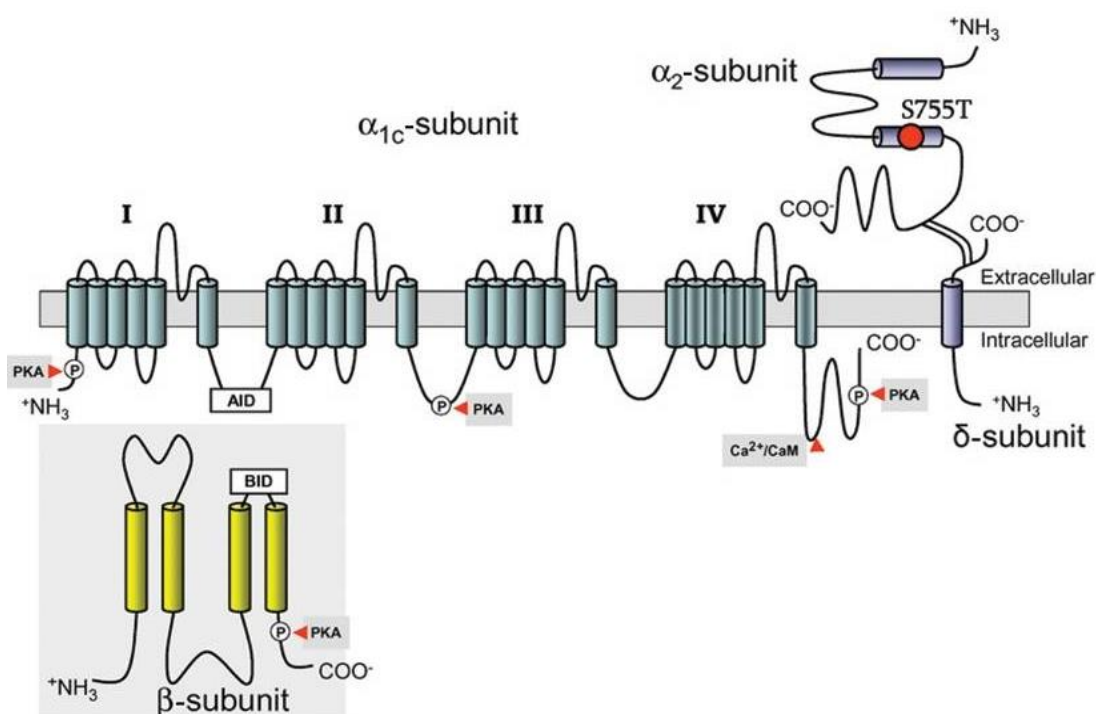


Figure 2.5: The predicted topology of the $\alpha_2\delta_1$ subunit of the *CACNA2D1* gene, indicating the position of the S755T (red circle) mutation at the external C terminal of the δ -1 subunit of the *CACNA2D1*. AID, α -subunit-interacting domain. BID, β -subunit-interacting domain [51].

2.5 Discussion

To date, SQTS mutations are identified in three potassium ion channels *KCNH2*, *KCNQ1*, *KCNJ2* and three calcium ion channels, *CACNA1C*, *CACNB2b*, *CACNA2D1* respectively. Probands having calcium channel mutations lead to diseases, such as Brugada syndrome or

early repolarisation syndrome [9, 30]. Table 2.2 described a short summary of all the SQTs and the genes related to them [8, 15, 47, 48].

SQTS	Gene	Mutation	Functionality
SQT1	KCNH2 (Brugada et al., 2004; Hong, Bjerregaard, Gussak, & Brugada, 2005)	N588K	Increase in I_{Kr} current.
SQT2	KCNQ1 (Bellocq et al., 2004)	V307L	Increase in I_{Kr} current.
SQT3	KCNJ2 (Priori et al., 2005)	D172N	Increase in I_{Kr} current.
SQT4	CACNA1C (Antzelevitch et al., 2007)	A39V G490R	Reduction in L-Type Ca^{2+} -channel current
SQT5	CACNB2b (Antzelevitch et al., 2007)	S481L	Reduction in L-Type Ca-channel current
SQT6	CACNA2D1 (Templin et al., 2011)	S755T	Reduction in L-Type Ca-channel current

Table 2.2: A short summary of all the Short QT Syndromes, the relevant experimental data, mutations and their effects on the relevant channel currents. SQT1 affects the I_{Kr} , SQT2 affects I_{Ks} , SQT3 is linked to I_{K1} , while SQT4-6 affects the α , β , and $\alpha2\delta-1$ subunits of the L-Type calcium channel current, I_{CaL} [8, 15, 47, 48].

Studies have suggested that the majority of SQTs patients have an autosome dominant pattern [8, 15, 47, 48] i.e. a single effected gene from one parent can cause this defect. A very rare case of SQTs is classified as sporadic and occurs in people with no apparent history of short QT syndrome in their family [8, 47, 48]. Short QT syndrome appears to be rare. At

least 100 cases have been identified worldwide since the condition was discovered in 2000 [47, 53]. However, the condition may be underdiagnosed because some affected individuals never experience any symptoms. In the healthy population, the prevalence of QTc <340 ms is approximately 0.5% [53, 54]. Males with QTc <330 ms and females with QTc <340 ms should be diagnosed with SQTS even if they don't show any related symptoms [53, 54], since these values are extremely unlikely in the general healthy population. The individuals with QTc intervals < 360 ms for males and QTc < 370 ms for females are considered diagnostic of SQTS only when backed by the symptoms or family history, as these QTc intervals overlap with the healthy population [21, 52].

The majority of patients diagnosed with Short QT Syndrome have been males at the age from new-born to very old [52]. Haissaguerre et al. [53] reported that, among patients with idiopathic ventricular fibrillation, the QT interval was shorter in patients with early repolarisation than in those without, suggesting a correlation of early repolarisation and QT interval shortening [53, 54]. Gene mutations reduce the heart's ability to pump blood effectively. The most common symptoms found in SQT patients are palpitations and unexplained syncope (loss of consciousness) [15, 47, 48, 53, 54]. This abnormal repolarisation appears as a short QT interval on an electrocardiogram [15, 53]. Cardiac arrest is another frequent symptom (34%) [47].

2.6 References

- [1] S. E. Rosenbaum and B. A. Kats, “Cardiac arrhythmia: Mechanisms, diagnosis and management,” *The Journal of the American Medical Association*, vol. 274, no. 14, pp. 1171–1172, Oct. 1995.
- [2] M. Baruscotti et al., “Deep bradycardia and heart block caused by inducible cardiac-specific knockout of the pacemaker channel gene *Hcn4*,” *Proc. Natl. Acad. Sci. U. S. A.*, vol. 108, no. 4, pp. 1705–1710, Jan. 2011.
- [3] P. Koenig, Z. Hijazi, and F. Zimmerman, *Essential paediatric cardiology*. McGraw Hill Professional, 2004.
- [4] S. Nattel, A. Shiroshita-Takeshita, B. J. J. M. Brundel, and L. Rivard, “Mechanisms of atrial fibrillation: lessons from animal models,” *Prog. Cardiovasc. Dis.*, vol. 48, no. 1, pp. 9–28, Aug. 2005.
- [5] E.J. Benjamin, P.A. Wolf, R.B. D’Agostino, H. Silbershatz, W.B Kannel, D. Levy “Impact of atrial fibrillation on the risk of death: the Framingham Heart Study”. *Circulation*, vol 10, pp. 946–952, 1998.
- [6] E. Anter, M. Jessup, and D. J. Callans, “Atrial fibrillation and heart failure,” *Circulation*, vol. 119, no. 18, pp. 2516–2525, May 2009.
- [7] C. Marionneau et al., Specific pattern of ionic channel gene expression associated with pacemaker activity in the mouse heart, *J. Physiol*, pp.223–234, 2005.
- [8] T. D. Butters et al., “Mechanistic links between Na^+ channel (*SCN5A*) mutations and impaired cardiac pacemaking in sick sinus syndrome,” *Circ. Res.*, vol. 107, no. 1, pp. 126–137, Jul. 2010.
- [9] C. Antzelevitch et al., “Loss-of-function mutations in the cardiac calcium channel underlie a new clinical entity characterized by ST-segment elevation, short QT intervals, and sudden cardiac death,” *Circulation*, vol. 115, no. 4, pp. 442–449, Jan. 2007.
- [10] F. M. Kusumoto, *ECG interpretation: From pathophysiology to clinical application*. Springer Science & Business Media, 2009.
- [11] S. Rolskov Bojsen et al., “The acquisition and retention of ECG interpretation skills after a standardized web-based ECG tutorial—a randomised study” *BMC Med. Educ.*, vol. 15, p. 36, 2015.
- [12] J. P. P. Smits, M. W. Veldkamp, and A. A. M. Wilde, “Mechanisms of inherited cardiac conduction disease,” *EP Europace Journal*, vol. 7, no. 2, pp. 122–137, Jan. 2005.
- [13] R. Dumaine et al., “Multiple mechanisms of Na^+ channel-linked long-QT syndrome,” *Circ. Res.*, vol. 78, no. 5, pp. 916–924, May 1996.

- [14] J. J. Schott et al., “Cardiac conduction defects associate with mutations in SCN5A,” *Nat. Genet.*, vol. 23, no. 1, pp. 20–21, Sep. 1999.
- [15] C. E. Clancy and R. S. Kass, “Inherited and acquired vulnerability to ventricular arrhythmias: Cardiac Na⁺ and K⁺ Channels,” *Physiol. Rev.*, vol. 85, no. 1, pp. 33–47, Jan. 2005.
- [16] R. S. Kass and A. J. Moss, “Long QT syndrome: novel insights into the mechanisms of cardiac arrhythmias,” *J. Clin. Invest.*, vol. 112, no. 6, pp. 810–815, Sep 2003.
- [17] M. R. Franz, “Mechano-electrical feedback in ventricular myocardium,” *Cardiovasc. Res.*, vol. 32, no. 1, pp. 15–24, Jul. 1996.
- [18] B. Rudic, R. Schimpf, and M. Borggrefe, “Short QT syndrome – review of diagnosis and treatment,” *Arrhythmia Electrophysiol. Rev.*, vol. 3, no. 2, pp. 76–79, Aug. 2014.
- [19] C. Giustetto, Di Monte F, C. Wolpert, et al. Short QT syndrome: clinical findings and diagnostic-therapeutic implications. *European Heart Journal*, pp.2440- 2447, 2006.
- [20] B. Surawicz and S. R. Parikh, “Differences between ventricular repolarisation in men and women: Description, mechanism and implications,” *Ann. Noninvasive Electrocardiol.*, vol. 8, no. 4, pp. 333–340, Oct. 2003.
- [21] S. Viskin, ‘The QT interval: Too long, too short or just right’, *Heart Rhythm*, vol. 6, no. 5, pp. 711–715, May 2009.
- [22] E. S. Kaufman, “Mechanisms and clinical management of inherited channelopathies: long QT syndrome, Brugada syndrome, catecholaminergic polymorphic ventricular tachycardia, and short QT syndrome,” *Heart Rhythm*, vol. 6, no. 8 Suppl, pp. S51-55, Aug. 2009.
- [23] E. Burns, “Short QT Syndrome - Life in the fast lane ECG library LITFL,” LITFL • Life in the Fast Lane Medical Blog, 16-Mar-2011.
- [24] F. Extramiana, P. Maury, P. Maison-Blanche, A. Duparc, M. Delay, and A. Leenhardt, “Electrocardiographic biomarkers of ventricular repolarisation in a single family of short QT syndrome and the role of the Bazett correction formula,” *Am. J. Cardiol.*, vol. 101, no. 6, pp. 855–860, Mar. 2008.
- [25] O. Anttonen et al., “Differences in twelve-lead electrocardiogram between symptomatic and asymptomatic subjects with short QT interval,” *Heart Rhythm*, vol. 6, no. 2, pp. 267–271, Feb. 2009.
- [26] I. Gussak et al., “Idiopathic short QT interval: A new clinical syndrome?” *Cardiology*, vol. 94, no. 2, pp. 99–102, 2000.
- [27] C. Patel, G.-X. Yan, and C. Antzelevitch, “Short QT syndrome: From bench to bedside,” *Circ. Arrhythm. Electrophysiol.*, vol. 3, no. 4, pp. 401–408, Aug. 2010.

- [28] M. H. Gollob, C. J. Redpath, and J. D. Roberts, “The short QT syndrome: Proposed diagnostic criteria,” *J. Am. Coll. Cardiol.*, vol. 57, no. 7, pp. 802–812, Feb. 2011.
- [29] G. Vorobiof, D. Kroening, B. Hall, R. Brugada, and D. Huang, “Brugada syndrome with marked conduction disease: dual implications of a SCN5A mutation,” *Pacing Clin. Electrophysiol. PACE*, vol. 31, no. 5, pp. 630–634, May 2008.
- [30] P.-S. Chen and S. G. Priori, “The Brugada Syndrome,” *J. Am. Coll. Cardiol.*, vol. 51, no. 12, pp. 1176–1180, Mar. 2008.
- [31] I. Adeniran, “Modelling the short QT Syndrome gene mutations: and their role in cardiac arrhythmogenesis”, 2014 edition. New York: Springer, pp.40-112, 2014.
- [32] J. M. Cordeiro, R. Brugada, Y. S. Wu, K. Hong, and R. Dumaine, “Modulation of I_{Kr} inactivation by mutation N588K in KCNH2: A link to arrhythmogenesis in short QT syndrome,” *Cardiovasc. Res.*, vol. 67, no. 3, pp. 498–509, Aug. 2005.
- [33] D. Hu et al., “The Phenotypic spectrum of a mutation hotspot responsible for the short QT syndrome,” *JACC Clin. Electrophysiol.*, p. 320, Feb. 2017.
- [34] C. Antzelevitch, “M Cells in the human heart,” *Circ. Res.*, vol. 106, no. 5, pp. 815–817, Mar. 2010.
- [35] K. Hong et al., “*De novo* KCNQ1 mutation responsible for atrial fibrillation and short QT syndrome in utero,” *Cardiovasc. Res.*, vol. 68, no. 3, pp. 433–440, Dec. 2005.
- [36] H. Zhang, S. Kharche, A. V. Holden, and J. C. Hancox, “Repolarisation and vulnerability to re-entry in the human heart with short QT syndrome arising from KCNQ1 mutation—A simulation study,” *Prog. Biophys. Mol. Biol.*, vol. 96, no. 1–3, pp. 112–131, 2008.
- [37] N. M. Plaster et al., “Mutations in Kir2.1 cause the developmental and episodic electrical phenotypes of Andersen’s syndrome,” *Cell*, vol. 105, no. 4, pp. 511–519, May 2001.
- [38] S. G. Priori et al., “A novel form of short QT syndrome (SQT3) is caused by a mutation in the KCNJ2 gene,” *Circ. Res.*, vol. 96, no. 7, pp. 800–807, Apr. 2005.
- [39] J. Tamarg, R. Caballero, R. Gómez, C. Valenzuela, and E. Delpón, “Pharmacology of cardiac potassium channels,” *Cardiovasc. Res.*, vol. 62, no. 1, pp. 9–33, Apr. 2004.
- [40] Y. Kato, H. Masumiya, N. Agata, H. Tanaka, and K. Shigenobu, “Developmental changes in action potential and membrane currents in fatal, neonatal and adult guinea-pig ventricular myocytes,” *J. Mol. Cell. Cardiol.*, vol. 28, no. 7, pp. 1515–1522, Jul. 1996.
- [41] J. M. D. Diego et al., “Ionic and cellular basis for the predominance of the Brugada syndrome phenotype in males,” *Circulation*, vol. 106, no. 15, pp. 2004–2011, Oct. 2002.
- [42] A. O. Verkerk et al., “Role of sequence variations in the human ether-a-go-go-related

- gene (HERG, KCNH2) in the Brugada syndrome,” *Cardiovasc. Res.*, vol. 68, no. 3, pp. 441–453, Dec. 2005.
- [43] S. P. Patel and D. L. Campbell, “Transient outward potassium current, ‘Ito’, phenotypes in the mammalian left ventricle: underlying molecular, cellular and biophysical mechanisms,” *J. Physiol.*, vol. 569, no. Pt 1, pp. 7–39, Nov. 2005.
- [44] G. Seeböhm, C. R. Scherer, A. E. Busch, and C. Lerche, “Identification of specific pore residues mediating KCNQ1 inactivation a novel mechanism for long QT syndrome,” *J. Biol. Chem.*, vol. 276, no. 17, pp. 13600–13605, Apr. 2001.
- [45] K. Hong et al., “De novo KCNQ1 mutation responsible for atrial fibrillation and short QT syndrome *in utero*,” *Cardiovasc. Res.*, vol. 68, no. 3, pp. 433–440, Dec. 2005.
- [46] P. C. Viswanathan, R. M. Shaw, and Y. Rudy, “Effects of I_{Kr} and I_{Ks} heterogeneity on action potential duration and its rate dependence,” *Circulation*, vol. 99, no. 18, pp. 2466–2474, May 1999.
- [47] N. Weiss and A. Koschak, Eds., *Pathologies of calcium channels*. New York: Springer, pp.225-238, 2013.
- [48] J. Clatot et al., “Dominant-negative effect of SCN5A N-terminal mutations through the interaction of Nav1.5 α -subunits,” *Cardiovasc. Res.*, vol. 96, no. 1, pp. 53–63, Oct. 2012.
- [49] P. L. Hedley et al., “The genetic basis of long QT and short QT syndromes: A mutation update,” *Hum. Mutat.*, vol. 30, no. 11, pp. 1486–1511, Nov. 2009.
- [50] I. Adeniran, J. C. Hancox, and H. Zhang, “In silico investigation of the short QT syndrome, using human ventricle models incorporating electromechanical coupling,” *Front. Physiol.*, vol. 4, pp. 1-13, Jul. 2013.
- [51] C. Templin et al., “Identification of a novel loss-of-function calcium channel gene mutation in short QT syndrome (SQTS6),” *Eur. Heart J.*, vol. 32, no. 9, pp. 1077–1088, May 2011.
- [52] R. Kobza et al., “Prevalence of long and short QT in a young population of 41,767 predominantly male Swiss conscripts,” *Heart Rhythm*, vol. 6, no. 5, pp. 652–657, May 2009.
- [53] M. Haïssaguerre et al., “Sudden cardiac arrest associated with early repolarization,” *N. Engl. J. Med.*, vol. 358, no. 19, pp. 2016–2023, May 2008.
- [54] R. Schimpf, C. Wolpert, F. Gaita, C. Giustetto, and M. Borggrefe, “Short QT syndrome,” *Cardiovasc. Res.*, vol. 67, no. 3, pp. 357–366, Aug. 2005

[55] R. Latham, The Twelve Leads-Looking at the Heart from Different Direction, Online, accessed December 2, 2017,
https://www.ole.bris.ac.uk/bbcswebdav/institution/Faculty%20of%20Health%20Sciences/MB%20ChB%20Medicine/Year%203%20Medicine%20and%20Surgery%20-%20Hippocrates/Cardiology%20-%20ECG/page_12.h

CHAPTER 3

Mathematical Electrophysiology

3.1 Introduction

Advanced computing plays a significant role in understanding the functionality of human organs. Hodgkin and Huxley published the first mathematical model of an Action Potential (AP) in the squid giant axon [1]. Their formulations of the ionic channels are based on passive ion currents. The cell membrane and different ionic currents were represented by different electrical components making up a simple electric circuit. This approach made their model very simple and open to wider applications. Almost all of the modern mathematical models of APs are based on Hodgkin and Huxley style equations. Denis Noble in 1962 used these equations for the first time to model the action potentials of the canine Purkinje fibre [2].

3.2 Cell Equivalent Circuit

The cell membrane acts as a capacitor, which separates intercellular and extracellular charges. The ion channels, pumps and exchangers act as a passage for ion translocation. The ion movement is dependent on the membrane potential and has an associated resistance, which can change over the course of time and voltage. Hence, cell membranes can be represented as variable resistors. The ion channels, pumps or exchangers are independent of each other and are aligned in parallel. A cell membrane is not a perfect insulator; Ohm's law describes the resistance experienced by the ionic current flowing across the cell membrane [3]:

$$R = \frac{V_m}{I_{ion}} \quad (3.1)$$

where R is the resistance in ohms (Ω), V_m is the potential of the membrane in volts (V) and I_{ion} is the ionic current in amperes (A). The membrane conductance (g , $\mu\text{S}/\text{cm}$) can be described as a reciprocal of the resistance [3]:

$$g = \frac{I_{ion}}{V_m} \quad (3.2)$$

To understand the physiological behaviour of the cardiac myocyte, it is very important to recall the basic phenomena of permeability and conduction as discussed in Chapter 1. Both allow the ions to flow across the cell membrane, but with completely different characteristics [4].

Permeability describes the flow of ions across the cell membrane in either direction. The permeability of a system at equilibrium, or near equilibrium, can be mathematically described as [5]:

$$J = -P_{\text{ion}} \frac{\partial C_{\text{ion}}}{\partial x} \quad (3.3)$$

Where J is the diffusion flux ($\text{mol}/\text{cm}^2\text{s}$), P_{ion} is the permeability coefficient, ∂C_{ion} is the difference in ion concentration on both sides of the cell membrane (mol/cm^3). Based on these equations, Ohm's law can be modified as:

$$I_{\text{ion}} = g_{\text{ion}} (V_m - E_{\text{ion}}) \quad (3.4)$$

where V_m is the membrane potential (mV), g_{ion} is the conductance ($\mu\text{S}/\text{cm}$) and E_{ion} is the transmembrane potential (mV) at equilibrium when there is no net flux across the membrane [5].

The plasma membrane of a cell acts as a parallel plate capacitor with a dielectric between the two plates. A conductive current can be described due to the movement of single ions across the cell membrane under the influence of an electromotive force. The capacitance of a parallel plate capacitor [3, 5] is equal to

$$C_m = \frac{Q}{V} \quad (3.5)$$

The charge stored by the capacitor is:

$$Q = C_m V \quad (3.6)$$

The capacitive current can be derived as [3, 4]:

$$I_c = \frac{dV}{dt} C_m \quad (3.7)$$

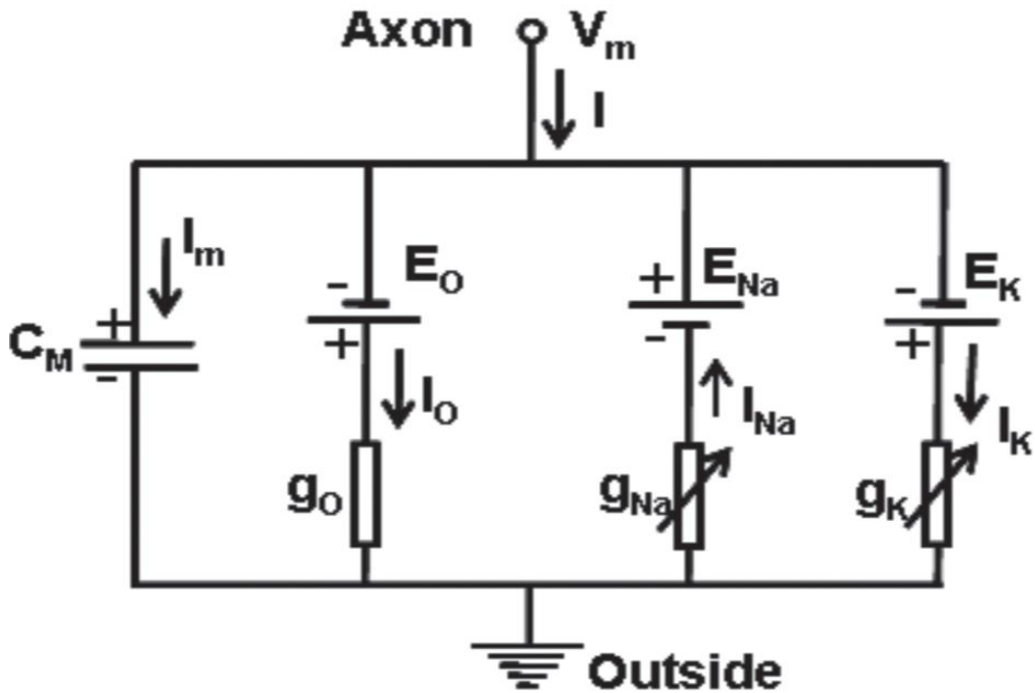


Figure 3.1: Electric Circuit equivalent of an excitable axonal cell membrane. I_K , I_{Na} and I_o represents the K^+ , Na^+ and leakage currents respectively. E_K , E_{Na} , E_o and g_K , g_{Na} , g_o represents the equilibrium potentials and conductance of the relevant current channels, while V_m and C_m represents the membrane potential and capacitance [Modified from 6].

The membrane current is the combination of ionic and capacitive current [3, 5],

$$I_m = I_{ion} + I_c \quad (3.8)$$

$$I_m = I_{ion} + \frac{dV}{dt} C_m \quad (3.9)$$

While the total ionic current can be described as [5]

$$I_{ion} = I_K + I_{Na} + I_L \quad (3.10)$$

Figure 3.1 explains the circuit analogy of a cell membrane [5].

The electromotive forces can change the membrane potentials. Any change in membrane potential can directly affect the flow of a specific ion by changing the conductance of the voltage gated channels for that specific ion [3, 7].

3.2.1 Nernst Equations

Nernst described the magnitude of forces acting on the ions on either side of a cell membrane [8]. The electromotive forces for a specific ion generate a concentration gradient for that ion across the membrane and control its diffusion [7]. An electrical

potential is generated due to the movement of those ions and prevents further ion diffusion across the membrane. An equilibrium is established, referred to as a Nernst potential. Simple thermodynamic laws govern the Nernst equation [8, 9].

The diffusive flux in Equation 3.3 can be described in terms of the diffusion coefficient, D_x (cm^2/s) and the local concentration (C_x) [9]:

$$J_x = -D_x \frac{\partial C_x}{\partial x} \quad (3.11)$$

The diffusive flux in-terms of ion mobility, U_x ($\text{m}^2\text{s}^{-1}\text{V}^{-1}$), local concentration, C_x (mol/m^3) and local potential, Φ (V) can be described as:

$$J_x = -U_x C_x \frac{\partial \Phi}{\partial x} \quad (3.12)$$

Based on the fundamental insights of Nernst and Planck, the above two diffusion fluxes are additive [8]:

$$J_x = -D_x \frac{\partial C_x}{\partial x} - U_x C_x \frac{\partial \Phi}{\partial x} \quad (3.13)$$

To construct the Nernst equation, recall the Nernst-Einstein relationship [8, 9]:

$$D_x = U_x \frac{RT}{Z_x F} \quad (3.14)$$

where R represents the universal gas constant ($\text{cal}/\text{mol} \cdot \text{K}$), T is the absolute temperature (K), F is the Faraday constant and Z_x is the valence number of a selective ion [5]. It should also be understood that the potential across the membrane is due to the ionic current, and not due to flux. The valence and Faraday constants can be used to convert diffusion into an ionic current density (I_x) [5].

$$I_x = J_x Z_x F \quad (3.15)$$

Using equation 3.13

$$I_x = (J_x Z_x F_x) = -D_x F Z_x \left(\frac{\partial C_x}{\partial x} + \frac{F Z_x C_x}{RT} \frac{\partial \Phi}{\partial x} \right) \quad (3.16)$$

In the Nernst equation, the equilibrium is established when the electrical gradient is balanced by the concentration gradient [8, 9], i.e., no net current passes through the cell membrane $I_x = 0$. Equation 3.16 can be rewritten as:

$$\frac{\partial \Phi}{\partial x} = - \left(\frac{RT}{Z_x C_x F} \right) \frac{\partial C_x}{\partial x} \quad (3.17)$$

Let's assume that equation 3.17 varies only in one direction, i.e. the x direction [5]. Integrating the cell from outside to inside gives the following equation:

$$\Phi_i - \Phi_o = \frac{-Z_x F}{RT} \ln \left(\frac{[C_x]_i}{[C_x]_o} \right) \quad (3.18)$$

$$V_m = \frac{-Z_x F}{RT} \ln \left(\frac{[C_x]_i}{[C_x]_o} \right) \quad (3.19)$$

where V_m is defined as the difference between the intracellular and extracellular potentials [5]:

$$V_m = \Phi_i - \Phi_o \quad (3.20)$$

This is the potential at which the rate of diffusion of an ion from one side of the membrane is balanced by the opposite side of the membrane. This is known as Nernst equilibrium, or more commonly as an equilibrium potential [3, 7, 8, 9].

3.3 The Hodgkin-Huxley Model

The first model for cellular ionic activity was developed by Alan Lloyd Hodgkin and Andrew Fielding Huxley in 1952 [1]. They were awarded the Nobel Prize for this achievement. Their cell model was capable of producing the Action Potential of the Squid Giant Axon, and the model was based on the ionic conductance of Na^+ and K^+ currents [1].

The Hodgkin-Huxley (HH) model formulations are still used as the basis for most later ionic channel model developments. It can be used in modern computational methods to estimate the mandatory parameters needed to replicate the experimental data. They concluded that a cell membrane has freely moving particles, which allows ion movement across the cell. They developed mathematical equations for ionic currents [1] and numerically solved these nonlinear ordinary differential equations using a simple computing device (a hand mechanical calculator), although their work did not identify ion channel proteins. Following further study, it has now been established that proteins within the membrane act as channels and gates or pathways. It has already been discussed that these protein pores are selectively permeable to different ions. The permeability of these pores is dependent on numerous aspects, including voltage sensitivity and ligand binding [10, 11]. The ionic data obtained from these cell models explain the activity of different ion channels, they show rapid transitions depending on the structural changes in proteins. Markov chain models illustrate these configurational changes more precisely through state diagrams. Markov chain models

explain ion channel kinetics more precisely than HH models [13]. The only disadvantage of Markov chain models with respect to the HH models is the complexity in calculating the obligatory variables from the experimental data.

3.3.1 The Hodgkin-Huxley Cell Model Formulation

Alan Lloyd Hodgkin and Andrew Fielding Huxley quantified the casual link between the membrane potential and the currents. Based on their experimental data, they were able to derive individual equations for three different ionic currents. This can be described by Figure 3.1, which represents their cell model. Using Figure 3.1, the following currents are used to construct the Hodgkin-Huxley cell model [1, 2, 5, 15].

- a) I_{Na} the inward Na^+ current (pA/pF),
- b) The outward component of K^+ current, I_K (pA/pF), and
- c) I_L , the leakage current translocated by other unclassified ions.

The total ionic current can be described as in equation 3.21:

$$I_{ion} = I_{Na} + I_K + I_L \quad (3.21)$$

The membrane potential and current illustrate a linear relationship (in the squid giant axonal membrane). The ionic current, I_{ion} , moves under the influence of the instantaneous function of potential. The driving force is equivalent to $V_m - E_x$, where V_m represents the membrane potential and E_x is the equilibrium potential of a particular protein channel, permeable to that specific ion [1, 5]. The second factor is the ion conductance, which describes the change in permeability of ion channels (the activation and inactivation of ion channels under the influence of membrane potential) [1, 5].

$$g_x = \frac{I_x}{V_m - E_x} \quad (3.22)$$

Conductance, g_x ($\mu S/cm$) represents a steady change in the permeability of a specific ion across the membrane. The mathematical equations for the Huxley and Hodgkin cell model for three ionic currents can be described as [5]:

$$I_{Na} = g_{Na}(V_m - E_{Na}) \quad (3.23)$$

$$I_K = g_K(V_m - E_K) \quad (3.24)$$

$$I_L = g_L(V_m - E_L) \quad (3.25)$$

Where V_m is the membrane potential (mV), g_{Na} , g_K , g_L are the conductance of Na^+ , K^+ and leakage current channels while I_{Na} , I_K and I_L and E_{Na} , E_K and E_L are the respective channel currents and equilibrium potentials. These equations quantitatively described the movement of the ionic current and the gating of ionic channels. It was postulated that the movement of ionic current is regulated by the membrane potential, and ions move in and out of the cell under the influence of a driving force. Any change in membrane potential can allow ions to translocate from the intracellular region to the extracellular region or vice versa. The opening or closing states of the channel gates depend on the voltage which regulates the ion movement through the cell membrane [1, 5].

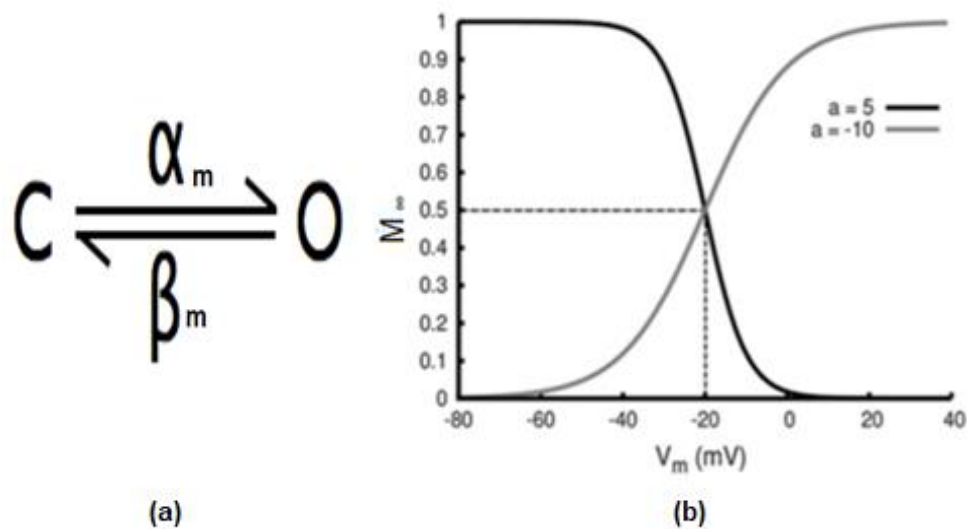


Figure 3.2: A two-state transition diagram of the HH model and the steady state gating variable example. (a) C represents the closed state and O stands for the open state. The transition rate contents, α_m and β_m explain the voltage dependent transition rate from one state to the other state, (b) the relationship between the steady state value of a gating variable (M_∞) and membrane potential (V_m), the sign of gradient (a) will define the direction of the variable. [Modified from 1].

Let's suppose that M is the fraction of gates in the open state, while $(1-M)$ is the fraction of gates in the closed state [1, 5]. The rate of change of the fraction of open gates can be defined as;

$$\frac{dM}{dt} = \alpha(1 - M) - \beta M \quad (3.26)$$

Where $dM/dt=0$ at the steady state. The fraction of open gates (M_∞) at steady state can be defined as,

$$M_\infty = \frac{\alpha}{\alpha + \beta} \quad (3.27)$$

A change in membrane potential will cause a deviation from the steady state and consequently, a change in the fraction of open gates. The time it takes for the channel to return to the steady state is given by the time constant:

$$\tau_M = \frac{1}{\alpha + \beta} \quad (3.28)$$

Based on the fraction of open gates, Hodgkin and Huxley represented the conductance of a channel by:

$$g_{Na} = \bar{g}_{Na} M^3 h \quad (3.29)$$

The final formulation for Hodgkin and Huxley equation for the Na⁺ current is:

$$I_{Na} = \bar{g}_{Na} M^3 h (V_m - E_{Na}) \quad (3.30)$$

where M³ represents three activated sodium channel gates, and h represent the fraction of the inactivated Na⁺ channel. \bar{g}_{Na} represents the maximum Na⁺ conductance. They assumed that potassium channels can be characterised by four identical, distinct voltage dependent activation gates (n), and postulated it as [1, 5, 14]:

$$g_K = \bar{g}_K n^4 \quad (3.31)$$

$$I_K = \bar{g}_K n^4 (V_m - E_K) \quad (3.32)$$

and the leakage current (I_L) carried by other unspecified ions is defined as:

$$I_L = g_L (V_m - E_L) \quad (3.33)$$

All the gates of an individual channel should be in the open state to conduct current. Depolarisation causes the M and n gates of Na⁺ and K⁺ channels to open. However, the h gate of the Na⁺ channel is closed by the depolarisation, resulting in the termination of the entire channel activity [1].

3.4 The Markov Chain Model

Although the Hodgkin-Huxley cell model can reproduce the microscopic characteristics of the currents very precisely, the theory of independent gating has not been supported by experimentation. For an ionic channel to be inactive, it must first be in an activated state. Markov chain models can be described as an alternative method to express the channel conductance (g). The formulation for maximum current flow is similar to the Hodgkin-Huxley model. However, Markov models use a chemical transition formulation to express the channels, instead of different gates [1, 12, 15,16].

The Markov chain model can be described by the state diagrams. These state diagrams illustrate the structural changes of the ion channels. The transition from one state to the other is assumed to be dependent only on the existing state. The HH model's formulation can be described by Markov chain models, but its reverse is not applicable [12, 16]. The Markov chain models describe different conformational states of the channel. The activation and inactivation states are independent of each other, according to the assumptions made by Hodgkin-Huxley formulations. However, Markov models show an interconnection. As compared to the basic HH model, Markov chain models are more complicated, as they contain a larger number of equations. Hence, they are more computationally intensive to solve [12, 16, 17].

3.5 The O'Hara & Rudy Model

Cellular electrophysiology has had a significant impact on modern cardiology and electrophysiology in trying to understand several cardiac structural and electrical diseases in humans [1, 13]. Early cardiac mathematical models were based on non-myocytes or non-human myocytes [13]. To understand a broad range of physiological phenomenon taking place in the heart, the development of an accurate model of healthy human ventricular action potentials (AP) was vital. This required not only extensive experimental data, but the additional missing elements in the Hodgkin-Huxley (HH) model [1, 13].

In 2011, O'Hara and Rudy et al [13] developed a validated mathematical human cardiac cell model by using substantial experimental data from human myocytes. The model responds identically to the pacing rate and premature beats, as in experiments. This model was capable of measuring the shift in intracellular calcium concentrations with every beat, at high pacing rates. The electrophysiological behaviour was observed to be the same as in human heart experiments [13].

To develop such a model, they acquired experimental data from a healthy human ventricular tissue. They modelled the Ca^{2+} dependent versus voltage dependent inactivation of the L-type Ca^{2+} current (I_{CaL}) and explained the kinetics of the transient outward current I_{to} , the rapid delayed rectifier potassium current (I_{Kr}), the $\text{Na}^+/\text{Ca}^{2+}$ exchange (I_{NaCa}) and the inward rectifier currents I_{K1} . They were able to calculate the APD at various physiological cycle lengths and also calculated the rate dependence and restitution of APD. They were able to develop several models for different transmural cell types, based on healthy human mRNA and the protein expression data [13].

L-type Ca^{2+} Current (I_{CaL}) modelling was based on two different studies, Magyar et al [18], estimated the steady state activation and inactivation and current voltage relationship. Fulop et al., [19] studied recovery from inactivation. However, neither model was able to separate Ca^{2+} dependent inactivation (CDI) from voltage dependent inactivation (VDI). They used different charge carriers to measure this effect [13].

O'Hara & Rudy's measurements were carried out at 37°C [13], with Ca^{2+} as the charge carrier, allowing both CDI and VDI, while VDI was allowed only with Ba^{2+} as the charge carrier. The simulated data for Ba^{2+} as the charge carrier showed a monotonically decreasing fractional remaining current, with an increase in membrane potential at all times after the peak current, which is justified as the inactivation is only dependent on the voltage in this case. Results for Ca^{2+} FRC curves were voltage independent, although they did not decrease monotonically with increasing voltage. They postulated that at certain voltages, Ca^{2+} ions caused an additional inactivation, where VDI-alone was relatively weak [13]. Their work validated the proposition that currents carried by Ba^{2+} ions inactivate due to VDI only, while Ca^{2+} current inactivation is caused by both VDI and CDI [13, 20]. To incorporate the concept of VDI and CDI, they introduced a gate n representing the fraction of channels operating in CDI mode, as the inactivation of I_{CaL} channel is dependent on both CDI and VDI [13]. The experimental data was obtained from Kim et al. [21].

A schematic diagram of the human ventricular AP model is described in Figure 3.3 [13]. This design is a modification of the recent dog ventricular model by Decker et al. [22]. It was largely unchanged but, based on new findings, additional targets for CaMK were included in the model. In their model, the formulations of currents represented by the green elements (Figure 3.3) in the model were based on human specific measurements [13].

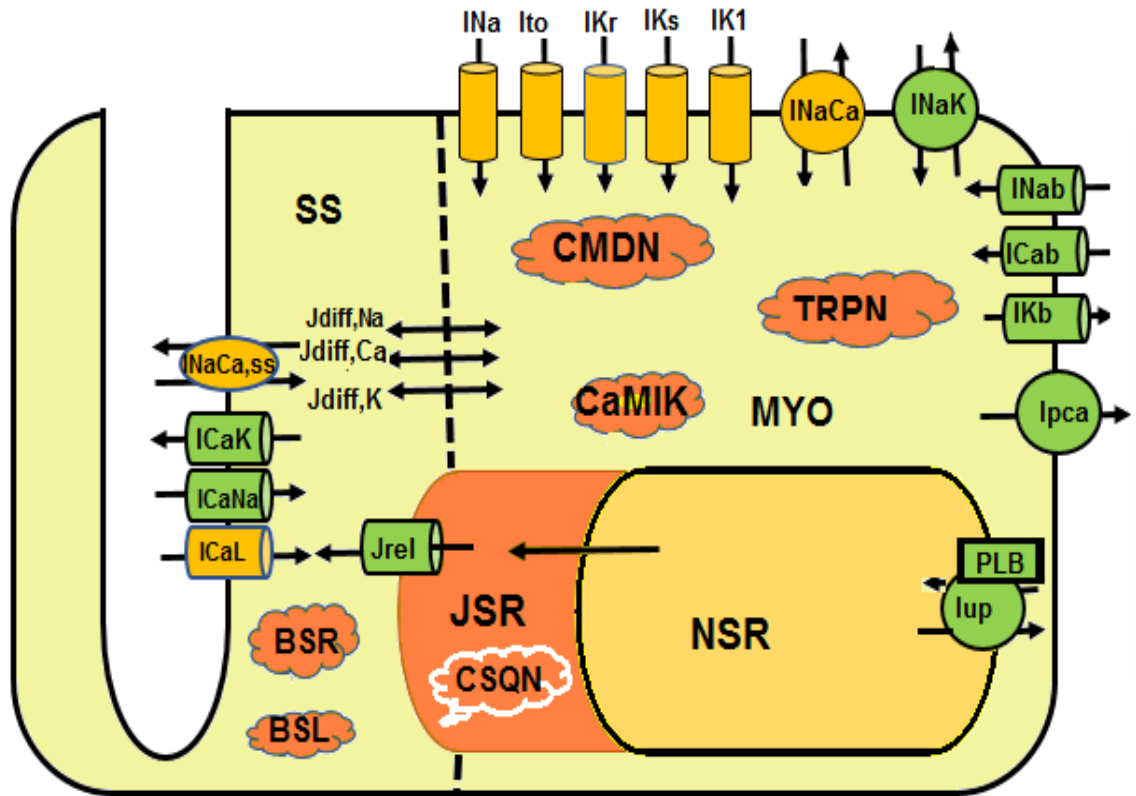


Figure 3.3: A schematic diagram of the O'HRd human ventricular myocyte model [13]. O'HRd Model includes four compartments, the bulk myoplasm (myo), the junctional sarcoplasmic reticulum (JSR), the network sarcoplasmic reticulum (NSR), and the subspace (SS), representing the space near the T-tubules. The myoplasm, subspace and background currents along with the sarcolemmal Ca^{2+} pump current, ionic fluxes, diffusion fluxes and Ca^{2+} buffers labelled in the above figure are defined in Appendix A.

3.6 Development of the SQT4-6 O'Hara & Rudy Models.

3.6.1 The Base I_{CaL} Model

The O'Hara and Rudy et al [13] formulations are modified to model SQT4-SQT6. The ORd I_{CaL} channel current equations were formulated by using data from the Magyar and Fulop et al. model [18, 19]. The O'Hara & Rudy current equations are based on the Hodgkin and Huxley formulations [13]. Computationally, the ORd model is very diverse.

The basic principle of the ORd model made it very simple for computer modelling as more comprehensive Markov models, or drug effects, can be added to the model, if required. Intracellular Ca^{2+} handling and various signalling pathways can be well explained [13].

The model has high stability as it prevents the system of differential-algebraic equations getting overly stiff [13]. The O'Hara & Rudy model formulations for I_{CaL} were thus modified to formulate the SQT4-SQT6 models.

To intergrade the experimentally perceived properties of the control type (WT), SQT4, SQT5 and SQT6, the base I_{CaL} O'Hara & Rudy model equations were modified to include the changes caused by the genetic mutations. These changes included the marked reduction of I_{CaL} current through Cav1.2 channel subunits, although the voltage at peak current remained unchanged for the SQT4 and SQT5 mutations with respect to the control type [23].

3.6.2 The SQT4 O'Hara & Rudy Model

The modified equations of WT, A39V and G490R, I_{CaL} current [23] were obtained by reforming the base model [13] parameters. The experimental current voltage (I-V) relationships for WT, A39V and G490R I_{CaL} were obtained by using the voltage clamp protocols from Antzelevitch et.al [23].

The voltage clamp protocol for the CACNA1C control type was performed for a holding potential of -90 mV with the total simulation time of 250 ms. The clamp voltage range was between -50 mV and 50 mV, with an increment of 10 mV for each step. The same voltage clamp protocol was applied for A39V and G490R. Simulations showed a decrease in the amplitude of A39V and G490R channel currents. The voltage at the peak current remained the same for WT, A39V and G490R, which satisfied the experimental data [23]. The modified model formulation was achieved by minimising the least squared difference between the simulation and the experimental data. The Nelder-Mead Simplex algorithm [48] was used for the minimisation of the new parameters. Equations 3.34-3.45 describe the parameters that yield perfect agreement of the macroscopic currents with respect to the experimental data and produced the best I-V fit. The modified SQT4 model closely reproduced the experimental data for the WT and both mutations.

WT

$$Z_a = 2.0 \quad (3.34)$$

$$\gamma_{Cai} = 0.80\text{ms}^{-1} \quad (3.35)$$

$$\gamma_{Cao} = 0.35\text{ms}^{-1} \quad (3.36)$$

$$\varphi_{CaL} = Z_a \frac{VF^2}{RT} \left(\gamma_{cai} [Ca^{2+}]_{ss} e^{\left(\frac{Z_a VF}{RT}\right)} - \frac{\gamma_{cao} [Ca^{2+}]_o}{e^{\left(\frac{0.995(Z_a VF)}{RT}\right)} - 1.0} \right) \quad (3.37)$$

A39V

$$Z_a = 2.0 \quad (3.38)$$

$$\gamma_{cai} = 0.97 \text{ms}^{-1} \quad (3.39)$$

$$\gamma_{cao} = 0.24 \text{ms}^{-1} \quad (3.40)$$

$$\varphi_{CaL} = 0.88 * Z_a \frac{VF^2}{RT} \left(\gamma_{cai} [Ca^{2+}]_{ss} e^{\left(\frac{Z_a VF}{RT}\right)} - \frac{\gamma_{cao} [Ca^{2+}]_o}{e^{\left(\frac{0.1818(Z_a VF)}{RT}\right)} - 1.0} \right) \quad (3.41)$$

G490R

$$Z_a = 2.0 \quad (3.42)$$

$$\gamma_{cai} = 0.98 \text{ms}^{-1} \quad (3.43)$$

$$\gamma_{cao} = 0.34 \text{ms}^{-1} \quad (3.44)$$

$$\varphi_{CaL} = 0.87 * Z_a \frac{VF^2}{RT} \left(\gamma_{cai} [Ca^{2+}]_{ss} e^{\left(\frac{Z_a VF}{RT}\right)} - \frac{\gamma_{cao} [Ca^{2+}]_o}{e^{\left(\frac{0.1265(Z_a VF)}{RT}\right)} - 1.0} \right) \quad (3.45)$$

3.6.3 The SQT 5 O'Hara & Rudy Model

The voltage clamp protocol for the β_2 subunit of the CACNB2b control type was performed for a holding potential of -90 mV with the total simulation time of 250 ms. The clamp voltage range was between -50 mV and 50 mV, with an increment of 10 mV for each step. The same voltage clamp protocol was applied for the S481L mutation conditions. The modified equations and parameters were obtained by minimising the least squared difference between the simulation and the experimental data. The Nelder-Mead Simplex algorithm [48] was used for the minimisation of the new parameters. Simulations showed a decrease in the amplitude of the S481L channel currents, which showed an agreement with the experimental data [23].

The modified formulation for CACNB2b/ I_{CaL} can be described as:

WT

$$Z_a = 2.0 \quad (3.46)$$

$$\gamma_{\text{Cai}} = 0.76 \text{ms}^{-1} \quad (3.47)$$

$$\gamma_{\text{Cao}} = 0.35 \text{ms}^{-1} \quad (3.48)$$

$$\varphi_{\text{CaL}} = Z_a \frac{VF^2}{RT} \left(\gamma_{\text{cai}} [\text{Ca}^{2+}]_{\text{ss}} e^{\left(\frac{Z_a VF}{RT}\right)} - \frac{\gamma_{\text{cao}} [\text{Ca}^{2+}]_o}{e^{\left(\frac{0.975(Z_a VF)}{RT}\right)} - 1.0} \right) \quad (3.49)$$

S481L

$$Z_{\text{Ca}} = 2.0 \quad (3.50)$$

$$\gamma_{\text{Cai}} = 1.67 \text{ms}^{-1} \quad (3.51)$$

$$\gamma_{\text{Cao}} = 0.35 \text{ms}^{-1} \quad (3.52)$$

$$\varphi_{\text{CaL}} = 4 * Z_a \frac{VF^2}{RT} \left(\gamma_{\text{cai}} [\text{Ca}^{2+}]_{\text{ss}} e^{\left(\frac{2(Z_a VF)}{RT}\right)} - \frac{\gamma_{\text{cao}} [\text{Ca}^{2+}]_o}{e^{\left(\frac{0.995(Z_a VF)}{RT}\right)} - 1.0} \right) \quad (3.53)$$

3.6.4 The SQT6 O'Hara & Rudy Model

The voltage clamp protocol for CACNA2D1 I_{CaL} was performed as follows: the holding potential was -80 mV and the clamp voltage range were between -60 mV and 60 mV, with an increment of 10 mV for each step. The clamp time was 200 ms. The modified formulation of SQT6 model was obtained by minimising the least squared difference between the simulation and the experimental data. The Nelder-Mead Simplex algorithm [48] was used for the minimisation of the new parameters.

The I-V relationship for I_{CaL} demonstrates a marked difference of I-V between the WT and S755T models (almost 69%) (Figure 6.1a), which is in accordance with the experimental data [24].

The modified formulation for CACNA2D1/ I_{CaL} can be described as:

WT

$$Z_a = 2.0 \quad (3.54)$$

$$\gamma_{\text{Cai}} = 1.12\text{ms}^{-1} \quad (3.55)$$

$$\gamma_{\text{Cao}} = 0.052\text{ms}^{-1} \quad (3.56)$$

$$\varphi_{\text{CaL}} = 0.88 * Z_a \frac{VF^2}{RT} \left(\gamma_{\text{cai}} [\text{Ca}^{2+}]_{\text{ss}} e^{\left(\frac{Z_a VF}{RT}\right)} - \frac{\gamma_{\text{cao}} [\text{Ca}^{2+}]_o}{e^{\left(\frac{1.9318(Z_a VF)}{RT}\right)} - 1.0} \right) \quad (3.57)$$

S755T

$$Z_a = 2.0 \quad (3.58)$$

$$\gamma_{\text{Cai}} = 1.25\text{ms}^{-1} \quad (3.59)$$

$$\gamma_{\text{Cao}} = 0.051\text{ms}^{-1} \quad (3.60)$$

$$\varphi_{\text{CaL}} = 0.88 * Z_a \frac{VF^2}{RT} \left(\gamma_{\text{cai}} [\text{Ca}^{2+}]_{\text{ss}} e^{\left(\frac{Z_a VF}{RT}\right)} - \frac{\gamma_{\text{cao}} [\text{Ca}^{2+}]_o}{e^{\left(\frac{0.238636(Z_a VF)}{RT}\right)} - 1.0} \right) \quad (3.61)$$

3.7 Experimental Protocols

3.7.1 APD₉₀

APD₉₀ is most commonly used in computational modelling to calculate the ventricular repolarisation time. APD₉₀ represents the action potential duration at 90% membrane repolarisation. Experimental studies have suggested that the dispersion of APD₉₀ and the QT interval are correlated [25, 26, 27].

3.7.2 Action Potential Duration Restitution

The APD restitution curve generally explains the recovery of the action potential duration (APD) as a function of cardiac diastolic interval (DI) [28]. The S1-S2 protocol is used as the most common tool to determine the restitution properties of cardiac myocytes [28]. For the current study, the cardiac myocyte was paced at a basic cycle length (BCL) of 1000 ms until it attained stability. The action potential was initiated by a train of 10 S1 stimuli, applied at

a pacing frequency of 1 Hz with twice the threshold value. A second premature stimulus (S2) was applied after a time interval by using a variable length of the DI.

The APD₉₀ restitution (APD-R) curves were obtained by reducing the length of DIs and plotting the APD₉₀ triggered by the S2 stimulus versus the diastolic intervals. The results suggested that the duration of each proceeding action potential depends on the previous diastolic interval (DI) [30-32]:

$$APD_n = f(DI_{n-1}) \quad (3.62)$$

For the nth cycle,

$$DI_n = BCL - f(DI_{n-1}) \quad (3.63)$$

where APD_n represents the nth action potential, DI_n is the nth diastolic interval and BCL is the basic cycle length.

3.7.3 Steady State Restitution Curves

The steady-state APD₉₀ restitution curves were computed by pacing the single myocyte models at several basic cycle lengths and plotting the APD₉₀ against the BCLs [30-32].

3.7.4 ERP Restitution Curves

Chapter 1 has a detailed discussion of the effective refractory period; a second premature stimulus can elicit an action potential during the relative refractory period only if the strength of S2 exceeds the normal threshold value. No activity is observed when S2 is applied during the absolute refractory period. ERP-R curves were computed at varying basic cycle lengths, the ERP was calculated as the shortest diastolic interval at which S2 stimulus can evoke an AP with an overshoot reaching 80% of the action potential triggered by the 10th S1 stimulus of each individual BCL [32, 33].

3.7.5 The Single Cell Model Simulation

The modified equations of SQT4-SQT6 models were incorporated into the 2011 O'Hara-Rudy human ventricular cell model [13]. For the single cell, the current equivalent circuit model approach was considered [5, 13]. The cell membrane served as a capacitor, the different ionic channels, exchangers and ionic pumps acted as variable resistances and batteries were connected parallel to the cell membrane. The electrophysiological behaviour of a cell can be described by equation 3.64,

$$\frac{dV}{dt} = \frac{1}{C_m} (-I_{ion} + I_{stim}) \quad (3.64)$$

where t is the time (ms), V the voltage (mV) and I_{stim} the stimulus current (pA/pF). I_{ion} and C_m represents the sum of all the ionic currents and the capacitance per unit surface area respectively [5, 31]

The explicit Euler method was applied to integrate the equations of the I_{CaL} O’Hara-Rudy model (SQT4-SQT6) with a time step of 0.05 ms. The Euler method is preferred to avoid the rigidity of the system of Ordinary Differential Equations (ODEs) [31].

3.7.6 1D Heterogeneous Transmural Strand Model

To construct a 1D network which correlates with the typical range of human transmural ventricle width [32, 35, 36], a 15 mm long single fibre was considered. The fibre was composed of 100, 150 μm cylindrical cells, with a spatial resolution of 0.15 mm.

The cell distribution is described in the Table 3.1.

Cell Type	Number of each cell type	Average length (mm)
EPI	40	6.00
MCELL	35	5.25
ENDO	25	3.75

Table 3.1: The distribution of EPI, MCELL and ENDO cell types along the 15 mm long strand. The strand is composed of 40 epicardial cells (EPI), 35 middle cells (MCELL) and 25 endocardial cells (ENDO) representing 6.00 mm, 5.25 mm and 3.75 mm of the EPI, MCELL and ENDO regions respectively on the 15 mm long strand [32, 35, 36].

This distribution of each region, i.e. EPI, MIDDLE and ENDO, is similar to the geometry used in other studies [32, 37, 38]. The value of the diffusion coefficient (D) was fixed at 0.00152 cm^2/ms , which gave a conduction velocity of 67 cm/s through the 1D strand at a rate of 1 Hz, very similar to the conduction velocity in the human ventricular myocardium which is approximately 70 cm/s [39].

3.7.7 AP Propagation in 1D Heterogeneous Transmural Ventricular Tissue Model

A continuum approach to model gap junctions is more practical than explicit modelling [32]. Let's suppose that the intracellular and extracellular conductivities are the same, the propagation of the AP can be defined by a Monodomain equation [11]. It explains the propagation of a conduction wave in a tissue model [11, 14-16]:

$$\frac{dV}{dt} = \nabla \cdot (D\nabla V) - \left(\frac{I_{ion}}{C_m} \right) \quad (3.65)$$

where D stands for the tensor of the diffusion coefficients (cm²/sec) defining the electrical conductivity in a tissue. ∇^2 is a 3D spatial Laplacian, I_{ion} is the total transmembrane current and C_m is the capacitance per unit area. As the cardiac tissue has a fibrous structure, propagation is faster along the fibre direction [34].

3.7.8 Computation of Conduction Velocity

The 1D strand model was used to calculate the conduction velocity [32]. The activation time was described for each point i.e. the time at which the maximum upstroke velocity was obtained. A train of 10 S1 conditioning stimuli was applied at a frequency of 1 Hz. The conduction velocity (CV) was calculated in the 1D tissue model by evaluating the time ΔT for the conducting wave to propagate from $x-\Delta x$ to $x+\Delta x$. The conduction velocity can be calculated as [32, 37, 38],

$$CV = \frac{2\Delta x}{\Delta T} \quad (3.66)$$

To construct a CV restitution curve, the CV was calculated over a range of BCLs. The CV was plotted against each BCL for which it was calculated.

3.7.9 Evaluation of the Tissue Excitation Threshold (TET)

The excitation threshold of the tissue is defined as the minimal stimulus strength, required to initiate and sustain the action potential in cardiac tissue [40]. In simulations, the S1-S2 protocol was utilised to measure the TET. A S1 stimulus with an amplitude of -80 uA/ μ F and spatial size of 0.2 mm, was applied at one end of the strand for a duration of 0.5 ms. A 2nd premature stimulus with an equal spatial size and duration as S1 was applied after a time

delay in the middle of the strand. The tissue excitation threshold was a measure of the minimal S2 strength that can initiate a propagating action potential along the 1D strand.

3.7.10 Computing the Pseudo-ECG

The Gima and Rudy [43] method was utilised to compute the pseudo-ECG in the 1D strand model. Extracellular unipolar potentials (Φ_e), generated by the fibre placed at positions x' , y' and z' , can be computed from the transmembrane potentials at position x , y and z on the strand using:

$$\Phi_e(x', y', z') = -\frac{(r^2 \sigma_i)}{(4\sigma)} \int \nabla V_m \left(\frac{1}{d}\right) dx \quad (3.67)$$

$$d = \sqrt{(x - x')^2 + (y - y')^2 + (z - z')^2} \quad (3.68)$$

where extracellular and intracellular conductivities are represented by σ_e and σ_i respectively, r is the radius and d represent the distance between the source point (x, y, z) and the field point (x', y', z') [43].

3.7.11 The Temporal Vulnerable Window Measurement

In a 1D tissue model an excitation wave was evoked by applying a S1 stimulus to the ENDO region. This conditioning excitation wave evoked so that S1 propagates from the ENDO to the EPI region, followed by a refractory tail. A second premature stimulus S2 was applied after a time delay. The excitation wave elicited by S2 could propagate in both directions along the strand, if S2 was applied too late after the refractory tail (bi-directional conduction) [11, 42], as the S2 site and surroundings were adequately recovered from the preceding excitation wave [11]. In our simulations, a complete conduction block was observed along the 1D strand, if S2 was applied too early after the refractory tail, as the tissue had still not recovered from the previous conducting wave. A temporal window known as the vulnerability window (VW) exists between these two extreme time periods. A premature test stimulus applied within the VW elicited an excitation wave that propagated uni-directionally i.e. either in the antegrade or retrograde direction. The time at which the test stimulus was applied, the tissue was still refractory either in retrograde (backward) or antegrade (forward) directions which led to a complete condition block in one direction and propagation of the excitation wave along the opposite direction in the 1D tissue strand [11, 42].

3.7.12 Induction of the Re-entry in the 2D Sheet

To initiate and propagate re-entry in an idealised 2D tissue model a standard S1-S2 protocol was used. A plane excitation conduction wave was initiated by applying a train of 10 S1 stimuli at the ENDO end of the 2D sheet. The excitation conduction wave evoked by S1 and it propagated from the ENDO end to the EPI end of the 2D tissue sheet. Following a time delay, S2 was applied in the EPI region (within the VW of EPI region of 2D sheet). The excitation wave evoked by S2 was blocked by unrecovered MCELL, as the MCELL region was still refractory due to the slower repolarisation as compared to the EPI and ENDO regions. This then gave rise to unidirectional conduction towards the EPI side. The unidirectional block facilitated the growth of spiral re-entrant excitation waves with their counterrotating tips moving towards each other. These re-entrant waves will sustain if their tips have a sufficient distance between them [11]. The length of the premature test stimulus (S2) plays a very important role in the development of spiral re-entrant excitation waves in the 2D tissue model. The tissue's susceptibility to re-entry is defined by the minimal spatial size of S2 [11, 42].

3.7.13 Tip Trajectories

The tip trajectories were computed by using the phase singularity method. Phase mapping allows for a closer look at the activation wave front of the spiral wave evoked by S2. It describes the wave front, the wave tail and the point at which the wave front meets the curved wave tail. As the cardiac impulse moves forward the wave front represents a region composed of depolarised cells, while the wave tail represents an area with a group of cells returning to rest (repolarisation). The point where the wave tail meets the wave front is explained by Gray et al [44, 45] as a phase singularity (PS). The singularity point plays an important role in understanding the characteristics of the spiral wave [46]. The phase of the spiral wave was calculated by using the formulation of M. A. Bary et.al [47],

$$\Phi(x, t) = \tan^{-1} \frac{v(x, t) - v'}{u(x, t) - u'} \quad (3.69)$$

where \tan^{-1} is the four-quadrant inverse tangent, such that $\phi(x, t)$ is in the range of $-\pi$ and π , u is the fast variable corresponding to the transmembrane potential and v represents the tissue recovery. The choice of origin points v' and u' in the state space plays an important role in the calculation of the phase of the spiral wave and it cannot be selected randomly [47]. In an ideal situation, the phase should progress through 2π during a complete rotation

and be uniquely defined at each spatial point. The condition relative to this specific point creates a phase-space trajectory which encloses an origin during the complete rotation through 2π . In the phase space the trajectories from points close to the filament form smaller orbits as the amplitude of the action potential reduces as it approaches the filament. The origin of an ideal state-space can be defined as a point encircled by all the trajectories regardless of its initial spatial location. The choice of origin points may differ for different excitable models. In the current models to choose u' and v' points, a 2D spiral wave simulation was performed using the WT compared with the mutation models for a complete rotation after the spiral had been fully formed. The trajectories of all the points were plotted in the phase space, the point encircled by the smallest trajectories was selected as the origin [47].

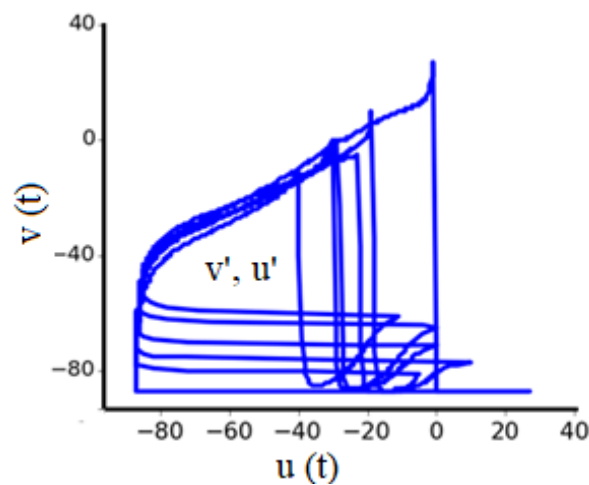


Figure 3.4: Trajectories in phase space from all the elements of a 2D idealised model containing a spiral wave, generated by the equational system described by M. A. Bery [47], where $u(t)$ is a fast variable analogous to the transmembrane potential, and $v(t)$ is a slow variable representing tissue recovery. The points (v', u') encircled by the smallest trajectories was selected as the origin point.

3.8 Numerical Methods

Different numerical methods can be used to discretise continuous equations, which makes them much easier to solve in an iterative manner on a computer. There are different numerical methods available, depending on different types of specific problems. In the current models, the governing mathematical equations are either ordinary differential equations (ODEs) or partial differential equations (PDEs). The numerical methods for solving these problems are introduced separately.

A group of ODEs are usually used to represent a single cell model. All the state variables are defined as first-order differentials over time. For non-stiff systems, the ODEs can be solved by using the forward Euler method. Although, the forward Euler method is very efficient in terms of computing, large time steps can incur stability concerns. For a system of stiff ODEs, the Euler method may not be favourable as this method could necessitate extremely small integration steps. In this case, other robust, implicit schemes should be implemented. There are many open source ODEs solvers available to use, including the Intel ODE [49] and CVODE [50].

The PDEs can be used to model tissue level structures. In cardiac modelling, the excitation wave propagation described by Equation (3.70) and the mechanics equations describing the beating of the heart are examples of PDEs. Currently, PDEs in cardiac modelling are solved by using the finite difference method (FDM). FDM is a simple and commonly used method for discretising the monodomain equations. In a 1D problem, for a given cell at location x , time step Δt and spatial interval Δx , the voltage in Equation (3.70) is solved using the FDM as:

$$V_x^{t+\Delta t} = V_x^t + \Delta t \frac{D}{(\Delta x)^2} (V_{x-\Delta x}^t + V_{x+\Delta x}^t - 2V_x^t) \quad (3.70)$$

The forward Euler method is used for the discretisation over time. The term $\Delta t D / (\Delta x)^2$ is related to the stability of the solution and must be smaller than 0.5 in order to achieve the convergences [11, 14-16, 34].

3.9 References

- [1] J. K. Peterson, “The basic Hodgkin–Huxley Model,” in *calculus for cognitive scientists*, Springer Singapore, pp. 401–484, 2016.
- [2] D. Noble, “A modification of the Hodgkin Huxley equations applicable to Purkinje fibre action and pacemaker potentials,” *J. Physiol.*, vol. 160, no. 2, pp. 317–352, Feb. 1962.
- [3] E. C. Fear and M. A. Stuchly, ‘A novel equivalent circuit model for gap-connected cells’, *Phys. Med. Biol.*, vol. 43, no. 6, pp. 1439, 1998.
- [4] W. F. Boron and E. L. Boulpeap, *Medical physiology*, 3e, 3rd edition. Philadelphia, PA: Elsevier, 2016.
- [5] R. Plonsey and R. C. Barr, *Bioelectricity: A quantitative approach*. Springer Science & Business Media, 2007.
- [6] K. M. Deka and S. Roy, “Biologically inspired circuit model for simulation of glutamate gated ion channels of the postsynaptic membrane at synaptic cleft,” *Ann. Neurosci.*, vol. 20, no. 4, pp.106-111, Oct. 2013.
- [7] D. C. Sigg and A. Hezi-Yamit, “Cardiac and vascular receptors and signal transduction,” in *handbook of Cardiac Anatomy, physiology, and devices*, P. A. Iaizzo, Ed. Humana Press, pp. 191–218, 2009.
- [8] D. Sterratt, B. Graham, A. Gillies, and D. Willshaw, *Principles of Computational modelling in Neuroscience*. Cambridge University Press, 2011.
- [9] A. L. Hodgkin and A. F. Huxley, “A quantitative description of membrane current and its application to conduction and excitation in nerve,” *J. Physiol.*, vol. 117, no. 4, pp. 500–544, Aug. 1952.
- [10] C. M. Armstrong and B. Hille, “Voltage-gated ion channels and electrical excitability,” *Neuron*, vol. 20, no. 3, pp. 371–380, Mar. 1998.
- [11] H.R. Guy and F. Conti, “Pursuing the structure and function of voltage-gated channels”, *Trends Neurosci.*, vol. 13, pp. 201–206, 1990
- [12] M. Kijima and K. Komoribayashi, ‘A Markov chain model for valuing credit risk derivatives’, <http://dx.doi.org/10.3905/jod.1998.408006>, 22-Feb-2009.
- [13] T. O’Hara, L. Virág, A. Varró, and Y. Rudy, “Simulation of the undiseased human cardiac ventricular action potential: model formulation and experimental validation,” *PLoS Comput. Biol.*, vol. 7, no. 5, p. e1002061, May 2011.
- [14] I. Adeniran, *Modelling the Short QT syndrome gene mutations: and their role in cardiac arrhythmogenesis*, 2014 edition. New York: Springer, 2014.

- [15] V. Iyer, R. Mazhari, and R. L. Winslow, "A computational model of the human left-ventricular epicardial myocyte," *Biophys. J.*, vol. 87, no. 3, pp. 1507–1525, Sep. 2004.
- [16] F. Fenton and E. Cherry, "Models of cardiac cell," *Scholarpedia*, vol. 3, no. 8, p. 1868, 2008.
- [17] C. Maffeo, S. Bhattacharya, J. Yoo, D. Wells, and A. Aksimentiev, "Modeling and simulation of ion channels," *Chem. Rev.*, vol. 112, no. 12, pp. 6250–6284, Dec. 2012.
- [18] J. Magyar et al., "Effects of endothelin-1 on calcium and potassium currents in undiseased human ventricular myocytes," *Pflügers Archiv.*, vol. 441, no. 1, pp. 144–149, Nov. 2000.
- [19] L. Fülöp, T. Bányász, J. Magyar, N. Szentandrassy, A. Varró, and P. P. Nánási, "Reopening of L-type calcium channels in human ventricular myocytes during applied epicardial action potentials," *Acta Physiol. Scand.*, vol. 180, pp. 39–47, 2004.
- [20] S. Morotti, E. Grandi, A. Summa, K. S. Ginsburg, and D. M. Bers, "Theoretical study of L-type Ca^{2+} current inactivation kinetics during action potential repolarization and early afterdepolarisations," *J. Physiol.*, vol. 590, no. 18, pp. 4465–4481, Sep. 2012.
- [21] J. Kim, S. Ghosh, D. A. Nunziato, and G. S. Pitt, "Identification of the components controlling inactivation of voltage-gated Ca^{2+} channels," *Neuron*, vol. 41, no. 5, pp. 745–754, Mar. 2004.
- [22] K. F. Decker, J. Heijman, J. R. Silva, T. J. Hund, and Y. Rudy, "Properties and ionic mechanisms of action potential adaptation, restitution, and accommodation in canine epicardium," *Am. J. Physiol. - Heart Circ. Physiol.*, vol. 296, no. 4, pp. H1017–H1026, Apr. 2009.
- [23] C. Antzelevitch et al., "Loss-of-function mutations in the cardiac calcium channel underlie a new clinical entity characterized by ST-segment elevation, short QT intervals, and sudden cardiac death," *Circulation*, vol. 115, no. 4, pp. 442–449, Jan. 2007.
- [24] C. Templin et al., "Identification of a novel loss-of-function calcium channel gene mutation in short QT syndrome (SQTS6)," *Eur. Heart J.*, vol. 32, no. 9, pp. 1077–1088, May 2011.
- [25] T. Kenny, "The cardiac cycle and hemodynamics," in *The Nuts and Bolts of Implantable Device Therapy Pacemakers*, John Wiley & Sons, Ltd, pp. 21–28, 2014.
- [26] M. Malik, V. N. Batchvarov, "Measurement, interpretation and clinical potential of QT dispersion", *Journal of the American College of Cardiology*, vol. 36, pp. 1749-1766, November 2000.
- [27] F. Extramiana, P. Maury, P. Maison-Blanche, A. Duparc, M. Delay, and A. Leenhardt, "Electrocardiographic biomarkers of ventricular repolarisation in a single family of short QT

- syndrome and the role of the Bazett correction formula,” *Am. J. Cardiol.*, vol. 101, no. 6, pp. 855–860, Mar. 2008.
- [28] M. R. Franz, “The electrical restitution curve revisited: steep or flat slope--which is better?” *J. Cardiovasc. Electrophysiol.*, vol. 14, no. 10 Suppl, pp. S140-147, Oct. 2003.
- [29] E. G. Tolkacheva, J. M. B. Anumonwo, and J. Jalife, “Action potential duration restitution portraits of mammalian ventricular myocytes: Role of calcium current,” *Biophys. J.*, vol. 91, no. 7, pp. 2735–2745, Oct. 2006.
- [30] E. M. Cherry and F. H. Fenton, “A tale of two dogs: analyzing two models of canine ventricular electrophysiology,” *Am. J. Physiol. Heart Circ. Physiol.*, vol. 292, no. 1, pp. H43-55, Jan. 2007.
- [31] Douglas Zipes, Jose Jalif, *Cardiac electrophysiology: From cell to bedside*, 6e, 6th edition. Philadelphia, PA: Saunders, 2013.
- [32] I. Adeniran, J. C. Hancox, and H. Zhang, “In silico investigation of the short QT syndrome, using human ventricle models incorporating electromechanical coupling,” *Front. Physiol.*, vol. 4, pp.1-13, Jul. 2013.
- [33] A. J. Workman, K. A. Kane, and A. C. Rankin, “The contribution of ionic currents to changes in refractoriness of human atrial myocytes associated with chronic atrial fibrillation,” *Cardiovasc. Res.*, vol. 52, no. 2, pp. 226–235, Nov. 2001.
- [34] M. A. Colman, ‘Atrial fibrillation’, in *mechanisms of atrial arrhythmias*, Springer International Publishing, pp. 201–225, 2014.
- [35] K. James and S. James, “Mathematical physiology - I: Cellular Physiology”, Springer, 2009.
- [36] G.-X. Yan, W. Shimizu, and C. Antzelevitch, “Characteristics and distribution of M cells in arterially perfused canine left ventricular wedge preparations,” *Circulation*, vol. 98, no. 18, pp. 1921–1927, Nov. 1998.
- [37] H. Zhang, S. Kharche, A. V. Holden, and J. C. Hancox, “Repolarisation and vulnerability to re-entry in the human heart with short QT syndrome arising from KCNQ1 mutation—A simulation study,” *Prog. Biophys. Mol. Biol.*, vol. 96, no. 1–3, pp. 112–131, 2008.
- [38] H. Zhang and J. C. Hancox, “In silico study of action potential and QT interval shortening due to loss of inactivation of the cardiac rapid delayed rectifier potassium current,” *Biochem. Biophys. Res. Commun.*, vol. 322, no. 2, pp. 693–699, 2004.
- [39] K. H. W. J. ten Tusscher, D. Noble, P. J. Noble, and A. V. Panfilov, “A model for human ventricular tissue,” *Am. J. Physiol. - Heart Circ. Physiol.*, vol. 286, no. 4, pp. H1573–H1589, Apr. 2004.

- [40] N. Tandon et al., “Electrical stimulation systems for cardiac tissue engineering,” *Nat. Protoc.*, vol. 4, no. 2, pp. 155–173, Jan. 2009.
- [41] R. M. Shaw and Y. Rudy, “The vulnerable window for unidirectional block in cardiac tissue: characterization and dependence on membrane excitability and intercellular coupling,” *J. Cardiovasc. Electrophysiol.*, vol. 6, no. 2, pp. 115–131, Feb. 1995.
- [42] Z. Qu, A. Garfinkel, and J. N. Weiss, “Vulnerable window for conduction block in a one-dimensional cable of cardiac cells, 1: Single extrasystoles,” *Biophys. J.*, vol. 91, no. 3, pp. 793–804, Aug. 2006.
- [43] K. Gima and Y. Rudy, “Ionic current basis of electrocardiographic waveforms a model study,” *Circ. Res.*, vol. 90, no. 8, pp. 889–896, May 2002.
- [44] R. A. Gray et al., “Nonstationary vortexlike re-entrant activity as a mechanism of polymorphic ventricular tachycardia in the isolated rabbit heart,” *Circulation*, vol. 91, no. 9, pp. 2454–2469, May 1995.
- [45] R. A. Gray, A. M. Pertsov, and J. Jalife, “Spatial and temporal organization during cardiac fibrillation,” *Nature*, vol. 392, no. 6671, pp. 75–78, Mar. 1998.
- [46] S. V. Pandit and J. Jalife, “Rotors and the dynamics of cardiac fibrillation,” *Circ. Res.*, vol. 112, no. 5, pp. 849–862, Mar. 2013.
- [47] M.-A. Bray and J. P. Wikswo, “Use of topological charge to determine filament location and dynamics in a numerical model of scroll wave activity,” *IEEE Trans. Biomed. Eng.*, vol. 49, no. 10, pp. 1086–1093, Oct. 2002.
- [48] J. A. Nelder, R. A. Mead, Simplex method for function minimization, *Computer Journal*, vol. 7, pp. 308–313, 1965.
- [49] Intel® Ordinary Differential Equations Solver Library | Intel® Software [Internet]. [cited 31 Dec 2016]. Available: <https://software.intel.com/en-us/articles/intel-ordinary-differential-equations-solver-library>
- [50] Cohen S, Alan, Hindmarsh C. Cvode, A stiff/nonstiff ODE Solver in C, *Computers in Physics*. pp. 138–143, 1996.

Overview of Chapters 4, 5 and 6

The work presented in Chapters 4, 5 and 6 is based on the single cell, transmural 1D and 2D models of WT, SQT4 (A39V and G490R), SQT5 (S481L) and SQT6 (S755T) mutations. The main objective of the current study was to investigate the functional behavior of the SQT mutations and investigate the arrhythmogenic consequences of the A39V, G490R, S481L and S755T mutations using 1D and 2D tissue models of the human ventricle cell. This study also attempted to normalise the QT interval by potential pharmacological action to enhance the I_{CaL} currents. Results have suggested an increase in the amplitude of the QRS interval instead of a normalised QT interval. In simulations, a different approach was used to normalise QT interval by blocking the I_{Kr} . The blockade of I_{Kr} normalised the QT interval, while ST segment elevation can be reduced by blocking I_{to} . The blockade of I_{to} not only controlled the J-wave elevation but also reduced the ST-segment elevation. Prior studies have suggested different pharmacological techniques to treat patients with the potassium-related SQT syndromes, although the pharmacological treatment for the short QT syndromes associated with L-type calcium channels are yet to be developed.

CHAPTER 4

CACNA1C Linked Short QT4 Syndrome

4.1 Introduction

The voltage-dependent L-type calcium channel (LTCC) Cav1.2 plays a vital role in the ventricular AP process [1]. LTCC channels activate with the depolarisation of the cell membrane, with a long-lasting nature as the inactivation process is very slow. After the early repolarisation phase (phase1), I_{to} channels deactivate, and calcium starts to enter the cell through L-type calcium channels, it plays an insignificant role during the upstroke and late repolarisation but dominant during the plateau phase of the ventricular AP (phase 2) as described in Chapter 1. The changes in the membrane potential are almost negligible during the plateau phase, as there is a balance between the inward and outward currents [1, 2, 4]. Voltage-dependent L-type calcium channels start deactivating at the end of phase 2 (plateau phase) [3], with the decline of I_{CaL} influx, and I_{Kr} channels start activating later in phase 2 of the AP [1, 2, 3].

Mutations in the voltage dependent current channels can be arrhythmogenic [10] which can lead to sudden cardiac deaths (SCD). For example, a loss of a functional mutation to the Cav1.2 channel encoded by CACNA1C protein, can result in the Brugada syndrome linked to a shorter than normal QT interval [9]. Such mutations can accelerate the ventricular repolarisation which could lead to a shorter than normal AP duration and an elevated ST interval on the electrocardiogram [5, 6, 9]. Similarly, a gain of function of the Kir2.1 channel encoded by the KCNJ2 gene can also lead to an accelerated ventricular AP with a shorter than normal QT interval. In this specific mutation condition, patients' electrocardiograms have revealed abnormally narrow and peaked T-waves [7, 8]. As discussed earlier in Chapter 2, SQT4 mutations, A39V and G490R, in voltage-dependent calcium channel CACNA1C, can lead to a loss in the function of the calcium channel current, which can cause palpitations, VF and AF. These mutations can be arrhythmogenic and lead to sudden cardiac deaths which are common in infants [8, 9].

The main object of the current study was to investigate the functional behavior of A39V and G490R on the $\alpha 1$ subunit of CACNA1C channel.

4.2 CACNA1C SQT4/G490R Mutation

The 1st case of the 4th variant of short QT syndrome was diagnosed in a white male of Turkish descent, proband exhibited AF, with a QTc interval < 346 ms. Genetic studies revealed a family history of sudden cardiac death. The patient's brother died of sudden cardiac arrest at the age of 45. A twelve lead ECG investigation revealed the ST segment elevation in V1 and V2 leads, while a very insignificant rate dependence was shown by the QT interval [9]. Coronary angiography ruled out any structural defects [9]. The study carried out by Antzelevitch et al. [9] described the proband with a mutation in exon 10 of CACNA1C, with a heterozygous exchange of an Adenine to Guanine, which resulted in a substitution of an Arginine to Glycine at position 490 and named it G490R. The family's genetic analysis showed the same mutation in two of his daughters with a QTc interval of 360 ms and 373 ms, respectively [9].

4.3 CACNA1C SQT4/A39V Mutation

The 2nd case of the SQT4S was found in a 44-year-old European male [9]. ECG exhibited a notable ST segment elevation in V2 and a marked J-wave in V3. Family history showed the mother with syncope led to SCD, while her 75 years old father showed no significantly abnormal ECGs [9]. Genetic screening of the proband showed a heterozygous C to T transition at position 116, which anticipated an exchange of a Valine to Alanine at position 39, A39V [9].

A direct demonstration of G490R and A39V mutations on the CACNA1C channel can be obtained by *in vitro* ventricular AP clamp experiments. The results of these experiments have shown a loss of function of Cav1.2 currents during the plateau phase of the AP [9]. Until now, there is very limited experimental data available for SQT4 [4, 8, 9, 10].

4.4 Simulation of Single Cell I_{CaL} for the CACNA1C $\alpha 1$ WT and SQT4/A39V /G490R Mutation Conditions

A detailed discussion of SQT4 modelling and equations for WT, A39V and G490R are given in Chapter 3. The voltage clamp protocol for the $\alpha 1$ subunit of the CACNA1C control type was performed for a holding potential of -90 mV with a total simulation time of 250 ms. The clamp voltage range was between -50 mV and 50 mV with an increment of 10 mV for each step. The same voltage clamp protocol was applied for mutation conditions A39V and G490R (Figure 4.1 d, e and f). Simulations showed a decrease in the amplitude of A39V and

G490R channel currents which showed an agreement with the experimental data (Figure 4.1, 4.2) [9].

The simulated (solid lines) and experimental (dots) data on I-V relationships for the WT, A39V and G490R mutations are presented in Figure 4.2a. The WT conductance was regulated to acquire a peak current density which corresponds well with the I_{CaL} formulation current density during the I-V relationship of the original O'Hara & Rudy model [11] (Figure 4.2b), maintaining the overall current densities, APD_{90} and functional characteristics of the O'Hara & Rudy human ventricular model [11]. Simulations (Figure 4.2a) show the voltage at peak current remains the same for WT, A39V and G490R which matches the experimental data [9].

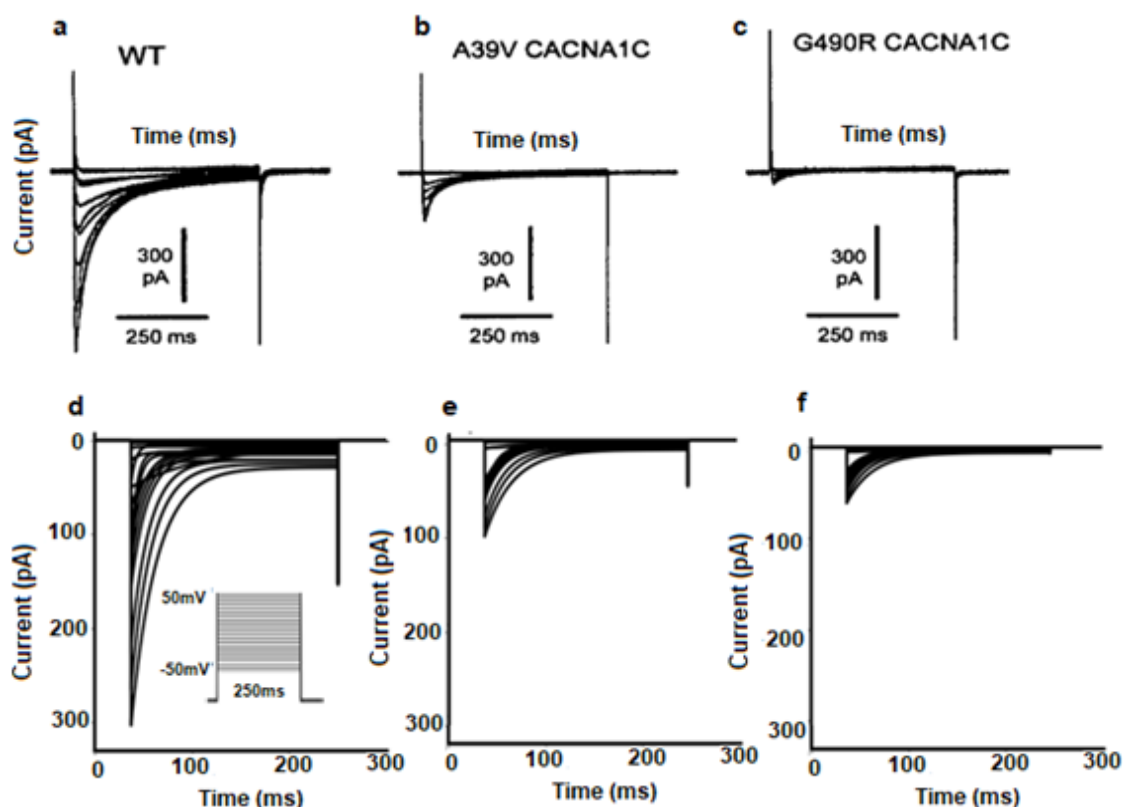


Figure 4.1: Voltage clamp protocol, experimental and simulated L-Type calcium current traces for the WT and mutations. (a, b, c) WT, A39V and G490R experimental current traces [9]; (d) the voltage clamp protocol (insert), the clamp range was between -50 mV and 50 mV with an increment of 5 mV. The total simulation time was 250 ms. (d, e, f) WT (4.1d), A39V (4.1e) and G490R (4.1f) are the simulated current traces corresponding to the experimental data (4.1 a, b, c)

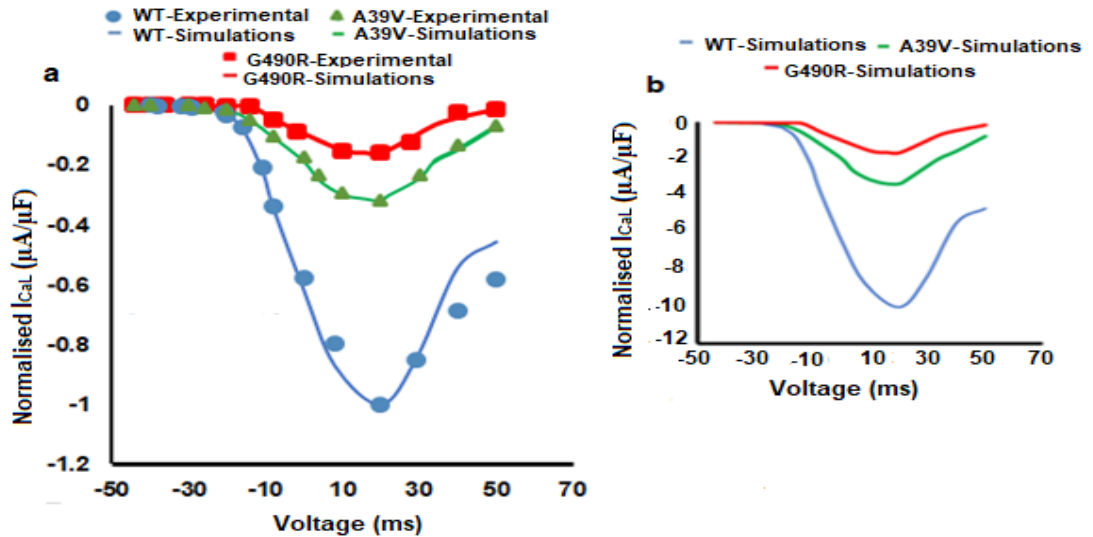


Figure 4.2: Computed I-V relationship for the L-Type calcium channel (CACNA1C α 1-subunit) with the WT, A39V and G490R conditions. (a) Normalised I-V relationship for WT (blue), A39V (green) and G490R (red), the solid lines represent the simulated data while the dotted points represent the experimental data. Simulations showed a decrease in the amplitude of A39V and G490R channel currents which showed an agreement with the experimental data [9]. (b) The WT conductance was regulated to acquire a peak current density which corresponds well with the I_{CaL} formulation current density during the I-V relationship of the original O'Hara & Rudy model [11].

To obtain physiologically accurate ventricular single cell and tissue models (1-2D) with structural and transmural heterogeneity, the modified equations of the $Cav1.2$ channel current for both the WT and the SQTS conditions were incorporated into the 2011 O'Hara & Rudy human ventricular cell model [11]. Figure 4.3 shows simulated action potentials and I_{CaL} (α 1-subunit of CACNA1C) current profiles for LVEPI, LVMCELL and LVENDO ventricular cells for the WT, A39V and G490R conditions respectively. Results showed that A39V and G490R mutations, shortened the action potential duration in all three cell types. For the WT condition, the early repolarisation (phase1) is caused by a transient outward current (I_{to}) [12]. However, the repolarisation is delayed and a plateau region can be seen in the ventricular AP due to an increase in the slow influx of calcium current through the L-type calcium channels, that open when the cell membrane depolarises to about -40 mV [12]. This plateau phase prolongs the action potential duration after which the I_{CaL} declined. This inward component of I_{CaL} , declined for A39V and G490R conditions (Figure 4.2), while the voltage for peak current remained the same for the WT and the mutations, which is consistent with the experimental data [9]. The peak currents for G490R and A39V mutations are significantly reduced as compared to the control type, which resulted in a significant

shortening of the APD in both the G490R and A39V conditions [9]. The APD₉₀ values were computed for WT, G490R and A39V conditions for LVEPI, LVENDO and LVMCELL cells. The AP values were decreased for the G490R and A39V conditions. The shortening of the AP duration was caused by the decreased influx of I_{CaL} during the phase 2 of the AP, as illustrated by the time-course of I_{CaL} (Figure 4.3). The reduction of APD₉₀ by the G490R and A39V conditions was rate-dependent. The simulated resting potential values were -88 mV, -87 mV and -88 mV for the WT, A39V and G490R conditions respectively.

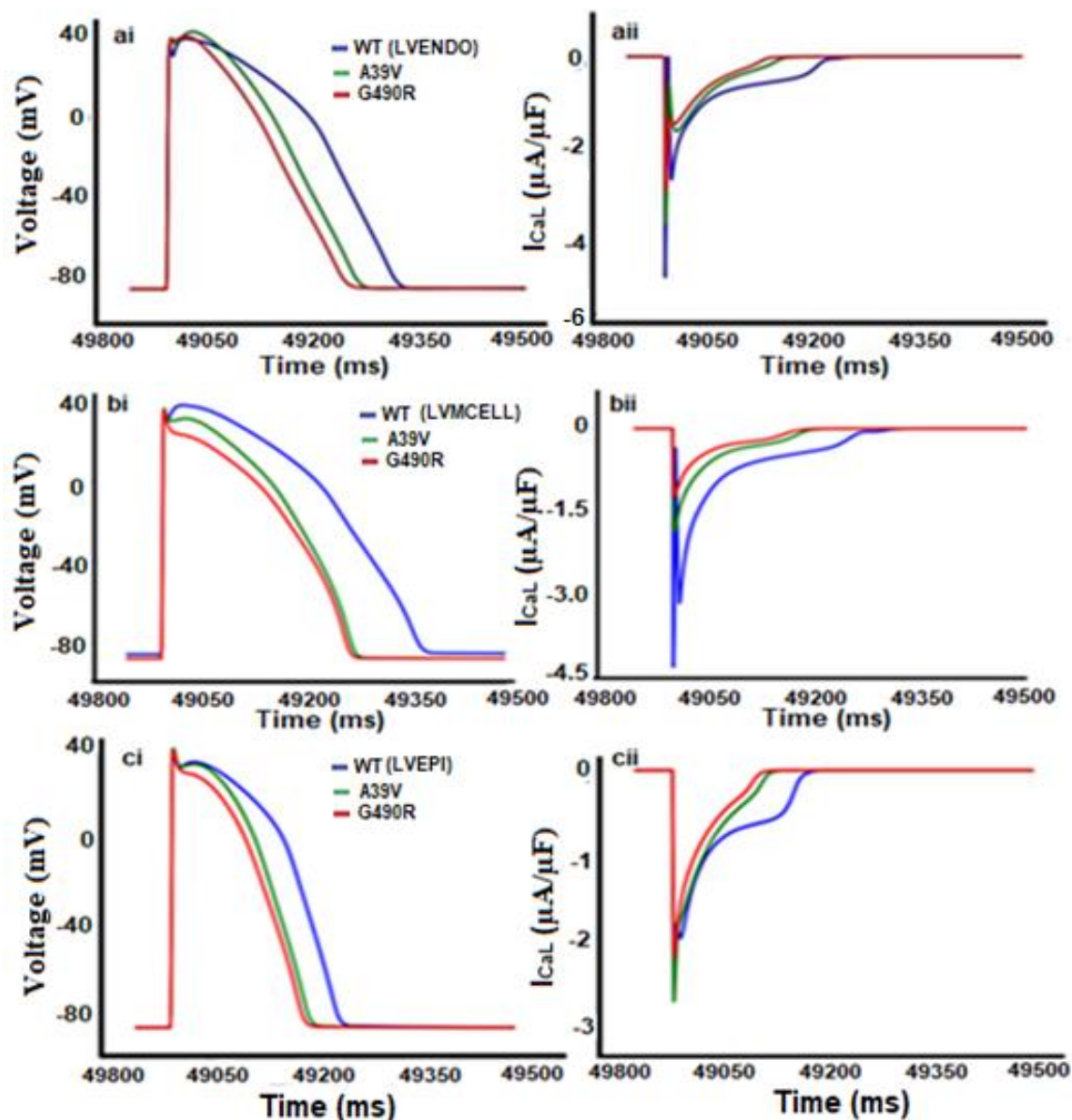


Figure 4.3: Simulated action potentials and I_{CaL} time traces. (ai, bi, ci) Action potential paced at the frequency of 1 Hz for LVENDO (ai), LVMCELL (bi) and LVEPI (ci) cells for WT (blue), A39V (green) and G490R (red) conditions. (aii, bii, cii) Relative CACNA1C I_{CaL} current profiles for LVENDO (aii), LVMCELL (bii) and LVEPI (cii) cells under WT (blue), A39V (green) and G490R (red) conditions.

	LVEPI (ms)	LVMCELL (ms)	LVENDO (ms)
WT	232	359	275
A39V	207	298	229
G490R	181	272	213

Table 4.1: Computed APD₉₀ (ms) values for the LVEPI, LVMCELL and LVENDO cell types for the WT, A39V and G490R mutation conditions.

Simulations (Table 4.1 and Figure 4.3) have shown that, the shortening of APD₉₀ for G490R and A39V conditions is non-uniform in different cell types. The extent of APD₉₀ shortening is of different amplitude in all three cell types (Table 4.2) with the greatest abbreviation in the LVMCELL cell for both the A39V and G490R conditions.

	LVEPI (ms)	LVMCELL (ms)	LVENDO (ms)
A39V	25	61	55
G490R	51	87	62

Table 4.2: APD₉₀ shortening in different cell types. The APD₉₀ reduction is the largest in the LVMCELL under both the A39V and G490R conditions.

Results showed that, the transmural dispersion of APD₉₀ across different cell types of the ventricular wall has been decreased in G490R and A39V conditions (Figure 4.16), which is similar to prior studies of SQTs1-3 [13-15].

4.5 Rate Dependent Restitution Properties of WT and SQT4 (A39V and G490R) Conditions

The reduction of APD₉₀ due to G490R and A39V mutation conditions was rate- dependent as shown in Figure 4.4(a-c) and 4.5(a-c). Simulations showed that, the values of APD₉₀ were smaller for G490R and A39V conditions as compared to the controlled condition over the range of the diastolic intervals (DIs) under investigation.

The APD restitution curve illustrates the recovery of action potential duration (APD) as a function of cardiac diastolic interval (DI), which is obtained by applying S1-S2 protocol as described in Chapter 3. Results have shown that, A39V and G490R mutations shortened the APD₉₀ in all three cell types (Figure 4.3), which caused a flattened APD₉₀ restitution curves

with a leftward shift and decreased maximal slopes (Figure 4.6). According to the previous studies, SQTs patients exhibit a poor rate-adaptation of their QT intervals [13, 16-18]. Single cell simulations indicated reduction of rate-adaptation of ventricular APD₉₀. The APD₉₀ abbreviation was rate-dependent as shown by the APD-Restitution (APD-R).

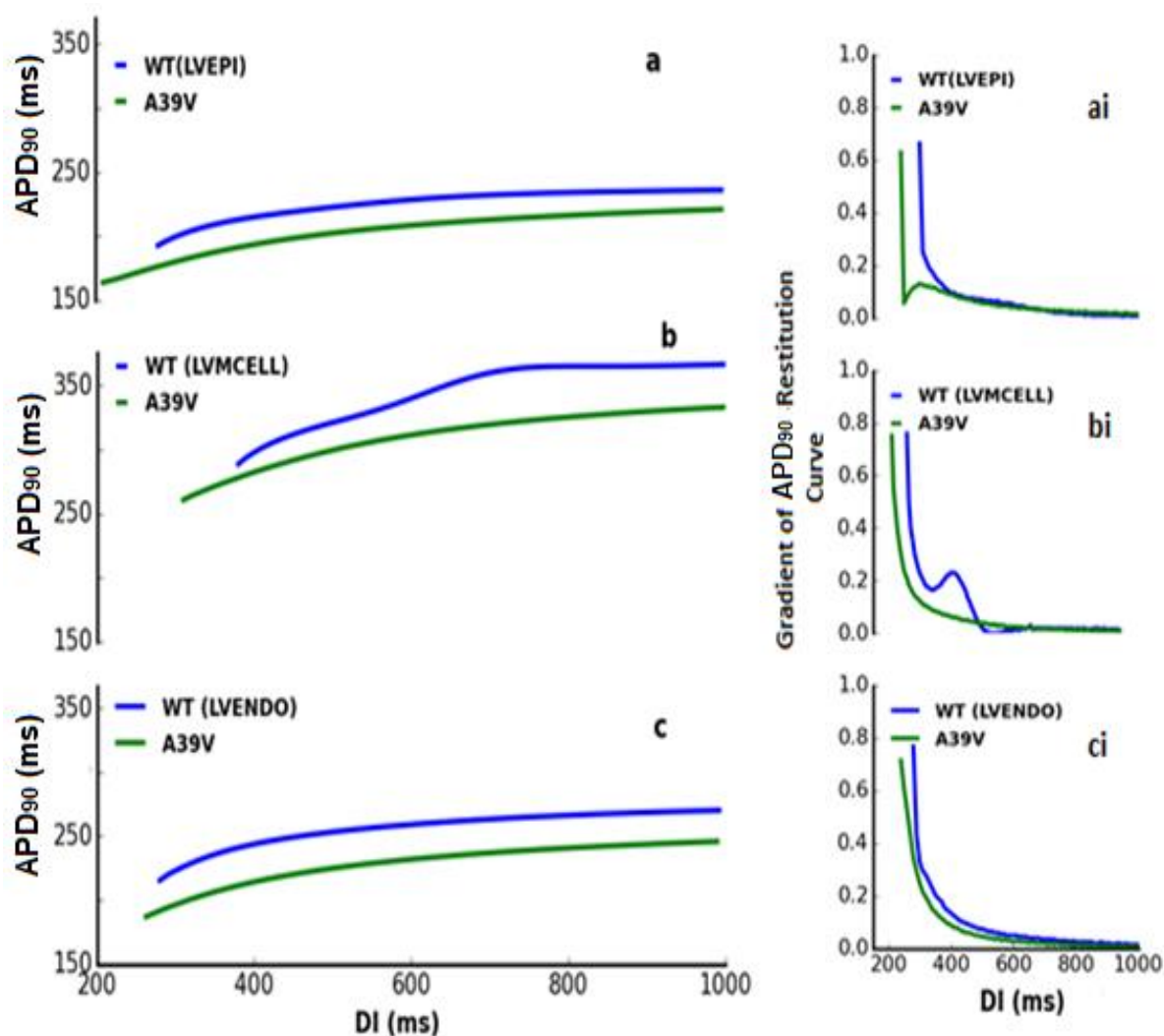


Figure 4.4: APD₉₀ restitution curves for WT and A39V. APD₉₀ is plotted against the diastolic interval (DI). (a, b, c) APD₉₀ restitution curves for the LVEPI (a), LVMCELL (b) and LVENDO (c) cells respectively under the WT (blue) and A39V (green) conditions. The A39V mutation caused the flattening of the APD₉₀ restitution curves with a prominent leftward shift in all three cell curves. (ai, bi, ci) Gradients of APD₉₀ restitution curves illustrating the change in the slope of APD₉₀ restitution curves as a function of DI (ms). Mutation has reduced the slopes of LVEPI and LVENDO curves.

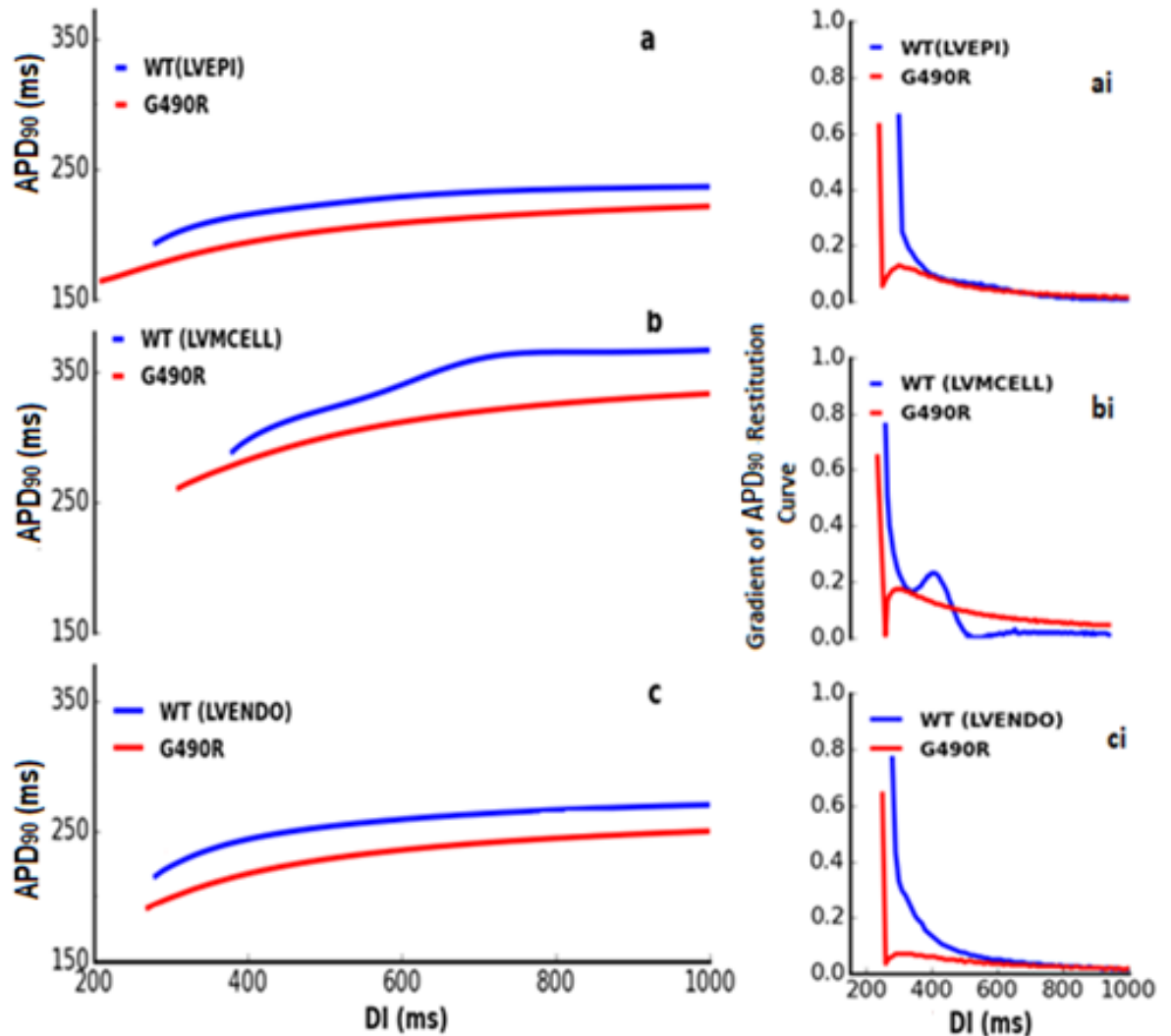


Figure 4.5: APD₉₀ restitution curves for WT and G490R. APD₉₀ is plotted against the diastolic interval (DI). (a, b, c) APD₉₀ restitution curves for the LVEPI (a), LVMCELL (b) and LVENDO (c) cells respectively for the WT (blue) and G490R (red) conditions. The G490R mutation caused the flattening of the APD₉₀ restitution curves with a prominent leftward shift in LVEPI and LVMCELL curves. (ai, bi, ci) Gradients of APD₉₀ restitution curves showing the change in slope as a function of DI (ms). Mutation has reduced the slopes of EPI and ENDO cell curves, although increased steepness can be seen at relatively slow heart rates (BCL >500) for the MCELL curve (bi) under the G490R condition.

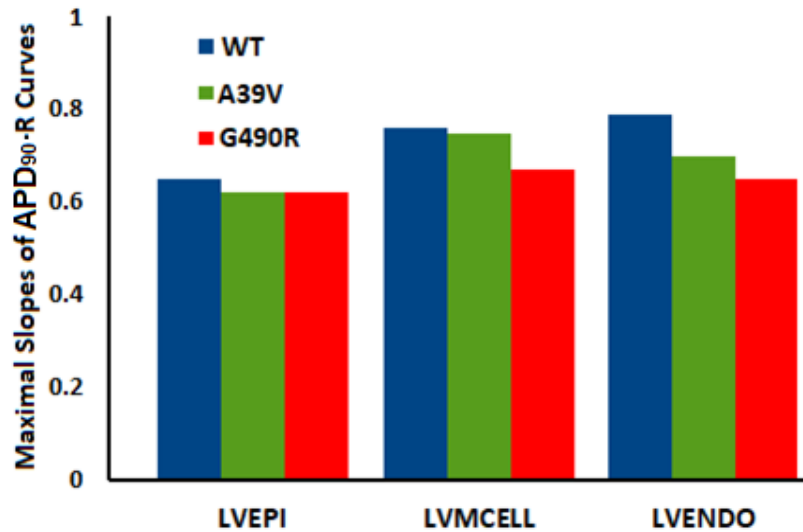


Figure 4.6: The maximal slope of the APD₉₀ restitution curves, WT (blue), A39V (green) and G490R (red) obtained from Figure 4.4 and 4.5 (ai, bi, ci). The slopes were measured at the minimum diastolic interval (DI) before the conduction block and calculated for the individual curves of LVEPI, LVMCELL and LVENDO cell types. The shortening of APD₉₀ under A39V and G490R conditions reduced the maximal slopes of the restitution curves. This reduction is more marked in the LVENDO cell model.

To further investigate the rate dependence of the APD₉₀ on the basic cycle length (BCL), the steady state restitution curves were plotted. The G490R and A39V mutations caused a leftwards shift and flattening of the restitution curves, Figure 4.7 and 4.8 (a, b, c). A small steepness in the steady state restitution curves of the LVEPI cells for the G490R condition can be seen between 600 ms and 1200 ms, Figure 4.8(ai).

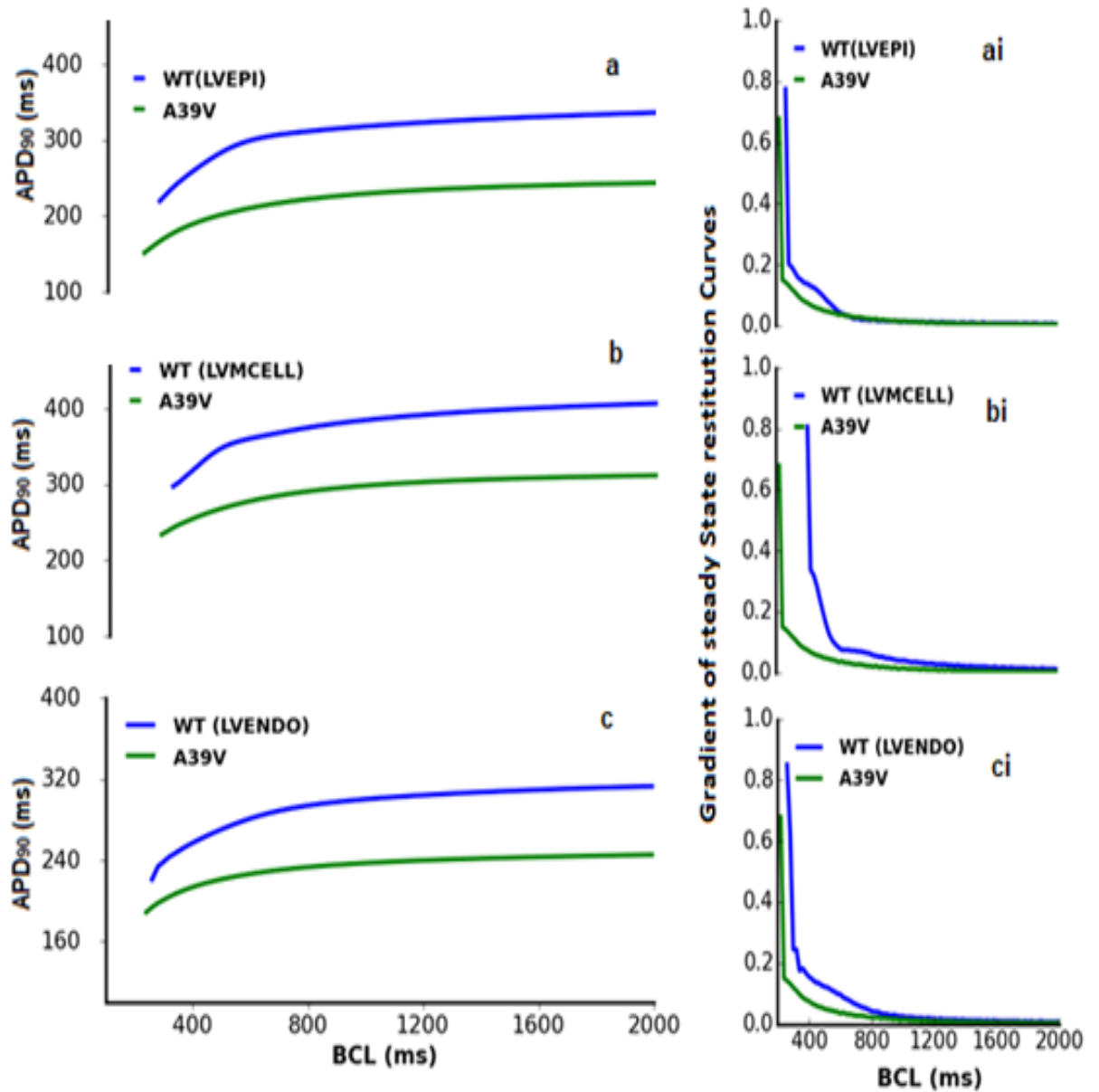


Figure 4.7: Steady-state APD₉₀ rate dependence curves for WT (blue) and A39V (green) condition. APD₉₀ is plotted against the basic cycle length (BCL). (a, b, c) Steady state APD₉₀ restitution curves for LVEPI (a), LVMCELL (b) and LVENDO (c) cells respectively for the WT (blue) and A39V (green) conditions. The steady state restitution curves were plotted to examine the rate dependence of APD₉₀(ms) with BCL (ms). The A39V model showed greater reduction of APD₉₀(ms) than the WT model, which suggest an attenuation of the rate adaption of the ventricular APD in the A39V model. (ai, bi, ci) Gradients of steady state restitution curves illustrating the behaviour of steady state restitution curves under the WT and A39V conditions.

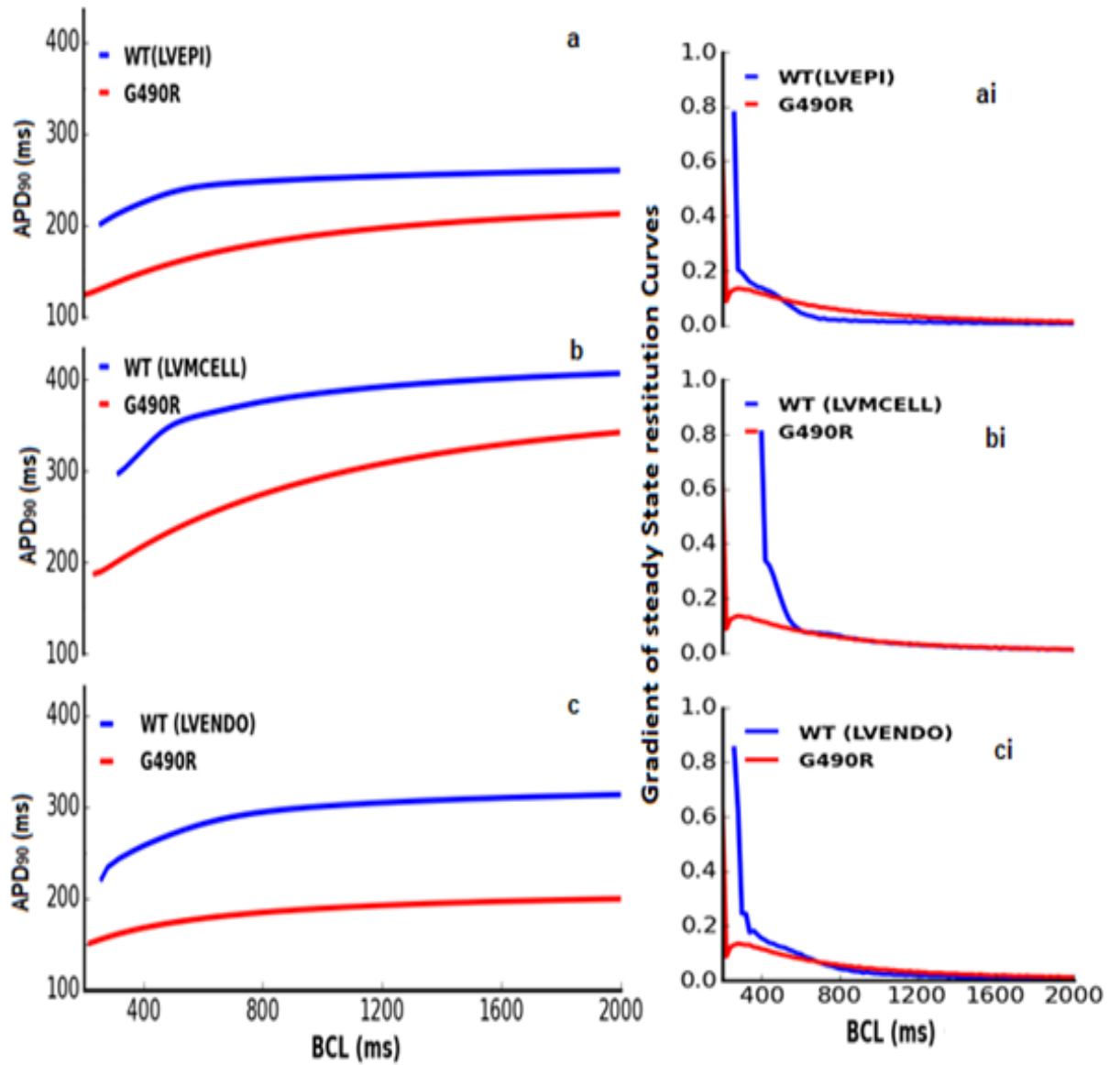


Figure 4.8: Steady state APD₉₀ rate dependence curves for WT (blue) and G490R (red) condition. APD₉₀ is plotted against basic cycle length (BCL). (a, b, c) Steady state APD₉₀ restitution curves for LVEPI (a), LVMCELL (b) and LVENDO (c) cells respectively for the WT and G490R conditions. APD-R curves showed a greater abbreviation of APD₉₀ under G490R mutation condition, which suggest a greater attenuation of rate adaption of the ventricular APD in the G490R model as compared to the WT and A39V mutation conditions. (ai, bi, ci) Gradients of steady state restitution curves illustrating the behaviour of steady state restitution curves under the WT and G490R conditions.

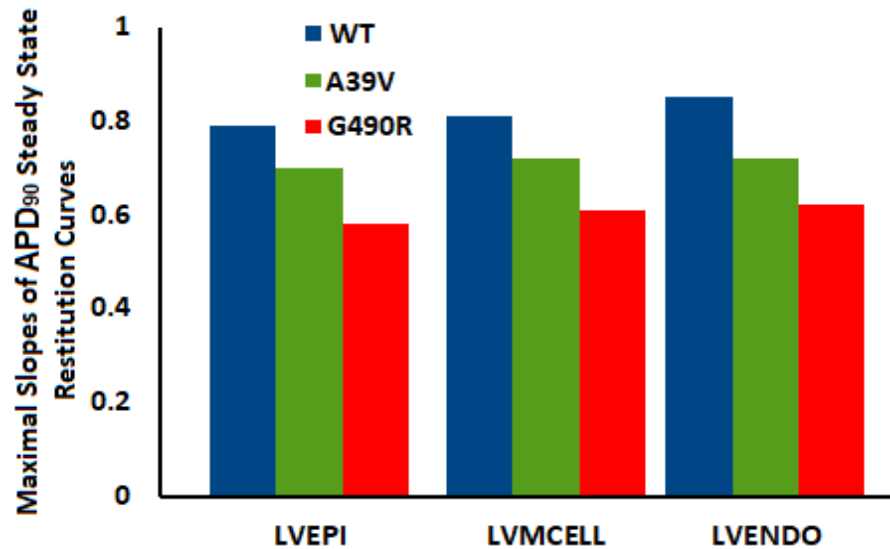


Figure 4.9: Slope for Steady-state APD₉₀ restitution curves for WT (blue), A39V (green) and G490R (red) obtained from Figure 4.7 and 4.8 (ai, bi, ci). A reduction in the slope of the steady state restitution curves can be seen with the reduced APD₉₀ for the A39V and G490R. A more dominant reduction of slope can be seen in the curve of the LVENDO cell under the G490R condition.

The effect of the A39V and G490R mutations on ERP restitution curves can be seen in Figures 4.10 and 4.11 (a, b, c). The ERP restitution curves were plotted as described in Chapter 3 (3.7.4). The leftward shift of the restitution curves permitted the ventricular cells to reinforce electrical activity at fast heart rates [14, 15, 16]. The reduction in the ERP was also rate-dependent [15, 21, 22, 27]. Results showed that the ERP values were reduced for G490R and A39V conditions across the range of basic cycle lengths. The restitution curve of the middle cell has a steeper slope (at slow heart rates BCL > 700 ms) for G490R condition Figure 4.11 (bi), while the slopes of ERP-R curves of LVEPI and LVENDO have been reduced for A39V and G490R. Results showed an attenuation of the rate adaptation of ERP under both the A39V and G490R mutation conditions (Figures 4.10, 4.11).

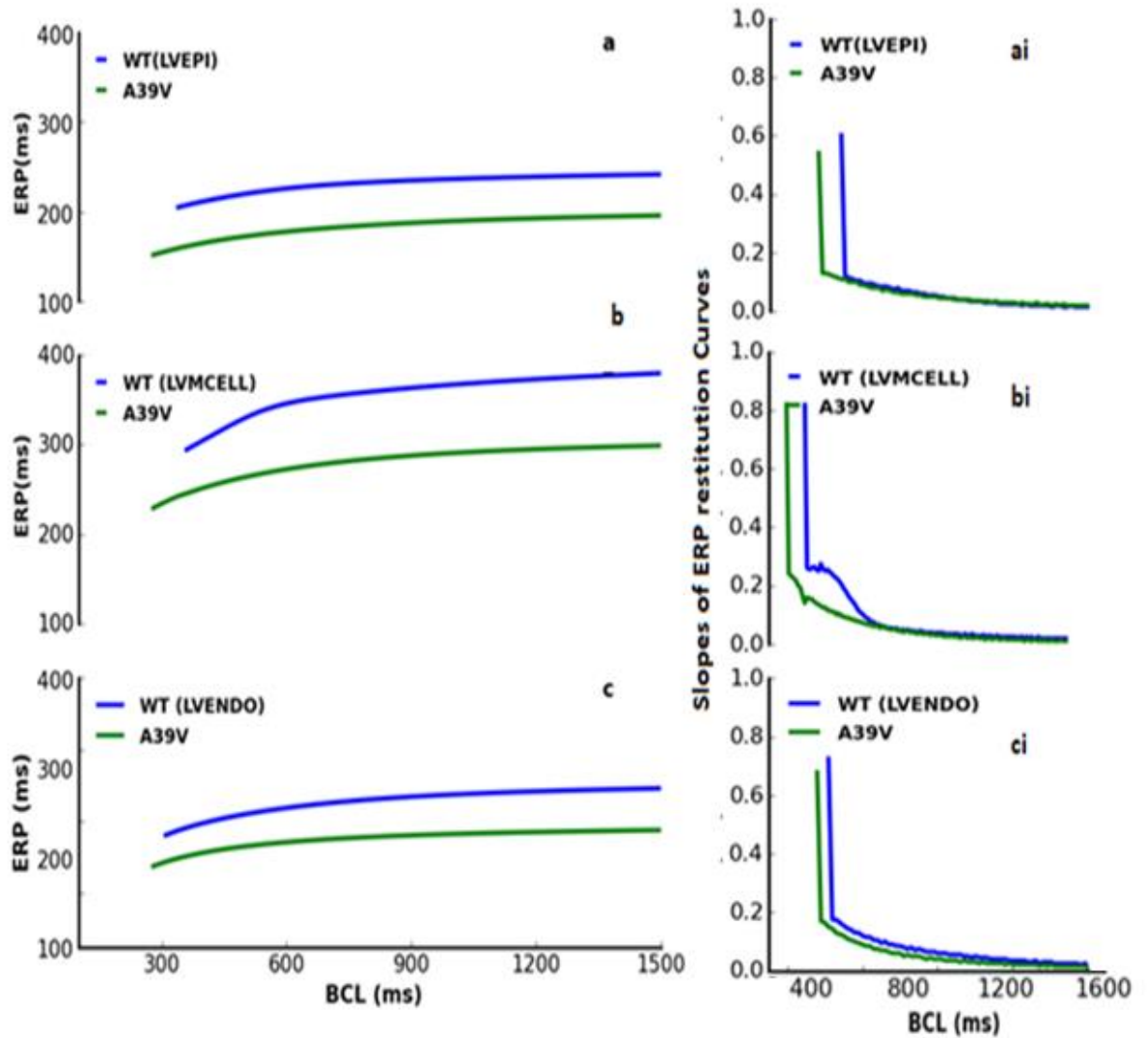


Figure 4.10: ERP restitution curves for WT and A39V were obtained by plotting the effective refractory period (ERP) against the basic cycle length (BCL). (a, b, c) ERP restitution curves for WT (blue) and A39V (green) models. (ai, bi, ci) Gradients of the steady state restitution curves illustrating the behaviour of the steady state restitution curves under WT and A39V condition. A reduction in the maximal slope of the ERP-R curves along with the shift of ERP-R curves towards left side for A39V condition can be seen in all three cell types.

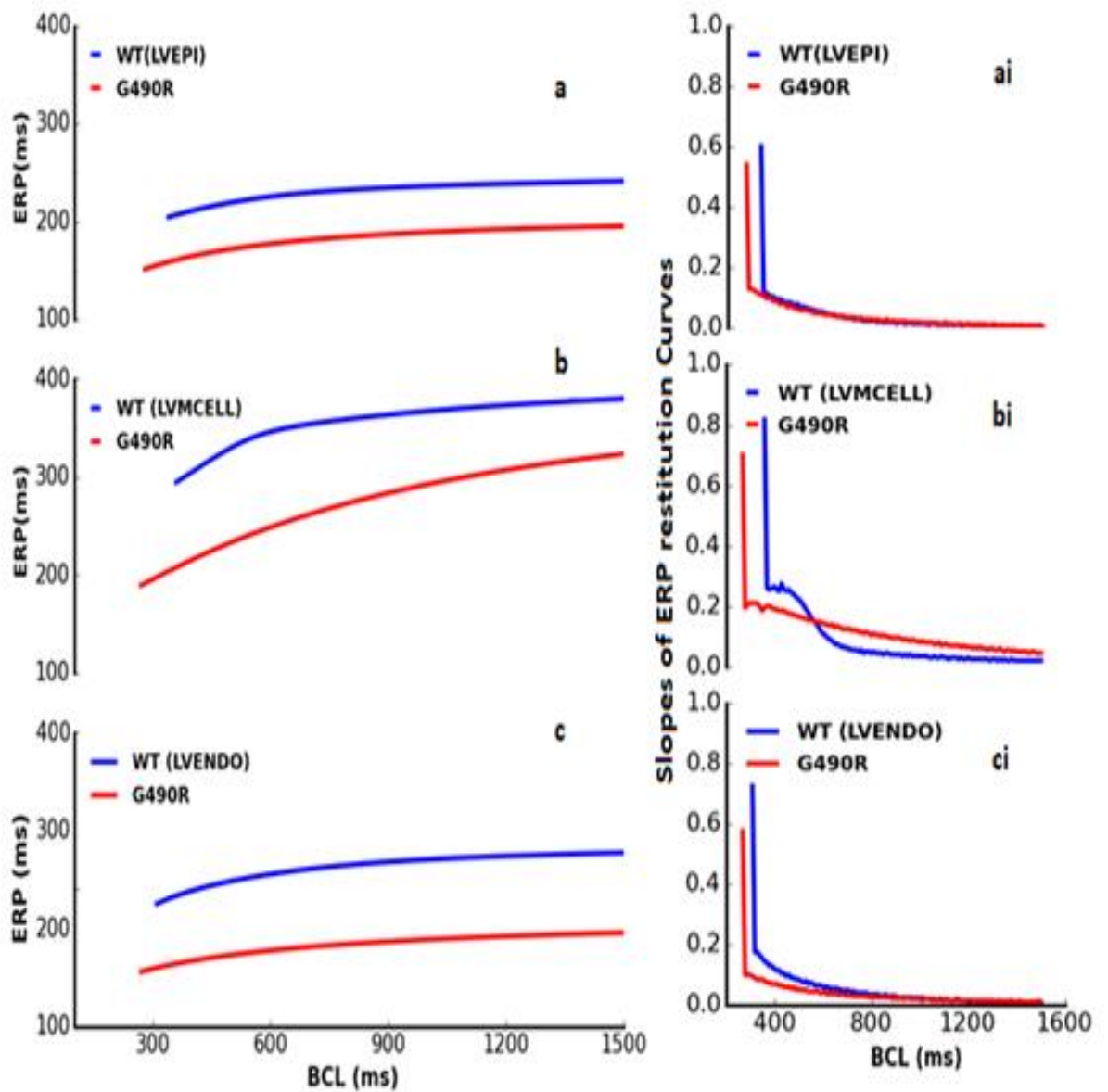


Figure 4.11: ERP restitution curves for LVEPI (a), LVMCELL (b) and LVENDO (c) cells for the α -subunit of CACNA1C/ I_{CaL} model formulation. ERP restitution curves for WT and G490R were obtained by plotting the effective refractory period (ERP) against the basic cycle length (BCL). (a, b, c) ERP restitution curves for the WT (blue) and G490R (red) models. (ai, bi, ci) Gradients of the steady state restitution curves illustrating the behaviour of the steady state restitution curves under the WT and G490R condition. G490R flattened the EPI and ENDO curves along with a leftward shift in all three cell types while change in steepness can be seen in the MCELL slope under the G490R condition at slow heart rates, BCL > 600 ms (bi).

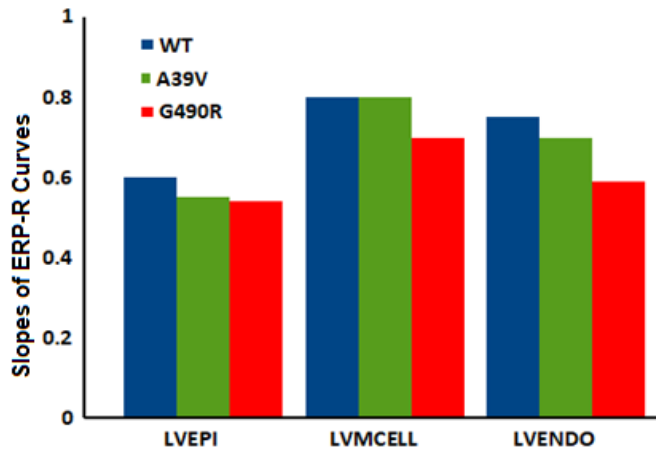


Figure 4.12: The maximal slope of ERP-R curves of the LVENDO, LVMCELL and LVEPI cell types. WT (blue), A39V (green) and G490R (red) obtained from Figure 4.10 and 4.11 (ai, bi, ci). A39V and G490R reduced ERP-R curve's slopes in all three cell types except for the LVMCELL maximal slope which remained unaffected under the A39V condition.

4.6 Membrane Potential Heterogeneity

In previous studies, Gima and Rudy [19] suggested that an increased spatial gradient of the membrane potential (δV) can cause a tall T-wave and is associated with hyperkalemia [20]. It was also found to be relevant in our laboratory [20, 21]. To investigate the effects of increased spatial gradient on the amplitude of T-wave for the G490R and A39V mutation condition, the effects were investigated on membrane potential heterogeneity (δV) during ventricular APs between the three cell types. The research shows a pair-wise differences of δV , over the course of time between the cell types for both the WT and SQT4S conditions. In Figure 4.13-4.14, membrane potential heterogeneity was calculated as the difference of membrane potential (V_m) between LVEPI, LVMCELL and LVENDO cell types. A decrease in δV for both G490R and A39V mutations can be seen in each pair-wise comparison of different cell types. As we have already discussed, the tall T-waves are associated with hyperkalemia, and medically it is associated with higher potassium levels in the blood which can cause nonspecific repolarisation abnormalities [19, 20]. To validate this, the values of δV were adjusted by using a heterogeneous distribution of I_{Kr} between LVEPI and LVMCELL [27]. With ratios of 1.6:1:1 (Figure 4.13b), the A39V mutation increased the δV between MIDDLE and LVEPI cells, whereas an increased δV could also be seen between MIDDLE and LVEPI cell with an I_{Kr} ratio of 1.6:1:1 for the G490R mutation (Figure 4.13d).

This can be considered to cause an increased T-wave amplitude in these simulation conditions [19, 21].

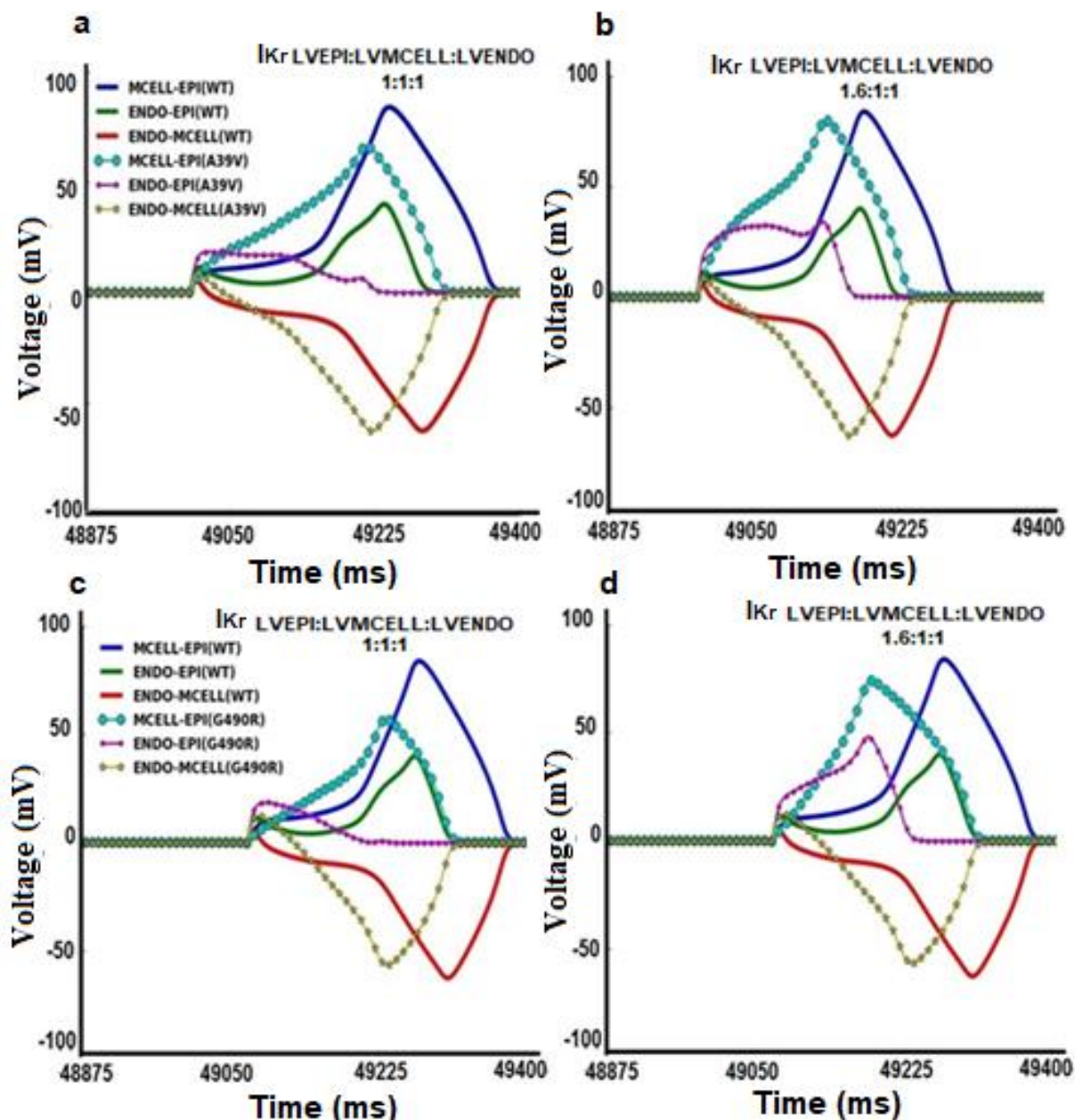


Figure 4.13: Membrane potential heterogeneity (δV) is plotted as a function of time. (a, b) δV versus time for WT (continuous lines) and A39V (dotted lines) conditions for different LVEPI: LVMCELL: LVENDO I_{Kr} density ratios; (a) 1.0:1:1 (b) 1.6:1:1. (c, d) δV versus time for WT (continuous lines) and G490R (dotted lines) conditions for different LVEPI: LVMCELL: LVENDO I_{Kr} density ratios; (c) 1.0:1:1 (d) 1.6:1:1.

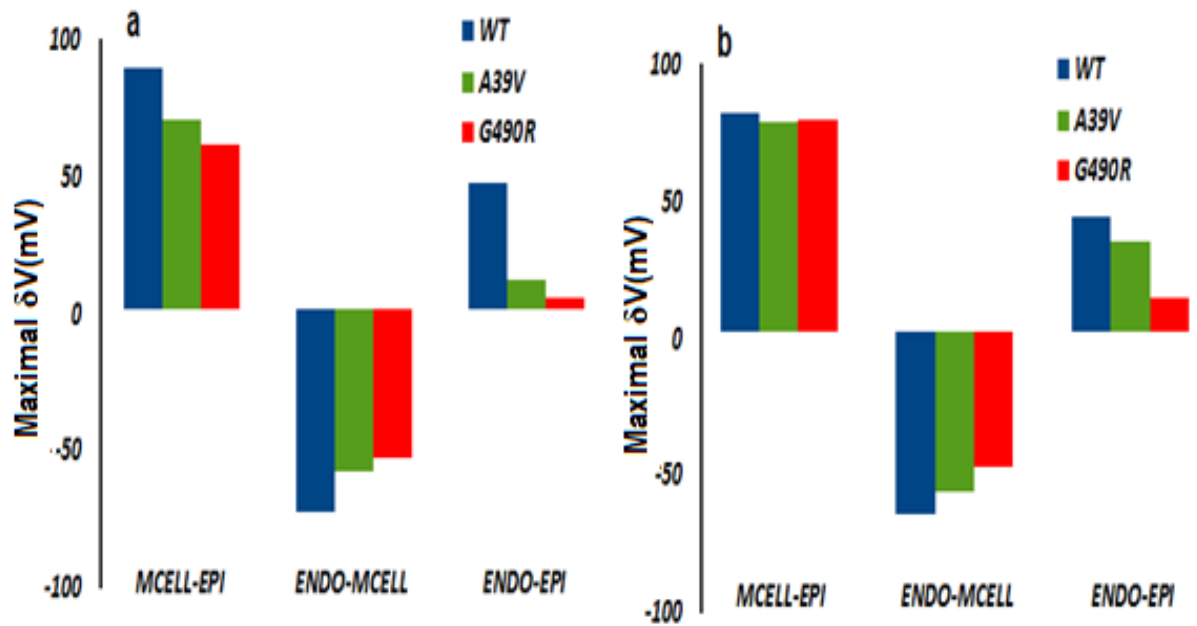


Figure 4.14: Maximum δV during repolarisation between the LVMCELL-LVEPI, LVENDO-LVEPI and LVENDO-LVMCELL cells in the WT, A39V and G490R conditions. (a) I_{Kr} density ratios of 1.0:1:1 for LVEPI: LVMCELL: LVENDO for WT (blue), A39V (green) and G490R (red) conditions, (b) I_{Kr} density ratio of 1.6:1:1 for LVEPI: LVMCELL: LVENDO for WT (blue), A39V (green) and G490R (red) conditions.

4.7 1D Simulations for CACNA1C WT and SQT4/A39V/G490R Conditions

The 1D strand model of the ventricular cells, explained in Chapter 3 has been utilised in the simulations. The wave propagated from the LVENDO end of the 1D strand towards the LVEPI end through the middle region (Figure 4.15 a-c). In Figure 4.15 (a-c), time runs horizontally from left to right, while space runs vertically from the LVENDO end at the bottom to the LVEPI end at the top of the 1D sheet. Figure 4.16 shows the spatial distribution of APD_{90} along the 1D strand.

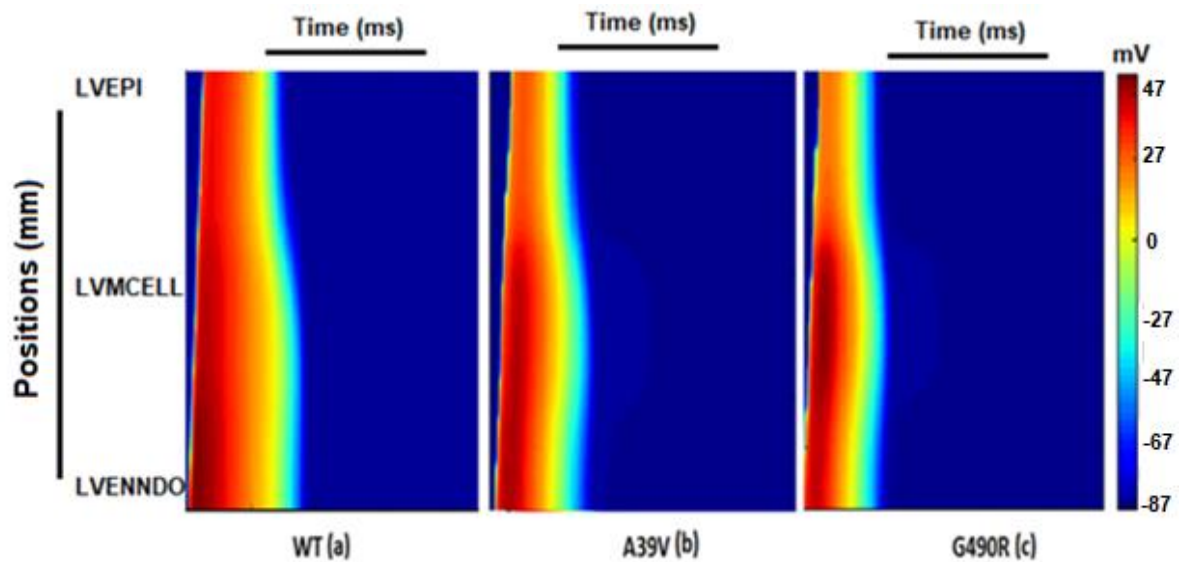


Figure 4.15: Space-time colour-mapping of membrane potential in a 15 mm long ventricular wall strand during the propagation of an action potential cycle (BCL=1000 ms). (a, b, c) WT (a), A39V (b) and G490R (c). Positions (mm) run vertically with LVEPI at the top and LVENDDO at the bottom, while the time (ms) runs horizontally. Colour mapping of membrane potentials of cells along the strand changes from blue (-87 mV) to red (47 mV).

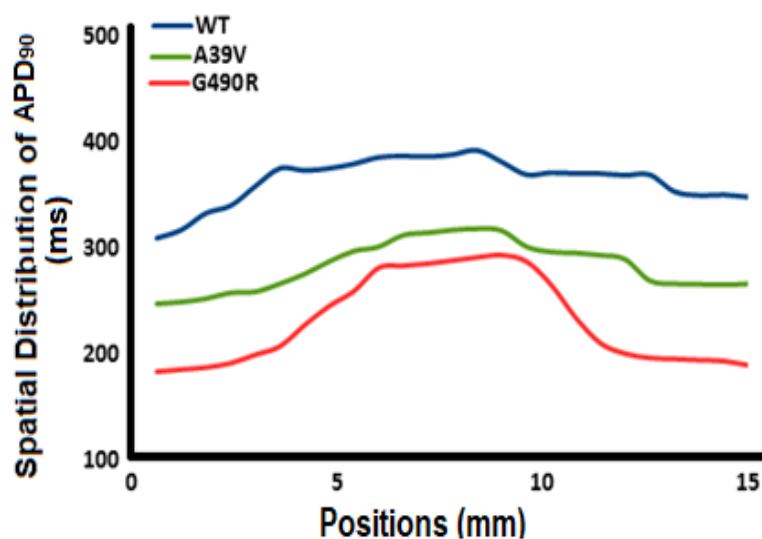


Figure 4.16: Spatial distribution of APD₉₀ along the 15 mm long 1D strand for the WT (blue), A39V (green) and G490R (red) models.

4.7.1 ECG and QT Interval

Pseudo-ECGs were computed for the WT, A39V and G490R conditions (Figure 4.17a). The value of the QT interval was 351 ms in the WT condition. Results have suggested that the QT interval reduced to 287 ms for the A39V and 262 ms for the G490R condition (Figure

4.17a). The time interval between the T-peak and T-end (the T-wave half width) was 49 ms for the WT condition.

The value of the T-wave half width changed to 72 ms for the G490R and 56 ms for the A39V condition. The short QT interval and the wider $T_{\text{peak}}-T_{\text{end}}$ width are the key features observed in the ECGs of the SQTs patients [14, 16, 17, 23, and 24]. Simulations thus reproduced these features. Another feature of the ECGs which is very prominent in SQT4 patients is the elevation of the ST segment [9, 24]. The ST segment elevation distinguishes the potassium related SQT syndromes from the calcium related SQT syndromes [9]. A study by Yan and Antzelevitch has suggested that a decrease in the amplitude of AP dome of EPI as compared to ENDO creates a transmural voltage gradient across the ventricular wall, which can elevate the ST segment [44, 45]. The ST segment elevation can be measured on the pseudo-ECG; the J-point plays a very important role to measure the elevation of the ST segment. Elevation of the ST segment can be measured at a local region on the ECG at 60 ms after the J-point [44]. Simulations have reproduced this feature for both the G490R and A39V mutation conditions. For the A39V mutation condition, the ST segment elevation was measured as 3 mm as compared to the WT baseline, while the elevation of the ST segment was 3.4 mm for G490R. The J-wave elevation has also been observed in G490R and A39V mutation conditions. Previous studies have suggested that, the J-wave elevation can be associated with the elevation of the ST segment (Brugada syndrome) [25, 26, 27]. The 1D strand model for A39V and G490R mutation reproduced the QT interval shortening and the ST segment elevation. It did not show tall T-waves for the SQT4 ECGs, which is consistent with the clinical observations [9].

Gima and Rudy [19] have suggested that the tall T-waves are linked with hyperkalemia which is associated with high levels of potassium in blood [20]. A study by I. Adeniran et al. [27] acquired a heterogeneous distribution of I_{K_r} along the 1D ventricular strand to obtain tall T waves. To investigate the key difference between the SQT4 and K^+ related SQTs ECGs, the same approach was followed in simulations, by considering a heterogeneous distribution of I_{K_r} density in the 1D strand model. The I_{K_r} density was adjusted between 1.3-1.6 times greater in the LVEPI region compared to the MIDDLE region. The model was able to reproduce the increased T-wave amplitude following this adjustment, but the QT value was further reduced due to an increased efflux of I_{K_r} current (Figure 4.17b). Based on these results (Table 4.3), it can be assumed that tall T-waves are linked with the increased potassium current efflux levels in the SQT1-3 syndrome patients. The potassium current density remained unaffected for SQT4 mutations.

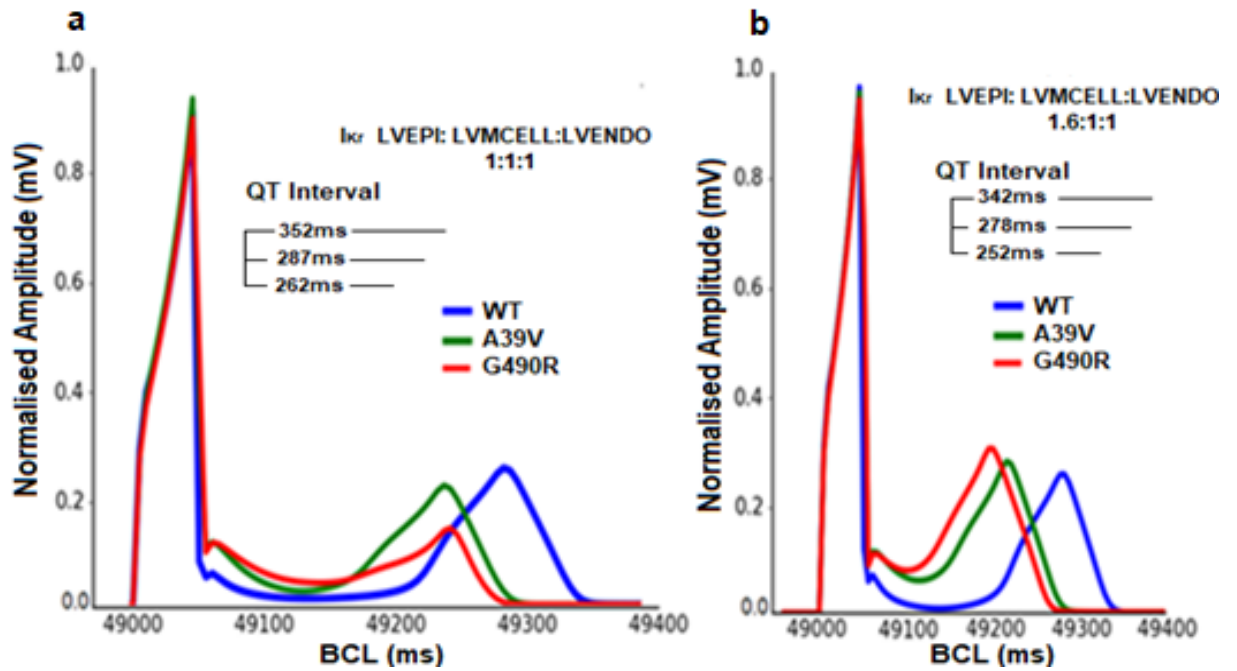


Figure 4.17: Pseudo-ECG associated with the WT and SQT4 (A39V and G490R) conditions. WT (blue), A39V (green) and G490R (red). a) ECGs with the I_{Kr} densities of 1:1:1 in the EPI: MCELL: ENDO cells for the WT, A39V and G490R conditions. b) ECGs with the I_{Kr} densities of 1.6:1:1 in the EPI: MCELL: ENDO for the WT, A39V and G490R conditions. The relevant parameters of the Pseudo-ECGs are given in Table 4.3, which describes the ST segment elevation, T-wave amplitude, T-wave half width and the QT interval under WT, A39V and G490R conditions.

	WT	WT	A39V	A39V	G490R	G490R
I_{Kr} LVEPI-LVENDO and LVMCELL density ratio.	1:1:1	1.6:1:1	1:1:1	1.6:1:1	1:1:1	1.6:1:1
QT Interval (ms)	351	341	287	276	262	252
T-Peak to T-end (ms)	49	57	58	60	72	76
ST Segment elevation (mm)	0 Baseline	0 Baseline	3.0	3.0	3.4	3.6
T-wave Amplitude		Increased	Decreased	Increased	Decreased	Increased

Table 4.3: Comparison of different features of ECGs with different I_{Kr} current densities, while the I_{CaL} ratio is 1:1:1 across LVEPI, MIDDLE and LVENDO cell types.

4.7.2 Investigation of the Arrhythmogenic Substrate in CACNA1C WT and SQT4 1D Simulations

The 1D strand model was constructed to investigate the behavior of the arrhythmogenic substrate in WT, A39V and G490R conditions. The susceptibility of the WT, G490R and A39V tissue to a unidirectional block was investigated by applying a premature stimulus during the refractory tail of a preceding excitation wave. A train of 10 S1 stimuli paced at a frequency of 1 Hz was applied at the LVENDO end of the 1D transmural strand to initiate a propagating wave. A second stimulus (S2) was applied after the 10th S1 following a time delay (ΔT). The amplitude and the duration for S1 and S2 were similar. ΔT ($T_2 - T_1$) represents the maximal and minimal values of a temporal window during which the propagation of the excitation wave initiated by the S2 stimulus was unidirectional in the 1D strand. Figure 4.18 (a-b) shows the width of the vulnerability window across the 1D strand. This width represents the time during which a premature stimulus can lead to re-entry. For the A39V mutation condition, the width of the vulnerability window was increased across the whole 1D strand Figure 4.18 (a). In G490R the vulnerability was increased across the 1D strand except in a very small region in the middle of the strand (Figure 4.18b). Although the 1D tissue model showed a greater vulnerability width for the G490R condition as compared to WT and A39V in the marked region. Figures 4.18-4.19 show the temporal vulnerability window width for the marked region under WT, G490R and A39V conditions. The width of the vulnerable window measured within the marked regions is 19.2 ms, 25.7 ms and 31.5 ms for the WT, A39V and G490R conditions respectively.

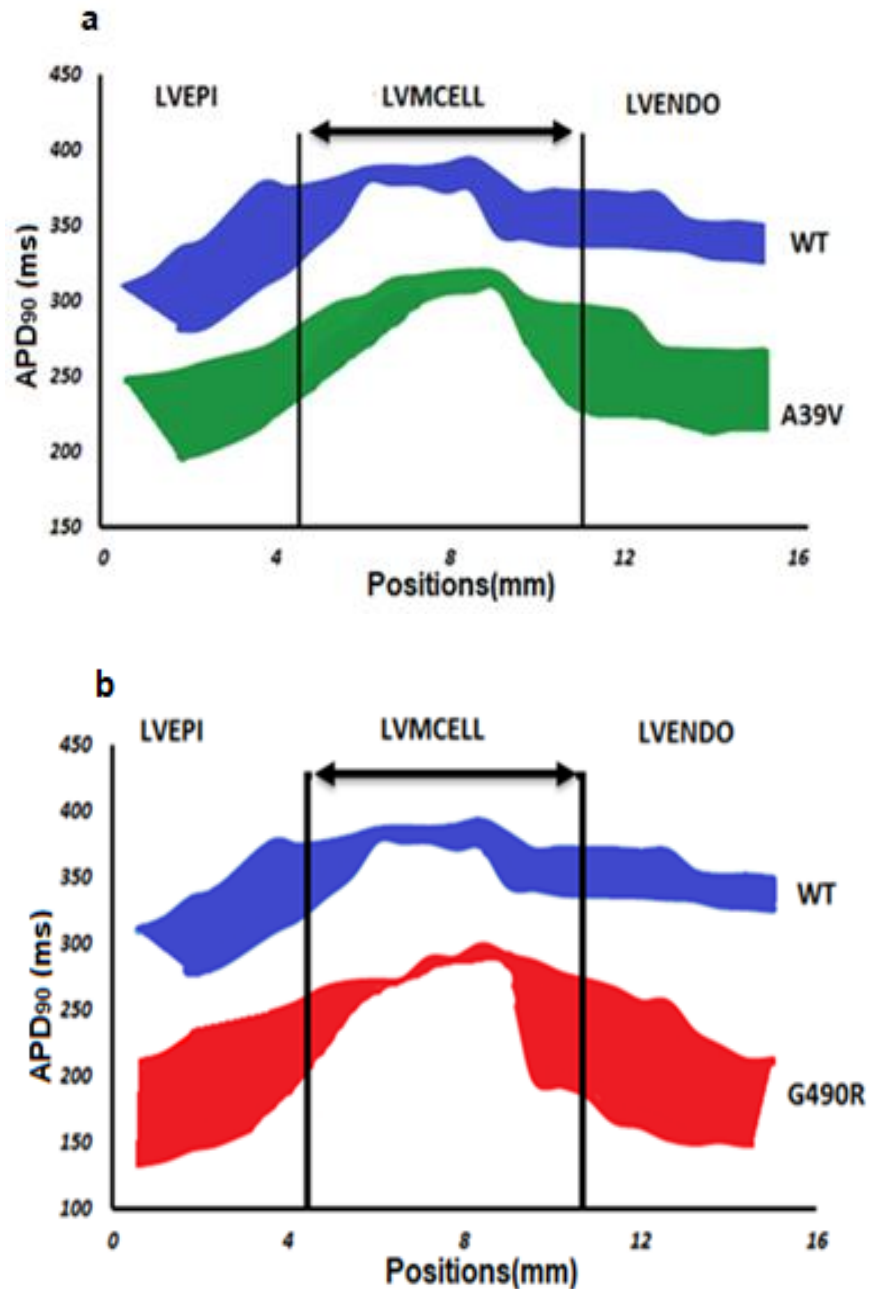


Figure 4.18: The Vulnerable Window across the transmural 1D strand was plotted as a function of position on a 15 mm long 1D strand of ventricular myocytes, with each cell having a spatial resolution of 0.15 mm. The width of the Vulnerable Window (VW) is measured between the marked region depicted by an arrow. a) VW for the WT and A39V, b) Vulnerable Window for the WT and G490R.

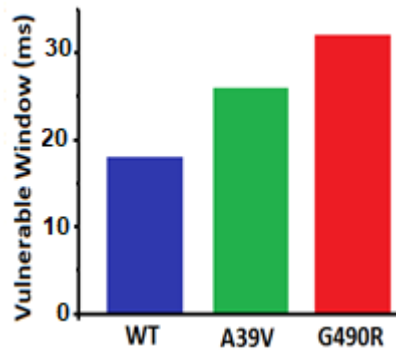


Figure 4.19: Measured Vulnerable Window (VW) widths within the marked region (an average of different VW widths within the marked region depicted by an arrow) in Figure 4.18, for WT (blue), A39V (green) and G490R (red).

4.7.3 Computation of the Conduction Velocity across the 1D Strand

For WT, G490R and A39V conditions, the conduction velocity (CV) was computed across the 1D ventricular strand model (Figure 4.20). Results have shown a decrease in CV at slow heart rates (rate < 109 beats/minute, PCL > 420 ms) due to the mutation. While an increase in CV under A39V and G490R can be seen at higher heart rates (280 ms < PCL < 360 ms). This trend of CV has been seen in previous studies [27, 28]. The reduced tissue excitability (Figure 4.21) at lower heart rates in A39V and G490R could be a reason for the lower values of CV at rates lower than 109 beats/minute as no change in the intercellular electrical coupling was considered at these rates.

The CVs were calculated at a rate of 60 beats/minute (BCL=1000 ms). The measured CV was 66 cm/s for the WT, 64 cm/s for A39V and 62 cm/s for the G490R conditions. However, the CV values measured at higher rates, between 130 and 170 beats/minute (280 ms >PCL< 340 ms) were higher in the A39V and G490R conditions as compared to WT. The increased CV in A39V and G490R at high rates is due to short effective refractory periods as compared to WT [29]. The fastest heart rate which supported conduction in ventricular tissue for the WT, A39V and G490R conditions was 134 beats/minute (SI<330 ms), 156 beats/minute (SI<280 ms) and 168 beats/minute (SI<260 ms) respectively. A large part of the tissue was still refractory in the WT, which caused the failure of conduction in WT at higher heart rates as compared to the mutations.

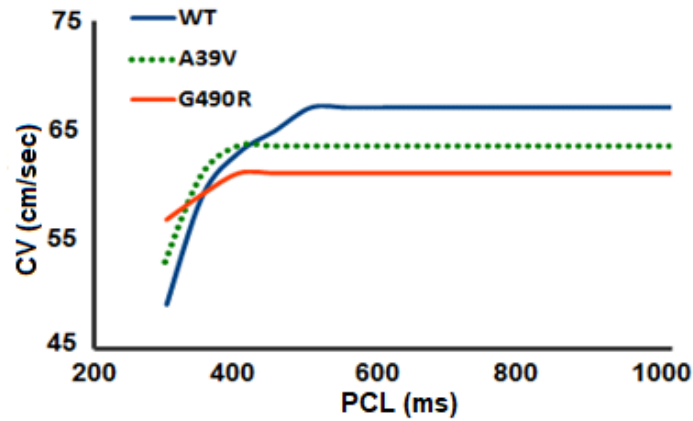


Figure 4.20: Conduction velocity (CV) restitution curves for the WT (blue), A39V (green) and G490R (red) conditions. The CV curve was plotted against the Pacing Cycle Length (PCL).

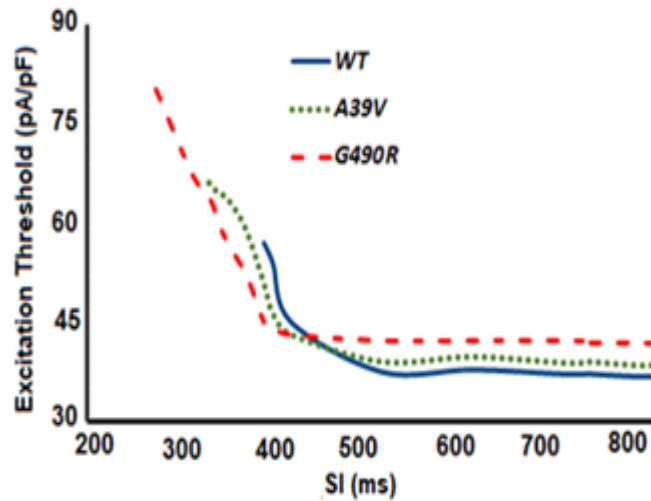


Figure 4.21: Excitation threshold plotted against the Stimulus Intervals (SI) for the WT (blue), A39V (green) and G490R (red) mutation conditions. The tissue excitation threshold is a measure of the minimal stimulus amplitude that can initiate a propagating action potential in a cardiac tissue [43]. The fastest heart rates which supported conduction in ventricular tissue for WT, A39V and G490R conditions were 134 beats/minute (SI < 330 ms), 156 beats/minute (SI < 280 ms) and 168 beats/minute (SI < 260 ms) respectively

4.8 Investigation of the Arrhythmogenic Substrate in an Idealised 2D Tissue Sheet

An idealised 2D ventricular tissue model was constructed to compute the minimal spatial length of a premature stimulus which can initiate and sustain a re-entrant wave in both WT

and mutations i.e. G490R and A39V conditions. To produce a 2D tissue model, the 1D strand was extended along the y-axis by keeping the regional symmetry the same as that of the x-axis. Similar to the 1D strand, the 2D tissue sheet had three distinct regions LVENDO, LVMCELL and LVEPI.

An excitation wave was evoked by applying a conditioning stimulus (S1) at the LVENDO end of the 2D sheet. The excitation wave initiated by the S1 stimulus propagated from the LVENDO end to the LVEPI end of the 2D tissue sheet. Following a time delay, a 2nd test stimulus (S2) was applied in a localised region of LVEPI section of the sheet (Figure 4.22 a, b, c). The time delay was chosen such that S2 was applied during the Vulnerable Window (VW) of LVEPI region of the 2D sheet. The excitation wave evoked by S2 was blocked by unrecovered LVMCELL, as the LVMCELL region is still refractory due to the slower repolarisation as compared to LVEPI and LVENDO regions (the refractory period of LVMCELL is longer than LVEPI and LVENDO). This hence gave rise to unidirectional conduction towards the LVEPI side. The same procedure was repeated for the A39V and G490R conditions. This unidirectional block resulted in the formation of spiral re-entrant excitation waves in the WT, A39V and G490R conditions. For WT, A39V and G490R, the time delay between S1 and S2 was 381 ms, 219 ms and 217 ms respectively. In WT, the excitation re-entrant wave terminated within 315 ms after the time of its initiation, but it was sustained for both the A39V and G490R (Figure 4.22). My results are consistent with the previous studies for SQT syndromes [27, 28, and 29] i.e., re-entry was sustained over the entire cycle of 1000 ms.

A sufficient S2 size is required to initiate a sustainable re-entry in a ventricular tissue, and it is proportional to the wavelength of the spiral wave (the product of the conduction velocity and APD₉₀). In order to evaluate the critical size of the re-entrant pathway of the tissue, the minimal spatial S2 length that is necessary to initiate and sustain re-entry was measured for WT and both mutation conditions (A39V and G490R). The minimal substrate lengths for WT, A39V and G490R were measured as 24 mm, 20 mm and 17.5 mm respectively (Figure 4.23). Results have suggested that it's much easier to induce re-entry in A39V and G490R as compared to the WT. Hence the tissue is more susceptible to ventricular arrhythmias in the A39V and G490R conditions.

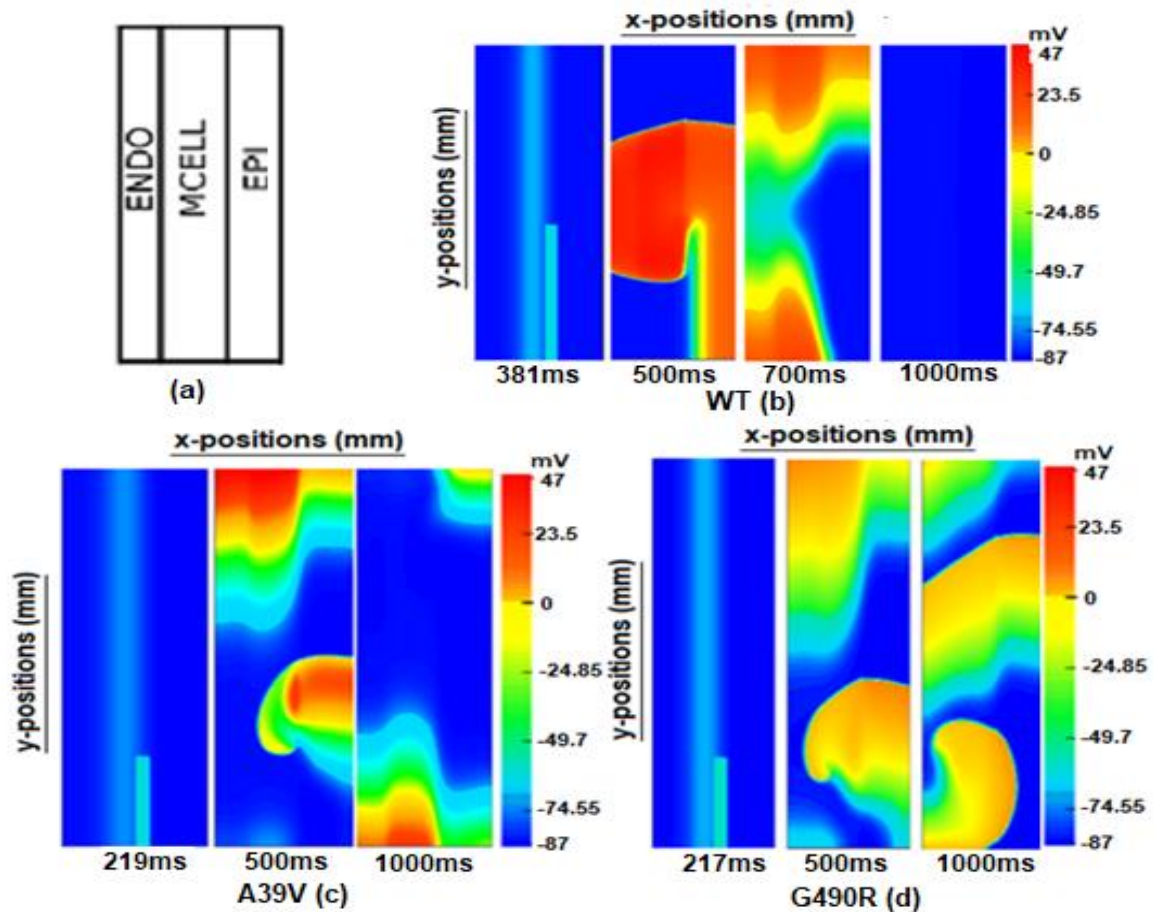


Figure 4.22: Snapshots of initiation and conduction of the spiral re-entrant excitation wave in a 2D idealised model. a) A schematic representation of the 2D model. (b, c, d) A spiral wave was developed by applying the S2 stimulus during the VW of LVEPI region for the WT and mutations (S2 was applied at 381 ms, 219 ms and 217 ms for the WT, A39V and G490R conditions). The spiral wave initiated by S2 was terminated under the WT condition after 319 ms, while it sustained over the entire cycle of 1000 ms for the A39V and G490R conditions.

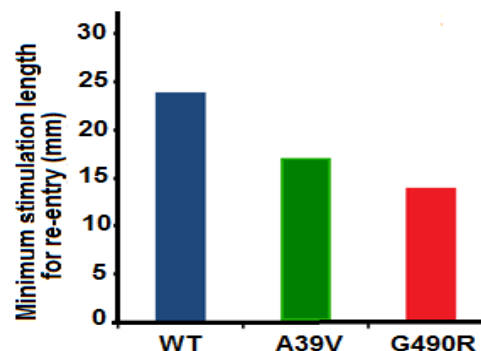


Figure 4.23: The minimal spatial length of the premature stimulus S2 that is necessary to initiate re-entrant spiral waves in the WT (blue), A39V (green) and G490R (red) 2D models.

4.9 Formation of a Spiral Wave and its Behavior in a 2D Idealised Tissue

The phase mapping technique allows for the precise identification of Phase Singularity (PS) points for the WT and mutations in space over time, as illustrated in Figure 4.26. Every phase in the excitation recovery cycle is defined by a colour. The point where all the phases converge is defined as the Phase Singularity (PS) point. However, the surrounding regions displayed a continuous progression of phases that is equal to $\pm 2\pi$ around the PS [31, 32]. Plotting the dynamics of the spiral wave on the phase space has many advantages, as it allows a more detailed study of the initiation, maintenance, and the termination of excitation waves under the normal and the mutation conditions [32]. In many cases, the spiral wave can be terminated if there is a collision of the PS with a boundary [31-33]. Phase mapping allows for a closer look at the activation wavefront of the spiral wave evoked by the S2. It illustrates the wave-front, the wave-tail and the point at which the wave-front meets the curved wave-tail. As the cardiac impulse moves forward, the wave-front represents a region composed of depolarised cells, while the wave tail represents an area with a group of cells returning to the resting potential (repolarisation). The point where the wave tail meets the wave-front is explained by Gray et al [32, 33] as a singularity point or Phase Singularity (PS), represented by a white asterisk in Figure 4.26 (a, b, c). The singularity point plays an important role in understanding the dynamics of the spiral wave tip trajectory [31] in space over time.

The wave tip and the core play a very important role to determine the trajectory of the spiral wave in a 2D tissue. The combination of both can yield different patterns i.e. a flower like pattern either with inward or outward petals. The direction of the petals is dependent on the direction of the core and the wave tip. Inward petals are formed when both the tip and the core of the spiral wave rotates in the same direction., i.e. clockwise (CW) rotation. On the other hand, an outward flower pattern is obtained when both the tip and the core rotate counterclockwise (CCW) [42]. It's not necessary to always expect to obtain flower like episodes. A drift pattern was also previously described by Pertsov et al. [30, 32]. Furthermore Dave T. Kim et al. has observed drift pattern in one episode of swine RV [31]

The tip trajectories for WT, A39V and G490R mutations were calculated by using the Phase Singularity method [32, 33], Figure 4.24. For the A39V condition, a drift can be seen in the tip of the spiral wave, Figure 4.24(aii). It illustrates a CW rotating excitation wave perpendicular to the fiber orientation, Figure 4.24(aiii) shows the behavior of the spiral excitation wave in the G490R model. The trajectory of the wave showed that the wave had

a stationary tip and a flower-like pattern, with outward petals. It can be assumed that both the wave tip and the core are rotating counter-clockwise (CCW) [31-33, 42]. For WT and A39V to calculate phase the computed values for v' and u' in this case were -40 mV and -50 mV respectively (v' and u' are the origin points in the state-space as defined in Chapter 3), while it is different for G490R. The values of v' and u' were -35 mV and -45 mV respectively. The total life span of the re-entrant excitation wave in the WT condition was measured as 220 ms (Figure 4.22a, Figure 4.25a). For A39V, the re-entry was sustained for the entire cycle of 1000 ms (Figure 4.22b, Figure 4.25a). In the case of G490R, the re-entrant wave also was sustained for the entire stimulus duration of 1000 ms (Figure 4.22c, Figure 4.25a). The power spectrum of the recorded local electrical activity for WT revealed a dominant frequency of 3.2 Hz, while the dominant frequencies for A39V and G490R were 3.6 Hz and 3.32 Hz respectively (Figure 4.25b).

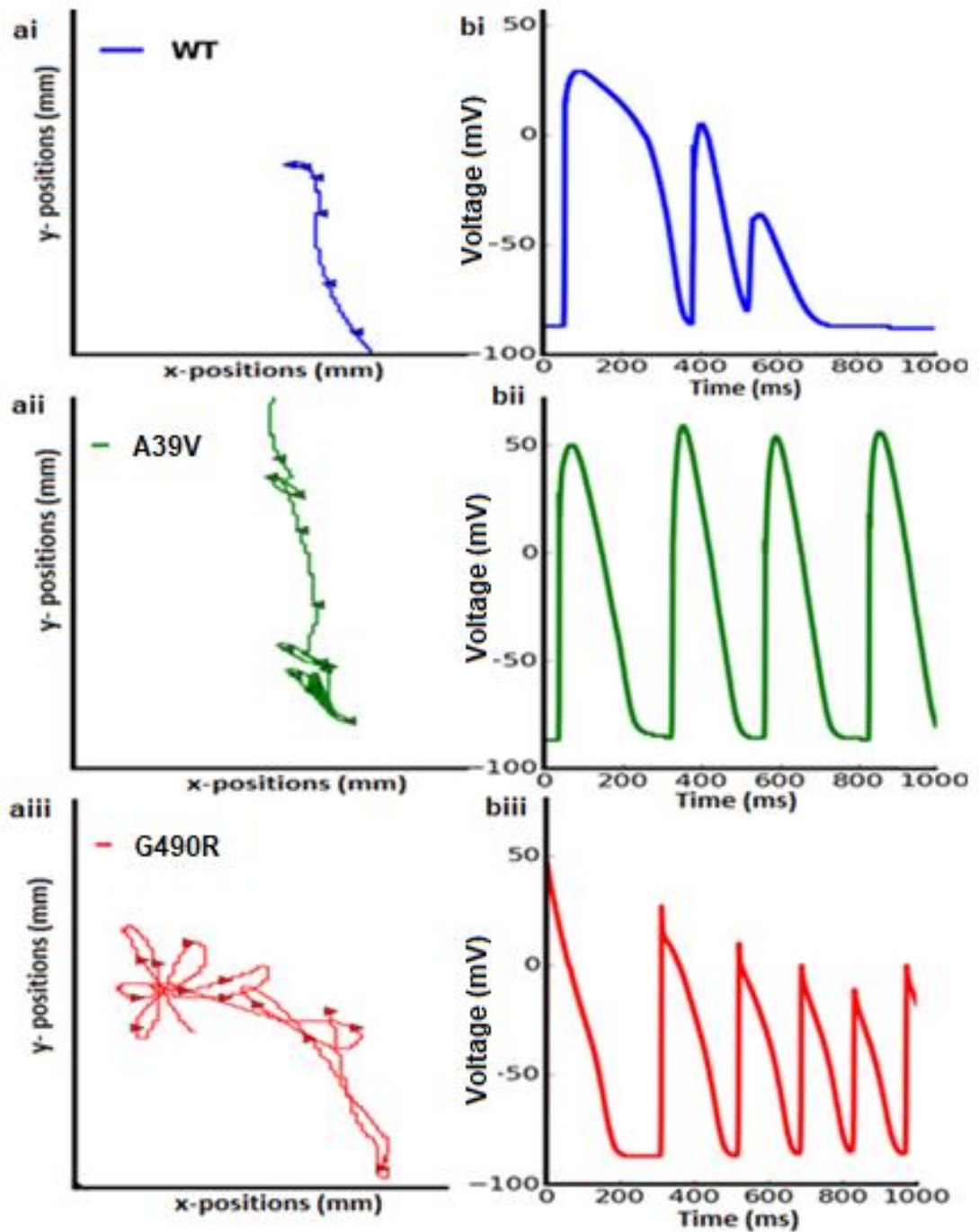


Figure 4.24: Illustration of the trajectories and the electrical activity of the spiral waves in a 2D model of the human ventricle cells. The geometry of the 2D sheet is same as described in Figure 4.22a. (ai, aii, aiii) The re-entrant wave tip trajectories for WT (blue), A39V (green) and G490R (red) in x and y space (mm) illustrate the path followed by the spiral wave in the 2D tissue sheet of the left ventricular cells. (bi, bii, biii) Time course of localised electrical activity illustrating the life span of the re-entrant wave.

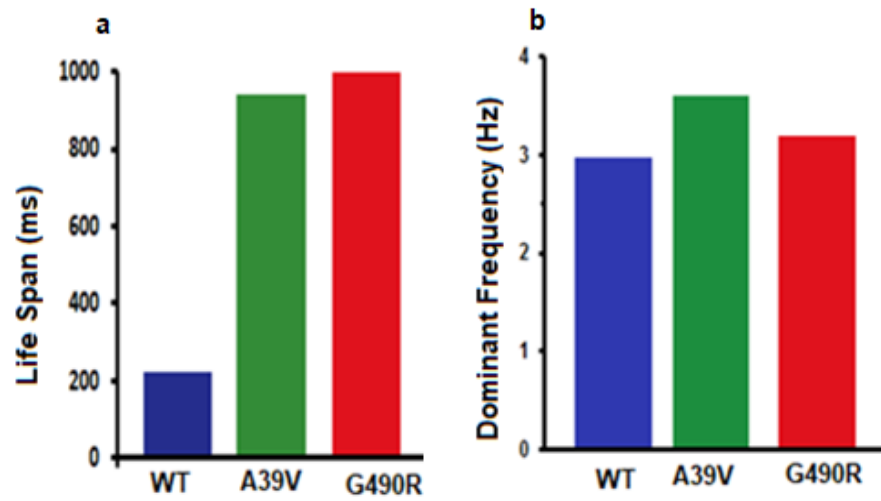


Figure 4.25: a) Life Span of the re-entrant spiral waves in the 2D tissue models of WT, A39V and G490R. b) The dominant frequency obtained from the power spectral density analysis of the WT, A39V and G490R conditions (Appendix C).

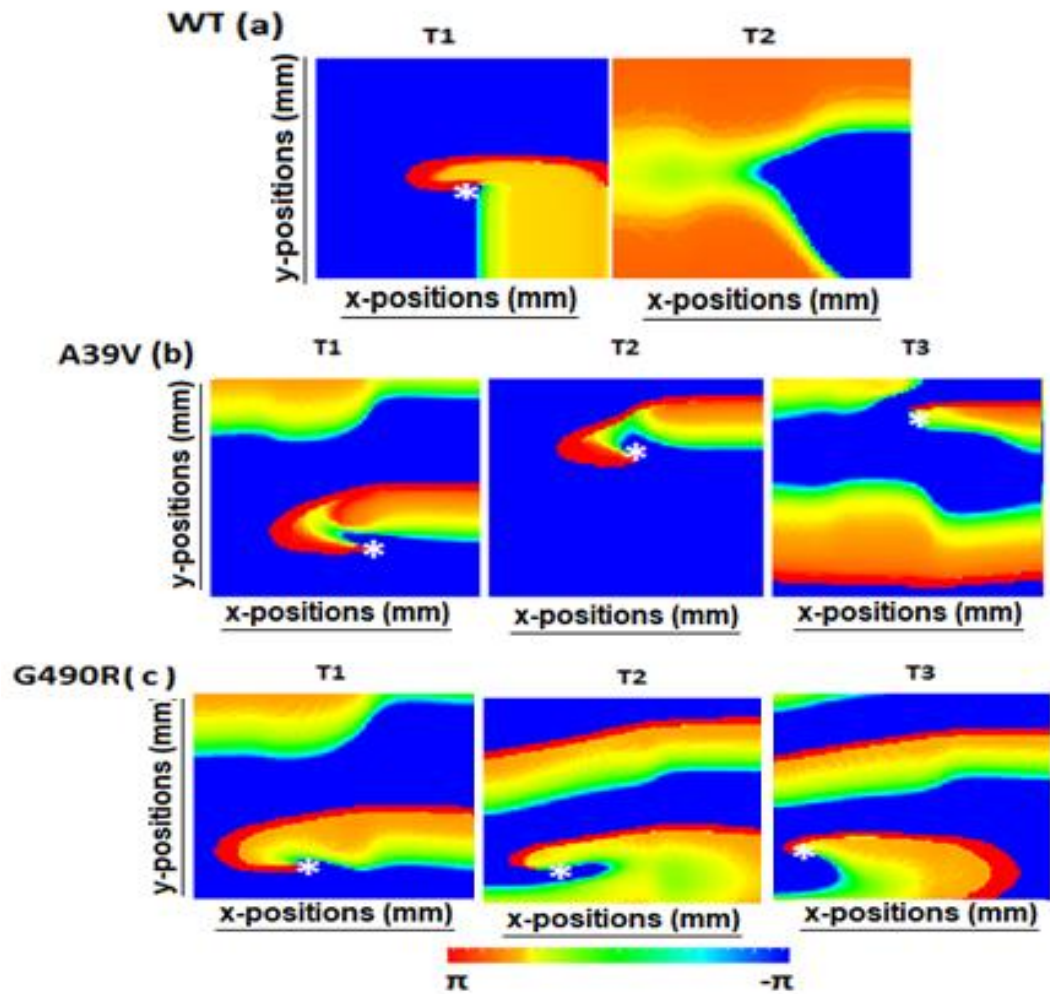


Figure 4.26: Phase mapping of the re-entrant excitation wave for the WT (a), A39V (b) and G490R (c) conditions. The layout of the 2D sheet is the same as that defined in Figure 4.22a. The white asterisk on the figures represents the phase singularity point where the wave tip meets the wave tail. The wave front represents the group of depolarised cells while the tail is composed of cells, returning to rest. T1, T2, T3 and T4 are the time intervals at which the activity of the spiral wave was recorded. $\pm\pi$ represents the changes in phase from $+\pi$ to $-\pi$ [31-34].

4.10 I_{CaL} Enhancement as a Potential Therapeutic Target in the SQT4

Implantable Cardiovascular Defibrillators (ICD) are commonly used to treat SQT syndrome patients [34, 35]. They are not suitable for every patient especially infants. Another issue is that ICDs do not restore the QT interval precisely. Therefore, it is very important to develop a pharmacological alternative which can restore the QT interval to its normal duration and protect it from arrhythmias and other side effects [36-38].

Pharmacologically, very little information is available on the SQT4 syndrome. I_{CaL} can be selectively enhanced by using calcium agonists or calcium channel enhancers [39]. These compounds have an ability to increase contractility by increasing the calcium ion movement across the cell wall [39, 40]. In SQT4 patients, the influx of I_{CaL} was reduced due to the A39V and G490R mutations; however, recently it has been seen that I_{CaL} influx can be enhanced by Aplidine [41]. Although no evidence has been found that it has been used to treat SQTs patients, Aplidine is a very useful drug for the treatment of congestive heart failure and atrial fibrillation.

4.10.1 Single Cell

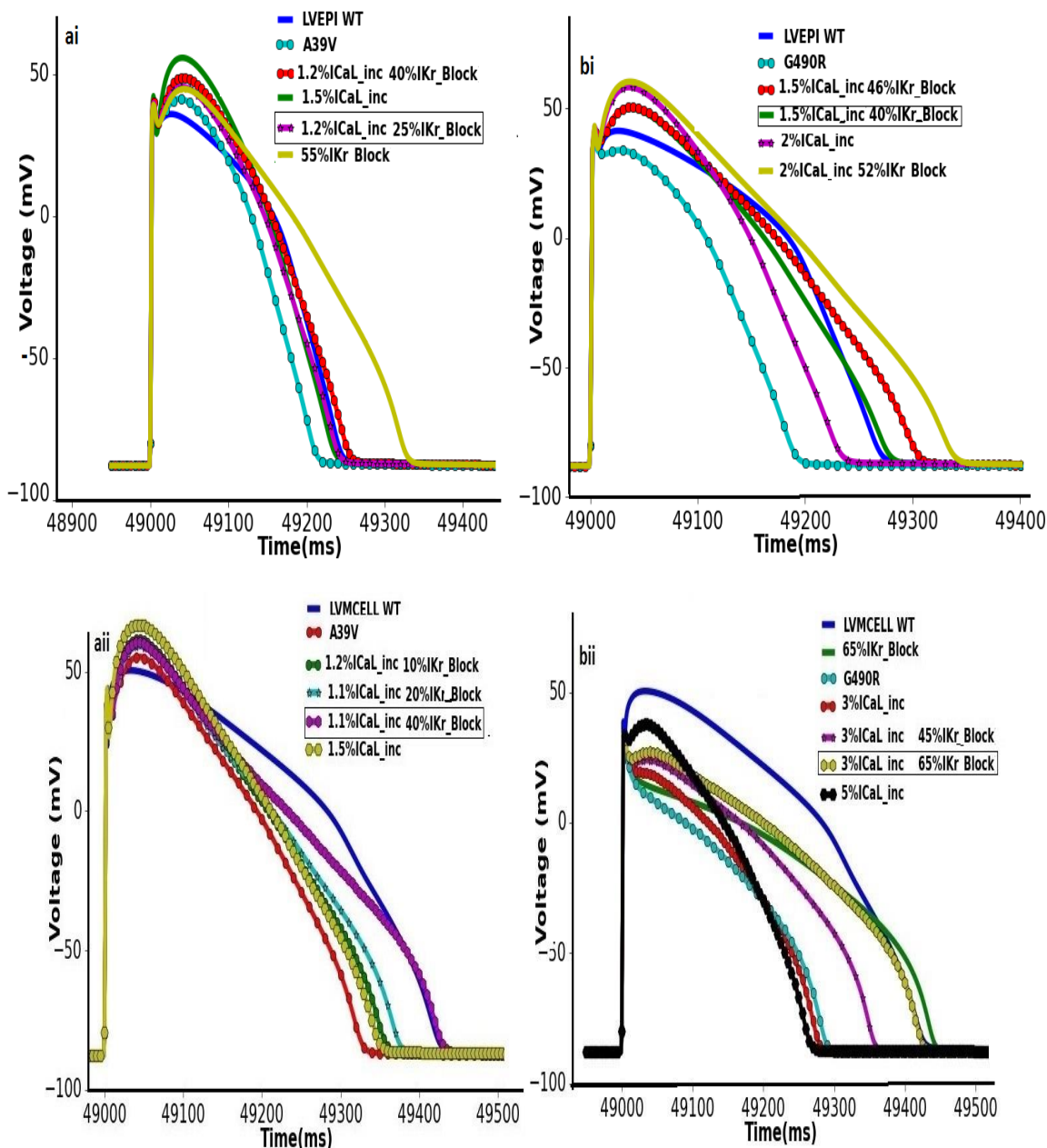
A theoretical “pseudo-pharmacological” approach to normalise QT interval in an adult SQT4 patient is to enhance the I_{CaL} influx density by drugs and determine the extent of enhancement required to normalise the QT interval. The increase of I_{CaL} influx by drugs was mimicked to determine the extent of enhancement required to normalise the QT interval. For A39V, I_{CaL} was enhanced to different percentages in the LVEPI, MIDDLE and LVENDO single cell types. Figure 4.27 shows the results for the LVENDO, LVMCELL and LVEPI cell types under A39V and G490R conditions. It has been observed that the increase of I_{CaL} influx will affect the shape of the plateau region of the AP (a hump-like shape of AP is obtained), Figure 4.27. A small change in calcium influx can be a massive effect on the AP morphology. To resolve this issue, another approach is applied in simulations, by blocking I_{Kr} at the same time. Figure 4.27 (ai, aii, aiii) illustrates the extent of I_{CaL} enhancement and I_{Kr} blockade to obtain normalised AP durations. For A39V (LVMCELL), 1.1 % increase of I_{CaL} and 40% I_{Kr} blockade was required to make the AP duration comparable to that of WT. For LVEPI cell I_{CaL} enhancement and the I_{Kr} blockade were 1.2% and 25% respectively. A 1.09% I_{CaL} increase and 28% blockade is required to normalise the APD in the LVENDO cell.

The same approach was applied for G490R, it gives the plateau region a hump-like shape. To control the I_{CaL} increment to a certain level and blocking I_{Kr} gave the required result as seen in Figure 4.27 (bi, bii, biii). Simulations were repeated for LVENDO, LVMCELL and LVEPI cells.

4.10.2 1D Strand Model

The 1D strand tissue model was used to investigate the effects of an increased influx of calcium ions on ECGs. In the tissue model, APDs are smoother due to the electrical coupling

between cells via gap junctions. The augmentation of I_{CaL} increased the amplitude of the QRS interval and an increased elevation of the J-point was observed in simulations. This issue was resolved by blocking I_{to} and I_{Kr} , for the A39V and G490R. Results suggested that the blockade of I_{to} controlled the elevation of the J-point and the ST segment while the I_{Kr} blockade normalised the QT interval and T-wave amplitude (Figure 4.28 a, b). In simulations, 45% I_{to} and 30% I_{Kr} blockades were necessary to normalise the QT interval for A39V. 35% I_{Kr} and 45% I_{to} was blocked to normalise QT interval in the G490R condition.



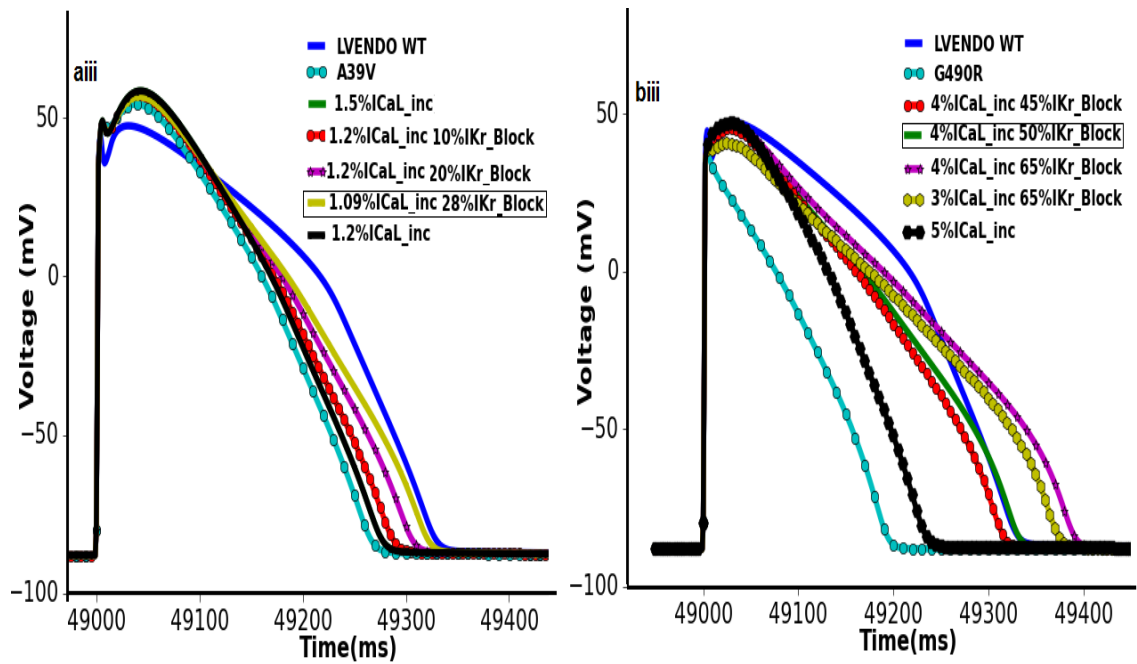


Figure 4.27: Current enhancement/blockade to normalise the AP durations under the A39V (ai-aiii) and the G490R (bi-biii) conditions. The extent of I_{CaL} enhancement and I_{Kr} blockade to obtain the normalised AP durations is demonstrated. For the A39V (LVMCELL), a 1.1 % increase of I_{CaL} and a 40% I_{Kr} blockade were required to make the AP duration comparable to that of the WT. For the LVEPI cell, I_{CaL} enhancement and the I_{Kr} blockade were 1.2% and 25% respectively. 1.09% I_{CaL} increase and 28% I_{Kr} blockade were required to normalise APD in the LVENDO cell. For the G490R (LVMCELL), a 3% increase of I_{CaL} and a 65% I_{Kr} blockade were required to make the AP duration comparable to that of the WT. For the LVEPI cell, I_{CaL} enhancement and the I_{Kr} blockade were 1.5% and 40% respectively. A 4% I_{CaL} increase and 50% I_{Kr} blockade is required to normalise the APD in the LVENDO cell.

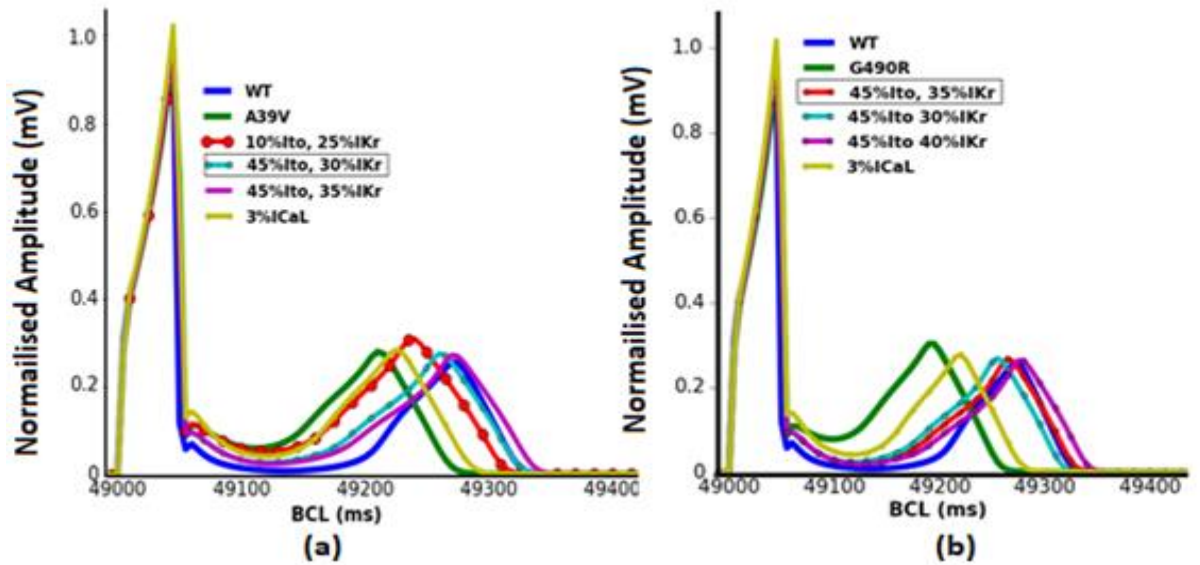


Figure 4.28: The current enhancement/blockade used to normalise the QT interval. A 45% I_{to} and a 30% I_{Kr} blockade was necessary to normalise the QT interval for A39V (a). A 35% I_{Kr} and a 45% I_{to} was blocked to normalise the QT interval in the G490R (b) condition.

4.11 Summary

In the absence of an accurate experimental SQT4 model for human ventricular myocyte, the use of *in silico* models provide an alternative means to understand the functional behavior of SQT mutations, which can be beneficial to avoid ventricular arrhythmias. The major findings of the present study are:

- a) A39V and G490R reduced the AP duration in all three cell types and caused the shortening of the QT intervals.
- b) Although simulations were unable to reproduce a tall T-peak, a ST segment elevation was observed in the simulation which was not found in short QT1-3 patients. In previous studies, Gima and Rudy [19] have suggested that a tall T-wave is associated with hyperkalemia, which represents high levels of the potassium current. To validate this, a heterogeneous I_{Kr} density along the 1D strand was considered. Tall T-waves were obtained for A39V and G490R, for I_{Kr} densities as 1.6:1:1 for LVEPI, LVMCELL and LVENDO. Similar to the previous studies [27], to obtain a tall T-wave, a heterogeneous I_{Kr} density across the ventricular strand model was found to be necessary.
- c) The tissue's temporal vulnerability at some localised regions was increased under the A39V and G490R mutation conditions. In the 2D tissue, the minimal substrate

size that was necessary to initiate and maintain the re-entry was decreased for the mutation condition.

- d) The ST Segment elevation was reproduced which shows that SQT4 mutations are also linked with Brugada syndrome [22].
- e) Blocking of I_{CaL} alone did not normalise the QT interval, instead it increased the amplitude of the QRS interval which is correlated with high blood pressure. My results are consistent with previous studies [34, 39, 40].

These findings gave a clear link between the shortening of the QT interval and the SQT4 mutation. It gave a detailed explanation of increased vulnerability to re-entry in A39V and G490R.

4.12 References

- [1] I. Bodi, G. Mikala, S. E. Koch, S. A. Akhter, and A. Schwartz, “The L-type calcium channel in the heart: the beat goes on,” *J. Clin. Invest.*, vol. 115, no. 12, pp. 3306–3317, Dec. 2005.
- [2] J. Striessnig, A. Pinggera, G. Kaur, G. Bock, and P. Tuluc, “L-type Ca^{2+} channels in heart and brain,” *Wiley Interdiscip. Rev. Membr. Transp. Signal.*, vol. 3, no. 2, pp. 15–38, Mar. 2014.
- [3] T. Narahashi and C. P. Bianchi, *Advances in general and cellular pharmacology*. Springer Science & Business Media, 2012.
- [4] A. S. Dhamoon and J. Jalife, “The inward rectifier current (IK1) controls cardiac excitability and is involved in arrhythmogenesis,” *Heart Rhythm*, vol. 2, no. 3, pp. 316–324, Mar. 2005.
- [5] Z. H and H. Jc, “*In silico* study of action potential and QT interval shortening due to loss of inactivation of the cardiac rapid delayed rectifier potassium current.,” *Biochem. Biophys. Res. Commun.*, vol. 322, no. 2, pp. 693–699, Sep. 2004.
- [6] I. Adeniran, ‘Proarrhythmia in KCNJ2-Linked Short QT Syndrome: Insights from Modelling’, in *Modelling the Short QT syndrome gene mutations*, Springer International Publishing, pp. 153–172, 2014.
- [7] A. A. M. Wilde and C. R. Bezzina, “Genetics of cardiac arrhythmias,” *Heart*, vol. 91, no. 10, pp. 1352–1358, Oct. 2005.
- [8] C. Patel, G.-X. Yan, and C. Antzelevitch, “Short QT syndrome: from bench to bedside,” *Circ. Arrhythm. Electrophysiol.*, vol. 3, no. 4, pp. 401–408, Aug. 2010.
- [9] C. Antzelevitch et al., “Loss-of-function mutations in the cardiac calcium channel underlie a new clinical entity characterized by ST-segment elevation, short QT intervals, and sudden cardiac death,” *Circulation*, vol. 115, no. 4, pp. 442–449, Jan. 2007.
- [10] M. Rubart and D. P. Zipes, “Mechanisms of sudden cardiac death,” *J. Clin. Invest.*, vol. 115, no. 9, pp. 2305–2315, Sep. 2005.
- [11] T. O’Hara, L. Virág, A. Varró, and Y. Rudy, “Simulation of the undiseased human cardiac ventricular action potential: Model formulation and experimental validation,” *PLoS Comput. Biol.*, vol. 7, no. 5, pp. 1-29, May 2011.
- [12] R. M. Anderson, “The Gross physiology of the cardiovascular system”, Tucson, AZ: Racquet Press, pp. 15-60, 1993.
- [13] R. H. Clayton and A. V. Holden, “Propagation of normal beats and re-entry in a computational model of ventricular cardiac tissue with regional differences in action

- potential shape and duration,” *Prog. Biophys. Mol. Biol.*, vol. 85, no. 2–3, pp. 473–499, Jul. 2004.
- [14] S. Viskin, “The QT interval: Too long, too short or just right,” *Heart Rhythm*, vol. 6, no. 5, pp. 711–715, May 2009.
- [15] I. Adeniran, J. Hancox, and H. Zhang, “*In silico* investigation of the short QT syndrome, using human ventricle models incorporating electromechanical coupling,” *Front. Physiol.*, vol. 4, pp. 1–13, 2013.
- [16] P. Taggart et al., “Inhomogeneous transmural conduction during early ischaemia in patients with coronary artery disease,” *J. Mol. Cell. Cardiol.*, vol. 32, no. 4, pp. 621–630, Apr. 2000.
- [17] W. Quan and Y. Rudy, “Unidirectional block and reentry of cardiac excitation: a model study,” *Circ. Res.*, vol. 66, no. 2, pp. 367–382, Feb. 1990.
- [18] I. Gussak et al., “Idiopathic short QT interval: A new clinical syndrome?” *Cardiology*, vol. 94, no. 2, pp. 99–102, 2000.
- [19] K. Gima and Y. Rudy, “Ionic current basis of electrocardiographic waveforms,” *Circ. Res.*, vol. 90, no. 8, pp. 889–896, May 2002.
- [20] W. A. Parham, A. A. Mehdiraz, K. M. Biermann, and C. S. Fredman, “Hyperkalemia Revisited,” *Tex. Heart Inst. J.*, vol. 33, no. 1, pp. 40–47, 2006.
- [21] H. Zhang, S. Kharche, A. V. Holden, and J. C. Hancox, “Repolarisation and vulnerability to re-entry in the human heart with short QT syndrome arising from KCNQ1 mutation--a simulation study,” *Prog. Biophys. Mol. Biol.*, vol. 96, no. 1–3, pp. 112–131, Apr. 2008.
- [22] J. Brugada, P. Brugada, and R. Brugada, “Brugada Syndrome: The syndrome of right bundle branch Block, ST segment elevation in V1 to V3 and sudden death,” *Indian Pacing Electrophysiol. J.*, vol. 1, no. 1, pp. 6–11, Oct. 2001.
- [23] I. Gussak, P. Brugada, J. Brugada, C. Antzelevitch, M. Osbakken, and P. Bjerregaard, “ECG phenomenon of idiopathic and paradoxical short QT intervals,” *Card. Electrophysiol. Rev.*, vol. 6, no. 1–2, pp. 49–53, Feb. 2002.
- [24] C. Antzelevitch et al., “Brugada syndrome: report of the second consensus conference: endorsed by the Heart Rhythm Society and the European Heart Rhythm Association,” *Circulation*, vol. 111, no. 5, pp. 659–670, Feb. 2005.
- [25] K. K. Sethi, K. Sethi, and S. K. Chutani, “Early repolarisation and J wave syndromes,” *Indian Heart J.*, vol. 66, no. 4, pp. 443–452, Jul. 2014.
- [26] C. Antzelevitch and G.-X. Yan, “J wave syndromes,” *Heart Rhythm Off. J. Heart Rhythm Soc.*, vol. 7, no. 4, pp. 549–558, Apr. 2010.

- [27] I. Adeniran, *Modelling the short QT syndrome gene mutations: and their role in cardiac arrhythmogenesis*, 2014 edition. New York: Springer, pp, 100-210, 2014.
- [28] A. Xu and M. R. Guevara, “Two forms of spiral-wave reentry in an ionic model of ischemic ventricular myocardium,” *Chaos Woodbury N*, vol. 8, no. 1, pp. 157–174, Mar. 1998.
- [29] I. Adeniran, M. J. McPate, H. J. Witchel, J. C. Hancox, and H. Zhang, “Increased vulnerability of human ventricle to re-entrant excitation in hERG-linked variant 1 short QT syndrome,” *PLOS Comput. Biol.*, vol. 7, no. 12, p. e1002313, Dec. 2011.
- [30] A. M. Pertsov, J. M. Davidenko, R. Salomonsz, W. T. Baxter, and J. Jalife, “Spiral waves of excitation underlie reentrant activity in isolated cardiac muscle.,” *Circ. Res.*, vol. 72, no. 3, pp. 631–650, Mar. 1993.
- [31] D. T. Kim et al., “Patterns of spiral tip motion in cardiac tissues,” *Chaos Interdiscip. J. Nonlinear Sci.*, vol. 8, no. 1, pp. 137–148, Mar. 1998.
- [32] R. A. Gray, A. M. Pertsov, and J. Jalife, “Spatial and temporal organization during cardiac fibrillation,” *Nature*, vol. 392, no. 6671, pp. 75–78, Mar. 1998.
- [33] R. A. Gray and N. Chattipakorn, “Termination of spiral waves during cardiac fibrillation via shock-induced phase resetting,” *Proc. Natl. Acad. Sci. U. S. A.*, vol. 102, no. 13, pp. 4672–4677, Mar. 2005.
- [34] R. Schimpf et al., “Congenital short QT syndrome and implantable cardioverter defibrillator treatment: inherent risk for inappropriate shock delivery,” *J. Cardiovasc. Electrophysiol.*, vol. 14, no. 12, pp. 1273–1277, Dec. 2003.
- [35] R. Schimpf, U. Bauersfeld, F. Gaita, and C. Wolpert, “Short QT syndrome: successful prevention of sudden cardiac death in an adolescent by implantable cardioverter-defibrillator treatment for primary prophylaxis,” *Heart Rhythm*, vol. 2, no. 4, pp. 416–417, Apr. 2005.
- [36] P. Bjerregaard, A. Jahangir, and I. Gussak, “Targeted therapy for short QT syndrome,” *Expert Opin. Ther. Targets*, vol. 10, no. 3, pp. 393–400, Jun. 2006.
- [37] T.-A. Ansah, L. H. Wade, and D. C. Shockley, “Effects of calcium channel entry blockers on cocaine and amphetamine-induced motor activities and toxicities,” *Life Sci.*, vol. 53, no. 26, pp. 1947–1956, Jan. 1993.
- [38] R. R. Shah, “Drug-induced QT interval shortening: potential harbinger of proarrhythmia and regulatory perspectives,” *Britist. J. Pharmacol.*, vol. 159, no. 1, pp. 58–69, Jan. 2010.
- [39] W. J. Crumb and G. T. Faircloth, “Aplidine as an I-type calcium channel enhancer,” EP0981352 A1, 01-Mar-2000.
- [40] C. Antzelevitch and J. M. Fish, “Therapy for the Brugada Syndrome,” *Handb. Exp. Pharmacol.*, no. 171, pp. 305–330, 2006.

- [41] E. J. Vigmond, M. Hughes, G. Plank, and L. J. Leon, "Computational tools for modeling electrical activity in cardiac tissue," *J. Electrocardiol.*, vol. 36, Supplement 1, pp. 69–74, Dec. 2003.
- [42] S. V. Pandit and J. Jalife, "Rotors and the dynamics of cardiac fibrillation," *Circ. Res.*, vol. 112, no. 5, pp. 849–862, Mar. 2013.
- [43] H. Zhang, C. J. Garrat, A.V. Holden, "Onset and termination of re-entrant excitation in homogeneous human virtual atrial tissue" *Int. J. Bifurcation Chaos*, vol. 13, pp. 3631-3643, Dec. 2003.
- [44] B. Benito et al., "Brugada Syndrome," *Rev. Esp. Cardiol.*, vol. 62, no. 11, pp. 1297–1315, Jan. 2009.
- [45] G. X. Yan and C. Antzelevitch, "Cellular basis for the Brugada syndrome and other mechanisms of arrhythmogenesis associated with ST-segment elevation," *Circulation*, vol. 100, no. 15, pp. 1660–1666, Oct. 1999.

CHAPTER 5

CACNB2b S481L SQT5 Syndrome

5.1 Introduction

As discussed in the previous chapters, mutations in the L-Type calcium channels can lead to shorter than normal QT intervals and are linked to the Brugada syndrome (BrS) [1]. The Brugada syndrome is a rare inherited disease which increases the risk of ventricular arrhythmia in young adults with apparently normal hearts and is more of a risk in healthy males than females [2]. BrS is characterised by an abnormal ECG morphology, in other words, an abnormal ST segment [3, 4]. It is important to understand the basic morphology of the ST segment to compute the ST segment elevation. The ST segment represents the time interval between the J-point (a notch at the end of an S-wave) and the start of the T-wave. Generally, it is a flat section on an ECG, as it represents the beginning of the ventricular repolarisation, or the plateau phase of the AP [5, 6, 7].

A recent study on canine ventricles has shown a loss of function of the L-type calcium channel $Cav1.2$ is linked with a BrS phenotype [8, 9]. The mutations in CACNA1C $\alpha1$ subunits and CACNB2b $\beta2$ subunits of L-type calcium are associated with accelerated inactivation of calcium channels, linked with both BrS and SQTs [9]. The mutation in the $\alpha1$ (CACNA1C) subunit of $Cav1.2$ and its effects on the electrophysiological behaviour of ventricular cell and tissue models were described in Chapter 4.

This chapter will describe the 5th variant of SQT syndrome associated with the $\beta2$ (CACNB2b) subunits of L-type calcium. The β -subunit of $Cav1.2$, $Cav\beta2$, is involved in the gating and trafficking modulation of L-type calcium channels [10]. The 1st case of the 5th variant of SQT syndrome was reported in a 25-year-old European male, diagnosed with ventricular fibrillation (VF), which led to SCD [1, 11]. ECGs presented a QTc interval of 330 ms, with a curved shape ST-segment elevation. The patient's genetic data revealed a heterozygous transition from C to T at position 1442 in exon 13, which anticipates a Leucine to Serine substitution at position 481 (S481L) of CACNB2b. His 23-year-old brother had also been symptomatic with syncope since the age of 21. A further clinical and genetic investigation of the family revealed a positive phenotype in six family members based on an ST-segment elevation (ST segment elevation > 2 mm at baseline or after ajmaline, and a QTc < 360 ms in males and QTc < 370 ms in females). S481L was present in all six family members with a positive phenotype. Few family members exhibited tall peaked T-waves,

with shorter-than-normal QT intervals. The mutation is in the C-linker region of the β subunit of Cav1.2 [1, 11, and 12]. The central and peripheral pattern of fluorescence suggested normal trafficking patterns for S481L channels [1].

5.2 Simulation of Single Cell I_{CaL} for the CACNB2b $\beta 2$ with Control and SQT5/S481L Mutation Conditions

A direct effect of the S481L mutation on the CACNB2b channel can be reproduced by the *in vitro* ventricular AP clamp experiments [1]. The results of these experiments have shown a loss of function of the Cav1.2, Cav $\beta 2$ channel current during the plateau phase of the AP [1]. A loss of function mutation linked with BrS in the L-type Ca²⁺ channel has yet not been fully established [1, 8].

The aim of this study is to examine the detailed impacts of S481L mutation on the $\beta 2$ subunit of the Cav1.2 channel encoded by the CACNB2b gene. A detailed discussion of the SQT5 model and the equations are presented in Chapter 3. The voltage clamp protocol for the $\beta 2$ subunit of the CACNB2b control type was performed for a holding potential of -90 mV with a total simulation time of 250 ms. The clamp voltage range was between -50 mV and 50 mV, with an increment of 10 mV for each step. The same voltage clamp protocol was applied for the S481L mutation condition. Simulations showed a decrease in the amplitude of S481L channel currents, which showed agreement with the experimental data [1].

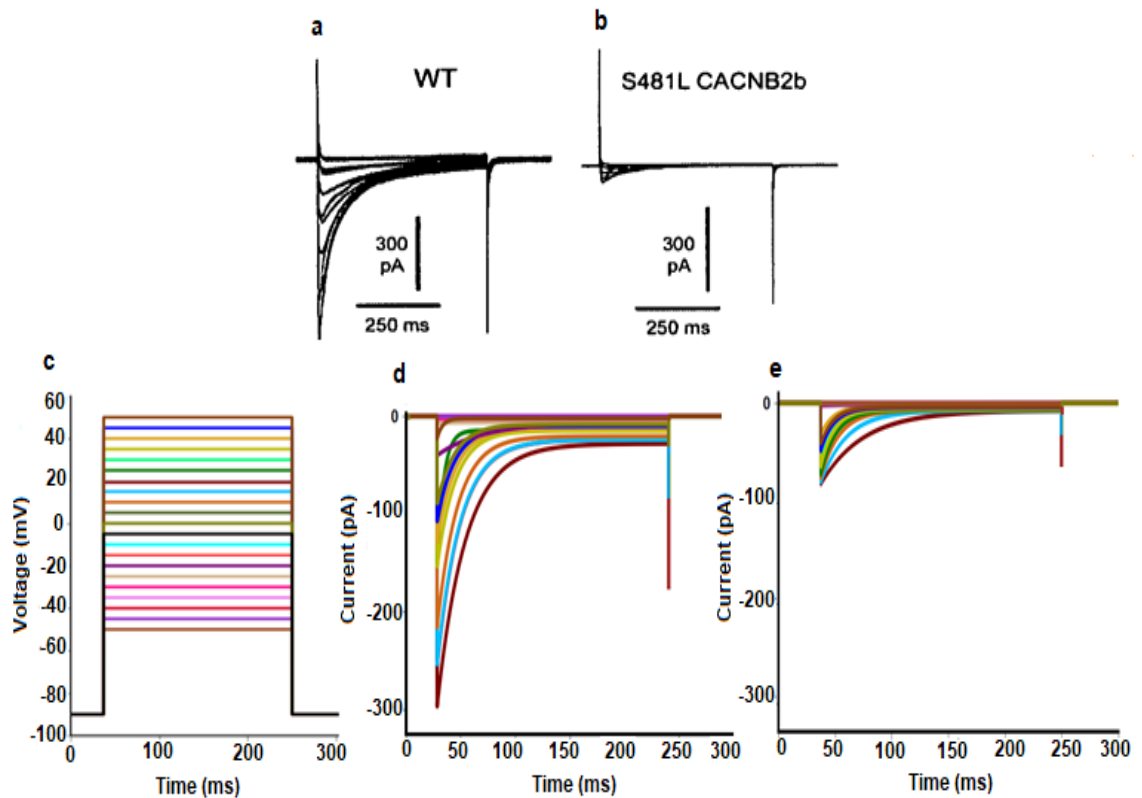


Figure 5.1: Voltage clamp protocol, experimental and simulated L-Type calcium current traces for the WT and mutation. Change in color in the voltage clamp protocol represents a voltage step of 5 mV. The color information is given in Appendix C. (a, b) WT and S481L experimental current traces [9]; (c) the voltage clamp protocol, the clamp range was between -50 mV and 50 mV with an increment of 5 mV. The total simulation time was 250 ms. (d, e) WT (5.1d) and S481L I_{CaL} (5.1e) are the simulated current traces corresponding to the experimental data (5.1a, b).

The simulated I-V relationship for the WT and S481L mutation are represented in Figure 5.2a. The WT conductance was regulated to acquire a peak current density which corresponds well with the I_{CaL} formulation current density during the I-V relationship of the original O'Hara & Rudy model [13] (Figure 5.2b), thus maintaining the overall current densities, APD_{90} and functional characteristics of the O'Hara & Rudy human ventricular model [13]. The voltage at the peak current remained unchanged for the S481L condition compared to the WT, which supports the experimental data [1].

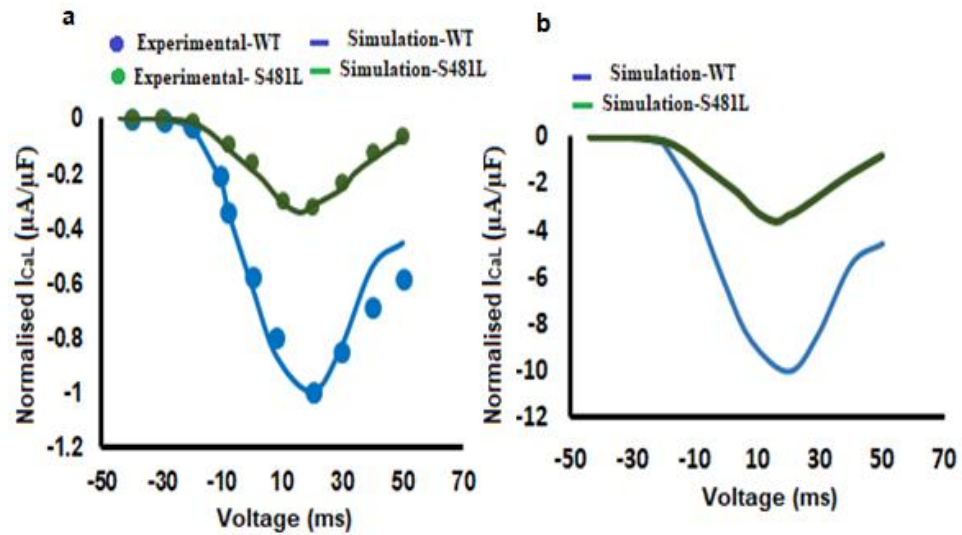


Figure 5.2: Computed I-V relationship for L-Type calcium channel (CACNB2b $\beta 2$ -subunit) for the WT (blue) and S481L (green) conditions, (a) Normalised I-V relationship for WT (blue) and S481L (green), the solid lines represent the simulated data while the dotted points represent the experimental data. Simulations showed a decrease in the amplitude of the S481L channel currents which showed an agreement with the experimental data [1]. (b) The WT conductance was regulated to acquire a peak current density which corresponds well with the I_{CaL} formulation current density during the I-V relationship of the original O'Hara & Rudy model [13].

The WT and the S481L formulation were incorporated into the 2011 O'Hara & Rudy model [13] to visualise the functional effects of the WT and the S481L mutation on ventricular APs. Figure 5.3 shows simulated action potentials and I_{CaL} ($\beta 2$ subunit of CACNB2b) current profiles over time (t) for LVEPI, LVMCELL and LVENDO ventricular cells, under the WT and S481L conditions respectively. The results suggest a shortening of AP in all three cell types for the S481L condition due to the loss of function of the CACNB2b $\beta 2$ calcium current, Figure 5.3 (aii, bii, cii).

The APD_{90} values were computed for LVEPI, LVMCELL and LVENDO cells for the WT and the S481L conditions. A reduction in the AP duration can be seen in the S481L conditions. The results suggest that this shortening of the AP is linked to the decreased influx of L-type calcium currents during the plateau phase of the AP (Figure 5.3 aii, bii, cii), which is consistent with previous studies [1, 8]. The shortening of the APD_{90} under the S481L conditions was rate-dependent. The simulated resting potential values were -86.72 mV and -86.64 mV for the WT and S481L conditions respectively.

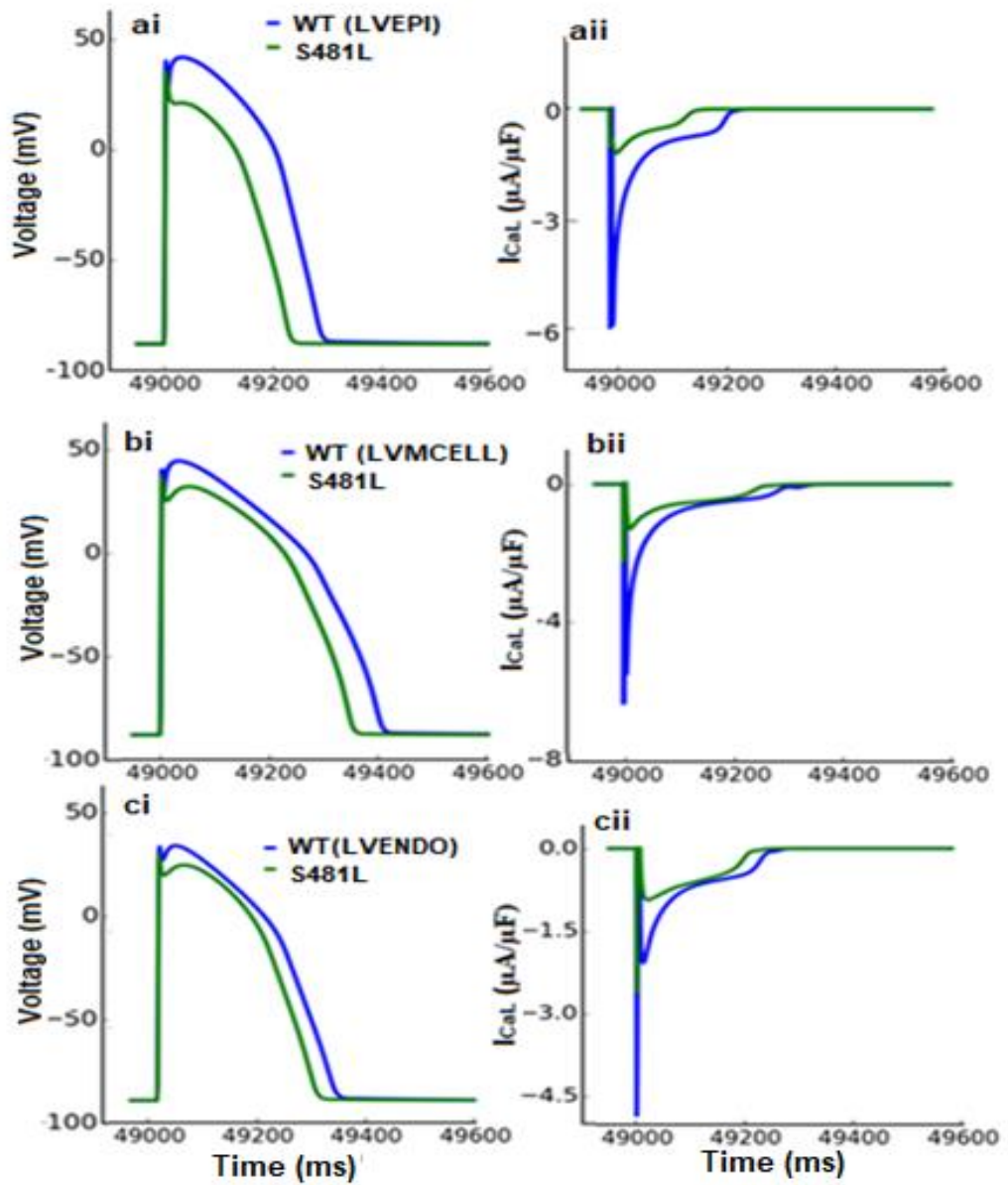


Figure 5.3: Simulated action potentials and I_{CaL} time traces. (ai, bi, ci) Action potential paced at the frequency of 1 Hz for LVEPI (ai), LVMCELL (bi) and LVENDO (ci) cells for WT (blue) and S481L (green) conditions. (aai, bii, cii) Relative CACNB2b I_{CaL} current profiles for LVEPI (aai), LVMCELL (bii) and LVENDO (cii) cells under WT (blue) and S481L (green) conditions.

	LVEPI (ms)	LVMCELL (ms)	LVENDO (ms)
WT	232	369	275
S481L	203	290	208

Table 5.1: Computed APD₉₀ (ms) values for the LVEPI, LVMCELL and LVENDO cell types under CACNB2b β_2 Cav1.2 for WT and the S481L mutation conditions.

The results suggest that the extent of APD₉₀ shortening is at different levels in different cell types under S481L conditions as shown in Table 5.2.

	LVEPI (ms)	LVMCELL (ms)	LVENDO (ms)
S481L	29	79	67

Table 5.2: Shortening of the APD₉₀ under the S481L mutation condition. The S481L reduced the APD₉₀ in all three cell types with a marked reduction in the LVMCELL type.

Results showed that the transmural dispersion of APD₉₀ across different cell types of ventricular wall has been decreased in the S481L condition (Figure 5.11), which is similar to prior studies of SQT5 [14-16]. A heterogeneous reduction of the action potential can lead to an increased transmural dispersion of repolarisation under S481L conditions with more risk of the development of the ventricular arrhythmia [14-16].

5.3 Rate Dependent Restitution Properties of the WT and SQT5/S481L

The reduction of APD₉₀ in S481L mutation conditions is rate-dependent. Figure 5.4 (a-c) described the APD₉₀ restitution (APD-R) curves for different cell types. The APD₉₀ over the range of diastolic intervals (DIs) under investigation decreased in the S481L condition as compared to the control condition. The obtained results suggest a leftward shift and flattening of APD₉₀ restitution curves. The abbreviated values of APD₉₀ decreased the maximal slopes of APD₉₀ restitution curves (Figure 5.4 ai, bi, ci). According to previous studies, SQT5 patients exhibit a poor rate-adaptation of their QT intervals [14, 18, and 19]. Results suggest a reduction of rate-adaptation of ventricular APD₉₀, which corresponds well with the prior studies [20].

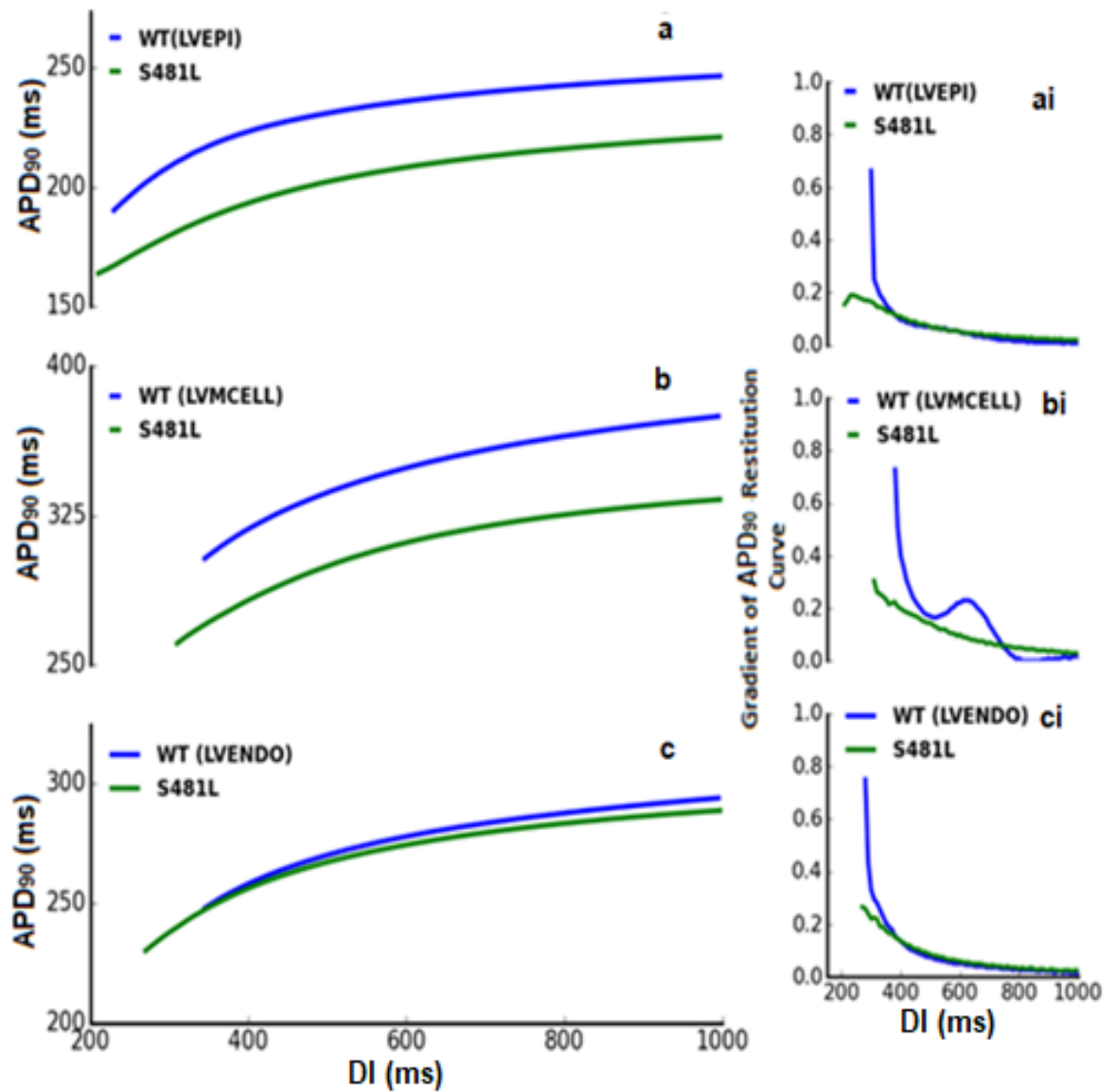


Figure 5.4: APD₉₀ restitution curves for WT and S481L. APD₉₀ is plotted against the diastolic interval (DI). (a, b, c) APD₉₀ restitution curves for the LVEPI (a), LVMCELL (b) and LVENDO (c) cells respectively for the WT (blue) and S481L (green) conditions. A prominent reduction of the APD₉₀ can be seen in the LVEPI and LVMCELL cell curves, while APD-R curve for the LVENDO cell remained least affected under the S481L condition. (ai, bi, ci) The S481L mutation has reduced the maximal slopes of the APD₉₀ curves in all the three cell types.

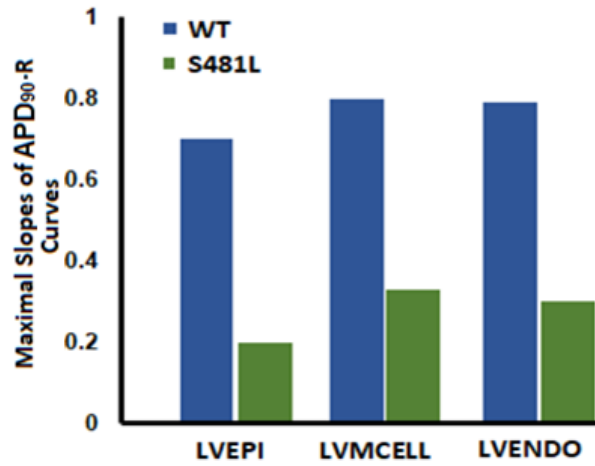


Figure 5.5: Maximal slopes of the APD₉₀ restitution curves, WT (blue) and S481L (green), obtained from Figure 5.4 (ai, bi, ci). The slopes were measured at the minimum diastolic interval (DI) before the conduction block and calculated for the individual curves of the LVEPI, LVMCELL and LVENDO cell types. The shortening of APD₉₀ under S481L condition reduced the maximal slopes of the restitution curves. This reduction is more marked in LVEPI cell type.

To investigate further, the steady state restitution curves were plotted for the WT and S481L conditions. The same behaviour was observed as for APD₉₀ restitution curves. In other words, mutation flattened the steady state restitution curve and caused a leftward shift (Figure 5.6 a, b, c).

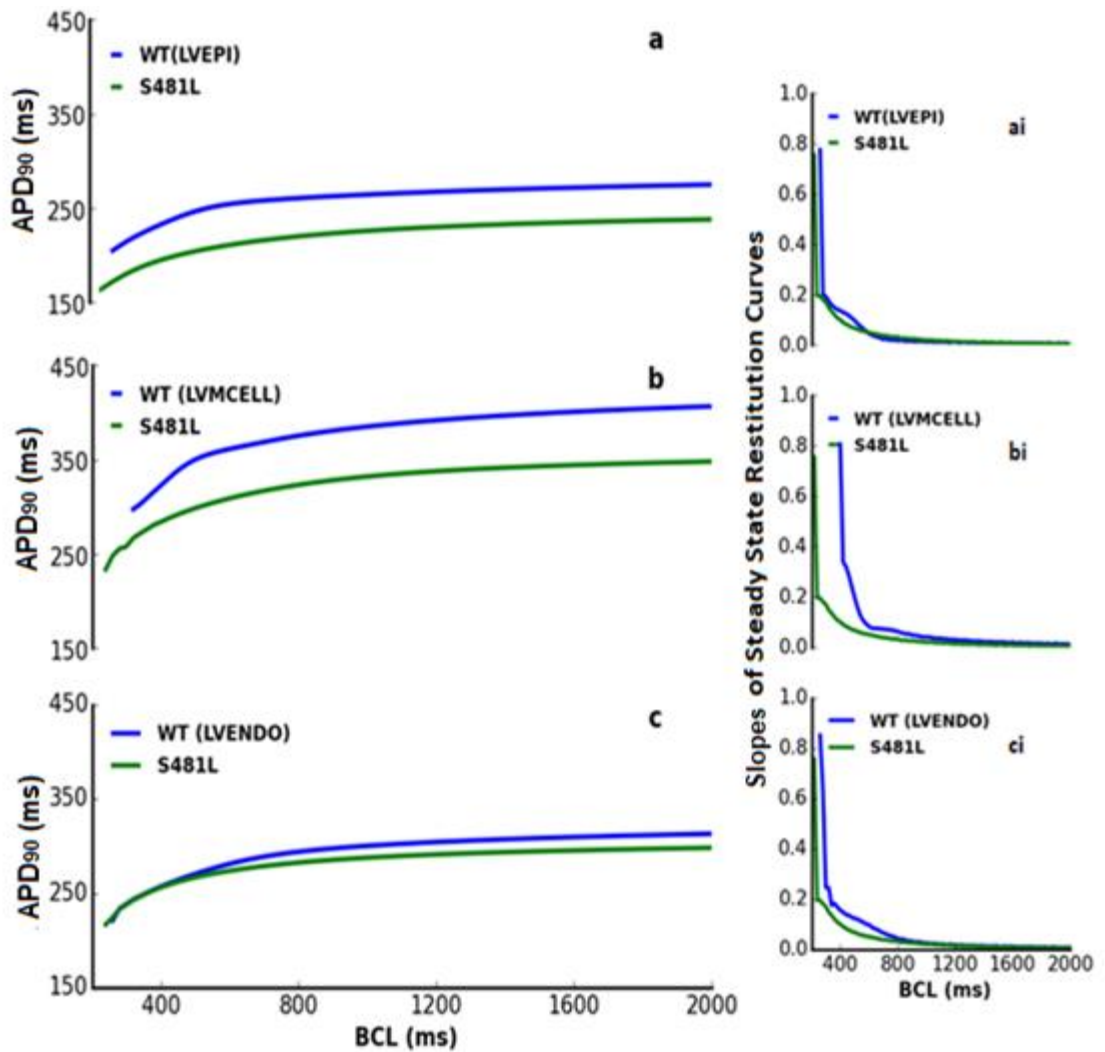


Figure 5.6: Steady-state APD₉₀ rate dependence curves under the WT (blue) and S481L (green) condition. APD₉₀ is plotted against the basic cycle length (BCL). (a, b, c) Steady state restitution curves for the LVEPI (a), MIDDLE (b) and LVENDO (c) cells for the WT (blue) and the S481L (green) conditions respectively. The S481L results have shown the flattening of all three curves, while a leftward shift is more prominent in the LVMCELL curve. (ai, bi, ci) Flattening of the restitution curves suggest a reduction of the maximal slopes, illustrating the effect of the S481L mutation on the slopes of the steady state-restitution curves.

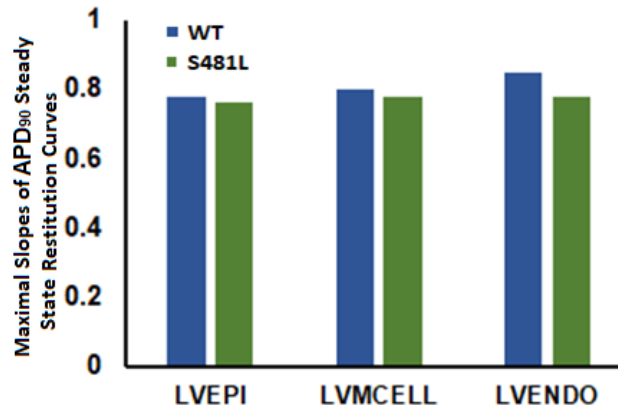


Figure 5.7: Maximal Slopes of the steady State restitution curves obtained from Figure 5.6 (ai, bi, ci). WT (blue) and S481L (green) for the LVEPI, LVMCELL and LVENDO cell types. A small reduction in the slopes of the steady state restitution curves can be seen with the reduced APD₉₀ for the S481L condition.

The reduction in the effective refractory period is also rate-dependent [20]. The effect of the S481L mutations on ERP restitution curves can be seen in Figure 5.8 (a, b, c). A reduction in the maximal slope of the ERP-R curves for LVEPI, LVMCELL and LVENDO can be seen in Figure 5.9. The effective refractory period was reduced under mutation as compared to the WT condition over the range of basic cycle lengths (BCL) investigated. The maximal slope of LVMCELL cell was reduced in Figure 5.8bi, while steepness can be seen in the beginning of the LVEPI and LVENDO ERP-R curves (Figure 5.8 ai, ci) at fast heart rates (BCL < 490 ms), which gradually settled down at slow heart rates (BCL > 500 ms).

A leftward shift can be seen in all three restitution curves (APD-R, APD-R steady state and ERP-R restitution curves) under S481L conditions for LVEPI, LVMCELL and LVENDO cell types. This leftward shift enables ventricular cells to support electrical activity [20, 27] at fast heart rates under the S481L condition. This condition is also commonly observed during VF and AF [20, 27].

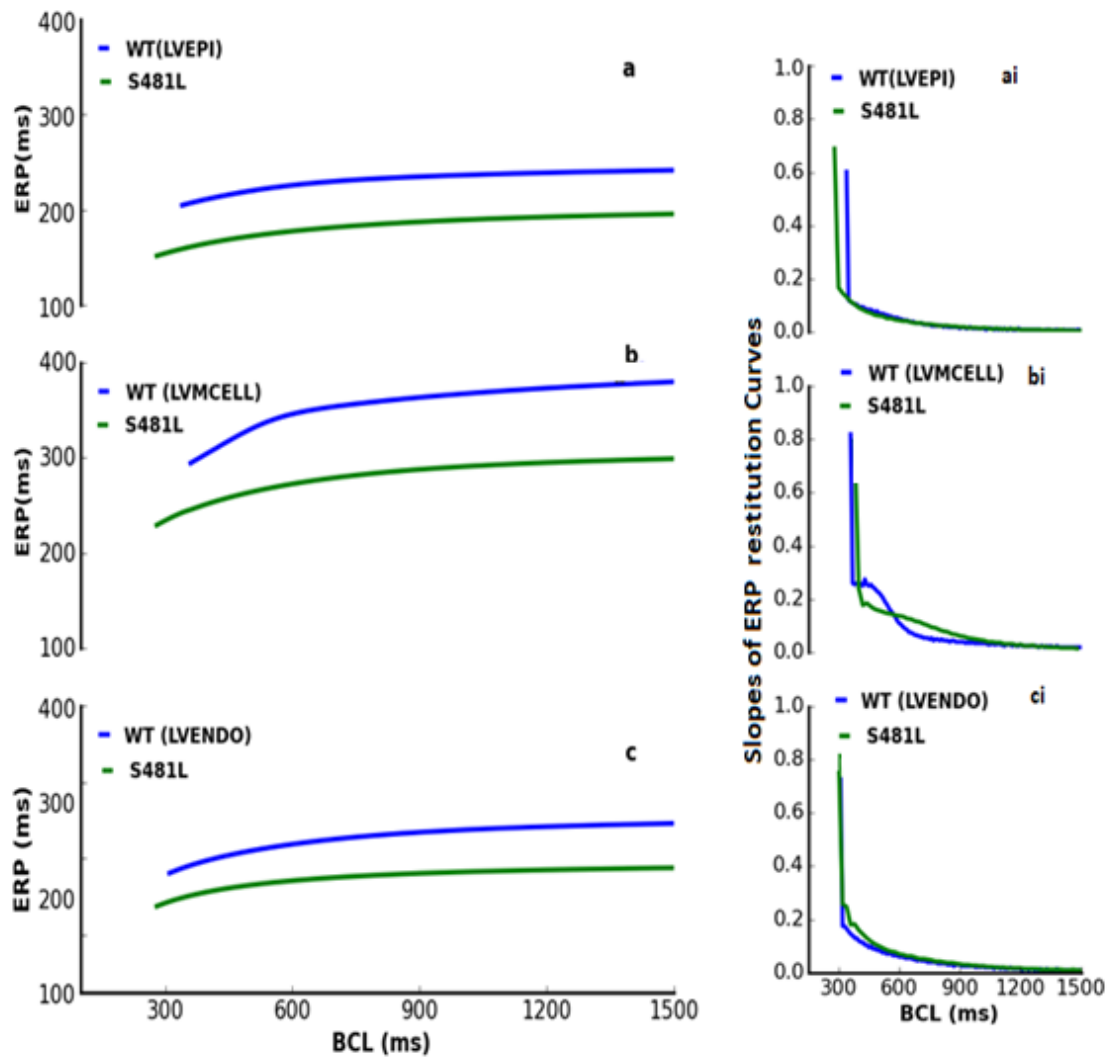


Figure 5.8: ERP restitution curves for the WT and the S481L were obtained by plotting the effective refractory period (ERP) against the basic cycle length (BCL). (a, b, c) ERP restitution curves for the LVEPI (a), MIDDLE (b) and LVENDO (c) cells for the WT (blue) and the S481L (green) conditions respectively. (ai, bi, ci) The maximal slope of LVMCELL curve was reduced, while steepness can be seen in the beginning of LVEPI and LVENDO ERP-R curves at fast heart rates (BCL < 350 ms), which gradually settled down at BCL > 400 ms.

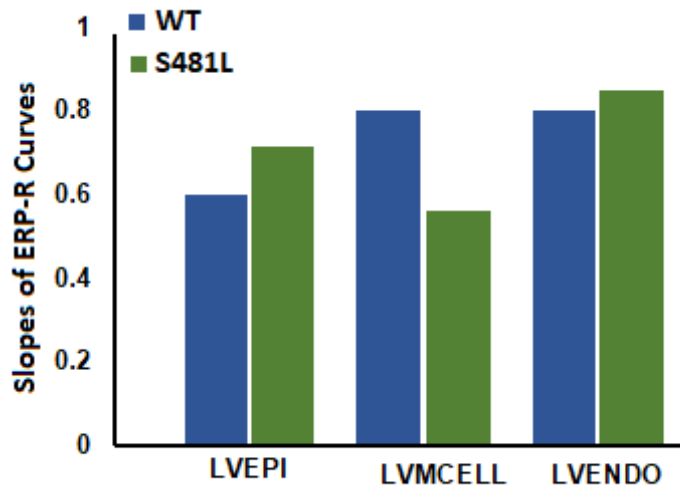


Figure 5.9: Slope of ERP restitution curves obtained from Figure 5.8 (ai, bi, ci). WT (blue) and S481L (green) for the LVEPI, LVMCELL and LVENDO cell types. The S481L reduced the ERP-R curves' slopes for the LVMCELL while the maximal slope of LVEPI and LVENDO cells increased under the S481L mutation condition.

5.4 Investigation of the QT Abbreviation and the Elevation of the ST Segment on the Electrocardiogram

5.4.1 1D Model Simulations

The 1D strand model of the left ventricular wall presented in Chapter 3 was used in the simulations. The wave once generated, propagates from the LVENDO end towards the LVEPI end (Figure 5.10 a-b) of the 1D strand. In Figure 5.10 (a-b), time runs horizontally from left to right, while space runs vertically from the LVENDO region at the bottom to the LVEPI region at the top of the 1D sheet.

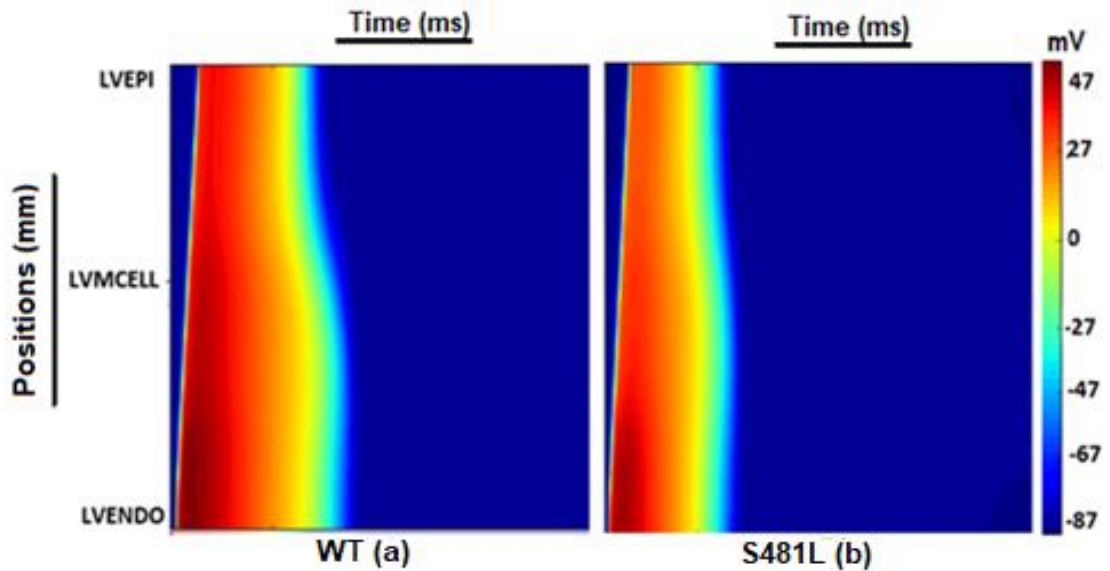


Figure 5.10: Space-time colour-mapping of the membrane potential in a 15 mm ventricular wall strand during the propagation of an action potential cycle (BCL=1000 ms). (a, b) WT (a) and S481L (b). Positions (mm) run vertically with LVEPI at the top and LVENDO at the bottom, while the time (ms) runs horizontally. Colour mapping of membrane potentials of cells along the strand changes from blue (-87 mV) to red (47 mV).

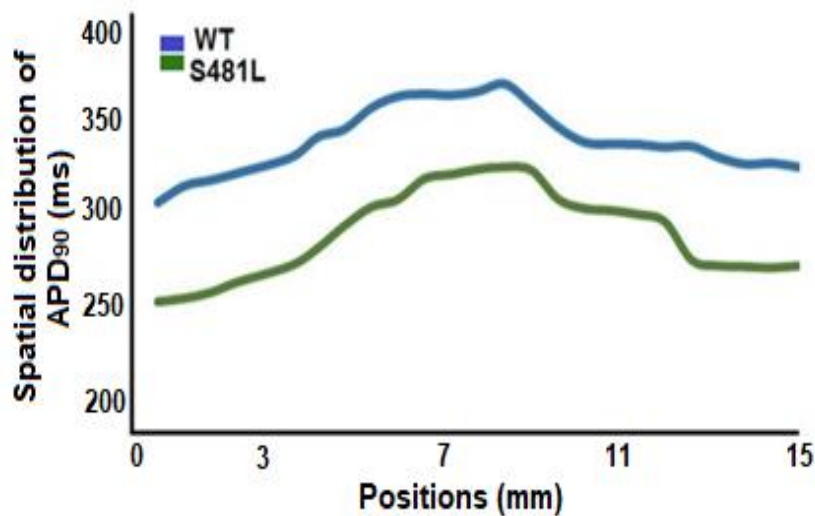


Figure 5.11: Distribution of APD₉₀ along the transmural 1D strand model of the ventricular cells for the WT (blue) and S481L (green) conditions.

5.4.2 ECGs

Pseudo ECGs were calculated for the WT and S481L conditions (Figure 5.12) by utilising the 1D strand model of the left ventricular cells. The value of the QT interval was 358 ms for the controlled condition, which was reduced to 294 ms for the S481L mutation condition

(Figure 5.12). The T-wave half width ($T_{\text{peak}}-T_{\text{end}}$) was 50 ms for the WT condition. The value of the T-wave half width changed to 56 ms for the S481L condition. Short QT interval and wider T-wave half widths are the major characteristics observed clinically in the ECGs of the SQT5 patients [1, 17, 18, 19, 21 and 22]. Simulations therefore reproduced these features.

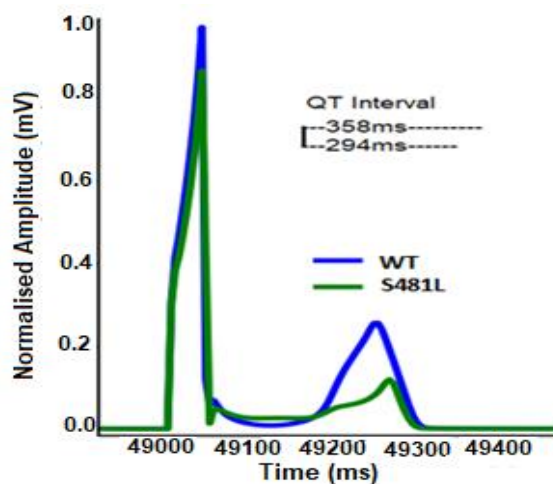


Figure 5.12: Pseudo-Electrocardiograms associated with the WT and SQT5S (S481L) conditions. WT (blue), S481L (green). The QT interval is 358 ms for the WT and 294 ms for the S481L model.

Another key feature that has been clinically observed for SQT5 patients is an elevated ST segment. It is the key link between BrS and SQT5 [1, 8]. The ST segment elevation can be measured on pseudo ECGs, with the J-point playing an important role in measuring the elevation of ST segments. Elevation of the ST segments can be measured in a local region on the ECG at 60 ms after the J-point [1, 8, 23, 24]. Simulations have reproduced this feature for the S481L mutation condition, although the elevation was not prominent, as seen in Chapter 4 for the A39V and G490R SQT4 mutations. For the S481L mutation condition, the measured ST segment elevation was < 2 mm, compared with the WT baseline. A study by Yan and Antzelevitch [25] suggested that a decrease in the amplitude of the AP dome of the EPI cells compared to ENDO cells creates a transmural voltage gradient across the left ventricular wall. This heterogeneous dispersion of the AP dome along the left ventricular wall increases transmural dispersion of repolarisation, which may not only elevate the ST segment, but can also lead to phase 2 re-entry and re-entrant substrate for VF [3, 25, 26].

5.5 Investigation of the Unidirectional Block and Arrhythmogenic Substrate in the SQT5

A 1D strand model was used to investigate arrhythmogenic substrates with the WT and S481L conditions. The susceptibility of the WT and S481L tissue to a unidirectional block was investigated by applying a premature stimulus during the refractory tail of a preceding excitation wave. A train of 10 S1 stimuli paced at a frequency of 1 Hz was applied at the LVENDO end of the 1D transmural strand to trigger a propagating wave. A second stimulus (S2) was applied after the 10th S1 following a time delay of ΔT . The amplitude and duration for S1 and S2 were similar. ΔT (T2-T1) represents the maximal and minimal values of a temporal window, during which the propagation of the excitation wave evoked by the S2 stimulus was unidirectional in the 1D strand. Figure 5.13 illustrates the width of the vulnerability window across the 1D strand. Prior studies have suggested that this temporal window corresponds to a time, during which the tissue is more vulnerable to a premature stimulus that can trigger arrhythmogenic events [14, 17, 20]. The width of the vulnerability window under S481L condition increased across the entire 1D strand (Figure 5.13). Figure 5.14 shows the width of the temporal vulnerability window within the marked region under the WT and S481L conditions. The 1D tissue model showed a greater vulnerability width for the S481L condition compared to the WT condition in the marked region. The vulnerability window width measured within the marked region is 19 ms for the WT and 26 ms for the S481L conditions respectively.

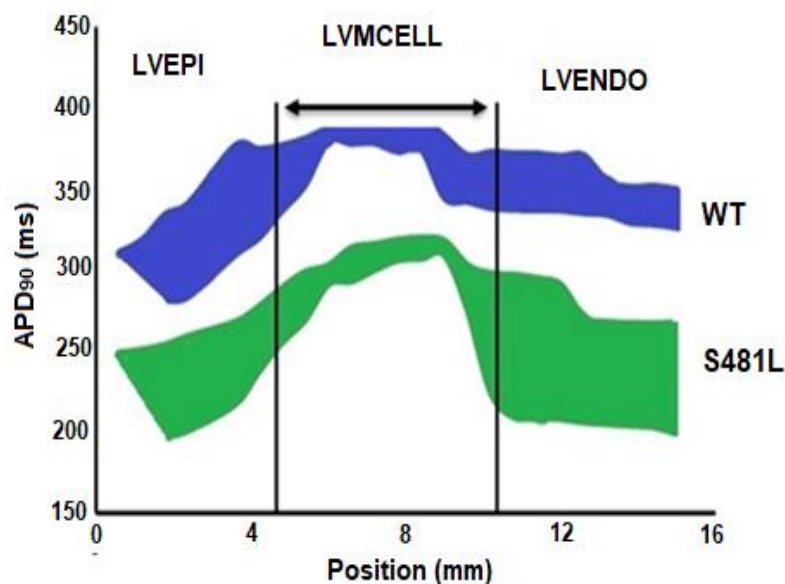


Figure 5.13: The Vulnerable Window across the transmural 1D strand plotted as a function of position on a 15 mm long 1D strand of ventricular cells, with each cell having a spatial resolution of 0.15 mm. The width of the Vulnerable Window (VW) is measured between the marked region depicted by the arrow. VW for the WT (blue) and S481L (green) models.

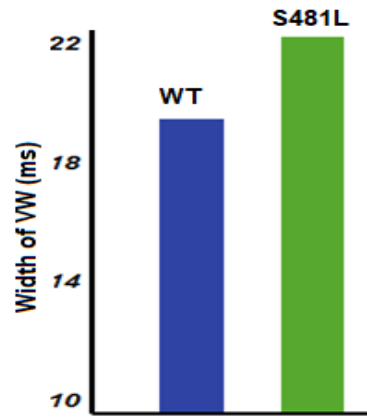


Figure 5.14: The measured Vulnerable Window (VW) width in the marked region (an average of different VW widths within the marked region depicted by arrow) in Figure 5.13 for the WT (blue) and S481L (green) models.

5.6 Computation of the Conduction Velocity and Excitation Threshold Across the 1D Strand

The conduction velocity was computed for the WT and S481L conditions across the 1D left ventricular strand (Figure 5.15) model. Results have shown a decrease in the CV at slow heart rates (heart rate < 125 beats/minute, PCL > 410 ms) due to the mutation, while an increase in CV under the S481L condition can be seen at fast heart rates (280 ms < PCL < 360 ms). This trend of CV has also been seen in previous studies [27, 20]. The reduced tissue excitability (Figure 5.16) at lower heart rates for the S481L could be a reason for the reduced CV at rates slower than 125 beats/minute, as no change in the intercellular electrical coupling was considered at those rates. CV was calculated at a rate of 60 beats/minute (BCL=1000 ms), the measured CV was 67 cm/s for the WT and 62 cm/s for the S481L conditions. However, the values measured for CV at higher rates, between 147 and 178 beats/minute (280 > PCL < 340), were slightly higher under the S481L conditions than those under WT conditions. The increased CV in the S481L at high rates is due to short effective refractory periods [28]. The fastest heart rates that supported conduction in ventricular tissue under WT and S481L conditions were 138 beats/minute (SI < 380 ms) and 178 beats/minute (SI < 320 ms) respectively. A large part of tissue was still refractory in WT conditions, which caused the failure of conduction at higher heart rates under these conditions compared to the mutations.

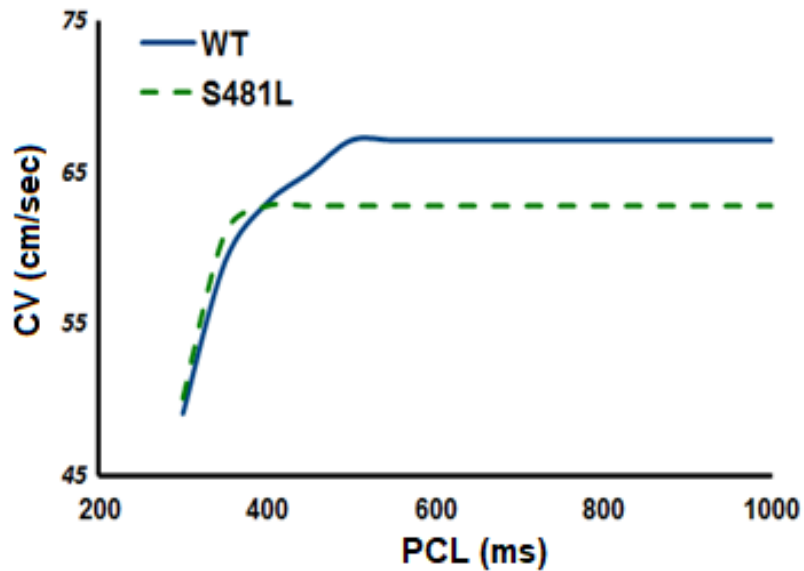


Figure 5.15: Conduction velocity (CV) restitution curves. WT (blue) and S481L (green) conditions. The CV curve was plotted against the Pacing Cycle Length (PCL).

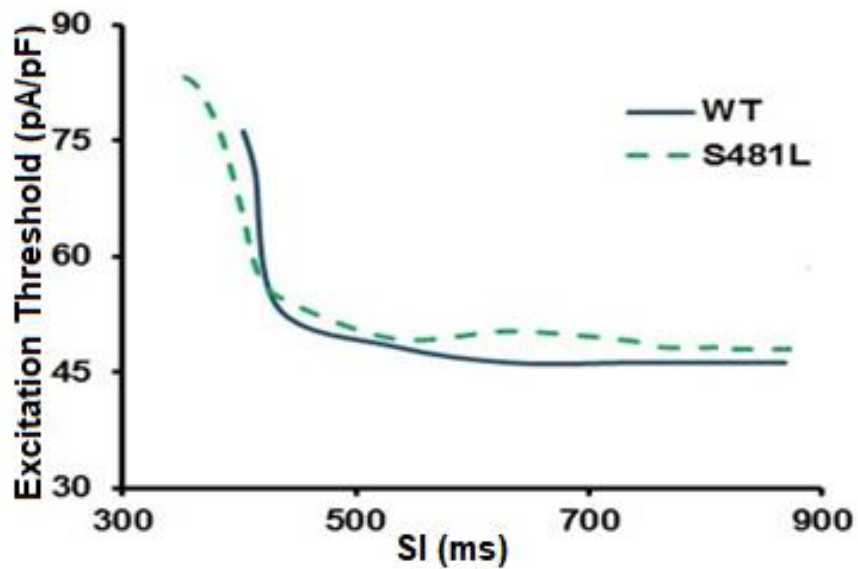


Figure 5.16: The relationship between the excitation threshold potential and the Stimulus Intervals (SI). WT (blue) and S481L (green) mutation conditions. The tissue's excitation threshold is a measure of the minimal stimulus amplitude that can initiate a propagating action potential in the cardiac tissue [27]. The fastest heart rates that supported conduction in ventricular tissue under the WT and S481L conditions are 138 beats/minute (SI < 380 ms) and 178 beats/minute (SI < 320 ms) respectively.

5.7 Investigation of Arrhythmogenic Substrate in the 2D Idealised Geometry for the WT and SQT5 Variants of CACNB2b β 2 $Ca_v1.2$

The idealised 2D ventricular tissue model was utilised to compute the minimal spatial length of a premature stimulus which can initiate and sustain a re-entrant wave in both WT and S481L mutation conditions. A propagating excitation wave was initiated by applying a conditioning stimulus (S1) at the LVENDO end of the 2D sheet. The excitation wave generated by S1 spread from the LVENDO end to the LVEPI end of the 2D tissue sheet under WT and S481L (Figure 5.17 b, c) conditions. Following a time interval, a second test stimulus (S2) was applied in the LVEPI region (a local region within the VW of the EPI region of the 2D sheet). The excitation wave triggered by S2 was blocked by the unrecovered middle region, as the LVMCELL region is still refractory due to the slower repolarisation compared to LVEPI and LVENDO regions (the refractory period of the LVMCELL is longer than LVEPI and LVENDO). It therefore gave rise to a unidirectional conduction towards the EPI side. This unidirectional block resulted in the formation of spiral re-entrant excitation waves in WT and S481L conditions. For WT and S481L, the time delays between S1 and S2 were 372 ms and 219 ms respectively. In WT, the excitation re-entrant wave terminated within 315 ms after the time it started, but it was sustained for the S481L condition (Figure 5.17c). My results are consistent with previous studies of SQT syndromes [22, 29 and 30].

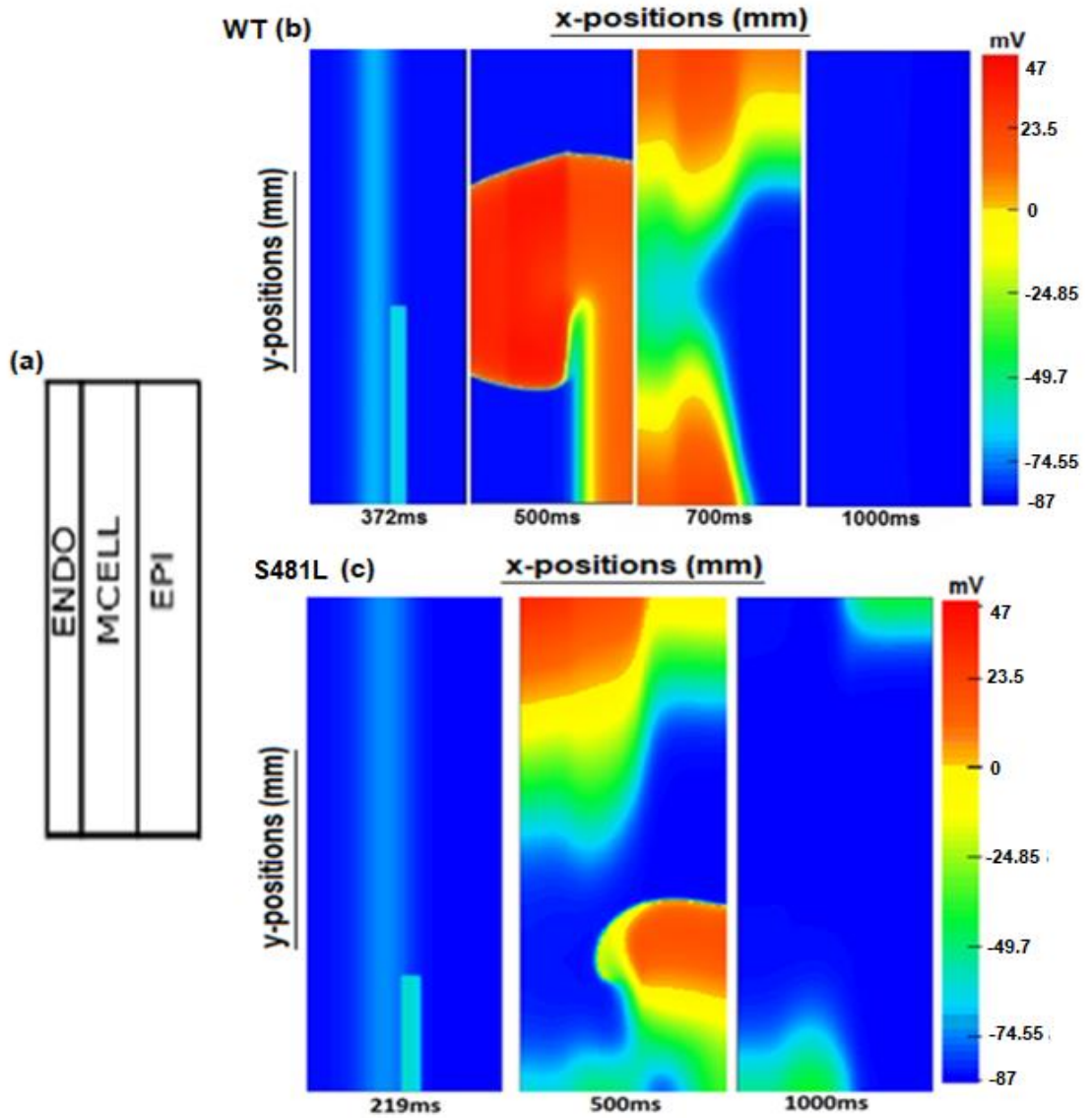


Figure 5.17: Snapshots of the initiation and conduction of the re-entrant excitation waves in a 2D idealised tissue model for the CACNB2b $\beta 2$ Cav1.2 WT and S481L models. a) A schematic representation of the 2D tissue model, b) WT and c) S481L. S2 was applied after a time delay of 372 ms and 219 ms for the WT and S481L conditions respectively. The excitation wave generated by S2 was terminated under the WT condition while it sustained over the entire BCL in the S481L mutation model.

The minimal tissue substrate length necessary to initiate re-entry was measured for both WT and S481L mutation conditions. The minimal substrate lengths for WT and S481L were measured as 29.8 mm and 11.5 mm respectively (Figure 5.18). The results suggest that it is much easier to induce a re-entrant wave under S481L condition than WT condition. The tissue is therefore more susceptible to ventricular arrhythmias under S481L condition.

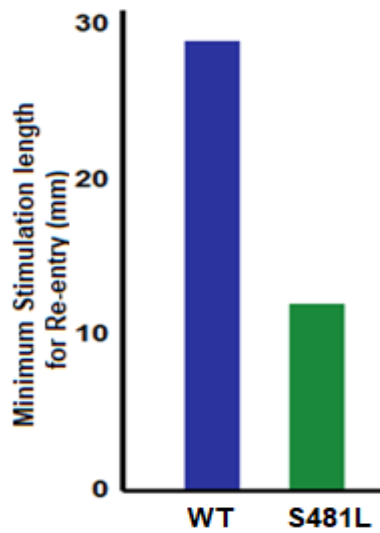


Figure 5.18: The minimal spatial length of the premature stimulus S2 that is necessary to initiate a re-entrant excitation wave under the WT (blue) and S481L (green) conditions.

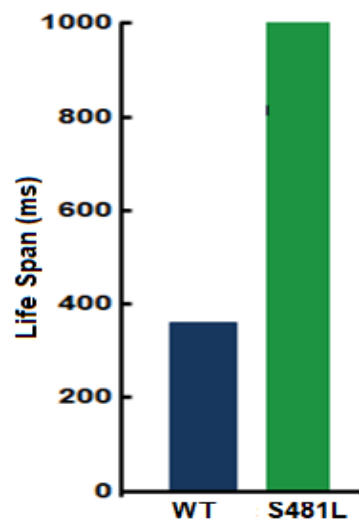


Figure 5.19: Total life span of the re-entrant excitation spiral wave in the 2D idealised tissue model for the WT (blue) and S481L/SQT5 (green) conditions.

The total life span of the re-entrant excitation wave under the WT condition was measured as 362 ms, for S481L the re-entry sustained over the entire cycle of 1000 ms (Figure 5.19).

5.8 Phase Mapping and the Trajectory of the Excitation Spiral Wave in 2D Idealised Tissue for CACNB2b β 2 WT and S481L

As explained in Chapter 4, phase mapping allows for the precise identification of Phase Singularity (PS) points for the WT and the mutations in space over time [31-34], as illustrated in Figure 5.20. Phase mapping allows for a closer look at the activation wavefront of the spiral wave evoked by the S2. It illustrates the wave-front, the wave-tail and the point at which the wave-front meets the curved wave-tail. The point where the wave tail meets the wave-front is defined by Gray et al [32, 33] as a singularity point or Phase Singularity (PS), represented by a white asterisk in the Figure 5.20 (a, b). The singularity point plays an important role in understanding the dynamics of the spiral wave tip trajectory [31] in space over time. The trajectory of the spiral wave is defined by the rotor. In other words, when the rotor is stationary, it rotates and forms a circular trajectory however, for a meandering rotor, the trajectory can be more complicated [31, 35]. To calculate phases, the computed values for v' and u' under the WT and S481L conditions were -40 mV and -50 mV respectively, where v' and u' are defined as origin points in the phase space and are explained in Chapter 3.

The rotor tip and the core play a very important role in determining the trajectory of the spiral wave in a 2D tissue [31-36]. The combination of both defines the pattern and the path followed by the excitation re-entrant wave in any medium, presenting a flower-like pattern or a drag episode, depending on the movement of the tip and the core of the wave. It is not necessary to always expect to obtain flower-like episodes. Drift patterns were also previously described by Pertsove et al. [34]. Dave T. Kim et al. observed drift patterns in one episode of swine RV [37].

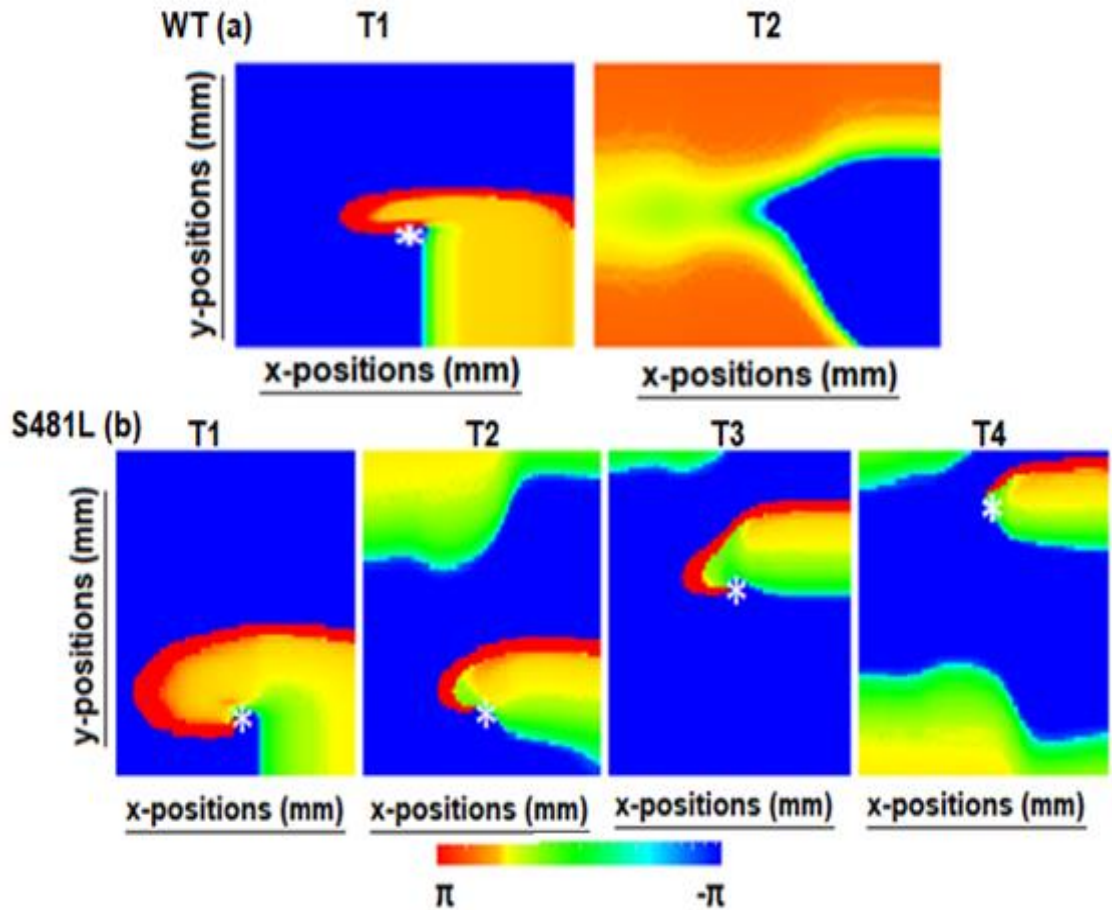


Figure 5.20: Phase mapping of the spiral wave in a 2D idealised tissue model of the left ventricular myocytes for the CACNB2b β 2 Cav1.2 WT (a) and S481L (b) conditions. The layout of the 2D sheet is the same as that defined in Figure 5.17a. The white asterisk in the figure represents the Phase Singularity point where the wave tip meets the wave tail. The wave front represents the group of depolarised cells while the tail is composed of cells that are returning to rest. T1, T2, T3 and T4 are the time intervals at which the activity of the spiral wave was recorded. $\pm\pi$ represents the change in the phase in the range of $+\pi$ to $-\pi$ [31-34].

The tip trajectories for WT and S481L mutations were computed using the Phase Singularity method [31, 37] in Figure 5.21 (ai, bi). For the S481L condition, a drift can be seen in the tip of the spiral wave Figure 5.21bi. The figure illustrates a CW rotating excitation wave perpendicular to the fibre orientation, with an outward movement of the tip.

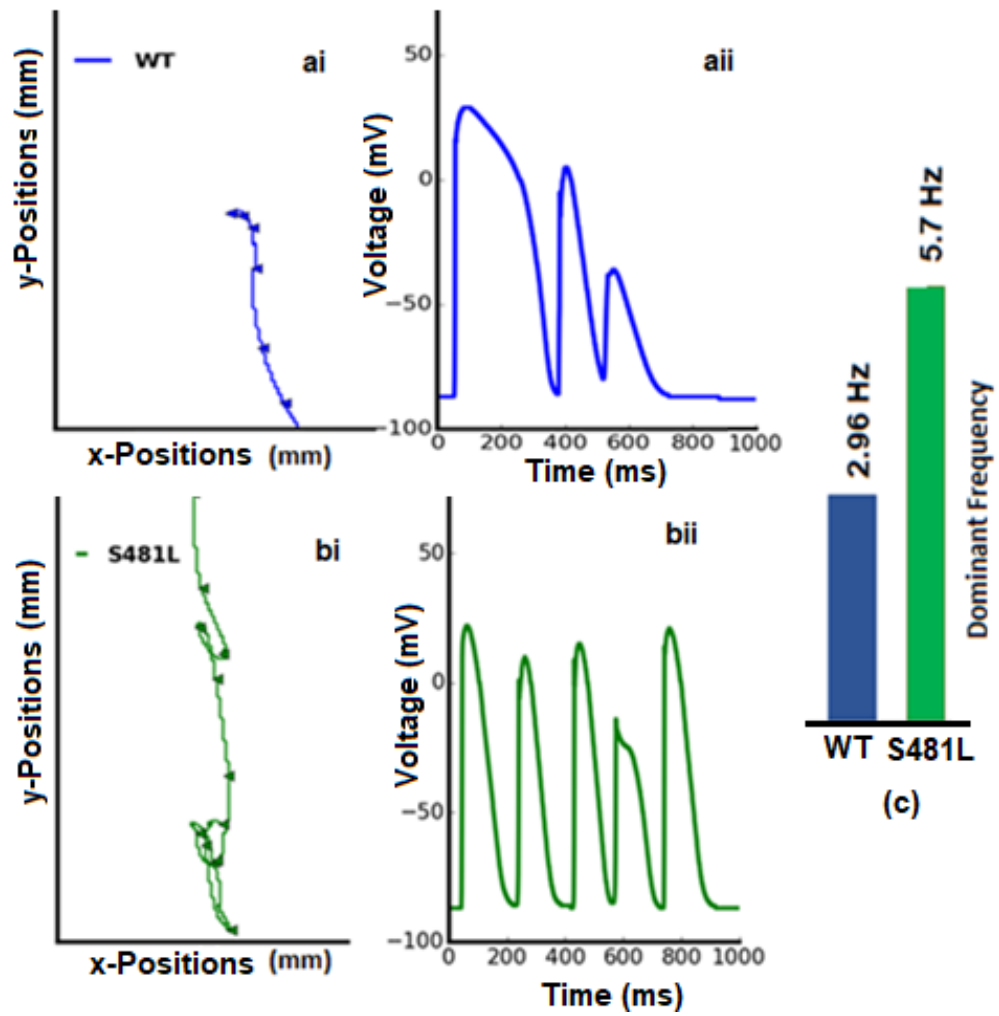


Figure 5.21: Behaviour of the re-entrant spiral wave in the 2D idealised tissue model for the WT and S481L variants of the CACNB2b β 2. The geometry of the 2D sheet is the same as that described in Figure 5.17a. (ai, bi) The re-entrant wave tip trajectories for WT (blue) and S481L (green) in the x and y space (mm) illustrate the path followed by the spiral wave in the 2D tissue sheet of the left ventricular cells. (aii, bii) The time course of localised electrical activity describing the life span of the re-entrant wave. (c) Dominant frequency values for the WT and S481L obtained from the power spectral analysis of the recorded electrical activity.

The dominant frequency was calculated by using a power spectrum analysis of the recorded local electrical activity. The values for the dominant frequencies were obtained as 3.2 Hz and 5.7 Hz for the WT and S481L respectively, Figure 5.21c and Figure C1 (Appendix C). These values are consistent with previous studies of the SQT syndromes [20, 27, 30].

5.9 Investigating the Enhancement of I_{CaL} as a Potential Therapeutic Target in the SQT5

As previously discussed, Implantable Cardiovascular Defibrillators (ICD) [38, 39] are not suitable for all cardiac patients, especially infants, because they do not restore the QT interval precisely. Development of a pharmacological alternative that not only restores the QT interval to its normal duration, but also protects it from arrhythmias and other side effects, is therefore very important [38-40].

L-type calcium influx can be selectively enhanced by using calcium agonists or calcium channel enhancers. These compounds have the ability to increase contractility by increasing the calcium ion movement across the cell wall [41]. In SQT5 patients, the influx of I_{CaL} was reduced under the S481L mutation condition [1]. However, it has recently been discovered that calcium influx can be enhanced by Aplidine [41]. Although no evidence of it being used to treat SQT5 patients has been found, Aplidine is a very useful drug for the treatment of congestive heart failure and atrial fibrillation [41].

A theoretical “pseudo-pharmacological” approach to normalise the QT interval in an adult SQT5 patient is to enhance the I_{CaL} influx density using drugs to determine the extent of enhancement required to normalise the QT interval. For S481L, I_{CaL} was enhanced to different percentages in the LVEPI, MIDDLE and LVENDO single cell models. Figure 5.22 shows the results for LVENDO, LVMCELL and LVEPI cell types under WT and S481L conditions. A small change in calcium influx could have an immense effect on the AP morphology (Figure 5.22b). In LVMCELL, 2% augmentation of I_{CaL} could normalise the AP duration. The AP duration can also be restored by blocking 40% I_{Kr} (Figure 5.22b). In LVENDO cells (Figure 5.22c), a 60% blockade of I_{Kr} restored the AP duration, while I_{Kr} blocking to restore the APD₉₀ in LVEPI cells was 40% (Figure 5.22a).

The 1D strand tissue model was used to investigate the effects of the increased influx of calcium ions on ECGs. In tissue models, APDs are smoother due to the electrical coupling between cells via gap junctions [19]. The augmentation of I_{CaL} affects the ST segment morphology in the simulations (increased the ST-segment elevation). This issue was resolved by blocking I_{Kr} , which normalised the QT interval. Results suggest that a 38% I_{Kr} blockade normalised the QT interval, while the T-wave amplitude was also increased by blocking I_{Kr} (Figure 5.23).

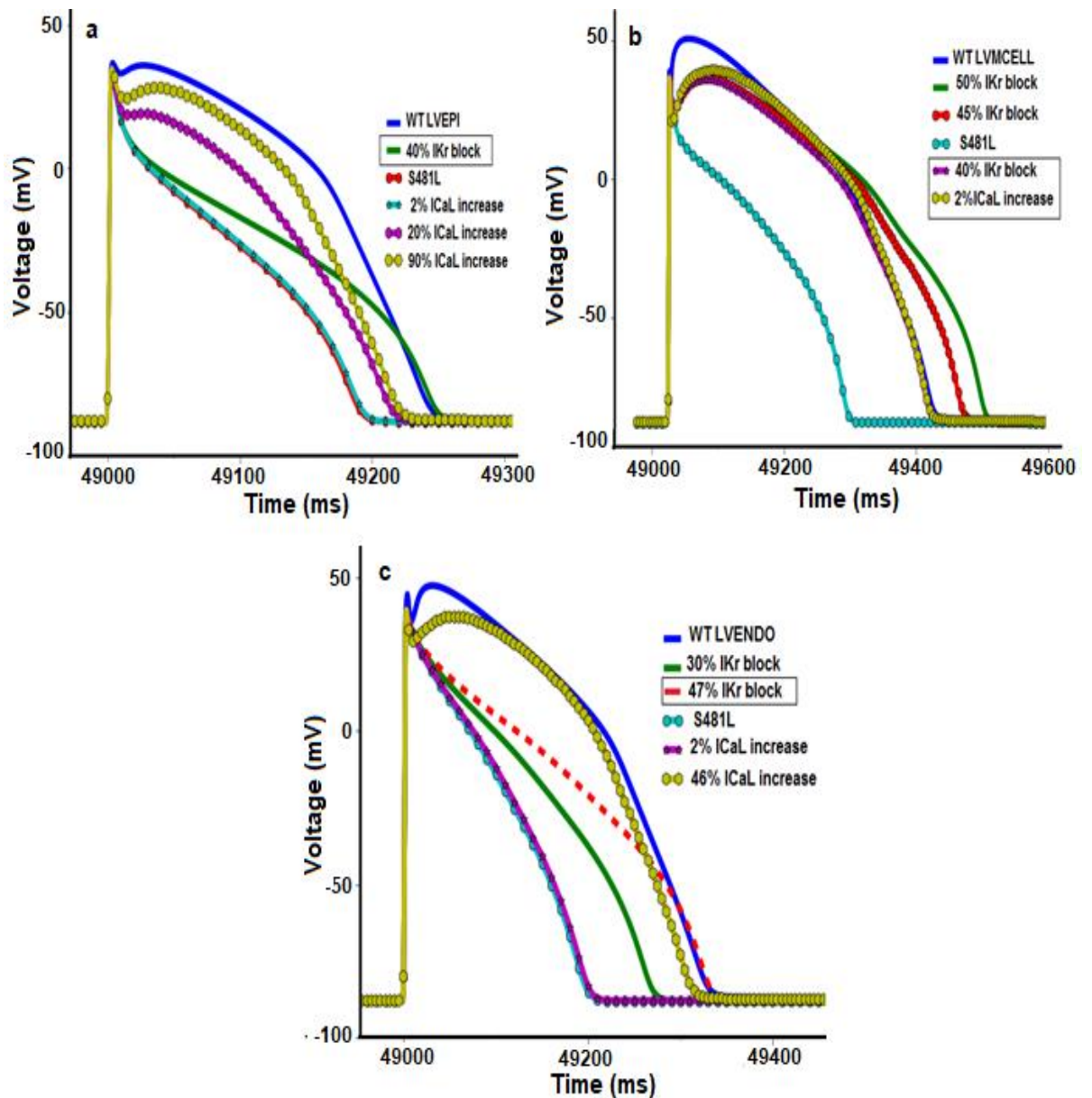


Figure 5.22: Current enhancement/blockade to normalise the AP duration under the S481L condition. (a, b, c) Show results for the LVEPI, LVMCELL and LVENDO cells respectively. In LVMCELL (b), a 2% augmentation of I_{CaL} normalised the AP duration. AP duration can also be restored by blocking 40% I_{Kr} . In LVENDO cells (c), a 60% blockade of I_{Kr} restored the AP duration, 40% I_{Kr} blockade restored the APD_{90} in the LVEPI cell (a).

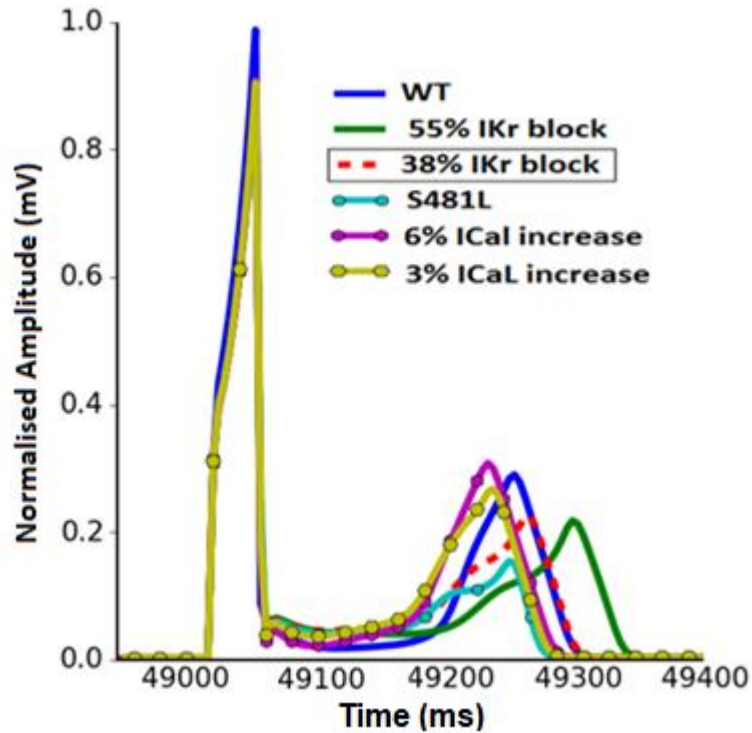


Figure 5.23: Current enhancement/blockade to normalise the QT interval. A 38% blockade of I_{Kr} normalised the QT interval under the S481L condition. The red dashed line represents the normalised QT interval.

5.10 Summary

In the absence of an accurate experimental SQT5 model for human ventricular myocyte, the use of *in silico* models provide an alternative method to understand the functional behaviour of SQT mutations on gene functionality, which can be beneficial to an understanding of this disease and help to develop different pharmacological alternatives to control and prevent VF or VT.

The major findings of the present study are:

- a) The CACNB2b S481L mutation reduced the AP duration in all three cell types and caused the shortening of QT interval on ECGs. Although the AP morphology was not as affected as under SQT4 A39V and G490R conditions, a depression can be seen during the plateau phase.
- b) The 1D model was unable to reproduce a tall T-peak for the S481L conditions. In previous studies, Gima and Rudy [19] have suggested that a tall T-wave is associated with hyperkalemia, which represents high levels of a potassium current as seen in SQT1-3 patients [20, 27]. To validate this, a heterogeneous distribution of I_{Kr} was considered along the strand i.e. the I_{Kr} density in LVEPI cell was increased

comparative to the middle region. A tall T-wave was obtained for S481L condition by adjusting the I_{Kr} densities to 1.5:1:1 for LVEPI, LVMCELL and LVENDO cells. Like the previous studies [15], to obtain a tall T-wave, a heterogeneous I_{Kr} density across the ventricular strand model was found to be necessary.

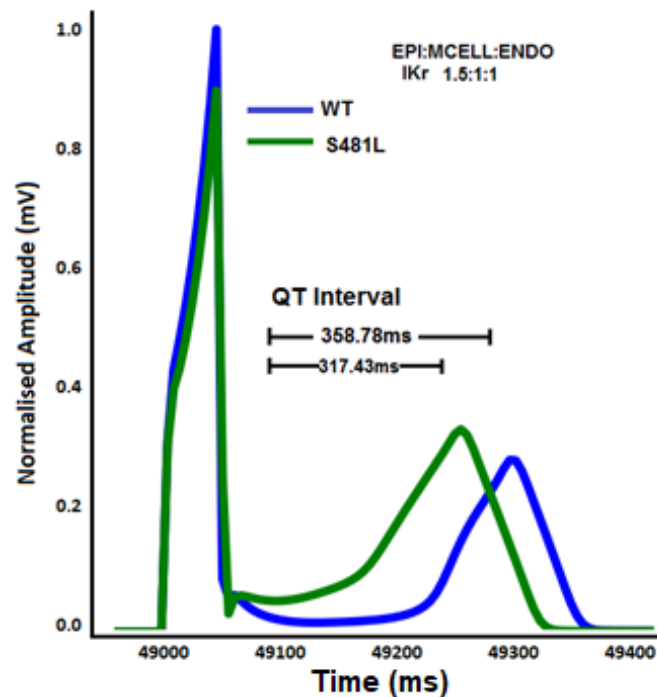


Figure 5.24: The effect of an increased I_{Kr} density on the amplitude of the T-wave. A tall T-wave was obtained for the S481L conditions by adjusting the I_{Kr} densities to 1.5:1:1 for the LVEPI, LVMCELL and LVENDO cells.

- c) An ST segment elevation was observed in the simulation, which was not found in short QT1-3 patients. ST segment elevation was reproduced, which depicts that, SQT5 mutations are linked with Brugada syndromes [3, 25].
- d) A study by Yan and Antzelevitch has suggested that a decrease in the amplitude of the AP dome of the LVEPI creates a transmural voltage gradient across the ventricular wall, which may not only elevate the ST, but can also lead to phase 2 re-entry and VF [3, 25].
- e) The tissue's temporal vulnerability at some localised regions was increased under the S481L condition.
- f) In 2D tissue, the minimal substrate length that is necessary to initiate and maintain the re-entry was decreased under the S481L condition.
- g) Blocking the calcium current normalised the AP duration, but a high amplitude of

the QRS interval on ECG could be seen by enhancing calcium influx, which is correlated with high blood pressure. My results are consistent with previous studies [40-43].

These findings gave a clear link between the shortening of the QT interval and the SQT5 mutation. It gave a detailed explanation of increased vulnerability to re-entry under the S481L CACNB2b condition.

5.11 References

- [1] C. Antzelevitch et al., “Loss-of-function mutations in the cardiac calcium channel underlie a new clinical entity characterized by ST-segment elevation, short QT intervals, and sudden cardiac death,” *Circulation*, vol. 115, no. 4, pp. 442–449, Jan. 2007.
- [2] J. Brugada, P. Brugada, and R. Brugada, “Brugada Syndrome: The syndrome of right bundle branch block, ST segment elevation in V1 to V3 and sudden death,” *Indian Pacing Electrophysiol. J.*, vol. 1, no. 1, pp. 6–11, Oct. 2001.
- [3] B. Benito et al., “Brugada Syndrome,” *Rev. Esp. Cardiol.*, vol. 62, no. 11, pp. 1297–1315, Jan. 2009.
- [4] D. M. Lloyd-Jones et al., “Association of electrocardiographic abnormalities with coronary artery calcium and carotid artery Intima-Media thickness in individuals without clinical coronary heart disease (From the Multi-Ethnic Study of Atherosclerosis [MESA]),” *Am. J. Cardiol.*, vol. 104, no. 8, pp. 1086–1091, Oct. 2009.
- [5] ML. Davigiue et al., “Association of nonspecific minor ST-T abnormalities with cardiovascular mortality: the Chicago Western Electric Study,” *The Journal of American Medical Association*, vol. 281, no. 6, pp. 530–536, Feb. 1999.
- [6] O. Anttonen et al., “Differences in twelve-lead electrocardiogram between symptomatic and asymptomatic subjects with short QT interval,” *Heart Rhythm*, vol. 6, no. 2, pp. 267–271, Feb. 2009.
- [7] G. Vorobiof, D. Kroening, B. Hall, R. Brugada, and D. Huang, “Brugada syndrome with marked conduction disease: dual implications of a SCN5A mutation,” *Pacing Clin. Electrophysiol. PACE*, vol. 31, no. 5, pp. 630–634, May 2008.
- [8] J. M. Cordeiro, M. Marieb, R. Pfeiffer, K. Calloe, E. Burashnikov, and C. Antzelevitch, “Accelerated inactivation of the L-type calcium current due to a mutation in CACNB2b underlies Brugada Syndrome,” *J. Mol. Cell. Cardiol.*, vol. 46, no. 5, pp. 695–703, May 2009.
- [9] J. M. Fish and C. Antzelevitch, “Role of sodium and calcium channel block in unmasking the Brugada Syndrome,” *Heart Rhythm Off. J. Heart Rhythm Soc.*, vol. 1, no. 2, pp. 210–217, Jul. 2004.
- [10] R. Coronel et al., “Right ventricular fibrosis and conduction delay in a patient with clinical signs of Brugada Syndrome,” *Circulation*, vol. 112, no. 18, pp. 2769–2777, Nov. 2005.
- [11] N. Weiss and A. Koschak, Eds., *Pathologies of calcium channels*. New York: Springer, pp. 225-238, 2014.
- [12] C. Patel, G.-X. Yan, and C. Antzelevitch, “Short QT syndrome: From bench to bedside,” *Circ. Arrhythm. Electrophysiol.*, vol. 3, no. 4, pp. 401–408, Aug. 2010.

- [13] T. O'Hara, L. Virág, A. Varró, and Y. Rudy, "Simulation of the undiseased human cardiac ventricular action potential: Model formulation and experimental validation," *PLoS Comput. Biol.*, vol. 7, no. 5, May 2011.
- [14] Z. H and H. Jc, "In silico study of action potential and QT interval shortening due to loss of inactivation of the cardiac rapid delayed rectifier potassium current.," *Biochem. Biophys. Res. Commun.*, vol. 322, no. 2, pp. 693–699, Sep. 2004.
- [15] I. Adeniran, J. Hancox, and H. Zhang, "In silico investigation of the short QT syndrome, using human ventricle models incorporating electromechanical coupling," *Front. Physiol.*, vol. 4, pp. 1-13, 2013.
- [16] P. Taggart et al., "Inhomogeneous transmural conduction during early ischaemia in patients with coronary artery disease," *J. Mol. Cell. Cardiol.*, vol. 32, no. 4, pp. 621–630, Apr. 2000.
- [17] W. Quan and Y. Rudy, "Unidirectional block and re-entry of cardiac excitation: a model study.," *Circ. Res.*, vol. 66, no. 2, pp. 367–382, Feb. 1990.
- [18] I. Gussak, P. Brugada, J. Brugada, C. Antzelevitch, M. Osbakken, and P. Bjerregaard, "ECG phenomenon of idiopathic and paradoxical short QT intervals," *Card. Electrophysiol. Rev.*, vol. 6, no. 1–2, pp. 49–53, Feb. 2002.
- [19] K. Gima and Y. Rudy, "Ionic current basis of electrocardiographic waveforms," *Circ. Res.*, vol. 90, no. 8, pp. 889–896, May 2002.
- [20] I. Adeniran, *Modelling the short QT syndrome gene mutations: And their role in cardiac arrhythmogenesis*, 2014 edition. New York: Springer, pp. 101-216, 2014.
- [21] I. Gussak et al., "Idiopathic short QT interval: A new clinical syndrome?" *Cardiology*, vol. 94, no. 2, pp. 99–102, 2000.
- [22] C. Antzelevitch and J. M. Fish, "Therapy for the Brugada syndrome," *Handb. Exp. Pharmacol.*, no. 171, pp. 305–330, 2006.
- [23] S. Ding et al., "Impact of early ST-segment changes on cardiac magnetic resonance-verified intramyocardial haemorrhage and microvascular obstruction in ST-elevation myocardial infarction patients," *Medicine (Baltimore)*, vol. 94, no. 35, Sep. 2015.
- [24] R. Nijveldt et al., "Early electrocardiographic findings and MR imaging-verified microvascular injury and myocardial infarct size," *JACC Cardiovasc. Imaging*, vol. 2, no. 10, pp. 1187–1194, Oct. 2009.
- [25] G. X. Yan and C. Antzelevitch, "Cellular basis for the Brugada syndrome and other mechanisms of arrhythmogenesis associated with ST-segment elevation," *Circulation*, vol. 100, no. 15, pp. 1660–1666, Oct. 1999.
- [26] C. Antzelevitch et al., "Brugada syndrome: report of the second consensus conference:

- endorsed by the Heart Rhythm Society and the European Heart Rhythm Association,” *Circulation*, vol. 111, no. 5, pp. 659–670, Feb. 2005.
- [27] I. Adeniran, A. El Harchi, J. C. Hancox, and H. Zhang, ‘Proarrhythmia in KCNJ2-linked short QT syndrome: insights from modelling’, *Cardiovasc. Res.*, vol. 94, no. 1, pp. 66–76, Apr. 2012
- [28] R. Tung, M. E. Josephson, V. Reddy, M. R. Reynolds, and SMASH-VT Investigators, “Influence of clinical and procedural predictors on ventricular tachycardia ablation outcomes: an analysis from the substrate mapping and ablation in Sinus Rhythm to Halt Ventricular Tachycardia Trial (SMASH-VT),” *J. Cardiovasc. Electrophysiol.*, vol. 21, no. 7, pp. 799–803, Jul. 2010.
- [29] J. Bai, K. Wang, Q. Li, Y. Yuan, and H. Zhang, “Pro-arrhythmogenic effects of CACNA1C G1911R mutation in human ventricular tachycardia: insights from cardiac multi-scale models,” *Sci. Rep.*, vol. 6, p. 31262, Aug. 2016.
- [30] I. Adeniran, M. J. McPate, H. J. Witchel, J. C. Hancox, and H. Zhang, ‘Increased vulnerability of human ventricle to re-entrant excitation in hERG-linked variant 1 short QT syndrome’, *PLOS Comput. Biol.*, vol. 7, no. 12, p. e1002313, Dec. 2011.
- [31] S. V. Pandit and J. Jalife, “Rotors and the dynamics of cardiac fibrillation,” *Circ. Res.*, vol. 112, no. 5, pp. 849–862, Mar. 2013.
- [32] R. A. Gray and N. Chattipakorn, “Termination of spiral waves during cardiac fibrillation via shock-induced phase resetting,” *Proc. Natl. Acad. Sci. U. S. A.*, vol. 102, no. 13, pp. 4672–4677, Mar. 2005.
- [33] R. A. Gray, A. M. Pertsov, and J. Jalife, “Spatial and temporal organization during cardiac fibrillation,” *Nature*, vol. 392, no. 6671, pp. 75–78, Mar. 1998.
- [34] A. M. Pertsov, J. M. Davidenko, R. Salomonsz, W. T. Baxter, and J. Jalife, “Spiral waves of excitation underlie re-entrant activity in isolated cardiac muscle,” *Circ. Res.*, vol. 72, no. 3, pp. 631–650, Mar. 1993.
- [35] M. A. Bray and J. P. Wikswo, “Use of topological charge to determine filament location and dynamics in a numerical model of scroll wave activity,” *IEEE Trans. Biomed. Eng.*, vol. 49, no. 10, pp. 1086–1093, Oct. 2002.
- [36] W.-J. Rappel, J. A. B. Zaman, and S. M. Narayan, “Mechanisms for the termination of atrial fibrillation by localized ablation: Computational and clinical studies,” *Circ. Arrhythm. Electrophysiol.*, vol. 8, no. 6, pp. 1325–1333, Dec. 2015.
- [37] D. T. Kim et al., “Patterns of spiral tip motion in cardiac tissues,” *Chaos Interdiscip. J. Nonlinear Sci.*, vol. 8, no. 1, pp. 137–148, Mar. 1998.
- [38] R. Schimpf, U. Bauersfeld, F. Gaita, and C. Wolpert, “Short QT syndrome: successful

- prevention of sudden cardiac death in an adolescent by implantable cardioverter-defibrillator treatment for primary prophylaxis,” *Heart Rhythm*, vol. 2, no. 4, pp. 416–417, Apr. 2005.
- [39] R. Schimpf et al., “Congenital short QT syndrome and implantable cardioverter defibrillator treatment: inherent risk for inappropriate shock delivery,” *J. Cardiovasc. Electrophysiol.*, vol. 14, no. 12, pp. 1273–1277, Dec. 2003.
- [40] P. Bjerregaard, A. Jahangir, and I. Gussak, “Targeted therapy for short QT syndrome,” *Expert Opin. Ther. Targets*, vol. 10, no. 3, pp. 393–400, Jun. 2006.
- [41] W. J. Crumb and G. T. Faircloth, “Aplidine as an l-type calcium channel enhancer,” EP0981352 A1, 01-Mar-2000.
- [42] L. S. Premkumar, “Selective potentiation of L-type calcium channel currents by cocaine in cardiac myocytes,” *Mol. Pharmacol.*, vol. 56, no. 6, pp. 1138–1142, Dec. 1999.
- [43] T.-A. Ansah, L. H. Wade, and D. C. Shockley, “Effects of calcium channel entry blockers on cocaine and amphetamine-induced motor activities and toxicities,” *Life Sci.*, vol. 53, no. 26, pp. 1947–1956, Jan. 1993.

CHAPTER 6

S755T CACNA2D1 $\alpha 2\delta$ -1 Linked Short QT 6 Syndrome

6.1 Introduction

The 6th variant of the SQTS was identified by Templin et al. in 2011[1]. The patient was a 17-year old Caucasian female with no apparent cardiac disorders. She suffered a sudden loss of consciousness due to ventricular fibrillation. The ventricular fibrillation was successfully abolished after two external defibrillation shocks. Her ECGs showed a QT interval of 317 ms (QTc = 329 ms) with a tall, narrow T-wave. Structural heart diseases were excluded by using transthoracic echocardiography techniques [1]. Genetic screening of the family revealed the father with a boarder-line QTc interval and an asymptomatic paternal grandmother. Both the family members had no history of syncope, seizures, or arrhythmic events and no SCD was previously recorded in the family. Baseline ECG did not exhibit a Brugada syndrome (BrS) pattern for either the father or grandmother. The T-wave morphology suggests an SQT Syndrome in the patient [1]. Genetic screening of the patient diagnosed no mutations in the previously known SQT genes i.e. KCNH2, KCNQ1, KCNJ2, CACNA1C, and CACNB2b genes [1, 2]. A genetic study revealed a heterozygous transition from G-to-C at nucleotide 2264 in the CACNA2D1 domain, assuming a Threonine to Serine substitution at position 755 (S755T) of CACNA2D1 [1, 2]. The S755T mutation was positioned at external C-terminal of the Ca_vα₂ that produced a large loss of currents with barium as the charge carrier [1].

A carboxy-terminal transmembrane helix fastens CACNA2D1 to the cellular membrane (Chapter 2). A large part of the protein is in the extracellular space, including the location of S755T, which is suggested to be located in a sensory domain with a position more towards the interior of the protein. The substitution of Threonine to Serine is not well accommodated by the protein core, as Threonine has an additional methyl group which cannot be accommodated by the core and clashes with the side chain of Val799 in the core. This may change the functionality of the CACNA2D1 protein. However, most of the functions of this protein channel are not yet completely known [1].

6.2 Simulation of Single Cell I_{CaL} for the CACNA2D1 $\alpha 2\delta$ -1 Control and SQT6/S755T Mutation Conditions

The experimental studies of the SQT6 syndrome have considered barium ions (I_{Ba}) as the charge carrier through the calcium channel for obtaining voltage clamp data on the I_{CaL} channel kinetics in the SQT6 condition [1]. In simulations, to obtain the best model equations which reproduce well the experimental data, the O'Hara & Rudy model was changed to the voltage dependent inactivation (VDI) mode ($n=0$). VDI mode only allows voltage dependent inactivation when Ba^{2+} is the charge carrier [3] and there is no additional inactivation due to the Ca^{2+} ions in the S755T model.

The voltage clamp protocol for the $\alpha 2\delta$ -1 subunit of the CACNA2D1 control type was performed for a holding potential of -80 mV with the total simulation time of 200 ms. The clamp voltage range was between -60 mV and 60 mV with an increment of 5mV for each step. The same voltage clamp protocol was applied to the S755T variant of the $Ca_v\alpha 2\delta$ -1 subunit of the L-type calcium channel [1].

Figure 6.1a shows the simulated (solid lines) I-V relationships for the WT and S775T mutation, which corresponds well with the experimental data (dotted lines) [1]. The conductance for the WT was adjusted to obtain the same peak current density as that of original O'Hara & Rudy model [3], Figure 6.1b, thus maintaining the overall current densities, APD_{90} , and the dynamic properties of the O'Hara & Rudy human ventricular model [3]. Simulations showed a decrease in the amplitude of I_{Ba} when expressed for the S755T variant of $Ca_v\alpha 2\delta$ -1 subunit which showed an agreement with the experimental data [1]. A small positive shift in the activation and inactivation voltages was overserved experientially [1]. S755T model was able to reproduce those effects, Figure 6.1c.

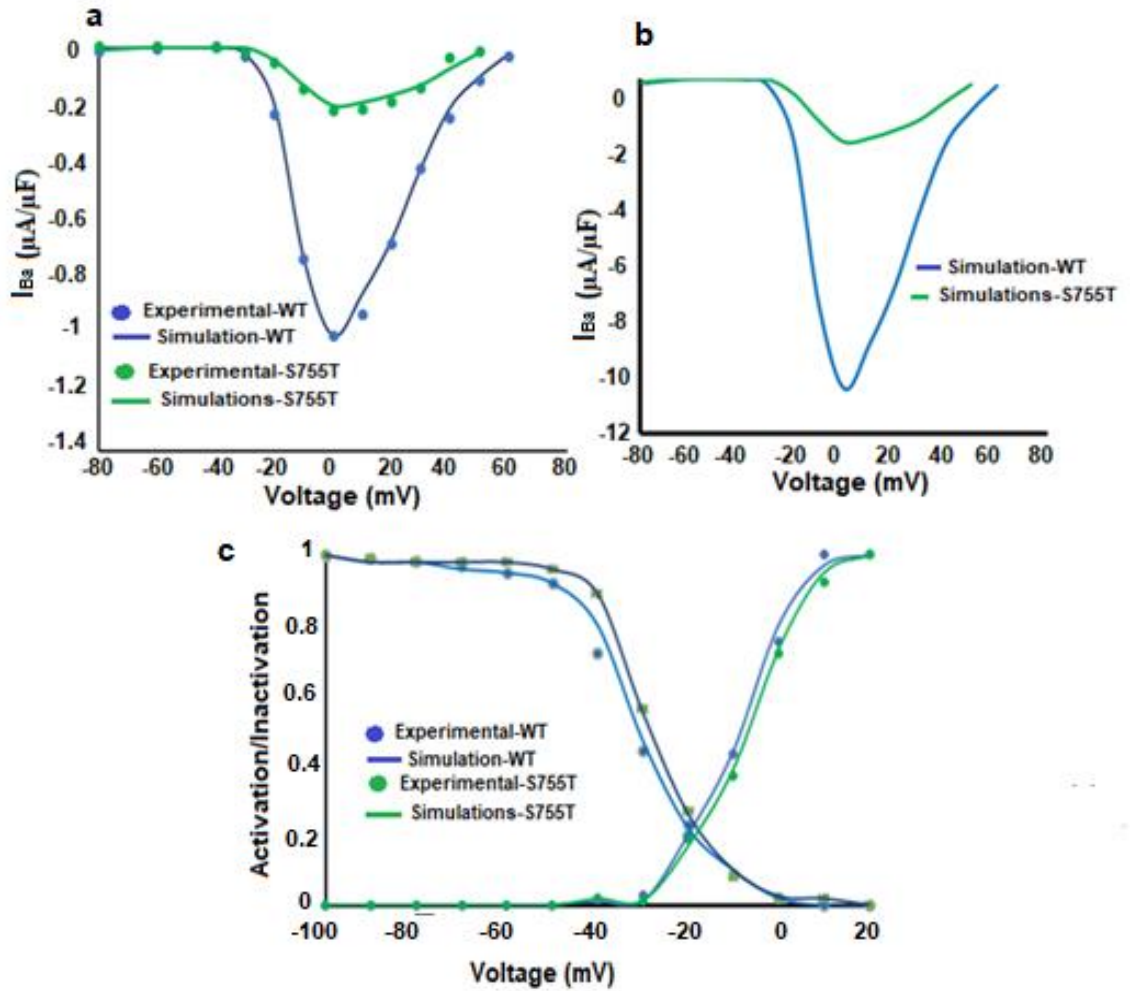


Figure 6.1: Computed I-V relationship for the WT and S755T models. (a) Normalised I-V relationship for WT (blue) and S755T (green). The solid lines represent the simulated data while the dotted points represent the experimental data. Simulations showed a decreased amplitude of S755T channel currents which matched to experimental data [1]. (b) The WT was adjusted to obtain the same peak current density as the original I_{CaL} of O’Hara & Rudy model [3], thus maintaining the overall current densities, APD_{90} , and dynamic properties of the O’Hara & Rudy human ventricular model. (c) Activation and inactivation mechanisms of the CACNA2D1 channel under the WT (blue) and S755T (green) conditions for I_{Ba} as the charge carrier.

The WT and S755T formulations were incorporated into the 2011 O’Hara & Rudy [3] single cell model to visualise the functional behaviour of S755T mutation on ventricular APs. Figure 6.2 shows simulated action potentials and I_{Ba} current profiles over the time “t” for LVEPI, LVMCELL and LVENDO cells under the WT and S755T conditions respectively.

The APD_{90} values were measured for left ventricular EPI, MCELL, and ENDO cells for the CACNA2D1 WT and S755T conditions. A reduction in the AP duration can be seen under

the S755T conditions. Results have suggested that this abbreviation of AP is linked to the decreased influx of barium ions through the L-type calcium channel during the plateau phase of the AP as shown by the time-course of the I_{Ba} (Figure 6.2 bi, bii, biii), which is consistent with previous studies [4, 5]. The abbreviation of APD_{90} under S755T condition was rate-dependent. The simulated resting potential values were -83.72 mV and -86.64 mV for the WT and S755T conditions respectively.

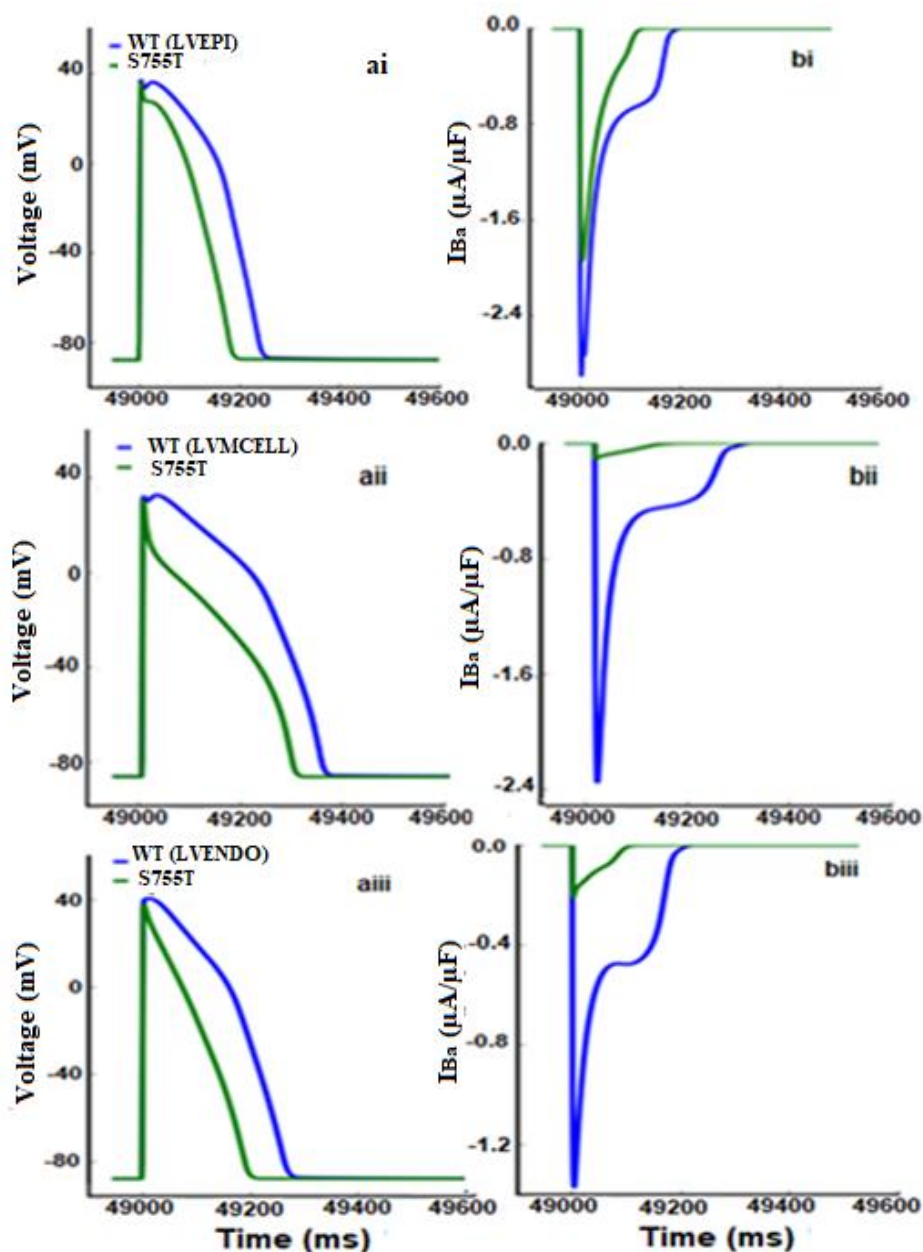


Figure 6.2: Simulated action potentials and I_{Ba} time traces. (ai, aii, aiii) Action potential paced at the frequency of 1 Hz for LVEPI (ai), LVMCELL (aii) and LVENDO (aiii) cells for WT (blue) and S755T (green) conditions. (bi, bii, biii) Relative CACNA2D1 I_{Ba} current profiles for LVEPI (bi), LVMCELL (bii) and LVENDO (biii) cells under the WT (blue) and S755T (green) conditions.

	LVEPI (ms)	LVMCELL (ms)	LVENDO (ms)
WT	268	349	285
S755T	200	298	211

Table 6.1: At a pacing of 1 Hz, Simulated APD₉₀ (ms) values for LVEPI, LVMCELL and LVENDO cell types under the WT and S755T mutation conditions.

The extent of APD₉₀ shortening is of a different amplitude in all three cell types for the S755T condition, with the greatest attenuation in the LVENDO cell, Table 6.2.

	LVEPI (ms)	LVMCELL (ms)	LVENDO (ms)
S755T	68	51	73

Table 6.2: Shortening of the APD₉₀ in different cell types under the S755T condition with the largest reduction in the LVENDO cell type, Figure 6.2 (ai-aiii).

Results showed that, the transmural dispersion of APD₉₀ across different cell types of ventricular wall has been decreased in the S755T condition (Figure 6.10), which is similar to prior studies of SQTs1-3 [6, 7]. A heterogeneous reduction of the action potential in different cell types can lead to an increased transmural dispersion of the repolarisation with a greater risk of the development of ventricular arrhythmia under the S755T condition [4, 5].

6.3 Rate Dependent Restitution Properties of WT and SQT6/S755T

A reduction in the total duration of the AP is observed for the S755T variant of Ca_v α₂ δ-1. This reduction in APD₉₀ under mutation conditions is rate-dependent [4, 5, 7, 12]. The APD₉₀ restitution (APD-R) curves are shown in Figure 6.3 (a-c). Observations show that the APD₉₀ has decreased for S755T conditions as compared to the WT condition in all three cell types, over the range of the diastolic intervals (DIs) investigated. Incorporation of S755T mutation led to a leftward shift in all three cell types as compared to the control variant of Ca_v α₂ δ-1. Flattening of APD₉₀ curves can also be seen for LVEPI and LVENDO cell types. For the Middle cell, APD₉₀ restitution curve shows a constant steepness over a selected range of diastolic intervals (DI > 600) Figure 6.3bi. The abbreviated values of APD₉₀ decreased the

maximal slopes of APD₉₀ restitution curves (Figure 6.4) in all three cell types. According to the previous studies, SQTs patients exhibit a poor rate-adaptation of their QT intervals [6, 9-10], and results suggested an attenuation of rate-adaptation of the ventricular APD₉₀, which is consistent with the previous studies of SQTs [11].

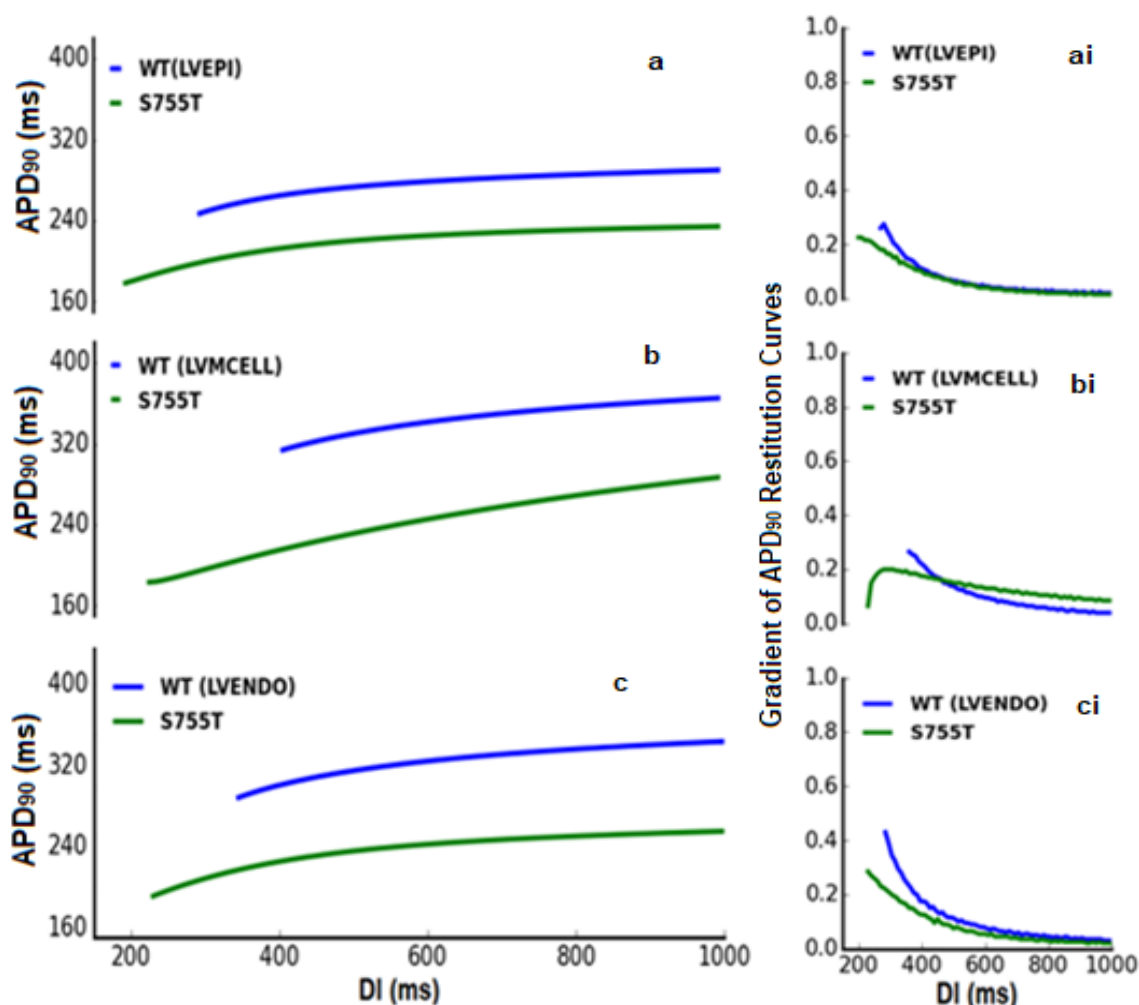


Figure 6.3: APD₉₀ restitution curves for WT and S755T. APD₉₀ is plotted against the diastolic interval (DI). (a, b, c) APD₉₀ restitution curves for the LVEPI (a), LVMCELL (b) and LVENDO (c) cells respectively under the WT (blue) and S755T (green) conditions. The S755T mutation caused the flattening of the APD₉₀ restitution curves with a prominent leftward shift in all three cell curves. (ai, bi, ci) Gradients of the APD₉₀ restitution curves illustrating the change in the slopes of APD₉₀ restitution curves as a function of DI (ms).

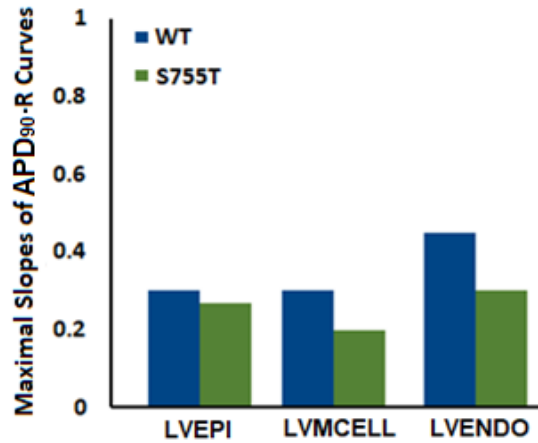


Figure 6.4: Maximal slopes of APD₉₀ restitution curves. The slopes of the APD₉₀ restitution curve for WT (blue) and S755T (green). The slopes were measured at the minimum diastolic interval (DI) before the conduction block and calculated for the individual curves of the LVEPI, LVMCELL and LVENDO cell types. The shortening of the APD₉₀ under the S755T condition reduced the maximal slopes of the restitution curves.

The steady state restitution curves were plotted for WT and S755T conditions to investigate the rate adaption phenomena in more detail. The same behaviour was observed, i.e. the mutation flattened the steady state restitution curve and caused a leftward shift in all three curves, Figure 6.5 (a, b, c). A small steepness can be seen in the LVMCELL curve at fast heart rates (BCL > 550 ms & BCL < 900 ms), which gradually settled down at slower heart rates, Figure 6.5bi.

Studies have suggested that the reduction in the effective refractory period is also rate dependent [12, 13]. The effect of the S755T mutations on ERP restitution curves can be seen in Figure 6.7 (a, b, c). A reduction in the maximal slope of the ERP-R curves for LVEPI, LVMCELL and LVENDO is very prominent, Figure 6.8. The effective refractory period was reduced under mutation as compared to the WT condition across the range of basic cycle lengths (BCLs) investigated. The slope of the LVEPI cell type did not change much, while steepness can be seen in the beginning of LVMCELL ERP-R curve (Figure 6.7bi) at fast heart rates, which slowed down at slow heart rates. This trend is consistent with the steady state restitution curves (Figure 6.5bi and Figure 6.7bi).

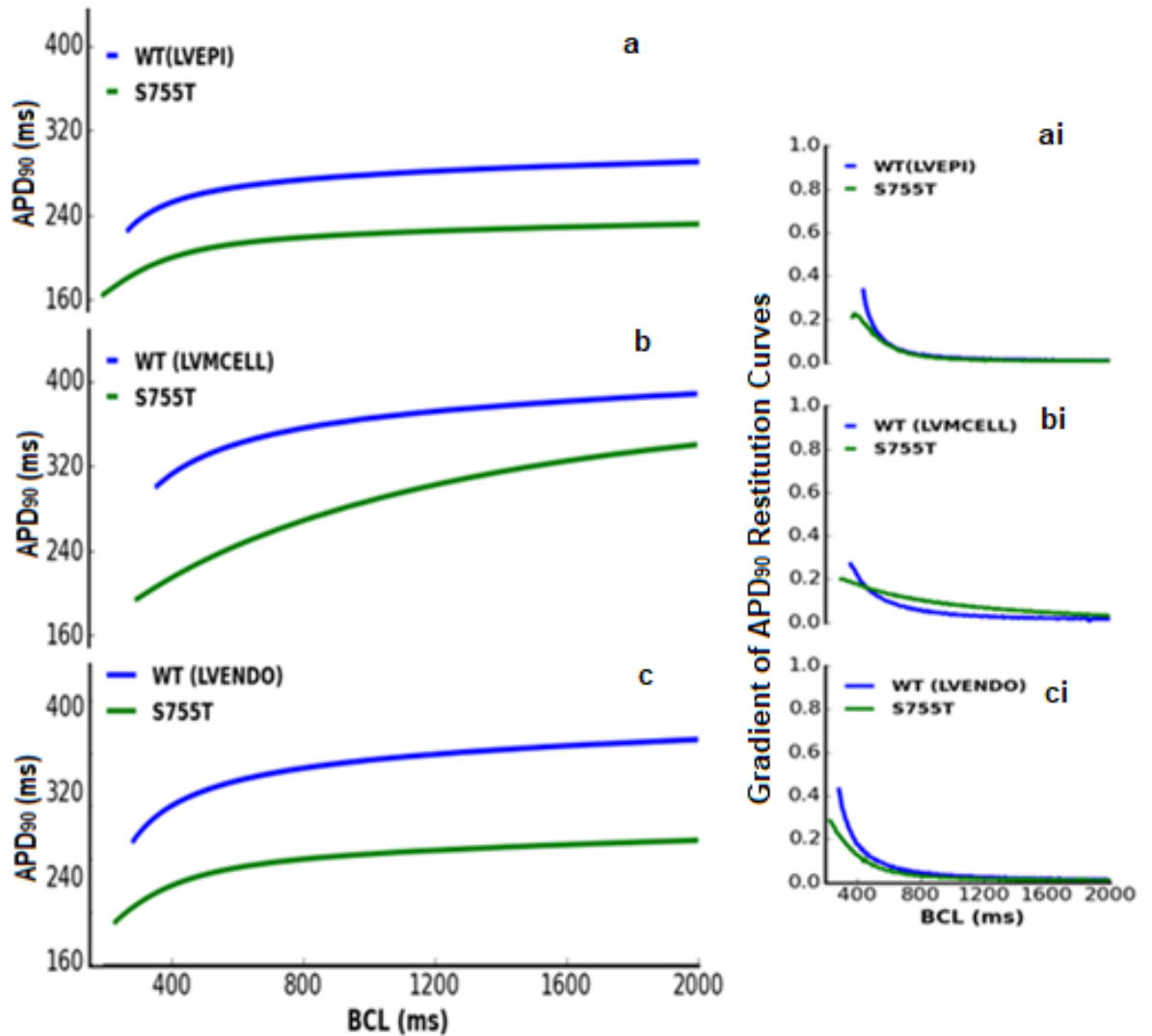


Figure 6.5: Steady-state APD₉₀ rate dependence curves for WT and S755T conditions. The APD₉₀ is plotted against the basic cycle length (BCL). (a, b, c) Steady state APD₉₀ restitution curves for LVEPI (a), LVMCELL (b) and LVENDO (c) cells respectively for the WT (blue) and S755T (green) conditions. The steady state restitution curves were plotted to examine the rate dependence of APD₉₀(ms) with the BCL (ms). The S755T model showed a greater abbreviation of the APD₉₀(ms), which suggest an attenuation of the rate adaption of the ventricular APD in the S755T model. (ai, bi, ci) Gradients of steady state restitution curves illustrating the behaviour of steady state restitution curves under the WT and S755T conditions.

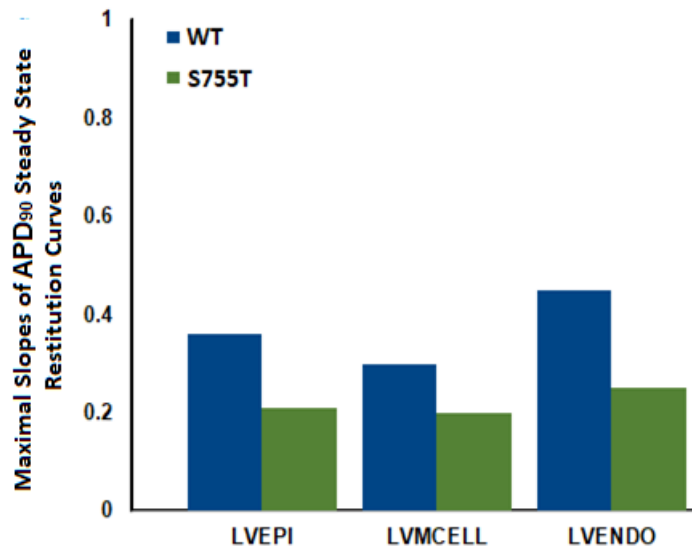


Figure 6.6: The maximal slope of steady-state restitution curves. WT (blue) and S755T (green) for the LVEPI, LVMCELL and LVENDO cell types. A reduction in the slope of the steady state restitution curves can be seen with the reduced APD₉₀ for the S755T condition. The LVENDO cell curve has a more marked reduction in its slope under the S755T condition.

A leftward shift can be seen in all three restitution curves, i.e. APD-R, APD-R steady state, and ERP-R restitution curves for a CACNA2D1 Ca_vα_{2δ}-1 S755T condition for the LVEPI, LVMCELL and LVENDO cell types. This leftward shift enabled ventricular cells to support electrical activity at fast heart rates [5, 12, 17] under the S755T condition (as normally seen during VT and VF), while the steepness of restitution curves represents the instability of the re-entrant excitation wave [14].

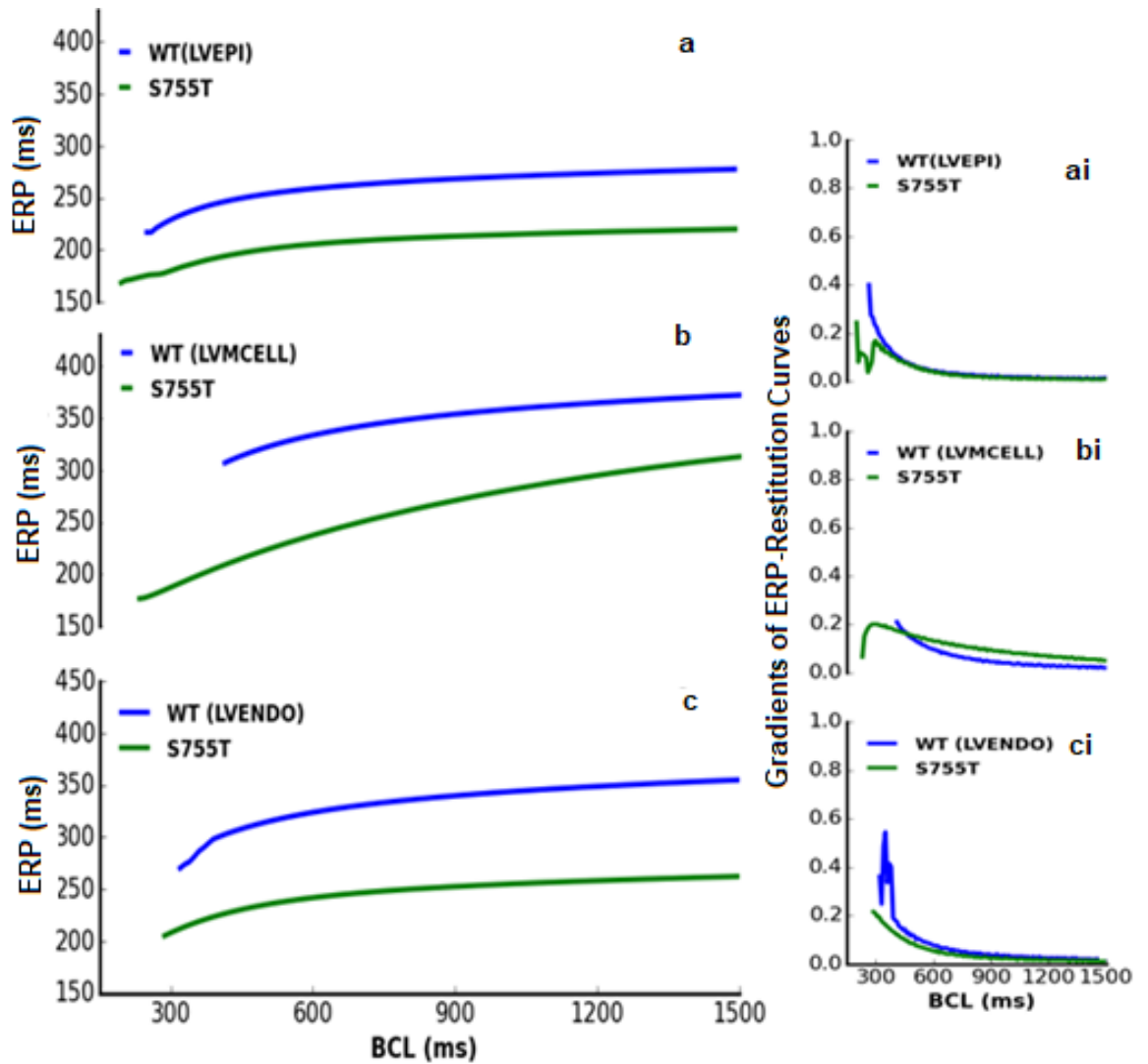


Figure 6.7: ERP restitution curves were obtained by plotting the effective refractory period (ERP) against the basic cycle length (BCL). (a, b, c) WT (blue) and S755T (green) ERP restitution curves for the LVEPI, LVMCELL and LVENDO cells. (ai, bi, ci) The slope of ERP restitution curves shows their behaviour under the WT and S755T conditions. A reduction in the maximal slopes of the ERP-R curves along with the shift of ERP-R curves towards the lower cycle lengths for the S755T condition can be seen in all three cell types, while steepness is also very prominent in the LVMCELL curve (bi).

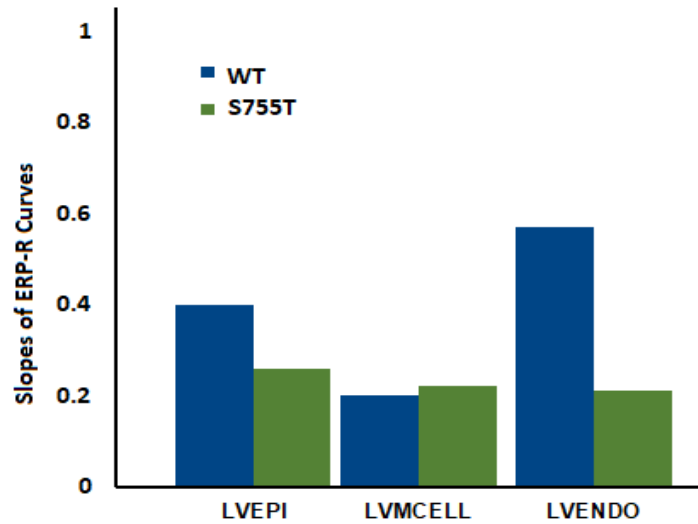


Figure 6.8: The slope of ERP restitution curve for WT (blue) and S755T (green). S755T reduced ERP-R curves slopes in all three cell types with a more marked reduction in the LVENDO cell, while the maximal slope of the LVMCELL curve is slightly higher for the S755T model as compared to the WT.

6.4 1D Tissue Modelling and ECG Computation

The 1D strand model of left ventricular cells as explained in Chapter 3 was utilised to investigate the effects of S755T on ventricular action potential along a 1D strand of 100 cells. The action potential was generated by applying a train of 10 S1 stimuli at the ENDO end of the strand. The wave generated propagated from the ENDO end towards the EPI end Figure 6.9 (a-b) of the 1D strand model. In Figure 6.9 (a-b), time runs horizontally from left to right, while space runs vertically from the ENDO end at the bottom to the EPI end at the top.

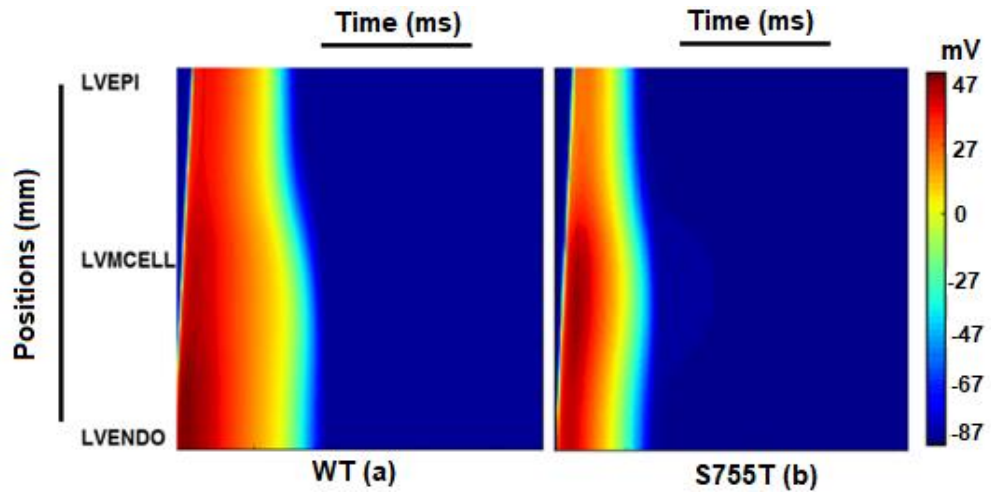


Figure 6.9: Space-time colour-mapping of the membrane potential in a 15 mm ventricular wall strand during the propagation of an action potential cycle (BCL=1000 ms). (a, b) WT (a) and S755T (b). Positions (mm) run vertically with LVEPI at the top and LVENDO at the bottom, while the time (ms) runs horizontally. The colour mapping of the membrane potentials of the cells along the strand was from blue (-87 mV) to red (47 mV).

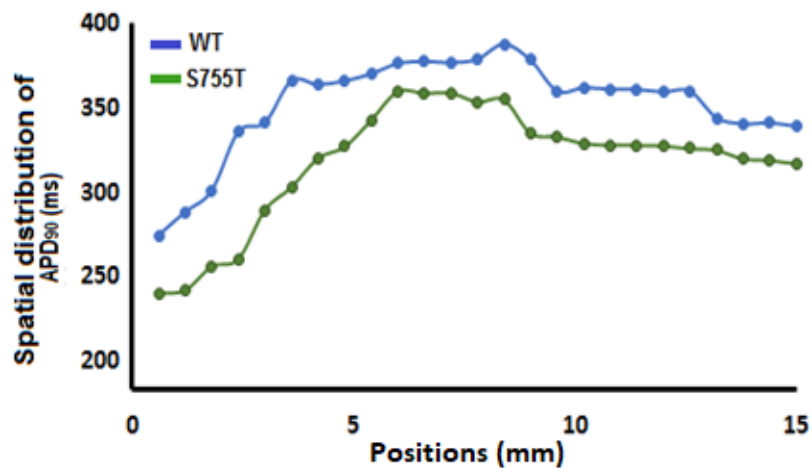


Figure 6.10: Spatial distribution of APD₉₀ along the transmural 1D strand model of the ventricular myocytes for the WT (blue) and S755T (green) conditions.

Pseudo ECGs were calculated for WT and S755T conditions (Figure 6.11) by utilising the 1D strand model of the left ventricular cells.

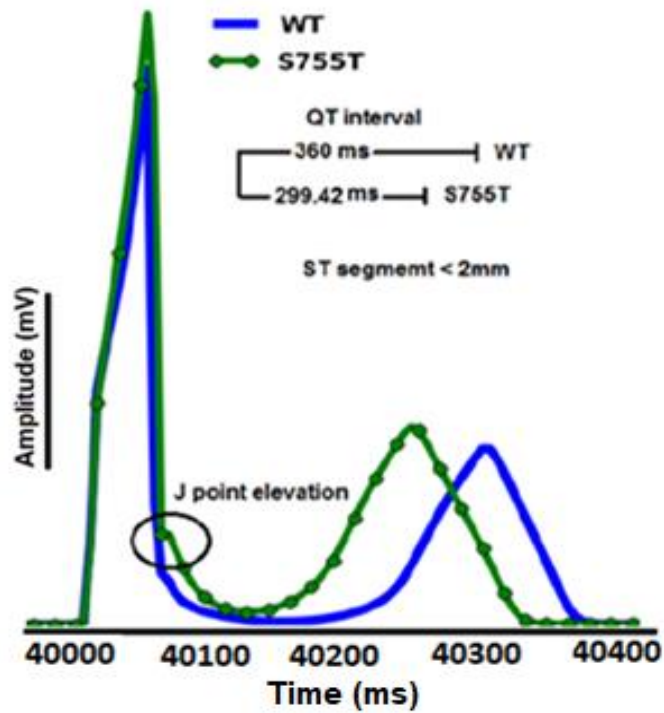


Figure 6.11: Pseudo-ECGs corresponding to the WT (blue) and SQT6 (S755T, green) conditions. The circle shows an elevation of the J-point under the S755T condition as compared to WT. A prominent T-wave can also be seen for the S755T model.

The value of the QT interval was 360 ms for the WT condition which was reduced to 299 ms for the S755T mutation condition (Figure 6.11). The time interval between T-peak and T-end (T-wave half width) was 62 ms and 68 ms for WT and S755T conditions respectively. For the Short QT6 Syndrome a tall and peaked T-wave is the key feature observed in the clinical ECGs of SQT6 syndrome patient [1]. My simulations thus reproduce this key feature. Another feature which has been clinically observed for SQT4-5 patients is an elevated ST segment. It is the key to linking the BrS to SQTS [4,5]. The SQT6 patient's ECG did not show any prominent elevation of the ST segment [1]. A study by Yan and Antzelevitch has suggested that a decrease in the amplitude of the AP dome of the EPI cell as compared to the ENDO cell creates a transmural voltage gradient across the ventricular wall, which can elevate the ST segment [20, 21]. In simulations, the depression in the ENDO dome is greater than EPI dome (Figure 6.2), which might control the elevation of the ST segment and amplitude of the T-wave for the S755T condition.

6.5 Investigation of the Unidirectional Conduction Block and Size of the Arrhythmogenic Substrate in 1D Strand Model of the Left Ventricular Myocyte for the CACNA2D1 $\alpha_2\delta$ -1 WT and S755T

The unidirectional conduction block in the WT and S755T models was investigated by utilising the 1D strand model. The arrhythmogenic substrate for WT and S755T conditions was computed by applying a premature stimulus during the refractory tail of a previous excitation wave. A train of 10 S1 stimuli paced at a frequency of 1 Hz was applied at the ENDO end of the 1D transmural strand to initiate a conducting wave. A second stimulus (S2) was applied after the 10th S1 stimulus, following a time delay ΔT . The amplitude and duration for S1 and S2 were similar. ΔT (T2-T1) represents the maximal and minimal values of a temporal window during which the propagation of the excitation wave triggered by the S2 stimulus was unidirectional in the 1D strand. Figure 6.12 shows the width of the vulnerable window across the 1D strand for both WT and S755T conditions. The width of the temporal window represents the time during which the tissue is more vulnerable to any premature stimulus that can trigger arrhythmic events. The width of vulnerability window for S755T condition increased across the entire 1D strand (Figure 6.12).

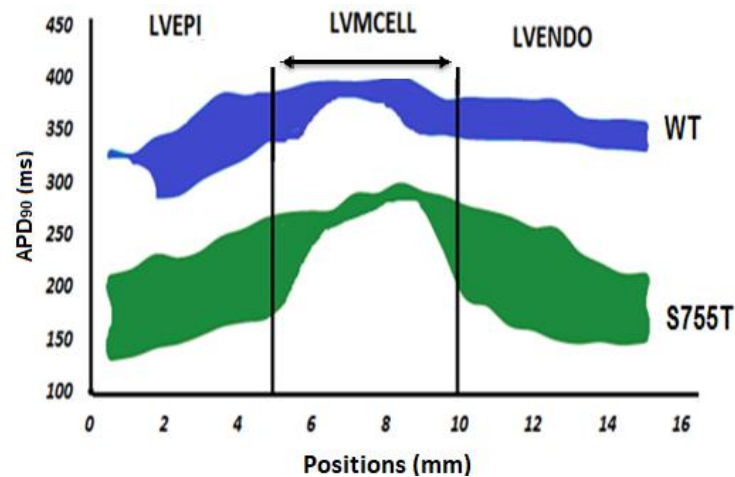


Figure 6.12: Vulnerable Window across the transmural 1D strand plotted as a function of position on a 15 mm long 1D strand of ventricular cells, with each cell having a spatial resolution of 0.15 mm. The width of the Vulnerable Window (VW) is measured between the marked region depicted by the arrow. VW is shown for the WT (blue) and S755T (green) models.

Figure 6.13 shows the temporal vulnerability window width for the marked region in the Figure 6.12. The width of the vulnerability window measured within the marked region is 21.3 ms for the WT and 30.2 ms for the S755T conditions respectively.

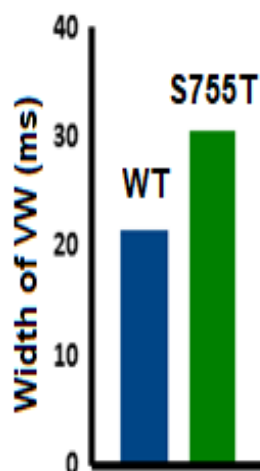


Figure 6.13: Measured Vulnerable Window (VW) width in the marked region (an average of different VW widths within the marked region depicted by arrow) in the Figure 6.12 for the WT (blue) and S755T (green) models.

6.6 Computation of Conduction Velocity and Excitation Threshold

Conduction velocity (CV) was computed along the 1D strand model (an array of the left ventricular cells) for the WT and S755T conditions (Figure 6.14). As seen previously [5, 12, 17], the SQT mutation reduced the conduction velocity at low heart rate while an increase in CV can be seen at fast heart rates [12, 22]. Similar results were obtained by computing CV for the S755T mutation. The CV decreases at slow heart rates (rate <119 beats/minute, PCL > 420 ms) while an increase in CV under S755T condition can be seen at fast heart rates (250 ms <PCL< 390 ms). The reduced tissue excitability (Figure 6.15) at lower heart rates could be a reason for the reduced values of CV at rates slower than 119 beats/minute, as changes in the intercellular electrical coupling were not very strong at those rates. CV was calculated at a rate of 60 beats/minute (BCL=1000 ms) and the measured CV was 64.14 cm/s and 62.7 cm/s for the WT and S755T conditions respectively. However, the values measured for the CV at higher rates between 128 and 201 beats/minute (250 ms >PCL< 390 ms) were slightly higher for the S755T condition as compared to WT. The increased CV for the S755T condition at high rates is due to short effective refractory periods as compared to the WT [15, 22, 23].

The fastest heart rates which supported conduction in the left ventricular tissue for WT and S755T conditions were 135 beats/minute (SI < 370 ms) and 203 beats/minute (SI < 245 ms) respectively. A large part of tissue was still refractory in WT, which caused a failure of conduction in WT at fast heart rates as compared to the mutations.

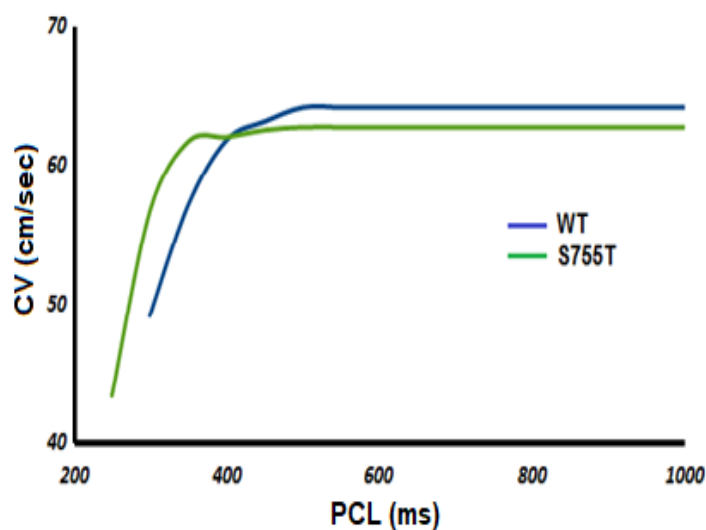


Figure 6.14: Conduction velocity (CV) restitution under the WT (blue) and S755T (green) conditions. The CV curve was plotted against the Pacing Cycle Length (PCL).

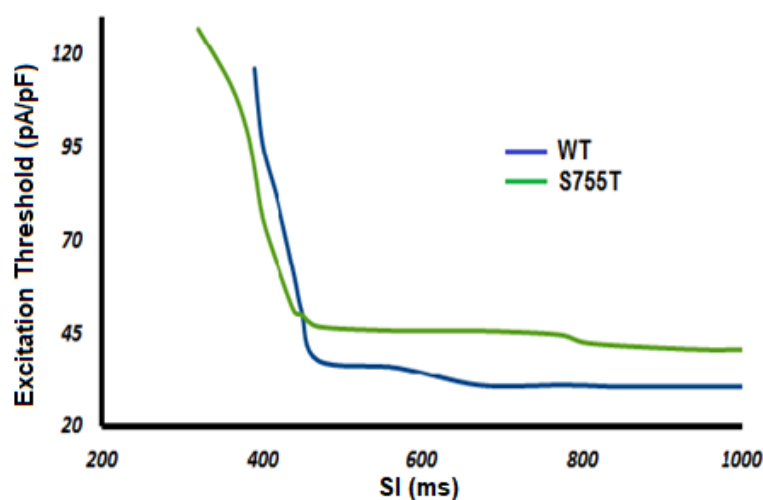


Figure 6.15: Excitation threshold plotted against Stimulus Intervals (SI) for the WT (blue) and S755T (green) mutation conditions. The tissue excitation threshold is a measure of the minimal stimulus amplitude that can initiate a propagating action potential in a cardiac tissue [22, 23]. The fastest heart rates which supported conduction in the left ventricular tissue for the WT and S755T conditions were 135 beats/minute (SI < 370 ms) and 203 beats/minute (SI < 245 ms) respectively.

6.7 Investigation of the Arrhythmogenic Substrate in an Idealised 2D Geometry for the CACNA2D1 WT and S755T

An idealised 2D tissue model of the left ventricular cells was utilised to investigate the behaviour of the re-entrant wave in WT and S755T conditions and compute the minimal spatial length of a premature stimulus required to initiate re-entry for both WT and S755T conditions. An excitation wave was evoked by applying a conditioning stimulus (S1) at the ENDO end of the 2D sheet. The excitation wave evoked by the S1, propagated from the ENDO end to the EPI end of the 2D tissue sheet under WT and S755T (Figure 6.16 a, b) conditions. Following a time delay, a 2nd test stimulus (S2) was applied within the VW of EPI region. As the MCELL region was still refractory due to the slower repolarisation as compared to EPI and ENDO regions, the excitation wave evoked by S2 was blocked by the unrecovered MCELL, which gave rise to a unidirectional conduction towards the EPI side. This unidirectional block resulted in the formation of spiral re-entrant excitation waves in both the WT and S755T conditions. For WT and S755T, the time delay between the S1 and S2 was 380 ms and 221 ms respectively. For WT, the excitation re-entrant wave was terminated within 390 ms (Figure 6.16a) after the time of its initiation, but it sustained for the S755T condition (Figure 6.16b). My results are consistent with the previous studies of SQT syndromes [12, 24 and 25]. The minimal tissue substrate lengths which were necessary to initiate re-entry were measured for WT and S755T mutation conditions as 26.8 mm and 13.5 mm respectively (Figure 6.17). Results have suggested that it is substantially easier to induce a re-entry in the S755T model as compared to the WT. Hence, the tissue has more susceptibility to ventricular arrhythmias under the S755T condition.

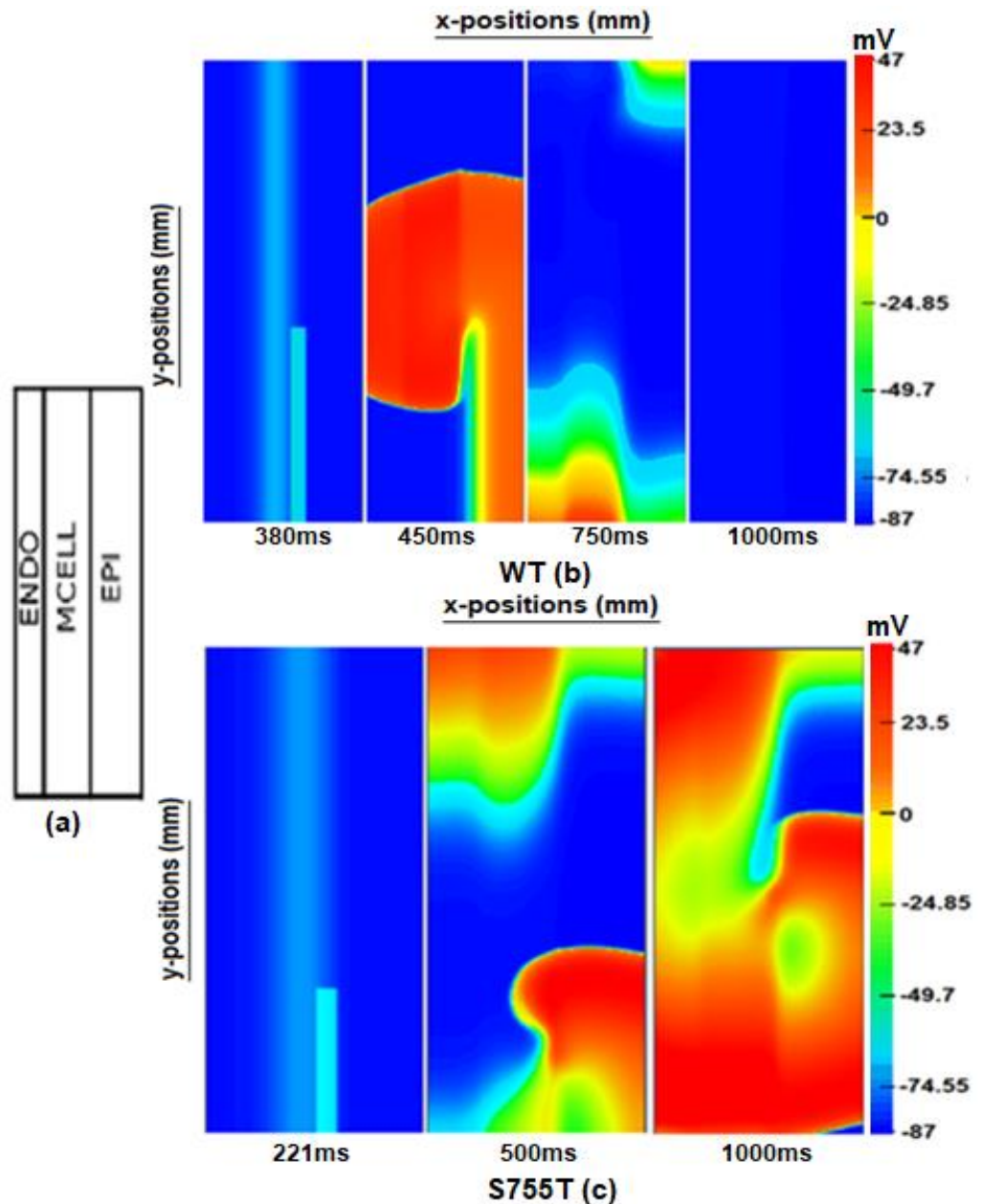


Figure 6.16: Snapshots of initiation and conduction of re-entry in a 2D idealised model. a) Schematic representation of the 2D tissue model. (b, c) S2 was applied after a time delay of 380 ms for the WT(a), the spiral excitation wave evoked by the S2 was terminated within 390 ms. For the S755T(b) S2 was applied after a time delay of 221 ms, the spiral wave initiated by the S2 under the S755T condition, sustained for the entire cycle of 1000 ms. Colour mapping of the membrane potentials of the cells along the 2D tissue sheet from blue (-87 mV) to red (47 mV).

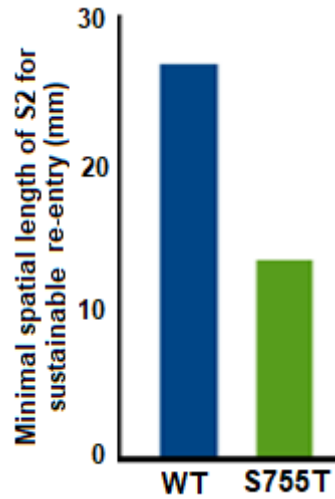


Figure 6.17: The minimal spatial length of the premature stimulus S2, that is sufficient to initiate re-entrant spiral waves in the WT (blue) and S755T (green) models.

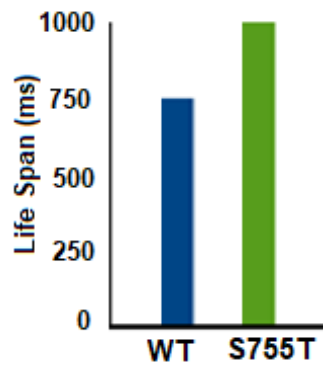


Figure 6.18: Total life span of the re-entrant excitation spiral wave in the 2D idealised tissue model for the WT (blue) and S755T/SQT6 (green) conditions, computed from Figure 6.16 (b, c).

The total life span of the re-entrant excitation wave for the WT condition was measured as 769 ms. For S755T, the re-entry sustained over the entire cycle of 1000 ms (Figure 6.18).

6.8 Phase Mapping of the Re-entrant Excitation Wave

Similar to Chapters 4 and 5, the phase mapping technique was applied for a clear identification of the Phase Singularity (PS) points in space over the entire cycle length investigated, for both the WT and S755T conditions. In the Figure 6.19, every phase point in the excitation recovery cycle is defined by a colour; the point where all the phases converged is defined as the Phase Singularity (PS) point. However, the surrounding regions displayed a continuous progression of phase that is equal to $\pm 2\pi$ around the PS point [26-29].

Phase mapping also allows for a closer look at the activation wave-front of the spiral wave evoked by the premature stimulus. It shows the wave front, wave tail, and the point at which wave-front meet the curved wave tail. The phase singularity point is represented by an asterisk in Figure 6.19. The trajectory of the spiral wave is defined by the rotor, i.e. when the rotor is stationary; it rotates and forms a circular trajectory. However, for a meandering rotor, a trajectory can be more complicated [26, 30]. The computed values for the v' and u' (origin points in phase space as explained in Chapter 3) under WT and S755T conditions were -37 mV and -48 mV.

The rotor tip and the core define the trajectory of the spiral wave in a 2D tissue. Their combination defines the pattern and the path followed by the excitation re-entrant wave in any medium, i.e. a flower-like pattern or a dragging episode. The tip trajectories for the WT and S755T mutation were computed by using the phase singularity method [26, 31] Figure 6.20 (ai, bi). For S755T condition, a drift can be seen in the tip of the spiral wave (Figure 6.20bi). The Figure 6.20bi illustrates a CCW rotating excitation wave perpendicular to the fibre orientation.

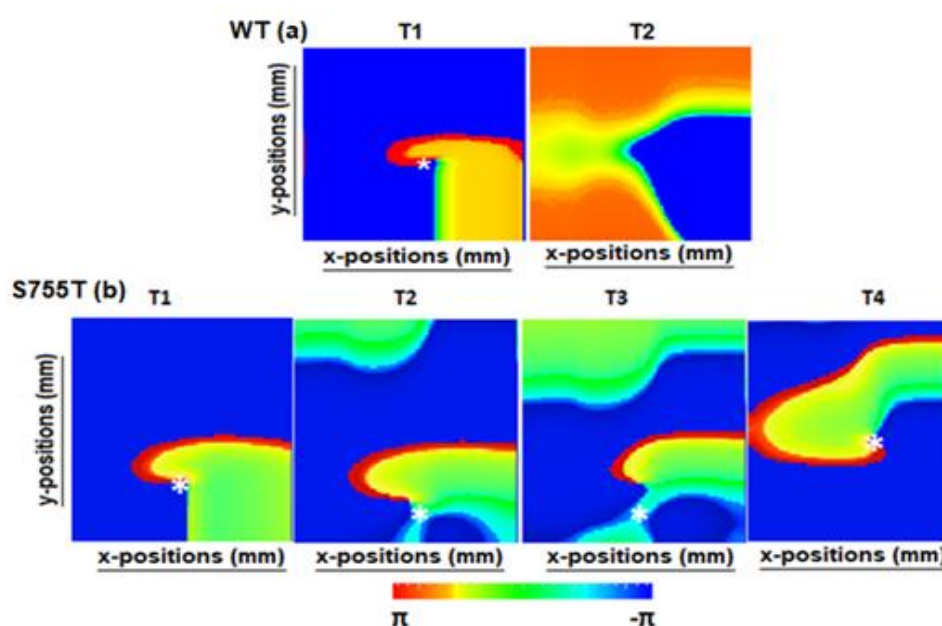


Figure 6.19: Phase mapping of the re-entrant excitation wave for the WT (a) and S755T (b) conditions. The layout of the 2D sheet is same as defined in Figure 6.16a. The white asterisk on the figures represents the phase singularity point where the wave tip meets the wave tail. The wave front represents the group of depolarised cells while the tail is composed of cells returning to rest. T1, T2, T3 and T4 are the time intervals at which the activity of the spiral wave was recorded. $\pm\pi$ represents the change in phase from $+\pi$ to $-\pi$ [31-34].

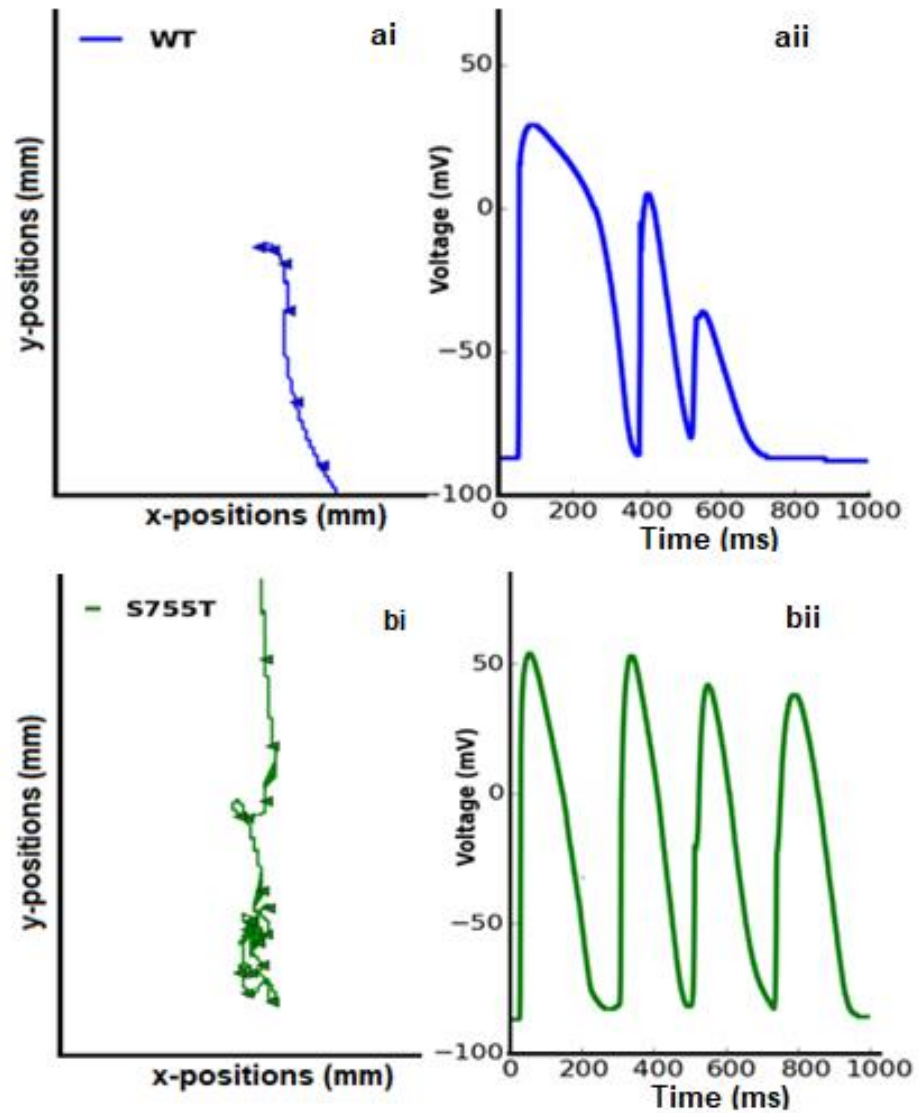


Figure 6.20: Behaviour of the re-entrant spiral wave in the 2D idealised tissue sheet for the WT and S755T models. The geometry of the 2D sheet is the same as described in Figure 6.16a. (ai, bi) The re-entrant wave tip trajectories for WT (blue) and S755T (green) in x and y space (mm) illustrate the path followed by the spiral wave in the 2D tissue sheet of the left ventricular cells. (aii, bii) The time course of localised electrical activity shows the total life span of the re-entrant wave in the 2D sheet for WT and S755T conditions.

The dominant frequencies for the WT and S755T were obtained by the power spectral density analysis (Appendix C) of the localised electrical activity, shown in the Figure 6.21.

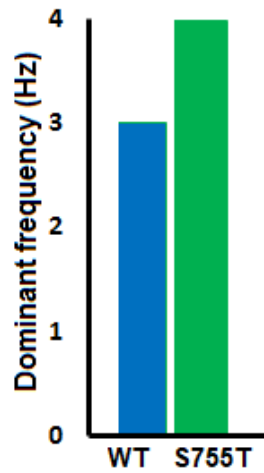


Figure 6.21: Dominant frequency values computed from the power spectral distribution function (Appendix C). The dominant frequency for the WT is 3.2 Hz and 4.0 Hz for the S755T model.

6.9 Summary

The major findings of the present study are:

- a) The CACNA2D1 $Ca_v\alpha_2\delta-1$ S755T mutation reduced the AP duration in all three cell types with a major attenuation in the middle cell and caused the shortening of QT interval on ECGs. A strong depression is very visible in the dome of the AP for all three cell types.
- b) The 1D model reproduced the Tall T-wave with a shorter than normal QT interval.
- c) A ST segment elevation was observed in the simulation, which was not found in short QT1-3 patients. The ST segment elevation was reproduced which depicts that SQT6 mutations are linked with Brugada syndromes [19, 20]. Although the elevation of ST segment was not very prominent i.e. $ST < 2$ mm, an elevated J-wave was observed in the 1D model, which depicts an early repolarisation pattern. Early repolarisation patterns associated with Brugada syndromes are seen in previous studies [34].
- d) A study by Yan and Antzelevitch has suggested that a decrease in the amplitude of AP dome of the EPI cell (as compared to the decrease in the amplitude of ENDO dome region) creates a transmural voltage gradient across the ventricular wall, which could elevate the ST segment [19, 20]. As illustrated in Figure 6.3, the difference in the amplitude of the EPI and ENDO dome regions is not very large, which may cause a very small elevation of the ST segment for S755T with respect to the WT baseline.

- e) The tissue's temporal vulnerability was increased for the S755T condition.
- f) In the 2D tissue, the minimal substrate size that is necessary to initiate and maintain the re-entry was decreased under the S755T condition.

These findings gave a clear link between the shortening of QT interval and SQT6 mutation. It gave a detailed explanation of the increased vulnerability to re-entry under the S755T CACNA2D1 condition.

6.10 References

- [1] C. Templin et al., “Identification of a novel loss-of-function calcium channel gene mutation in short QT syndrome (SQTS6),” *Eur. Heart J.*, vol. 32, no. 9, pp. 1077–1088, May 2011.
- [2] S. I. McDonough, *Calcium channel pharmacology*. Springer Science & Business Media, 2011.
- [3] T. O’Hara, L. Virág, A. Varró, and Y. Rudy, “Simulation of the undiseased human cardiac ventricular action potential: model formulation and experimental validation,” *PLoS Comput. Biol.*, vol. 7, no. 5, p. e1002061, May 2011.
- [4] C. Antzelevitch et al., “Loss-of-function mutations in the cardiac calcium channel underlie a new clinical entity characterized by ST-segment elevation, short QT intervals, and sudden cardiac death,” *Circulation*, vol. 115, no. 4, pp. 442–449, Jan. 2007.
- [5] I. Adeniran, A. El Harchi, J. C. Hancox, and H. Zhang, “Proarrhythmia in KCNJ2-linked short QT syndrome: insights from modelling,” *Cardiovasc. Res.*, vol. 94, no. 1, pp. 66–76, Apr. 2012.
- [6] H. Zhang and J. C. Hancox, “In silico study of action potential and QT interval shortening due to loss of inactivation of the cardiac rapid delayed rectifier potassium current,” *Biochem. Biophys. Res. Commun.*, vol. 322, no. 2, pp. 693–699, 2004.
- [7] I. Adeniran, J. C. Hancox, and H. Zhang, “In silico investigation of the short QT syndrome, using human ventricle models incorporating electromechanical coupling,” *Front. Physiol.*, vol. 4, pp.1-13, Jul. 2013.
- [8] C. Antzelevitch, “Cardiac repolarisation. The long and short of it,” *Eur. Eur. Pacing Arrhythm. Card. Electrophysiol. J. Work. Groups Card. Pacing Arrhythm. Card. Cell. Electrophysiol. Eur. Soc. Cardiol.*, vol. 7, no. Suppl 2, pp. 3–9, Sep. 2005.
- [9] K. Gima and Y. Rudy, “Ionic current basis of electrocardiographic waveforms a model study,” *Circ. Res.*, vol. 90, no. 8, pp. 889–896, May 2002.
- [10] C. Antzelevitch, “Heterogeneity and cardiac arrhythmias: An overview,” *Heart Rhythm Off. J. Heart Rhythm Soc.*, vol. 4, no. 7, pp. 964–972, Jul. 2007.
- [11] I. Gussak, P. Brugada, J. Brugada, C. Antzelevitch, M. Osbakken, and P. Bjerregaard, “ECG phenomenon of idiopathic and paradoxical short QT intervals,” *Card. Electrophysiol. Rev.*, vol. 6, no. 1–2, pp. 49–53, Feb. 2002.
- [12] I. Adeniran, *Modelling the short QT syndrome gene mutations: and their role in cardiac arrhythmogenesis*, 2014 edition. New York: Springer, 2014.
- [13] I. Adeniran, M. J. McPate, H. J. Witchel, J. C. Hancox, and H. Zhang, “Increased

- vulnerability of human ventricle to re-entrant excitation in hERG-linked variant 1 short QT syndrome,” *PLOS Comput. Biol.*, vol. 7, no. 12, p. e1002313, Dec. 2011.
- [14] P. Taggart et al., “Inhomogeneous transmural conduction during early ischaemia in patients with coronary artery disease,” *J. Mol. Cell. Cardiol.*, vol. 32, no. 4, pp. 621–630, Apr. 2000.
- [15] I. Gussak et al., “Idiopathic short QT interval: a new clinical syndrome?” *Cardiology*, vol. 94, no. 2, pp. 99–102, 2000.
- [16] A. A. M. Wilde et al., “Proposed diagnostic criteria for the Brugada syndrome,” *Circulation*, vol. 106, no. 19, pp. 2514–2519, Nov. 2002.
- [17] S. Ding et al., “Impact of early ST-segment changes on cardiac magnetic resonance-verified intramyocardial haemorrhage and microvascular obstruction in ST-elevation myocardial infarction patients,” *Medicine (Baltimore)*, vol. 94, no. 35, pp. 1-10, Sep. 2015.
- [18] R. Nijveldt et al., “Early electrocardiographic findings and MR imaging-verified microvascular injury and myocardial infarct size,” *JACC Cardiovasc. Imaging*, vol. 2, no. 10, pp. 1187–1194, 2009.
- [19] B. Benito et al., “Brugada Syndrome,” *Rev. Esp. Cardiol.*, vol. 62, no. 11, pp. 1297–1315, Jan. 2009.
- [20] G. X. Yan and C. Antzelevitch, “Cellular basis for the Brugada syndrome and other mechanisms of arrhythmogenesis associated with ST-segment elevation,” *Circulation*, vol. 100, no. 15, pp. 1660–1666, Oct. 1999.
- [21] C. Antzelevitch et al., “Brugada syndrome: report of the second consensus conference: endorsed by the Heart Rhythm Society and the European Heart Rhythm Association,” *Circulation*, vol. 111, no. 5, pp. 659–670, Feb. 2005.
- [22] H. Zhang, S. Kharche, A. V. Holden, and J. C. Hancox, “Repolarisation and vulnerability to re-entry in the human heart with short QT syndrome arising from KCNQ1 mutation—A simulation study,” *Prog. Biophys. Mol. Biol.*, vol. 96, no. 1–3, pp. 112–131, 2008.
- [23] R. Tung, M. E. Josephson, V. Reddy, M. R. Reynolds, and SMASH-VT Investigators, “Influence of clinical and procedural predictors on ventricular tachycardia ablation outcomes: an analysis from the substrate mapping and ablation in Sinus Rhythm to Halt Ventricular Tachycardia Trial (SMASH-VT),” *J. Cardiovasc. Electrophysiol.*, vol. 21, no. 7, pp. 799–803, Jul. 2010.
- [24] J. Bai, K. Wang, Q. Li, Y. Yuan, and H. Zhang, “Pro-arrhythmogenic effects of CACNA1C G1911R mutation in human ventricular tachycardia: insights from cardiac multi-scale models,” *Sci. Rep.*, vol. 6, p. 31262, Aug. 2016.

- [25] A. Xu and M. R. Guevara, "Two forms of spiral-wave reentry in an ionic model of ischemic ventricular myocardium," *Chaos Woodbury N*, vol. 8, no. 1, pp. 157–174, Mar. 1998.
- [26] S. V. Pandit and J. Jalife, "Rotors and the dynamics of cardiac fibrillation," *Circ. Res.*, vol. 112, no. 5, pp. 849–862, Mar. 2013.
- [27] R. A. Gray et al., "Nonstationary vortexlike re-entrant activity as a mechanism of polymorphic ventricular tachycardia in the isolated rabbit heart," *Circulation*, vol. 91, no. 9, pp. 2454–2469, May 1995.
- [28] R. A. Gray, A. M. Pertsov, and J. Jalife, "Spatial and temporal organization during cardiac fibrillation," *Nature*, vol. 392, no. 6671, pp. 75–78, Mar. 1998.
- [29] S. V. Pandit et al., "Mechanisms underlying the anti-fibrillatory action of hyperkalemia in Guinea pig hearts," *Biophys. J.*, vol. 98, no. 10, pp. 2091–2101, May 2010.
- [30] M.-A. Bray and J. P. Wikswo, "Use of topological charge to determine filament location and dynamics in a numerical model of scroll wave activity," *IEEE Trans. Biomed. Eng.*, vol. 49, no. 10, pp. 1086–1093, Oct. 2002.
- [31] A. M. Pertsov, J. M. Davidenko, R. Salomonsz, W. T. Baxter, and J. Jalife, "Spiral waves of excitation underlie re-entrant activity in isolated cardiac muscle.," *Circ. Res.*, vol. 72, no. 3, pp. 631–650, Mar. 1993.

CHAPTER 7

Electromechanical Cardiac Myocyte Model

7.1 Introduction

In the previous Chapters (4-6) the results were based purely on the electrophysiological behaviour of the O'Hara & Rudy model [1]. The results represented in Chapter 4-6 have described the localised electrical activity of the human left ventricular myocyte under control and SQTS conditions. These results have provided a path to examine the functional behaviour of the conduction of cardiac electrical excitation wave under control and SQTS conditions.

The previous studies [2, 3] have suggested that the repolarisation time can have a great impact on electromechanical coupling in the SQTS episodes. An electromechanically coupled model was utilised to interrogate the impact of the short QT syndrome on cardiac mechanical functionality.

7.2 Myofilament Model

In simulations, Rice et al.'s [4] myocyte contraction model (RMM) was utilised to illustrate the mechanical dynamics of cardiac myocyte. The mechanical contraction was based on the cross-bridge cycling model [2, 3]. The model was capable of reproducing a wide range of cardiac mechanical dynamics which includes:

- sarcomere length-steady state force relations;
- calcium-steady state force relations;
- calcium-steady state sarcomere length relations.

7.2.1 Electromechanical Modelling

The intracellular calcium concentration $[Ca^{2+}]_i$ and the Ca^{2+} handling dynamics related to it, are the key links to couple the electrophysiological model and the myofilament mechanics model (MM). The intracellular calcium $[Ca^{2+}]_i$ generated from the electrophysiological model serves as an input to trigger the mechanical model [1, 2, 3]. In the O'Hara & Rudy electrophysiological model, the concentration of myoplasmic calcium is computed using Equation 7.1 [1]:

$$\frac{d[Ca^{2+}]_i}{dt} = B_{cai} \left(- (I_{PCa} + I_{Cab} - 2.0 I_{NaCa_i}) \frac{A_{cap}}{2.0 F V_{myo}} - \frac{J_{up} V_{nsr}}{V_{myo}} + \frac{J_{diff.Ca} V_{ss}}{V_{myo}} \right) \quad (7.1)$$

To couple the electrophysiological model to the myofilament mechanics model, the change in the calcium to troponin binding from the mechanics model is added to the Equation 7.1, The myoplasmic calcium concentration for the electromechanical model can be written as:

$$\frac{d[Ca^{2+}]_i}{dt} = B_{cai} \left(- \left(I_{PCa} + I_{Cab} - 2.0 I_{NaCa_i} + \frac{I_{sac}}{3.0} \right) \frac{A_{cap}}{2.0 F V_{myo}} - \frac{J_{up} V_{nsr}}{V_{myo}} + \frac{J_{diff.Ca} V_{ss}}{V_{myo}} - \frac{TropToT_{dt}}{1000.0} \right) \quad (7.2)$$

TropToT illustrates the concentration of calcium linked to the troponin. To reproduce an effectively coupled electromechanical model of a human ventricular myocyte, all the relevant state variables along with equation 7.2 were added to the O'Hara & Rudy [1] model. The new model is based on a system of differential-algebraic equations (DAE) [4, 5]. Stretch activated channels were introduced in the model to investigate the effect of stretch on the mechanical systole for the WT and SQT mutation conditions.

7.2.2 Stretch-Activated Channel

Different categories [6-10] of stretch activated channels have been discovered in a wide range of cell types after stretch was first identified in chick skeleton muscles by Guharay and Sachs et al. [13, 25, and 26]. In a cardiac cell, different types of stretch-activated channels have been identified; i.e. Cl⁻-selective anion channels, ATP-sensitive potassium channels, non-selective cation channels and potassium-selective channels [6-12]. Stretch-activated channels are considered as a mechano-transducer of the mechano-electric feedback [14]. In cardiac tissue, many ionic channels have been identified [14-17] which are activated by the mechanical stretch. It is well established that the mechanical stretch can induce changes to the myocardial Ca²⁺ transient levels [14, 18], which have very strong links with the stretch-activated reforms in the contractile force and electrical activity [6]. An increase in the open probability of stretch-activated channels has been noticed as a response of mechanical stimulus, rather than the channel conductance [19]. The work done by Kelderman and Panfilov [20], Youm et al. [21], and Kohl and Sachs [19] formulated expression to describe stretch-activated channels:

$$I_{sac} = g_{sac} P_m (V_m E_{sac}) \quad (7.3)$$

where V_m is the membrane potential (mV), g_{sac} is the maximum membrane conductance ($\mu\text{S}/\text{cm}$), and E_{sac} is the reversal potential (mV). For an electromechanical model, the value of E_{sac} is typically 1 [23, 24]. The channel's open probability is defined as P_m and is described as [21, 22]:

$$P_m = \frac{1.0}{1 + e^{\left(\frac{\varepsilon + \varepsilon_{1/2}}{2}\right)/k_\varepsilon}} \quad (7.4)$$

k_ε is the activation slope, ε and $\varepsilon_{1/2}$ are the full and the half-activation strains [21, 22] respectively.

For this typical electromechanical model, ε has a strong dependence on the sarcomere length. There is enough evidence that the stretch-activated channels are not only permeable to Ca^{2+} , but are persistently cation selective, i.e. they are selective to other monovalent cations such as Na^+ and K^+ ; studies have suggested that in a few cases they are more selective to K^+ than Na^+ [25, 26]. In the electromechanical model, the values of P_{Ca} : P_{Na} : P_K were set to 1:1:1, where P_{Ca} , P_{Na} , and P_K represent the relative permeability of Ca^{2+} , Na^+ , and K^+ respectively.

7.2.3 Tissue Mechanics Model

In a tissue mechanics model, under the hypothetical network of the nonlinear finite element method, the boundary value problem is composed of three fundamental concepts [27, 28],

- a) Equations of motion,
- b) Constitutive relations,
- c) Kinematics.

The motion and deformation of the cardiac tissue is governed by the equations of the kinematics. These equations define the link between the displacement of the body and the strain field. The equations of the motion describe the fundamental laws of physics governing the motion of a continuum, while the constitutive relations describe the response of a particular material to an applied load [27, 28, 29].

Similar to the I. Aderinran et al. [3] model, the electromechanical cardiac tissue is modelled as an incompressible, inhomogeneous, anisotropic nonlinear material [3]. In this study, an active strain approach was adopted, as it does not require adjustment of the active forces produced by the single cell models to drive observed deformations in the cardiac tissue. The

two-field variational principle was used to formulate the potential energy, deformation vector \mathbf{u} and hydrostatic pressure p as the two fields [3, 29]. The total potential energy was formulated as:

$$\mathbf{\Pi}(\mathbf{u}, p) = \mathbf{\Pi}_{\text{int}}(\mathbf{u}, p) + \mathbf{\Pi}_{\text{ext}}(\mathbf{u}) \quad (7.5)$$

where $\mathbf{\Pi}(\mathbf{u}, p)$ is the total strain energy of the body, $\mathbf{\Pi}_{\text{int}}(\mathbf{u}, p)$ and $\mathbf{\Pi}_{\text{ext}}(\mathbf{u})$ are the internal and external potential energies representing that potential energy is linked to the external loading of the body. The deformation gradient (F) is an important quantity in nonlinear continuum mechanics, as it transforms elements from the undeformed configuration to the deformed configuration. Within the composition of the active strain, the deformation gradient F is disintegrated into two components, an active component and a passive component [3, 29]:

$$F = F_e F_o \quad (7.6)$$

where the active component F_o describes the micro-scale change in the length due to the active contraction and the passive component F_e describes the passive mechanical deformation caused by both the internal microscopic deformation and the external loads. The active component F_e is linked with the microscopic active strain through:

$$F_o = I + \eta \mathbf{f} \otimes \mathbf{f} \quad (7.7)$$

where I is the identity tensor, η is the active strain field that is dependent on the sarcomere length of the cells and \mathbf{f} is the fibre orientation. η can be defined as:

$$\eta = \frac{SL - SL_o}{SL_o} \quad (7.8)$$

where SL_o is the sarcomere length of a cell at rest.

Therefore, the passive (macroscopic) component F_e can be obtained from:

$$F_e = FF_o^{-1} \quad (7.9)$$

thus, the resultant Right Cauchy-Green strain tensor is given as:

$$C = F_e^T F_e \quad (7.10)$$

It quantifies the squared length of infinitesimal fibres in the deformed configuration.

7.2.4 Mechanical Feedback in the Electrophysiology Tissue Model

Monodomain equations are applied to define electrical activity in the electrophysiological tissue model explained in Chapter 3. The relation in Chapter 3 can be modified to account for the effect of deforming the tissue in terms of diffusion [30, 31]:

$$C_m \frac{dV}{dt} = -(I_{ion} + I_{stim}) + \nabla \cdot (D C^{-1} \nabla V) \quad (7.11)$$

where C_m is the cell capacitance per unit surface area, V_m is the membrane potential, I_{ion} is the total ionic currents, I_{stim} represents an externally applied stimulus current, D is the diffusion tensor governing the intercellular electrical coupling and C^{-1} represents the inverse of the right Cauchy-Green deformation tensor [30]. Based on this we can assume that the propagation of the electrical wave across the gap junctions in the deformed and non-deformed tissue is different [30].

7.3 Single Cell Electromechanical Simulations without Stretch- Activated Current I_{sac}

7.3.1 SQT Syndrome 4 \ Cav1.2 CACNA1C $\alpha 1$ A39V and G490R

Equation 7.2 and all the state variables defining the parameters of the myofilament [4, 28] model were added to the single cell O'Hara & Rudy [1] electrophysiological model to investigate the dynamics of the intracellular Ca^{2+} concentration, sarcomere length (SL) and the growth of the active force for an electromechanically coupled single cell model. The results were computed for both control and mutations (A39V and G490R).

As discussed earlier, the APD_{90} is abbreviated under A39V and G490R SQT4 mutation conditions. The extent of the AP abbreviation is different for A39V and G490R for different cell types as seen in Chapter 4. The human left ventricular single cell electromechanical model was able to reproduce the action potentials for LVEPI, LVMCELL and LVENDO cell types. The abbreviation of the AP under SQT4 A39V and G490R conditions is shown in Figure 7.1, LVEPI (Figure 7.1ai), LVMCELL (Figure 7.1bi), and LVENDO (Figure 7.1ci).

Consider Table 4.1, to compare the values of the AP reproduced by the pure electrophysiological model to the AP values obtained from the mechanically coupled single cell model in Table 7.1. The computed AP values for LVEPI and LVMCELL cell types indicate that the shortening of the AP for both models has no significant differences (less than 1%); although, the extent of the AP abbreviation for the LVENDO cell is different for both the models. For the LVENDO cell type the difference is quite significant; for the A39V condition the difference is 17.12% while this difference is 24% for the G490R SQT4 condition (Table 4.1 and Table 7.1),

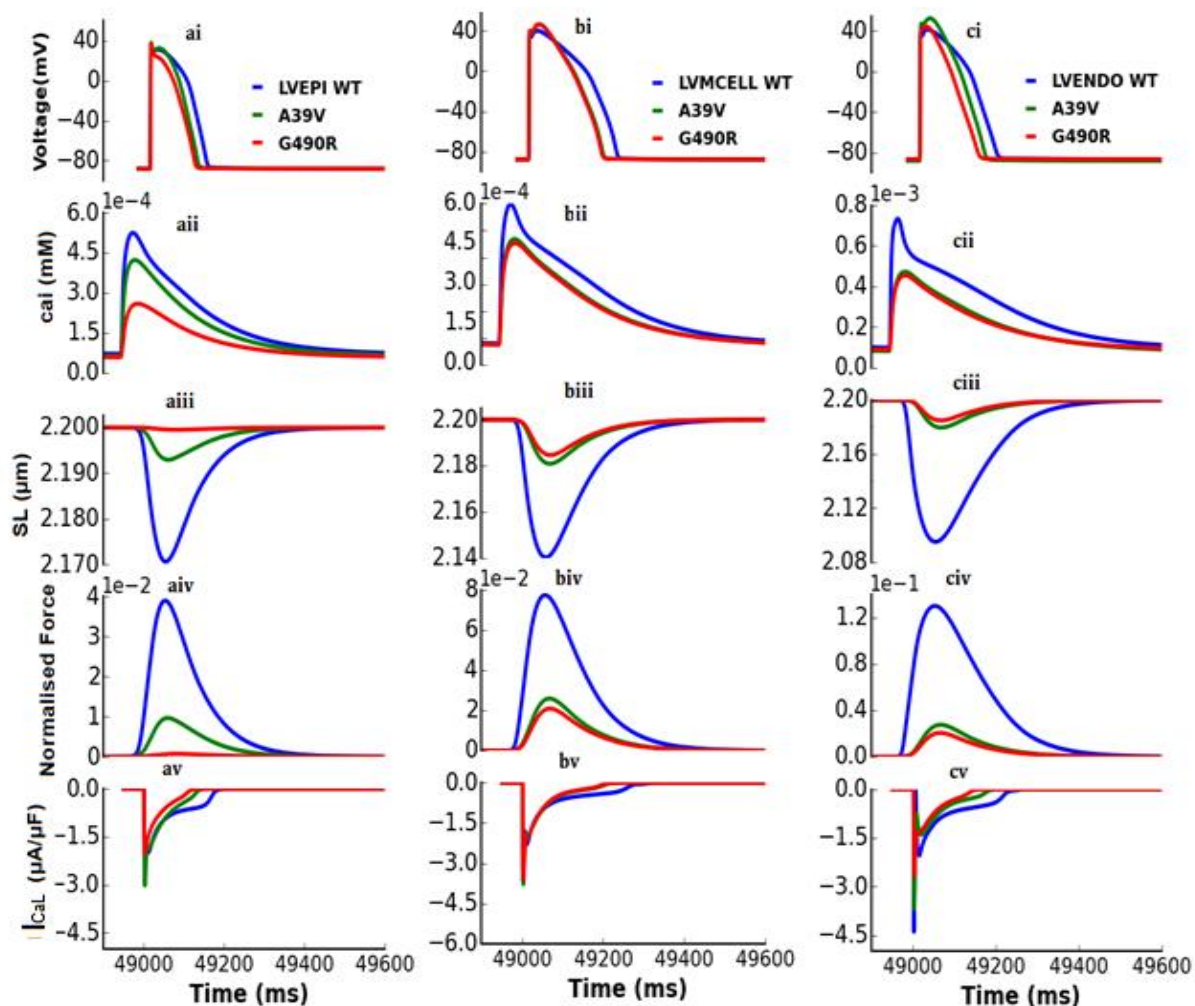


Figure 7.1: Simulated single cell electromechanical dynamics from the WT, A39V and G490R mutation models. The action potential was paced at a frequency of 1 Hz. (ai, bi, ci) The computed APD₉₀ for the 49th AP, the corresponding intracellular calcium concentration (Ca²⁺) (a_{ii}, b_{ii}, c_{ii}), the sarcomere length (a_{iii}, b_{iii}, c_{iii}), the normalised force (a_{iv}, b_{iv}, c_{iv}), and the time course of I_{CaL} (a_v, b_v, c_v) for the LVEPI, LVMCELL and LVENDO cell types under the WT (blue), A39V (green) and G490R (red) conditions.

	LVEPI (ms)		LVMCELL (ms)		LVENDO (ms)	
	EP	EM	EP	EM	EP	EM
WT	232	236	359	358	275	295
A39V	207	207	298	298	229	257
G490R	181	191	272	288	213	243

Table 7.1: The APD₉₀ values for the LVEPI, LVMCELL and LVENDO cell types obtained from the electrophysiological (EP) and the electromechanically (EM) coupled single cell models at a pacing frequency of 1 Hz.

At a pacing frequency of 1 Hz, the intracellular calcium concentration is lower in the A39V and G490R models as compared to the WT. Figure 7.1 (a_{ii}, b_{ii}, c_{ii}) shows that intracellular calcium activity was reduced by ~22% in LVEPI and by ~41% in the LVENDO cells for A39V, while the C_{ai} reduction was ~53% and ~42% for the G490R condition in the LVEPI and LVENDO cells respectively. The abbreviation of intracellular calcium concentration was ~32% in the LVMCELL for the A39V and G490R mutation conditions respectively (Figure 7.1b_{ii}). The initial sarcomere length was set to 2.2 μm for all cell types under the WT, A39V and G490R conditions (Figure 7.1 a_{iii}, b_{iii}, c_{iii}). The minimum contracted sarcomere length (SL) in the WT condition was ~2.17 μm (LVEPI), ~2.14 μm (LVMCELL), and ~2.10 μm (LVENDO). For A39V the SL was reduced to ~2.19 μm (LVEPI), ~2.18 μm (LVMCELL), and ~2.18 μm (LVENDO) respectively. Under the G490R condition the reduction was computed as ~2.2 μm (LVEPI), ~2.19 μm (LVMCELL), and ~2.19 μm (LVENDO), Figure 7.1 (a_{iii}, b_{iii}, c_{iii}) for LVEPI, LVMCELL and LVENDO respectively.

For both A39V and G490R the reduction in the intracellular calcium concentration was produced by a reduction in the contractile force which can be seen in Figure 7.1 (a_{iv}, b_{iv}, c_{iv}). The sarcomere length is dependent on the contraction force i.e. the greater the force of contraction, the smaller is the sarcomere length [2, 3, 4].

Table 7.2 contains a detailed summary of all the relevant results.

SL (μm)				Normalised force (%)		
	LVEPI	LVMCELL	LVENDO	LVEPI	LVMCELL	LVENDO
WT	2.17	2.14	2.10	100	100	100
A39V	2.19	2.18	2.18	28	30	20
G490R	2.20	2.19	2.19	3	25	18

Table 7.2: Computed minimal contracted sarcomere length from the WT, A39V and G490R models and the consequent normalised force relative to WT at the pacing frequency of 1 Hz. The initial sarcomere length was set to 2.2 μm . The smaller the sarcomere length, the greater is the force of contraction.

7.3.2 CACNB2b β 2 SQT5/S481L

The S481L SQT5 mutation reduced the calcium concentration in all cell types (Figure 7.2 aii, bii, cii). Results have suggested that the intracellular calcium transient was reduced by ~45% in the LVEPI and LVENDO cell types, while the abbreviation of intracellular calcium concentration was 54% in the LVMCELL under the SQT5 mutation condition respectively (Figure 7.2 aii, bii, cii). The initial sarcomere length was set to 2.20 μm for LVEPI, LVMCELL and LVENDO cell types for the WT and S481L conditions (Figure 7.2 aiii, biii, ciii). The minimum contracted sarcomere length (SL) under the WT was ~2.08 μm for LVEPI, ~2.11 μm for LVMCELL and ~2.07 μm for LVENDO cell types. For S481L the SL was ~2.19 μm for LVEPI, ~2.18 μm for LVMCELL and ~2.19 μm for the LVENDO cell types respectively. The intracellular calcium concentration reduction was associated with the abbreviation of the contractile force which can be seen in Figure 7.2 (aiv, biv, civ).

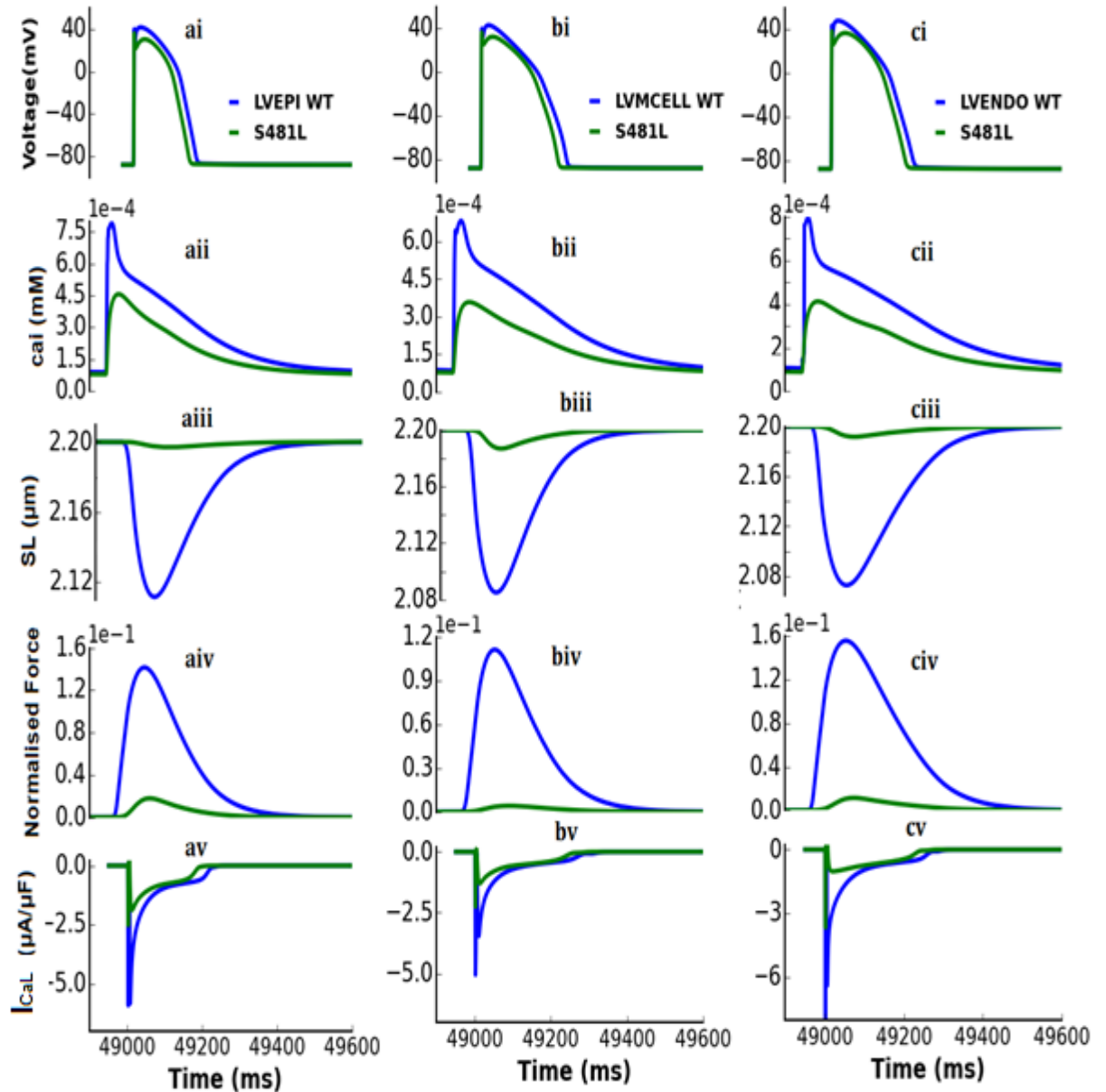


Figure 7.2: Simulated single cell electromechanical dynamics from the CANCB2b $\beta 2$ WT and S481L models. The action potential was paced at a frequency of 1 Hz. (ai, bi, ci) The computed APD₉₀ for the 49th AP, the corresponding intracellular calcium concentration (Ca^{2+}) (aii, bii, cii), the sarcomere length (aiii, biii, ciii), the normalised force (aiv, biv, civ), and the time course of I_{CaL} (av, bv, cv) for the LVEPI, LVMCELL and LVENDO cell types with the WT (blue) and S481L (green) conditions.

	SL (μm)			Normalised force (%)		
	LVEPI	LVMCELL	LVENDO	LVEPI	LVMCELL	LVENDO
WT	2.08	2.115	2.075	100	100	100
S481L	2.19	2.18	2.19	12	5	10

Table 7.3: Computed minimal contracted sarcomere length from the WT and S481L models and the consequent normalised force relative to the WT at the pacing frequency of 1 Hz. The initial sarcomere length was set to 2.2 μm . The smaller the sarcomere length, the greater is the force of contraction.

7.3.3 CACNA2D1 $\alpha 2\delta$ -1 SQT6/S755T

The SQT6 electrophysiological model was incorporated with the electromechanical model [1, 4, 30] to see the effects of mutation on the mechanical dynamics of a single cell. A reduction can be seen in the calcium concentration in all cell types under the S755T mutation conditions (Figure 7.3 aii, bii, cii). Results have suggested an abbreviation of $\sim 35\%$ for LVEPI and $\sim 40\%$ for LVENDO cells, while the abbreviation of the intracellular calcium concentration was $\sim 36\%$ for the LVMCELL. The initial length of the sarcomere was set to 2.20 μm for LVEPI, LVMCELL and LVENDO cell types for the WT and S755T conditions (Figure 7.3 aiii, biii, ciii). The minimum contracted sarcomere length (SL) for the WT condition was $\sim 2.15 \mu\text{m}$, $\sim 2.15 \mu\text{m}$, and $\sim 2.16 \mu\text{m}$ for LVEPI, LVMCELL and LVENDO respectively. For the S755T mutation the SL was 2.18 μm , and 2.19 μm for LVEPI, LVMCELL and LVENDO respectively. Results suggested a marked reduction in the intracellular calcium concentration (7.3 aii, bii, cii) which resulted in a reduction of contractility, Figure 7.3 (aiv, biv, civ).

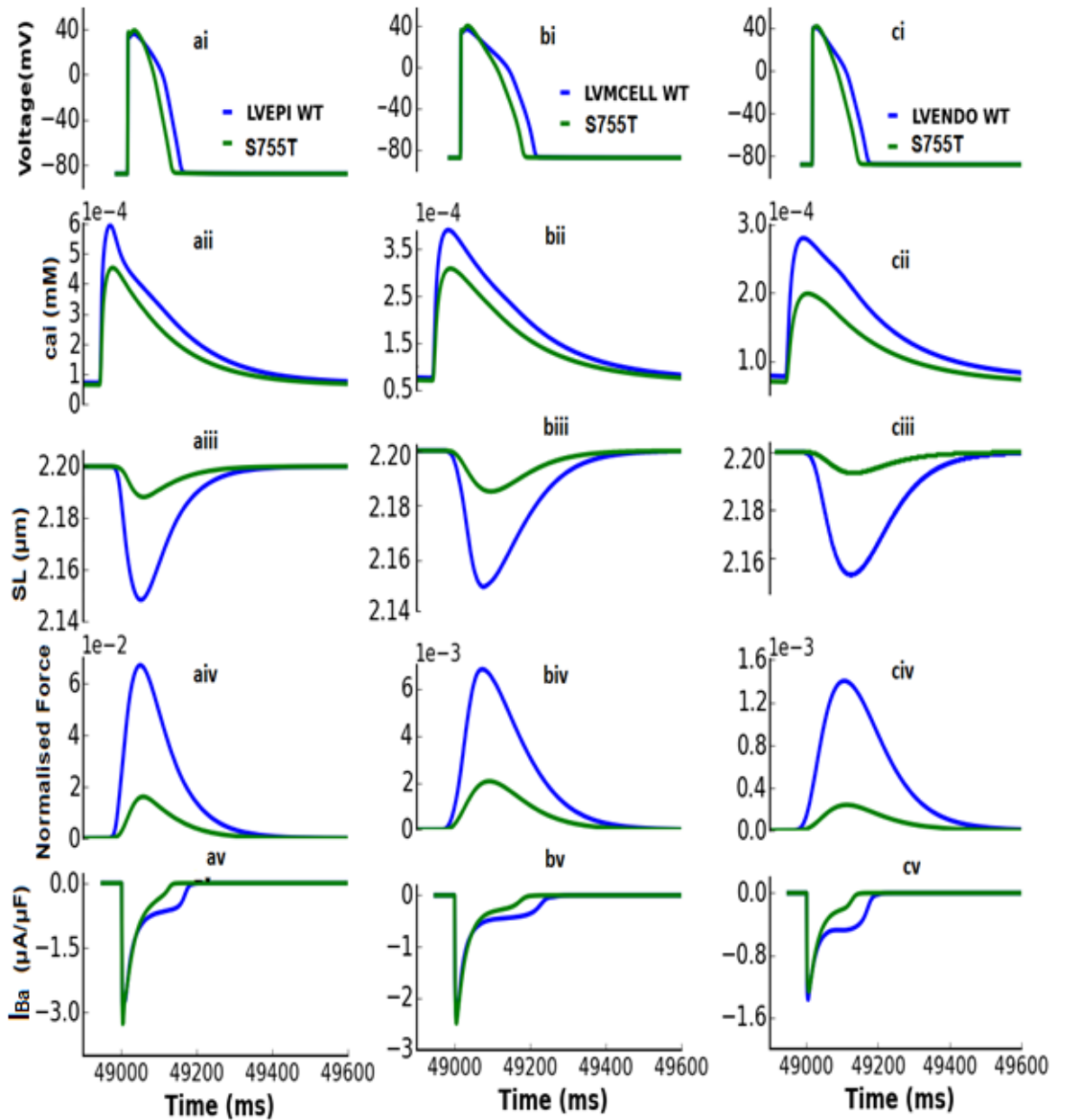


Figure 7.3: Simulated single cell electromechanical dynamics from the WT and S755T models. The action potential was paced at a frequency of 1 Hz. (ai, bi, ci) The computed APD₉₀ for the 49th AP, the corresponding intracellular calcium concentration (Ca²⁺) (aii, bii, cii), the sarcomere length (aiii, biii, ciii), the normalised force (aiv, biv, civ), and the time course of I_{Ba} (av, bv, cv) for the LVEPI, LVMCELL and LVENDO cell types with the WT (blue) and S755T (green) conditions.

SL (μm)			Normalised force (%)			
	LVEPI	LVMCELL	LVENDO	LVEPI	LVMCELL	LVENDO
WT	2.15	2.15	2.16	100	100	100
S755T	2.19	2.18	2.19	24	26	17

Table 7.4: The computed minimal contracted sarcomere length from the WT and S755T models and the consequent normalised force relative to the WT at the pacing frequency of 1 Hz. The initial sarcomere length was set to 2.2 μm . The smaller the sarcomere length, the greater was the force of contraction.

7.4 Single Cell Electromechanical Dynamics with Stretch Activated Channels

To investigate the effects of stretch-activated channels, equation 7.3 was incorporated into the electromechanically coupled [4, 30] model. APD₉₀ values for LVEPI, LVMCELL and LVENDO cells were obtained from an EM coupled model for SQT4-SQT6 with the stretch given in Tables 7.5, 7.7, and 7.9.

APs and intracellular Ca²⁺ transients are inter-related; all mechanisms which can increase the amplitude of Ca²⁺ transients would have a sensitive impact on the shape of APs. This phenomenon is strongly dependent on the initial length of the AP [32]. This has suggested that activation of the same Ca²⁺ pathway has a different impact on AP for the different types of myocytes [33]. Incorporation of I_{sac} (at the permeability of P_{Na}: P_{Ca}: P_K =1:1:1) has resulted in the lengthening of the AP in all three cell types for the WT and mutation conditions, which has also been observed in previous studies [2, 3, 34, and 35]. Results have suggested that the changes in AP can be linked to the inward Ca²⁺ current. The exchanger current I_{NaCa} is dependent on the inward [Ca²⁺]_i, and I_{NaCa} is also suggested to couple these two cellular events [3, 35]. This complex relation between the action potential and Ca²⁺ transients makes it difficult to describe these cellular events induced by mechanical stretch.

7.4.1 SQT4

The following results have been obtained by incorporating I_{sac} to the SQT4 single cell electromechanical model;

- a) An increased amplitude of the intracellular Ca²⁺ concentration (Figure 7.4 aii, bii,

cii),

b) An increased sarcomere length shortening (Figure 7.4 aiii, biii, ciii),

c) An increased active force of contraction (Figure 7.4 aiv, biv, civ).

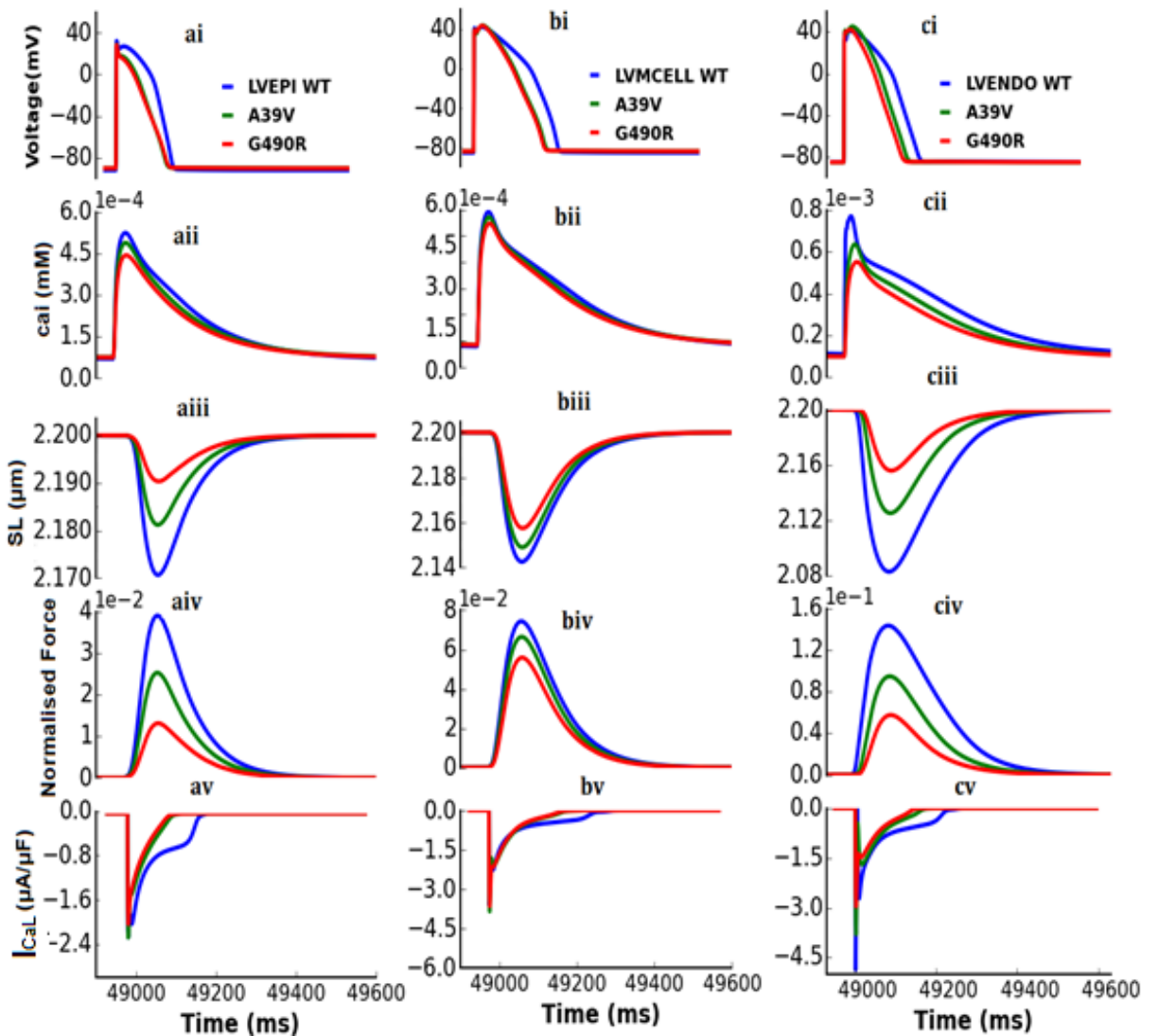


Figure 7.4: The role of the I_{sac} on the dynamics of the SQT4 electromechanical single cell model. The action potentials were paced at a frequency of 1 Hz. (ai, bi, ci) The computed APD₉₀ for the 49th AP, the corresponding intracellular calcium concentration (Ca^{2+}) (aii, bii, cii), the sarcomere length (aiii, biii, ciii), the normalised force (aiv, biv, civ), and the time course of I_{Ca} (av, bv, cv) for the LVEPI, LVMCELL and LVENDO cell types under the WT (blue), A39V (green) and G490R (red) conditions.

Tables 7.5-7.6 give a quantitative comparison of the action potentials, SL shortening, and increased active force respectively.

	LVEPI (ms)	LVMCELL (ms)	LVENDO (ms)
WT	245	366	275
A39V	229	311	257
G490R	216	298	223

Table 7.5: Changes in the APD₉₀ (ms) with the incorporation of the I_{sac}. At the pacing frequency of 1 Hz, the APD₉₀ is computed for the 49th AP with the WT, A39V and G490R models. The incorporation of I_{sac} increased the AP duration in all three cell types as compared to the EM cell model without the consideration of stretch (Table 7.1).

	SL (μm)	LVEPI (μm)	LVMCELL (μm)	LVENDO (μm)	Normalised Force (%)	LVEPI (%)	LVMCELL (%)	LVENDO (%)
WT		2.17	2.14	2.09		100	100	100
A39V	2.18	2.15	2.13	58	85	59		
G490R	2.18	2.16	2.16	26	75	35		

Table 7.6: Role of I_{sac} on the minimal contracted sarcomere length and the corresponding normalised force. At the pacing frequency of 1 Hz, the minimal length of the contracted sarcomere and the normalised force were computed for the WT, A39V and G490R conditions with the consideration of stretch activated current (I_{sac}). The initial sarcomere length is 2.2 μm. The smaller the sarcomere length, the greater is the force of contraction.

7.4.2 SQT5

The following results have been obtained by incorporating I_{sac} into the SQT5 single cell models;

- a) An increased amplitude of the intracellular Ca²⁺ concentration (Figure 7.5 aii, bii, cii),
- b) An increased shortening of the sarcomere length (Figure 7.5 aiii, biii, ciii),

c) An increased active force of contraction (Figure 7.5 aiv, biv, civ).

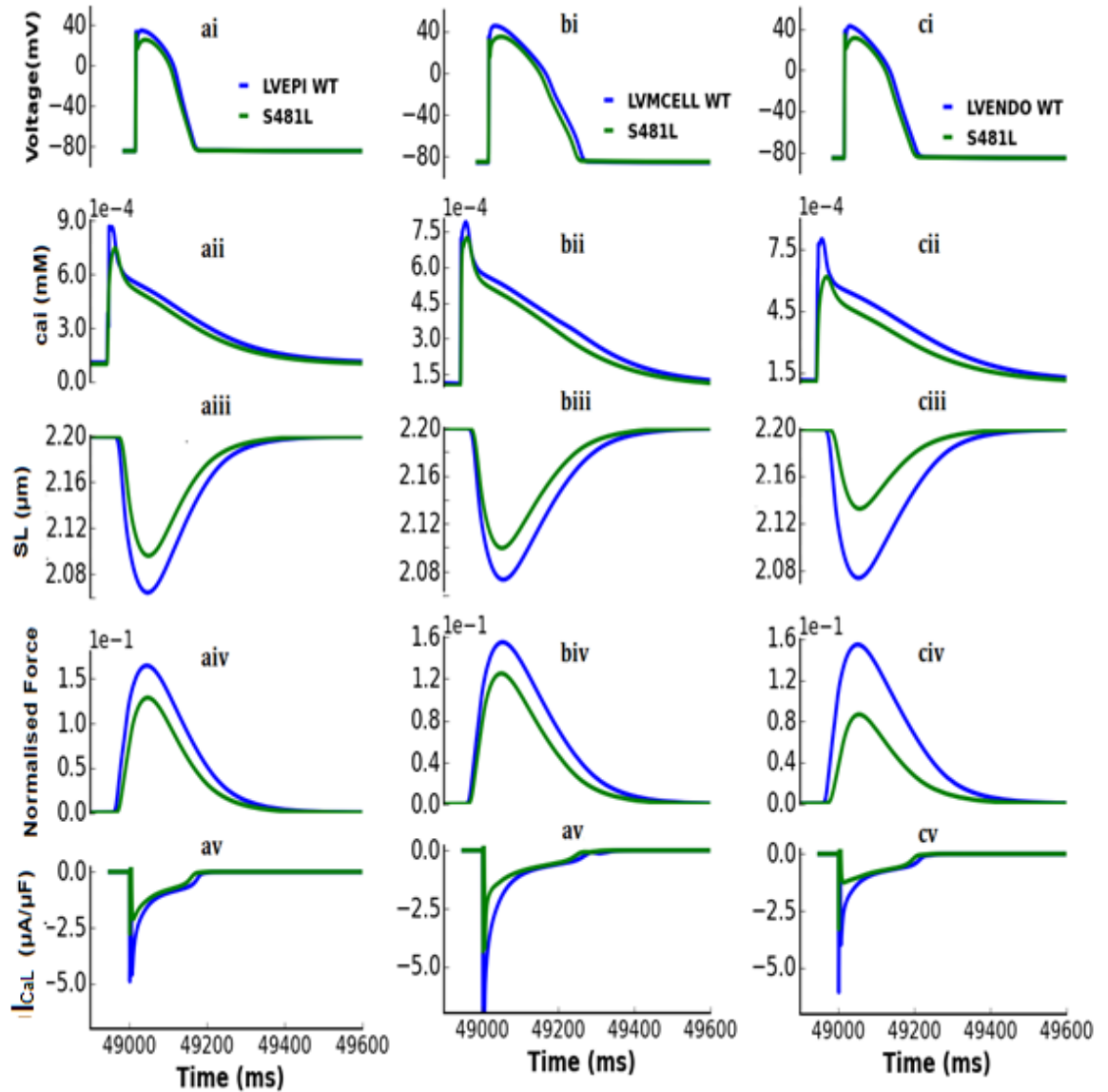


Figure 7.5: The role of I_{sac} on the dynamics of the SQT5 electromechanical single cell model. The action potential was paced at a frequency of 1 Hz. (ai, bi, ci) The computed APD_{90} for the 49th AP, the corresponding intracellular calcium concentration (Ca^{2+}) (aii, bii, cii), the sarcomere length (aiii, biii, ciii), the normalised force (aiv, biv, civ), and the time course of I_{Ca} (av, bv, cv) for the LVEPI, LVMCELL and LVENDO cell types with WT (blue) and S481L (green) models.

Tables 7.7-7.8 give the quantitative values of the action potentials, SL shortening, and active force respectively.

	LVEPI (ms)	LVMCELL (ms)	LVENDO (ms)
WT	245	367	269
S481L	237	346	250

Table 7.7: Changes in the APD₉₀ due to the I_{sac}. At 1 Hz the APD₉₀ is computed for the 49th AP with the WT and S481L models. The incorporation of stretch activated current (I_{sac}) increased the AP duration in all three cell types.

	SL (μm)	LVEPI (μm)	LVMCELL (μm)	LVENDO (μm)	Normalised Force (%)	LVEPI (%)	LVMCELL (%)	LVENDO (%)
WT		2.07	2.08	2.07		100	100	100
S481L	2.16	2.10	2.14	71	75	50		

Table 7.8: The role of the I_{sac} on the minimal contracted sarcomere length and the corresponding normalised force. At the pacing frequency of 1 Hz, the minimal length of the contracted sarcomere and the normalised force were computed for the WT and S481L conditions with the consideration of stretch activated current (I_{sac}). The initial sarcomere length is 2.2 μm. The smaller the sarcomere length, the greater is the force of contraction.

7.4.3 SQT6

The following results have been obtained by incorporating I_{sac} into the SQT6 single cell models;

- a) An increased amplitude of the intracellular Ca²⁺ concentration (Figure 7.6 aii, bii, cii),
- b) An increased sarcomere length shortening (Figure 7.6 aiii, biii, ciii),
- c) An increased active force of contraction (Figure 7.6 aiv, biv, civ).

Tables 7.9-7.10 give the quantitative values of AP, SL shortening, and increased active force respectively.

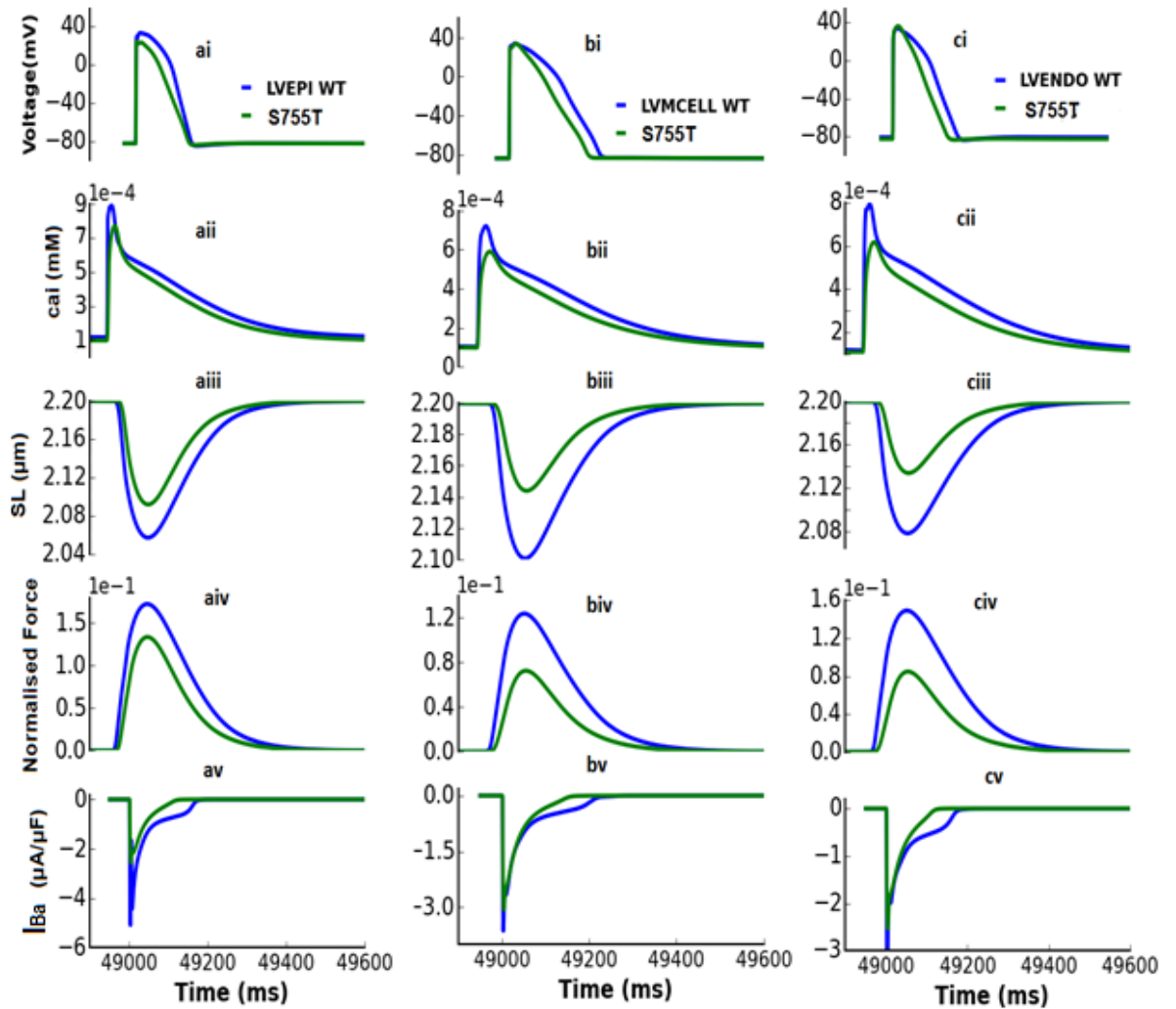


Figure 7.6: Role of the I_{sac} on the dynamics of WT and S755T variant of CACNA2D1 electromechanical single cell model. Action potential was generated by pacing the model at 1 Hz. (ai, bi, ci) The computed APD₉₀ for the 49th AP, the corresponding intracellular calcium concentration (Ca^{2+}) (aii, bii, cii), the sarcomere length (aiii, biii, ciii), the normalised force (aiv, biv, civ), and the time course of I_{Ba} (av, bv, cv) for the LVEPI, LVMCELL and LVENDO cell types under WT (blue) and S755T (green) conditions.

	LVEPI (ms)	LVMCELL (ms)	LVENDO (ms)
WT	313	412	368
S755T	299	376	326

Table 7.9: Changes in the APD₉₀ due to the I_{sac} . At 1 Hz the APD₉₀ was computed for the 49th AP with the WT and S755T models. The incorporation of stretch activated current increased the AP duration in all three cell types.

	SL (μm)	LVEPI	LVMCELL	LVENDO	Normalised Force (%)	LVEPI	LVMCELL	LVENDO
		(μm)	(μm)	(μm)		(%)	(%)	(%)
WT		2.06	2.10	2.08		100	100	100
S755T		2.09	2.14	2.14		73	61	53

Table 7.10: Role of I_{sac} on the minimal contracted sarcomere length and the corresponding normalised force. At the pacing frequency of 1 Hz, the minimal length of the contracted sarcomere and the normalised force were computed for the WT and S755T conditions with the consideration of stretch activated current (I_{sac}). The initial sarcomere length was 2.2 μm . The smaller the sarcomere length, the greater was the force of contraction.

7.5 Tissue Simulations

7.5.1 Re-entrant Excitation Wave Dynamics in a 2D Electromechanical Tissue Model

To investigate the dynamics of re-entrant excitation waves and the minimal substrate size to initiate and sustain re-entry in SQT4, SQT5, and SQT6 electromechanical models, a 2D transmural, idealised electromechanical sheet of the left ventricular ENDO, MCELL and EPI cells was created.

The S1S2 protocol was utilised to initiate the re-entry into the 2D electromechanical model; an excitation wave was evoked by applying a train of 10 S1 stimuli paced at 1 Hz at the ENDO end of the 2D sheet. The excitation wave generated by S1 propagates from the ENDO end to the EPI end of the 2D tissue sheet for the WT (Figure 7.7a) and (Figure 7.7 b-e) mutation conditions (SQT4, SQT5, and SQT6). A second premature stimulus (S2) was applied after a time delay. S2 was applied to a localised region in EPI region within its VW. The excitation wave evoked by S2 was blocked by an unrecovered middle region, as the MCELL region was still refractory due to the slower repolarisation comparative to the ENDO and EPI regions. Hence, this gave rise to a unidirectional conduction towards the EPI side. This unidirectional block evoked spiral re-entrant excitation waves in the WT (Figure 7.7) SQT4, SQT5, and SQT6 conditions. Results described for the pure electrophysiological

model have suggested that re-entry was terminated in the WT, while it was sustained for the mutation condition (SQT4, SQT5, and SQT6).

In an electromechanically coupled 2D model, for the WT condition, the spiral re-entrant wave was terminated after 660 ms (within 340 ms after its initiation) while it was sustained for a longer duration in a pure electrophysiological model; i.e. it was terminated after 851 ms, 851 ms, and 855 ms for the control variants of CACNA1C, CACNB2b, and CACNA2D1 calcium channels respectively. For A39V SQT4 S2 was applied after a time delay of 275 ms; S2 was applied at 236 ms for the A39V electrophysiological tissue model, which indicates that there are longer AP lengths in mechanically coupled tissue models. As discussed earlier, the re-entrant wave was sustained in the A39V electrophysiological 2D tissue model (Chapter 4). In an electromechanically coupled model re-entry was terminated after 675 ms (within 400 ms of its initiation) (Figure 7.7c). For G490R the S2 was applied after a time delay of 270 ms; the excitation-re-entrant wave was terminated after 688 ms, and it was sustained for 418 ms in an electromechanically coupled 2D sheet (Figure 7.7d). For S481L the re-entrant wave was terminated within 370 ms after the time of its initiation. For SQT6 S755T re-entry was sustained over a span of 490 ms, which is 330 ms shorter than the electrophysiological tissue model. Although the difference between the time spans of re-entrant waves is not very significant in the WT and mutation conditions, the life span of the re-entrant wave is still shortest for the WT electromechanical 2D tissue model.

The length of the S2 is very important for the generation of the spiral re-entrant excitation waves. The minimal tissue substrate length which is necessary to initiate and maintain re-entry was measured for the WT and mutation conditions. The minimal substrate length for the WT was measured as 30 mm; for A39V and G490R the minimal substrate lengths to initiate re-entry were 26 mm and 28 mm respectively. For SQT5 S481L it was 28 mm while the length of the substrate to initiate re-entry for SQT6 S755T was 27 mm. Results have suggested that the length of substrate to induce re-entry into the WT was almost the same for both the electrophysiological and electromechanical 2D tissue models. However, a much larger sized substrate is needed to trigger re-entry into the SQTs electromechanical tissue sheets (Figure 7.7).

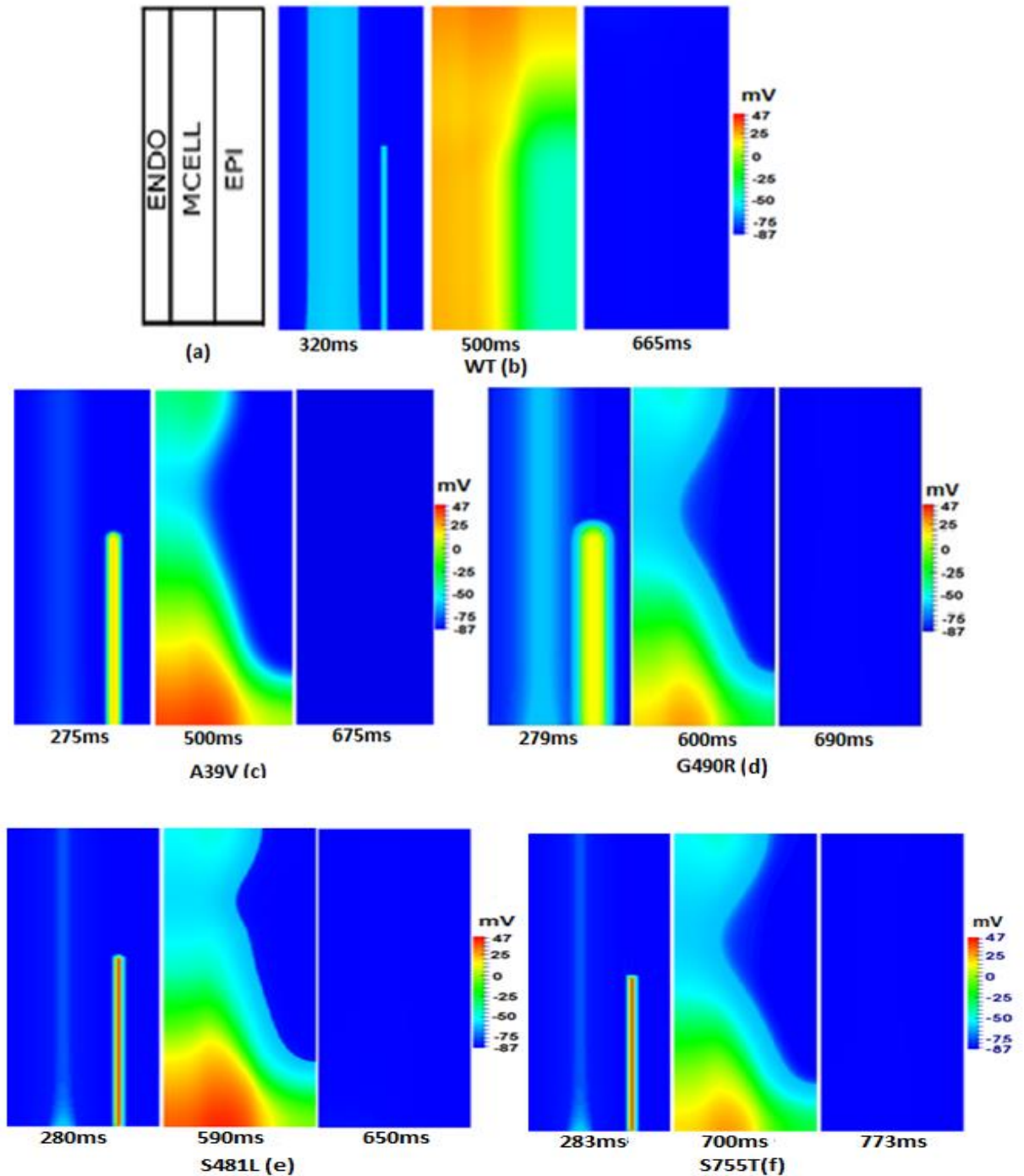


Figure 7.7: Snapshots of the initiation and conduction of the re-entrant excitation waves in a 2D idealised tissue model of the left ventricular cells. The geometry of the 2D sheet (a) is the same as described for the 2D idealised electrophysiological model. (b, c, d, e, f) A spiral wave was developed by applying the S2 stimulus during the VW of the LVEPI region for the WT and mutations (S2 was applied at 380 ms, 275 ms, 279 ms, 280 ms and 283 ms for WT, A39V, G490R, S481L and S755T conditions). In the electromechanically coupled model, the spiral wave initiated by S2 was terminated in all conditions before 800 ms.

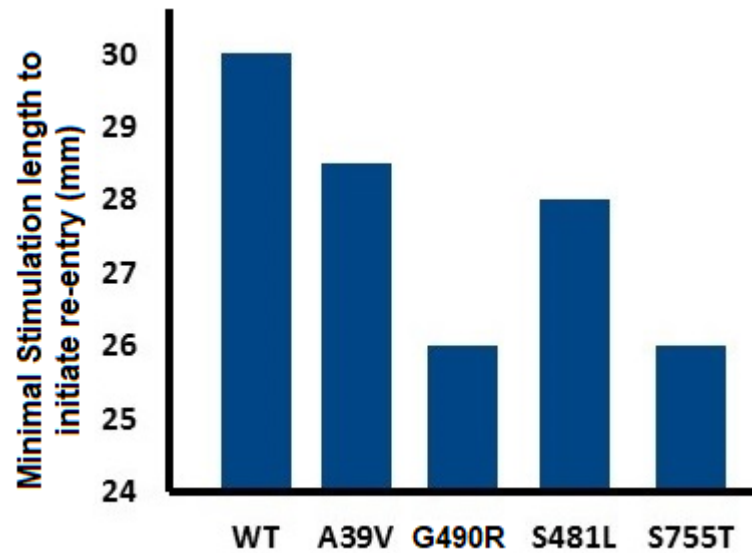


Figure 7.8: Minimal length of the S2 stimulus necessary to initiate re-entry in the 2D electromechanical tissue models of the WT, A39V, G490R, S481L and S755T.

7.5.2 3D Electromechanical Consequences of SQT Syndromes

Structural heart diseases, electrical disorders, non-cardiac diseases, and metabolic disorders are considered to be the most common causes of sudden cardiac deaths (SCD). The remaining cases were considered as idiopathic disease [36, 37]. These idiopathic cases have been reduced to a large extent with the invention of several complex molecular mechanisms that can generate potentially life-threatening arrhythmias. SQTs patients have a high risk of sudden cardiac death (SCD) [40]. A reduced or enlarged ejection fraction can be a criterion to diagnose therapies for patients with a risk of heart failure [38]. An ejection fraction of 50% to 75% is considered normal for LV, while for the RV between 45% and 55% is considered normal [39, 40].

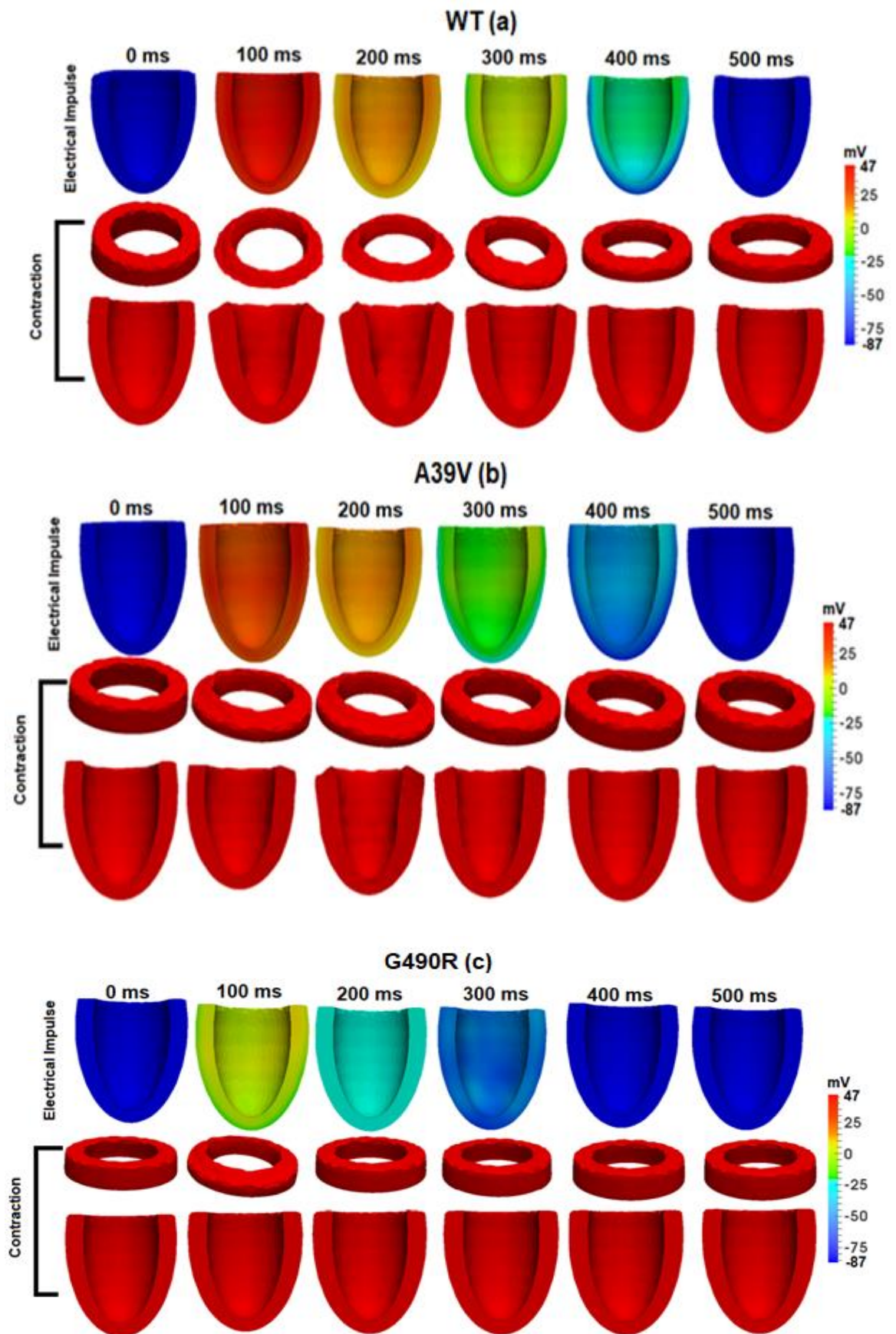
In this section a three-dimensional (3D) left ventricular tissue model [2, 4, 30] has been utilised to examine the impact of short QT syndrome on the mechanical systole and ejection fraction.

To compare the reduction in contractility under the WT and SQT mutation conditions, a truncated ellipsoids geometry for the left ventricular (LV) has been used for the 3D simulations in this section. The left ventricle is geometrically segmented into three explicit regions, endocardial (60%), central (30%) and epicardial (10%) regions. The proportion of cells selected for each region reflects the experimental data for cells spanning the left

ventricular wall of the human heart [46]. Although the existence and functionality of MCELLs in the human heart is controversial [47], we included MCELLs in our model based on the studies of Li et al., [48] that demonstrate their existence in cells isolated from the right ventricle of the patients with heart failure, and a study by Drouin et al., [46] which give proof of their existence in a perfused piece of left ventricular wall. The conditional activation sites were empirically determined across the ventricle wall and were validated by reproducing the activation sequence and QRS complex as measured in the 64-channel ECG of a 34 years old healthy male [49].

Figure 7.9 illustrates the incorporation of the single cell WT and SQTs electromechanical models into a three-dimensional truncated ellipsoid representation of LV. The changes in the ejection fraction due to the reduced contractility of left ventricular for SQTs models are shown in Figure 7.10. The ejection fraction is calculated as the stroke volume (mL) divided by the end-diastolic volume (mL) [41, 42].

In simulation at 0ms, the LV is at rest before the activation. At about 100 ms, the LV was completely activated for the WT and A39V models, but the depolarisation process has already begun for the G490R, S481L and S755T conditions. This electrical impulse is followed by the contraction in the WT, A39V, G490R, S481L and S755T conditions. By 200 ms, repolarisation has started in the LV under all conditions, and LV was undergoing relaxation. By 425 ms, repolarisation and relaxation were completed in the WT model, however, the repolarisation and relaxation timing are reduced under the mutation conditions as compared to the WT (Figure 7.9). These simulation results can account for a loss of cardiac contractility and a reduced left ventricular Ejection Fraction (at the 3D organ level Figure 7.10) in the short QT syndrome conditions. Few experimental results have suggested that the shortening of the action potential duration may result in a reduction in contractility [42, 43].



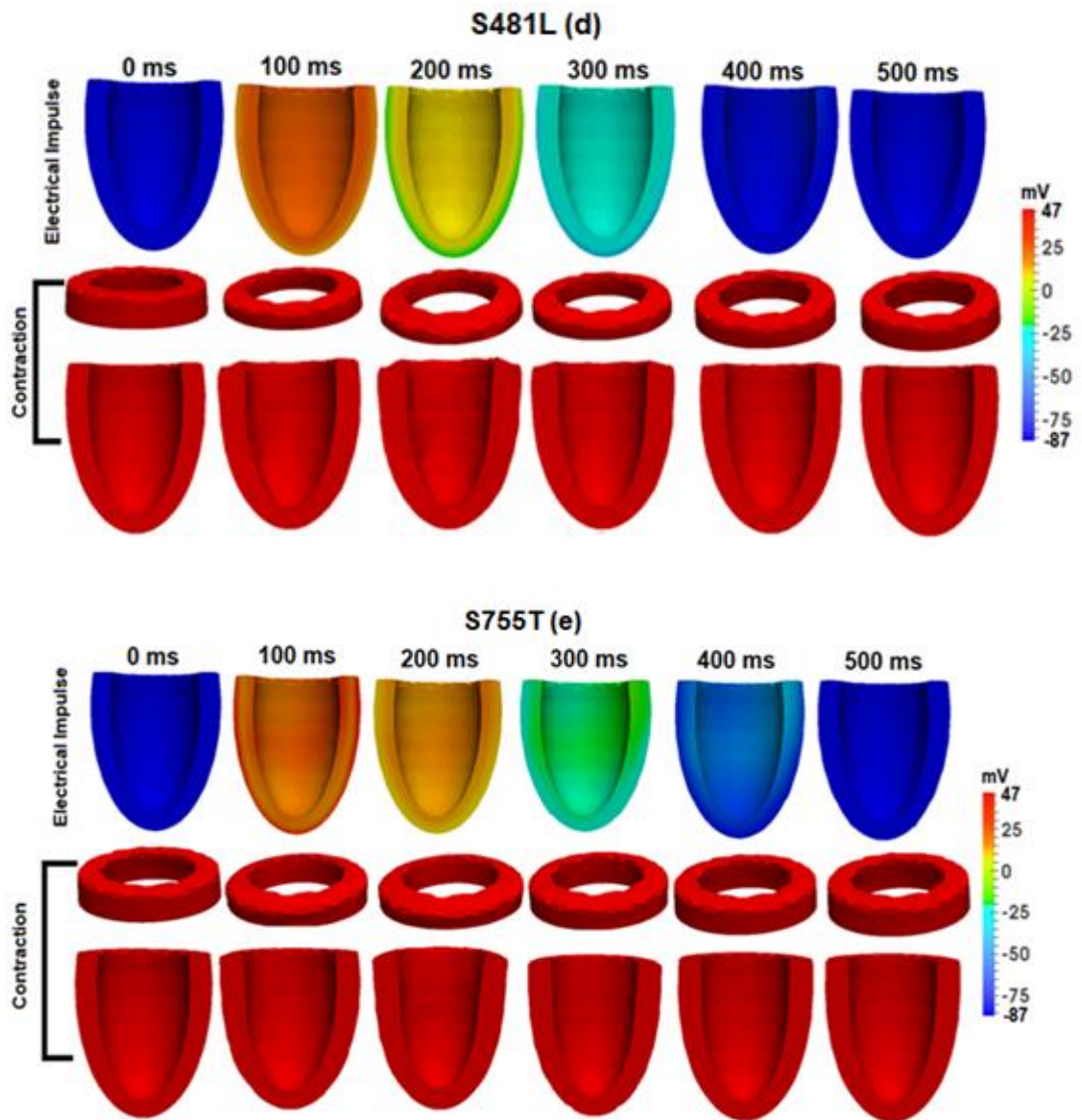


Figure 7.9: Snapshots of the electrical wave propagation and mechanical contraction at 0 ms, 100 ms, 200 ms, 300 ms, 400 ms and 500 ms in the 3D model of left ventricular cells under WT (a), A39V (b), G490R (c), S481L (d), and S755T (e) mutation conditions. An early repolarisation and reduced contractility can be seen in all mutation conditions, while the reduction in contractility is severe in the G490R (c) condition.

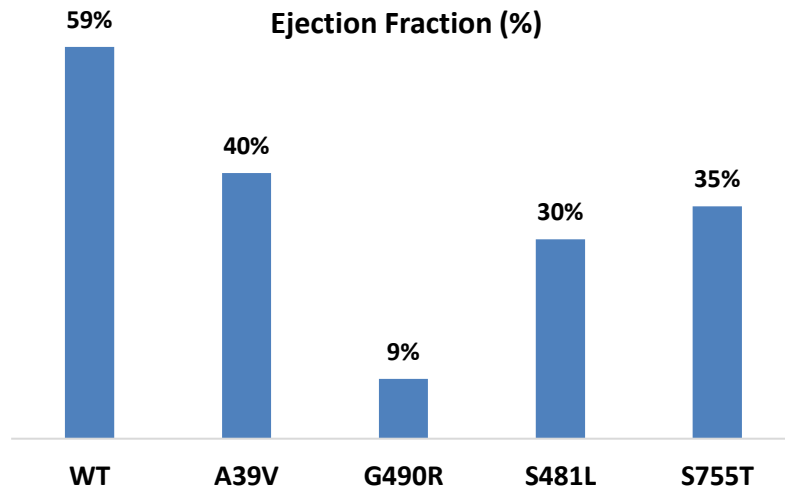


Figure 7.10: The Ejection Fraction is a measure of the % blood flowing out of the LV with each contraction. A reduction in the effective contractility (Figure 7.9) lead to a reduced EF in all the mutation conditions. Ejection fraction is severely affected under the G490R condition.

7.6 Discussion

The active force of contraction is associated with the sarcomere length. Results have shown that the active force was severely affected in the absence of I_{sac} as seen in the single cell simulations. The force generated was only 25% in EPI, 30% in MCELL and 20% in ENDO for the A39V condition. It was only 3% in EPI, 25% in MCELL and 20% in ENDO in the G490R condition. This behaviour is also observed for the S755T and S481L conditions, and the generated force was also severely affected in S481L and S755T conditions. In mutation conditions the greater force of contraction in MCELL is due to the longer AP duration than the EPI and ENDO cells. This major reduction in the contraction force is very drastic. It can cause heart failure, heart collapse and the death of the patient [45, 46].

It is very important to relate and validate the results produced by these models to the experimental data of the SQTS patients. Very limited SQTS experimental data on the ventricular mechanical contraction is available at present to compare and validate with the above results. Two individual families identified with SQTS, first reported were studied by Gaita et al. [44]. He found no structural irregularities in the hearts of any of the family members. Bellocq et al. [45] also studied a 70-year old male, who was diagnosed with a SQTS2 mutation. Further investigation revealed no structural abnormality in his heart, while the ejection fraction from the left ventricle was 49% [45]. Schimpf et al. [40] made a few

very important findings; in their study of the SQTs, they found that both control cases and the SQTs patients had no major differences in ejection fraction, end diastolic volume and end systolic volume. Their findings put a question mark on the marked reduction in contractility in the SQT4-6 electromechanical simulation results without the incorporation of I_{sac} ; although, a study by Aderiran et al. [3] has also shown a severe reduction of mechanical contraction in SQT1 and SQT2 patients in the absence of stretch. Still, clinically it has been seen that SQTs is identified with an increased risk of sudden death [32]. Studies have suggested that a drastic reduction in the contractility in SQTs could be related to reduced SR Ca^{2+} loading [32]. Abbreviated AP values alter the dynamics and provide less time for the SR Ca^{2+} loading, which consequently reduces the contraction [32].

7.7 References

- [1] T. O'Hara, L. Virág, A. Varró, and Y. Rudy, "Simulation of the undiseased human cardiac ventricular action potential: model formulation and experimental validation," *PLoS Comput. Biol.*, vol. 7, no. 5, p. e1002061, May 2011.
- [2] I. Adeniran, *Modelling the short QT syndrome gene mutations: and their role in cardiac arrhythmogenesis*, 2014 edition. New York: Springer, pp.109-200, 2014.
- [3] I. Adeniran, J. C. Hancox, and H. Zhang, "*In silico* investigation of the short QT syndrome, using human ventricle models incorporating electromechanical coupling," *Front. Physiol.*, vol. 4, pp. 5-12, Jul. 2013.
- [4] J. J. Rice, F. Wang, D. M. Bers, and P. P. de Tombe, "Approximate model of cooperative activation and crossbridge cycling in cardiac muscle using ordinary differential equations," *Biophys. J.*, vol. 95, no. 5, pp. 2368–2390, Sep. 2008.
- [5] N. A. Trayanova, J. Constantino, and V. Gurev, "Electromechanical models of the ventricles," *Am. J. Physiol. - Heart Circ. Physiol.*, vol. 301, no. 2, pp. H279–H286, Aug. 2011.
- [6] H. Hu and F. Sachs, "Stretch-activated ion channels in the heart," *J. Mol. Cell. Cardiol.*, vol. 29, no. 6, pp. 1511–1523, Jun. 1997.
- [7] W. J. Sigurdson, C. E. Morris, B. L. Brezden, and D. R. Gardner, "Stretch activation of a K^+ channel in molluscan heart cells," *J. Exp. Biol.*, vol. 127, no. 1, pp. 191–209, Jan. 1987.
- [8] G. C. L. Bett and F. Sachs, "Whole-cell mechanosensitive currents in rat ventricular myocytes activated by direct stimulation," *J. Membr. Biol.*, vol. 173, no. 3, pp. 255–263, Feb. 2000.
- [9] N. Hagiwara, H. Masuda, M. Shoda, and H. Irisawa, "Stretch-activated anion currents of rabbit cardiac myocytes," *J. Physiol.*, vol. 456, pp. 285–302, Oct. 1992.
- [10] D. Kim, "Novel cation-selective mechanosensitive ion channel in the atrial cell membrane," *Circ. Res.*, vol. 72, no. 1, pp. 225–231, Jan. 1993.
- [11] A. Ruknudin, F. Sachs, and J. O. Bustamante, "Stretch-activated ion channels in tissue-cultured chick heart," *Am. J. Physiol.*, vol. 264, no. 3 Pt 2, pp. H960-972, Mar. 1993.
- [12] J. Hoyer, A. Distler, W. Haase, and H. Gögelein, " Ca^{2+} influx through stretch-activated cation channels activates maxi K^+ channels in porcine endocardial endothelium.," *Proc. Natl. Acad. Sci. U. S. A.*, vol. 91, no. 6, pp. 2367–2371, Mar. 1994.
- [13] F. Guharay and F. Sachs, "Stretch-activated single ion channel currents in tissue-cultured embryonic chick skeletal muscle.," *J. Physiol.*, vol. 352, pp. 685–701, Jul. 1984.
- [14] C. M. Baumgarten, *Origin of mechanotransduction: stretch-activated ion channels.*

Landes Bioscience, pp. 1-38, 2013.

[15] C. E. Morris, "Mechanosensitive ion channels," *J. Membr. Biol.*, vol. 113, no. 2, pp. 93–107, Feb. 1990.

[16] M. A. Suleymanian, H. F. Clemo, N. M. Cohen, and C. M. Baumgarten, "Stretch-activated channel blockers modulate cell volume in cardiac ventricular myocytes," *J. Mol. Cell. Cardiol.*, vol. 27, no. 1, pp. 721–728, Jan. 1995.

[17] F. Sachs, "Mechanical transduction by ion channels: A cautionary tale," *World J. Neurol.*, vol. 5, no. 3, pp. 74–87, Sep. 2015.

[18] H. Sackin, "Stretch-activated ion channels," *Kidney Int.*, vol. 48, no. 4, pp. 1134–1147, Oct. 1995.

[19] P. Kohl and F. Sachs, "Mechanoelectric feedback in cardiac cells," *Philos. Trans. R. Soc. Lond. Math. Phys. Eng. Sci.*, vol. 359, no. 1783, pp. 1173–1185, Jun. 2001.

[20] A. V. Panfilov, R. H. Keldermann, and M. P. Nash, "Self-organized pacemakers in a coupled reaction-diffusion-mechanics system," *Phys. Rev. Lett.*, vol. 95, no. 25, p. 258104, Dec. 2005.

[21] J. B. Youm et al., "Role of stretch-activated channels in the heart: action potential and Ca^{2+} transients," in *mechanosensitivity in cells and tissues*, A. Kamkin and I. Kiseleva, Eds. Moscow: Academia, 2005.

[22] M. Zabel, S. Portnoy, and M. R. Franz, "Electrocardiographic indexes of dispersion of ventricular repolarisation: An isolated heart validation study," *J. Am. Coll. Cardiol.*, vol. 25, no. 3, pp. 746–752, Mar. 1995.

[23] N. Trayanova, W. Li, J. Eason, and P. Kohl, "Effect of stretch-activated channels on defibrillation efficacy," *Heart Rhythm*, vol. 1, no. 1, pp. 67–77, May 2004.

[24] P. Kohl, P. Hunter, and D. Noble, "Stretch-induced changes in heart rate and rhythm: clinical observations, experiments and mathematical models," *Prog. Biophys. Mol. Biol.*, vol. 71, no. 1, pp. 91–138, 1999.

[25] F. Sachs, "Stretch-activated ion channels: what are they?," *Physiol. Bethesda Md*, vol. 25, no. 1, pp. 50–56, Feb. 2010.

[26] H. Sackin, "Mechanosensitive channels," *Annu. Rev. Physiol.*, vol. 57, no. 1, pp. 333–353, 1995.

[27] A. Ibrahimbegovic, *Nonlinear solid mechanics: theoretical formulations and finite element solution methods*, 1st ed. Springer Publishing Company, Incorporated, pp. 21-124, 2009.

[28] N. Krishnamurthy, "Finite element method," in *application of the finite Element method in implant dentistry*, P. J. Geng, P. W. Yan, and D. W. Xu, Eds. Springer Berlin Heidelberg,

pp. 1–41, 2008.

[29] I. Adeniran, D. H. MacIver, C. J. Garratt, J. Ye, J. C. Hancox, and H. Zhang, “Effects of persistent atrial fibrillation-induced electrical remodelling on atrial electro-mechanics – insights from a 3D model of the human atria,” *PLOS ONE*, vol. 10, no. 11, p. e0142397, Nov. 2015.

[30] A. E. (Albert E. Green and J. E. Adkins, *Large elastic deformations*. Oxford: Clarendon Press, 1970.

[31] Douglas P. Zipes, Jose Jalife, *Cardiac electrophysiology: from cell to bedside*, 6e, 6 edition. Philadelphia, PA: Saunders, 2013.

[32] D. E. Hansen, “Mechanoelectrical feedback effects of altering preload, afterload, and ventricular shortening,” *Am. J. Physiol.*, vol. 264, no. 2 Pt 2, pp. H423-432, Feb. 1993.

[33] A. Belus and E. White, “Streptomycin and intracellular calcium modulate the response of single guinea-pig ventricular myocytes to axial stretch,” *J. Physiol.*, vol. 546, no. Pt 2, pp. 501–509, Jan. 2003.

[34] T. Zeng, G. C. Bett, and F. Sachs, “Stretch-activated whole cell currents in adult rat cardiac myocytes,” *Am. J. Physiol. Heart Circ. Physiol.*, vol. 278, no. 2, pp. H548-557, Feb. 2000.

[35] B. Crozatier, “Stretch-induced modifications of myocardial performance: from ventricular function to cellular and molecular mechanisms,” *Cardiovasc. Res.*, vol. 32, no. 1, pp. 25–37, Jul. 1996.

[36] M. L. R. C. Pavão, V. C. Ono, E. Arfelli, M. V. Simões, J. A. Marin Neto, and A. Schmidt, “Sudden cardiac death and short QT syndrome,” *Arq. Bras. Cardiol.*, vol. 103, no. 3, pp. e37–e40, Sep. 2014.

[37] S. Modi and A. D. Krahn, “Sudden cardiac arrest without overt heart disease,” *Circulation*, vol. 123, no. 25, pp. 2994–3008, Jun. 2011.

[38] W. C. Little, “Heart failure with a normal left ventricular ejection fraction: diastolic heart failure,” *Trans. Am. Clin. Climatol. Assoc.*, vol. 119, pp. 93–102, 2008.

[39] L. J. Gula et al., “Ejection fraction assessment and survival: An analysis of the Sudden Cardiac Death in Heart Failure Trial (SCD-HeFT),” *Am. Heart J.*, vol. 156, no. 6, pp. 1196–1200, Dec. 2008.

[40] R. Schimpf et al., “Electromechanical coupling in patients with the short QT syndrome: Further insights into the mechanoelectrical hypothesis of the U wave,” *Heart Rhythm Off. J. Heart Rhythm Soc.*, vol. 5, no. 2, pp. 241–245, Feb. 2008.

[41] R. Erbel, P. Schweizer, J. Meyer, H. Grenner, W. Krebs, and S. Effert, “Left ventricular volume and ejection fraction determination by cross-sectional echocardiography in patients

- with coronary artery disease: A prospective study,” *Clin. Cardiol.*, vol. 3, no. 5, pp. 377–383, Oct. 1980.
- [42] J. M. Cordeiro, R. Brugada, Y. S. Wu, K. Hong, and R. Dumaine, “Modulation of I_{Kr} inactivation by mutation N588K in *KCNH2*: A link to arrhythmogenesis in short QT syndrome,” *Cardiovasc. Res.*, vol. 67, no. 3, pp. 498–509, Aug. 2005.
- [43] R. Sah et al., “Regulation of cardiac excitation-contraction coupling by action potential repolarisation: role of the transient outward potassium current ($I_{(to)}$),” *J. Physiol.*, vol. 546, no. Pt 1, pp. 5–18, Jan. 2003.
- [44] F. Gaita et al., “Short QT syndrome,” *Circulation*, vol. 108, no. 8, pp. 965–970, Aug. 2003.
- [45] C. Bellocq et al., “Mutation in the *KCNQ1* gene leading to the short QT-interval syndrome,” *Circulation*, vol. 109, no. 20, pp. 2394–2397, May 2004.
- [46] E. Drouin, F. Charpentier, C. Gauthier, K. Laurent, and H. Le Marec, ‘Electrophysiologic characteristics of cells spanning the left ventricular wall of human heart: evidence for presence of M cells’, *J. Am. Coll. Cardiol.*, vol. 26, no. 1, pp. 185–192, Jul. 1995.
- [47] Wilson L. D., Jennings M. M., Rosenbaum D. S. Point: M cells are present in the ventricular myocardium. *Heart Rhythm* 8, 930–933, 2011.
- [48] Li G. R., Feng J., Yue L., Carrier M. Transmural heterogeneity of action potentials and I_{to1} in myocytes isolated from the human right ventricle. *Am. J. Physiol.* 275, H369–H377, 1998.
- [49] D.U.J Keller, R. Kalayciyan, O. Dössel and G. Seemann, Fast creation of endocardial stimulation pro- files for the realistic simulation of body surface ECGs. Proceedings of the World Congress on Medical Physics and Biomedical Engineering IFMBE, Munich, 7-12 September, PP. 145-148, 2009.

CHAPTER 8

8.1 Discussion

The work presented in this thesis is focused on the *in silico* investigation of the functional impact of the L-type calcium channel mutations associated with short QT syndromes, the cardiac L-type calcium channel is an oligomeric complex consisting of α_1 , β , and $\alpha_2\delta$ subunits [1]. The pore-forming $\text{Ca}_v1.2$ α -1C subunit is encoded by the *CACNA1C* gene, while the $\text{Ca}_v\beta_2$ and $\text{Ca}_v\alpha_2\delta$ -1 subunits are encoded by *CACNB2b* and *CACNA2D1* respectively, they control the biophysical properties and trafficking of Ca_v channels [2, 3]. The $\text{Ca}_v1.2$ channel modulates the calcium channel activity in the human ventricular cells and is responsible for the dome appearance of the action potential. It also regulates excitation-contraction coupling by inducing Ca^{2+} release from the sarcoplasmic reticulum (SR) [2, 3]. Genetic mutations in Ca_v subunits can cause various phenotypes, including short QT syndrome, Brugada syndrome, and early repolarisation syndrome [4, 5]. Short QT syndrome associated with L-type calcium channels is a relatively new and rare clinical entity that consists of an ST segment elevation and shorter than normal QT intervals [4, 5]. A short QT interval with an elevated ST segment can contribute to cardiac arrhythmia, ventricular fibrillation, and sudden cardiac death (SCD) syndrome [2, 4, 5].

The work presented in this thesis is a computational model to explain the functional behaviour of the SQT syndromes, propagation and maintenance of ventricular arrhythmias, and impairment of the ventricular contraction. Three different mathematical models for SQT4, SQT5, and SQT6 were developed by using extant biophysical experimental data [4, 5]. The LTCC Hodgkin-Huxley formulation of the O'Hara & Rudy [6] human ventricular single cell model (ORd) was reformed to integrate the kinetic properties of WT, SQT4 (A39V and G490R), SQT5 (S481L), and SQT6 (S755T) mutations. The validated formulations were then incorporated into the O'Hara & Rudy ventricular single cell and anatomically detailed tissue models to demonstrate how these variants advance to ventricular arrhythmias. The ORd electrophysiological short QT models were coupled with the myofilament model to investigate the functional impact of the mutation on the mechanical coupling in single cell and 3D models. Simulated results showed that each mutation uniquely enhanced the temporal vulnerability window to the premature excitation stimulus, leading to increased risk of arrhythmia, it also reduced contractility in all three short QT models.

8.1.1 SQT4/A39V and G490R

The major findings of the current SQT4S study are:

- a) A39V and G490R reduced the AP duration in all three cell types and caused a shortening of the QT intervals.
- b) Although simulations were unable to reproduce a tall T-peak, a ST segment elevation was observed in the simulation which was not found in short QT1-3 patients. In previous studies, Gima and Rudy [7] have suggested that a tall T-wave is associated with hyperkalemia, which represents high levels of potassium current. Adeniran et al. [8] have suggested that to obtain a tall T-wave, a heterogeneous I_{Kr} density across the ventricular strand model was found to be necessary. To validate this, a heterogeneous I_{Kr} density along the 1D strand was considered. Tall T-waves were obtained for A39V and G490R models, for the I_{Kr} densities of 1.6:1:1 for LVEPI, LVMCELL and LVENDO cells.
- c) The tissue's temporal vulnerability at some localised regions was increased under the A39V and G490R mutation conditions. In the 2D tissue, the minimal substrate size that is necessary to initiate and maintain the re-entry was decreased under mutation conditions.
- d) ST Segment elevation was reproduced which shows that SQT4 mutations are also linked with Brugada syndrome [9].
- e) Blocking of I_{CaL} alone did not normalise QT intervals; instead it increased the amplitude of QRS interval which predicts high blood pressure. My results are consistent with previous studies [10, 11].

The results provide a clear correspondence between the shortening of QT intervals and the SQT4 mutation. The models give a detailed explanation of increased vulnerability to re-entry in A39V and G490R.

The work done on SQT4 mutations in this thesis is the first attempt to investigate the arrhythmogenic consequences of the A39V and G490R mutations using 1D and 2D tissue models of the human ventricles. This study also attempted to normalise the QT interval by enhancing the I_{CaL} currents. Results have suggested an increase in the amplitude of the QRS interval instead of a normalised QT interval. In simulations, a different approach was

used to normalise QT interval, by blocking the I_{Kr} . The blockade of I_{Kr} normalised the QT interval, while ST segment elevation could be reduced by blocking I_{to} . The blockade of I_{to} not only controlled the J-wave elevation but also reduced the ST-segment elevation. Prior studies [8, 12] have suggested different pharmacological techniques to treat patients with the potassium-related SQT syndromes, although the pharmacological treatment for the SQT

syndromes associated with L-type calcium channels are yet to be developed.

The current study has also investigated the minimal substrate length to trigger and facilitate the re-entry in both electrophysiological and electromechanically coupled idealised 2D tissue models. The minimal substrate length necessary to facilitate and sustain re-entry was reduced for the A39V and G490R mutation conditions in an electrophysiological model. A larger size of the tissue substrate was required to initiate re-entry in a 2D idealised electromechanical model for A39V and G490R. For the electromechanical model, the re-entrant wave sustained longer for A39V and G490R mutations as compared to the WT but did not sustain for the entire cycle length of 1000 ms as seen for the electrophysiological model.

8.1.2 CACNB2b β 2 SQT5/ S481L

The major findings of the present study are:

- a) The CACNB2b S481L mutation reduced the AP duration in all three cell types and caused the shortening of the QT interval on ECGs. Although the AP morphology was not as affected as under SQT4 A39V and G490R, a depression can be seen during the plateau phase.
- b) The clinical ECGs of the SQT5 patients did not show any tall T-waves, although they have suggested an elevation of the ST segment [4].
- c) An ST segment elevation was observed in the simulation which was not found in short QT1-3 patients. ST segment elevation was reproduced which indicates that SQT5 mutations are linked with Brugada syndromes [4, 13]. A study by Yan and Antzelevitch [13] has suggested that a decrease in the amplitude of the AP dome of LVEPI creates a transmural voltage gradient across the ventricular wall, which may not only elevate the ST but may also lead to phase 2 re-entry and VF [13, 14].
- d) The tissue's temporal vulnerability at some localised regions was increased under the S481L condition.
- e) In an idealised electrophysiological 2D tissue model, the minimal length of the substrate that is necessary to trigger and maintain the re-entry was decreased for the S481L condition. The minimal substrate length necessary to initiate the re-entry is larger for the electromechanical model, although it was still unable to sustain the re-entry for both WT and S481L conditions.
- f) In a 1D idealised tissue model, a high amplitude of the QRS interval and a J point elevation were seen by enhancing the calcium influx, which predicts high blood pressure and an early repolarisation syndrome [15-18]. The QT interval was normalised by blocking ~38% of I_{Kr}

instead of enhancement of I_{CaL} to control the amplitude of QRS interval and J-wave elevation. My results are consistent with previous studies [10, 11].

- g) The steepness in the slopes of the APD-R and ERP-R curves is linked to the increased vulnerability of re-entrant excitation waves, which are more prone to break up into several re-entrant excitation wavelets [7, 8].

Similar to the SQT4 model these results show a clear relationship between the shortening of the QT interval, arrhythmogenic events, and the CACNB2b SQT5 mutation. It gives a detailed explanation of increased susceptibility to re-entry under S481L CACNB2b $\beta 2$ condition. The work done on SQT5 mutations in this thesis is the first attempt to investigate the arrhythmogenic consequences of the A39V and G490R mutations using 1D and 2D tissue models of the human ventricles.

The idealised 1D O'Hara & Rudy S481L model was able to reproduce the elevation of the ST segment which was clinically observed for the SQT5 patients [4]. Results have suggested an increased tissue temporal vulnerability at some localised regions for the S481L condition. Yan and Antzelevitch [13] suggested that an elevation of the ST-segment can lead to a phase 2 re-entry, but no prior study has discussed the detailed phenomena involving AF and VF in S481L/SQT5 patients.

8.1.3 CACNA2D1 $\alpha 2\delta$ -1 SQT6/S755T

The significant findings of the current study are:

- a) Unlike the SQT4 and SQT5 mutations, SQT6 experimental data was based on Barium ions as the charge carrier through the calcium channel. The simulated results were obtained by switching the O'Hara & Rudy model to VDI mode ($n=0$) only. This shows the CDI mode is switched off and the inactivation of L-type calcium channel for the S755T model is only voltage dependent when Ba^{2+} is the charge carrier (CDI and VDI models are explained in Chapter 3).
- b) The CACNA2D1 $Ca_v\alpha 2\delta$ -1 S755T mutation reduced the AP duration in all three cell types with a major attenuation in the middle cell and caused the shortening of QT interval on ECGs. A strong depression is very visible in the dome of AP for all three cell types, which leads to the elevation of the ST segment.
- c) The 1D model reproduced the Tall T-wave with a shorter than normal QT interval.
- d) A ST segment elevation, $ST < 2$ mm, an elevated J-wave, and a prominent T-wave were reproduced by the idealised 1D tissue model. The ST segment elevation and early

repolarisation patterns (J-wave elevation) are associated with the Brugada syndromes that can lead to the AF and VF [19].

- e) A study by Yan and Antzelevitch [13] suggested that a decrease in the amplitude of AP dome of EPI (as compared to the decrease in the amplitude of ENDO dome region) creates a transmural voltage gradient across the ventricular wall, which could elevate the ST segment. As seen in the results, the difference in the amplitude of EPI and ENDO dome regions is not very large, which may cause a very small elevation of ST segment for S755T with respect to the WT baseline.
- f) The tissue's temporal vulnerability was increased for the S755T condition.
- g) In the 2D tissue, the minimal substrate length that is necessary to start and maintain the re-entry was decreased under the S755T condition.

The above results show a clear relationship between the shortening of QT interval and SQT6 mutation. They give a detailed explanation of increased vulnerability to re-entry under S755T CACNA2D1 condition.

8.2 SQT4, SQT5 and SQT6 Electro-Mechanical Model

The active force of contraction and the shortening of the sarcomere are correlated. The shorter the length of the sarcomere, the greater the force of contraction, which can be seen in the results of the electromechanical single cell model. Results have suggested that the active force was severely affected in the simulations of the single cell model, without stretch activated channel consideration.

- a) For A39V and G490R the reduction in the contractile force was ~74% and ~82% respectively, without the consideration of I_{sac} . This major reduction in the contraction force is very drastic. It could cause the death of the patient in a real heart. Previous studies have suggested that incorporation of stretch activated channels improved the contractile force [8, 20]. The simulated results have suggested that the abbreviation of the normalised force was reduced to ~32% and 44% for A39V and G490R after the incorporation of stretch.
- b) Similar to the A39V and G490R mutations the force of contraction is much stronger in S481L and S755T conditions, with only the consideration of stretch.
- c) A premature stimulus was able to evoke re-entry in the idealised 2D tissue models of SQT4-SQT6, although these re-entrant waves were terminated after a short duration.

The work in this thesis has suggested a severe reduction of mechanical contraction in SQT4, SQT5 and SQT6 patients in the absence of stretch, which is consistent with the study of

Aderiran et al. [3]. His work has also shown a severe reduction of mechanical contraction in SQT1 and SQT2 patients in the absence of stretch. Studies have suggested that a drastic reduction in the contractility in SQTS could be related to reduced SR Ca^{2+} loading [21]. Abbreviated AP values alter the dynamics and provide less time for SR Ca^{2+} loading, which consequently reduces the contraction [21].

8.3 Common Mechanisms between the SQT 1-6 Variants

Short QT syndrome is a relatively new and rare cardiac condition [22, 23]. Short QT patients are diagnosed with two different genetic patterns:

- a) An autosomal dominant pattern in patients with family history of Short QT [22, 23].
- b) People with no known history of Short QT syndrome in their family have been diagnosed with Sporadic dominant patterns [23].

To date, a total of six mutations have been identified in potassium and calcium channel genes. A gain-of-function mutation of the potassium channel and a loss-of-function mutation of the calcium channels result in the abbreviation of repolarisation phase of the AP, which causes a shortening of the QT interval. The most recently diagnosed short QT variants (SQT4, SQT5 and SQT6) described in this thesis and the first three variants of SQT syndrome share common elements. All these elements make the SQT Syndromes pro-arrhythmic thus enabling them to stabilise, accelerate and perpetuate re-entry.

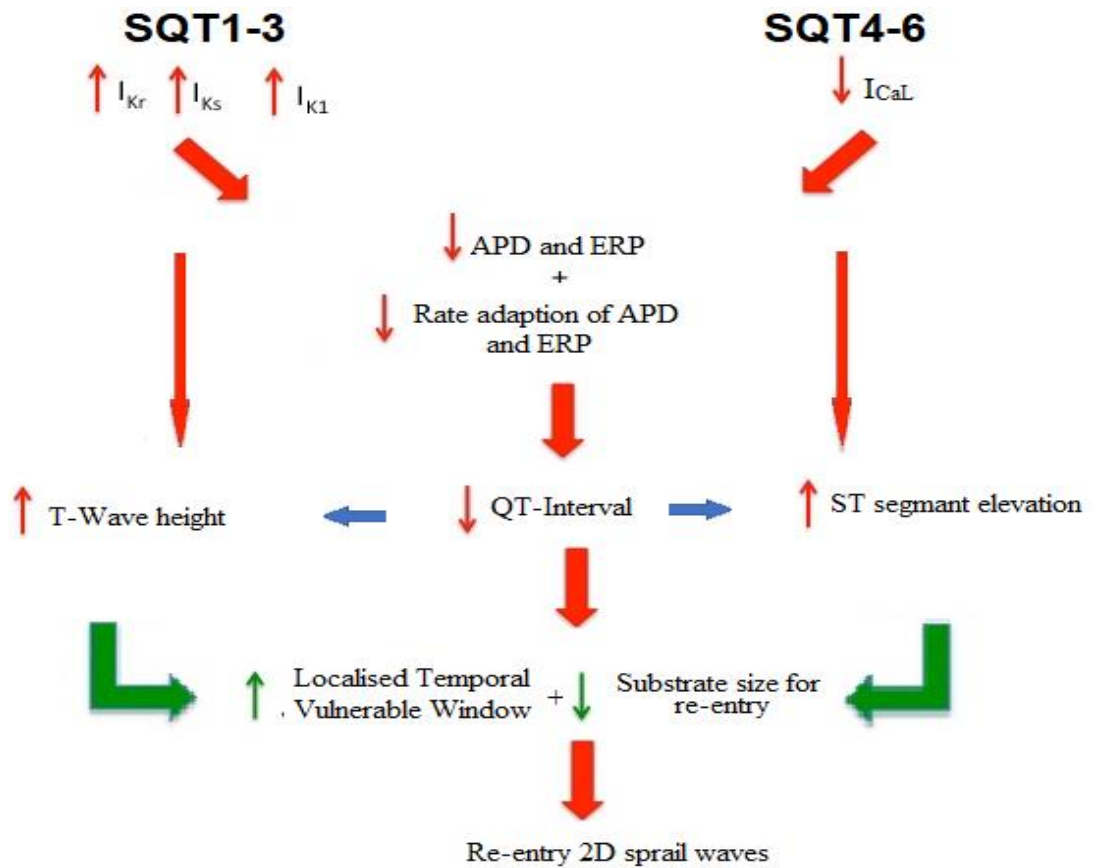


Figure 8.1: Common mechanism observed in SQT1-6 mutation. These elements make the SQTs pro-arrhythmic thus enabling them to stabilise, accelerate and perpetuate re-entry.

8.4 Limitations

- The O'Hara & Rudy ventricular single cell model increases the human specific accuracy as it is based on healthy human experimental data. It is suggested to be the most recent and well-defined model to investigate the phenomena of re-entrant arrhythmia [6]. Although most of its integral ion channel kinetics are obtained from human ventricular experimental data [6], it still has its limitations. For example, direct measurement of I_{NaK} in the healthy human ventricular myocyte is lacking [1]. The ENDO APs were measured in small tissue preparations to avoid possible enzymatic degradation of K^+ channel proteins [24, 25], affecting the currents and the action potential.
- The distribution of EPI, MIDDLE, and ENDO cell types in the ventricular wall is not very clear to date due to the lack of the experimental data [26] of human ventricular myocyte. For the 1D tissue simulations, a cell type proportion was considered such that the measured value

of conduction velocity across the ventricular wall corresponds well with the experimentally observed values [26]. This proportion has been used in prior studies [8, 27, 28, 29].

- c) There is a disagreement regarding the M-cell presence and its role in the human heart [8]. Drouin et al. [30] observed the presence of M-cell APs in the human heart, and more recently it has been identified by Glukhov et al. [31]. In the current model M-cell was defined by its transmural location as observed by Glukhov [31].
- d) All the tissue simulations resume a mono-domain representation of tissue structure as opposed to a bi-domain representation.

Although understanding the possible limitations of the models used in this thesis is very important, they do not reproduce any conflicting effect on the conclusions, explained by the substrates and the corresponding mechanisms which can initiate, stabilise, and sustain arrhythmia for SQT4, SQT5 and SQT6 mutations.

8.5 Future Developments

The work presented in this thesis is based on the experimental data obtained from the intact L-Type calcium channel. As discussed in Chapter 1, the L-type calcium channel is an oligomeric complex, composed of α , β_2 and $\alpha_2\delta-1$ subunits. The functional impacts of the mutations associated with these genes will be better understood if specific experimental data of these subunits and the relative formulation of LTCC are available.

Another significant finding illustrated in this thesis is the elevation of the J-wave which represents the early repolarisation syndrome. The SQTs models developed in this thesis can be used to investigate the relationship between the J-wave and the SQTs.

Contractility is severely reduced in simulations. Prior studies have suggested that the experimental and *in silico* data to reach a definite conclusion is not enough for the electromechanical modelling [32]. Based on the simulations represented in this thesis, additional investigations can be performed to understand the behaviour of the mechanical systole in SQT4-6 patients.

8.6 Closing Words

In silico models of the most recent variants of the SQTs that affect calcium channels have been developed; O'Hara & Rudy models for the SQT4, SQT5, and SQT6. These models have been further used to investigate the functional impact of SQT 4-6 in the human left

ventricular at the single cell, 1D, 2D, and 3D levels.

The observations in this thesis provide an extensive explanation for clinical findings of these SQTS in terms of abbreviation of repolarisation and vulnerability to arrhythmia. The multiscale ventricular models are further used to understand the mechanisms initiating and facilitating arrhythmia and the investigation of therapeutic interventions for the SQTS.

8.7 References

- [1] W. Rottbauer, K. Baker, Z. G. Wo, M.-A. P. K. Mohideen, H. F. Cantiello, and M. C. Fishman, “Growth and function of the embryonic heart depend upon the cardiac-specific L-type calcium channel $\alpha 1$ subunit,” *Dev. Cell*, vol. 1, no. 2, pp. 265–275, Aug. 2001.
- [2] F. Hofmann, V. Flockerzi, S. Kahl, and J. W. Wegener, “L-type $\text{Ca}_{\text{v}1.2}$ calcium channels: from *In vitro* findings to *In vivo* function,” *Physiol. Rev.*, vol. 94, no. 1, pp. 303–326, Jan. 2014.
- [3] S. I. McDonough, *Calcium channel pharmacology*. Springer Science & Business Media, pp. 9-15, 2011.
- [4] C. Antzelevitch et al., “Loss-of-function mutations in the cardiac calcium channel underlie a new clinical entity characterized by ST-segment elevation, short QT intervals, and sudden cardiac death,” *Circulation*, vol. 115, no. 4, pp. 442–449, Jan. 2007.
- [5] C. Templin et al., “Identification of a novel loss-of-function calcium channel gene mutation in short QT syndrome (SQTS6),” *Eur. Heart J.*, vol. 32, no. 9, pp. 1077–1088, May 2011.
- [6] T. O’Hara, L. Virág, A. Varró, and Y. Rudy, “Simulation of the undiseased human cardiac ventricular action potential: model formulation and experimental validation,” *PLoS Comput. Biol.*, vol. 7, no. 5, p. e1002061, May 2011.
- [7] K. Gima and Y. Rudy, “Ionic current basis of electrocardiographic waveforms a model study,” *Circ. Res.*, vol. 90, no. 8, pp. 889–896, May 2002.
- [8] I. Adeniran, *Modelling the short QT syndrome gene mutations: and their role in cardiac arrhythmogenesis*, 2014 edition. New York: Springer, pp. 101-217, 2014.
- [9] E. J. Vigmond, M. Hughes, G. Plank, and L. J. Leon, “Computational tools for modeling electrical activity in cardiac tissue,” *J. Electrocardiol.*, vol. 36, pp. 69–74, Dec. 2003.
- [10] W. J. Crumb and G. T. Faircloth, “Aplidine as an l-type calcium channel enhancer,” EP0981352 A1, 01-Mar-2000.
- [11] C. Antzelevitch and J. M. Fish, “Therapy for the Brugada syndrome,” *Handb. Exp. Pharmacol.*, no. 171, pp. 305–330, 2006.
- [12] B. Rudic, R. Schimpf, and M. Borggrefe, “Short QT syndrome – review of diagnosis and treatment,” *Arrhythmia Electrophysiol. Rev.*, vol. 3, no. 2, pp. 76–79, Aug. 2014.
- [13] G. X. Yan and C. Antzelevitch, “Cellular basis for the Brugada syndrome and other mechanisms of arrhythmogenesis associated with ST-segment elevation,” *Circulation*, vol. 100, no. 15, pp. 1660–1666, Oct. 1999.
- [14] B. Benito et al., “Brugada Syndrome,” *Rev. Esp. Cardiol.*, vol. 62, no. 11, pp. 1297–

1315, Jan. 2009.

[15] I. Gussak and P. Bjerregaard, "Short QT syndrome—5 years of progress," *J. Electrocardiol.*, vol. 38, no. 4, pp. 375–377, Oct. 2005.

[16] C. Antzelevitch et al., "Brugada syndrome: report of the second consensus conference: endorsed by the Heart Rhythm Society and the European Heart Rhythm Association," *Circulation*, vol. 111, no. 5, pp. 659–670, Feb. 2005.

[17] L.S. Premkumar, "Selective potentiation of L-type calcium channel currents by cocaine in cardiac myocytes", *The American Society for Pharmacology and Experimental Therapeutics*, vol. 56: pp. 1138 –1142, August 1999.

[18] T. A. Ansah, L. H. Wade, and D. C. Shockley, "Effects of calcium channel entry blockers on cocaine and amphetamine-induced motor activities and toxicities," *Life Sci.*, vol. 53, no. 26, pp. 1947–1956, 1993.

[19] K. K. Sethi, K. Sethi, and S. K. Chutani, "Early repolarisation and J wave syndromes," *Indian Heart J.*, vol. 66, no. 4, pp. 443–452, Jul. 2014.

[20] I. Adeniran, J. C. Hancox, and H. Zhang, "In silico investigation of the short QT syndrome, using human ventricle models incorporating electromechanical coupling," *Front. Physiol.*, vol. 4, pp. 1-13, Jul. 2013.

[21] I. Bodi, G. Mikala, S. E. Koch, S. A. Akhter, and A. Schwartz, "The L-type calcium channel in the heart: The beat goes on," *J. Clin. Invest.*, vol. 115, no. 12, pp. 3306–3317, Dec. 2005.

[22] F. Gaita et al., "Short QT syndrome: pharmacological treatment," *J. Am. Coll. Cardiol.*, vol. 43, no. 8, pp. 1494–1499, Apr. 2004.

[23] A. Mazzanti et al., "Novel Insight into the Natural History of Short QT Syndrome," *J. Am. Coll. Cardiol.*, vol. 63, no. 13, pp. 1300–1308, Apr. 2014.

[24] S. Rajamani et al., "Specific serine proteases selectively damage KCNH2 (hERG1) potassium channels and I(Kr)," *Am. J. Physiol. Heart Circ. Physiol.*, vol. 290, no. 3, pp. H1278-1288, Mar. 2006.

[25] G. R. Li, J. Feng, L. Yue, M. Carrier, and S. Nattel, "Evidence for two components of delayed rectifier K⁺ current in human ventricular myocytes," *Circ. Res.*, vol. 78, no. 4, pp. 689–696, Apr. 1996.

[26] C. Antzelevitch, "M Cells in the human heart," *Circ. Res.*, vol. 106, no. 5, pp. 815–817, Mar. 2010.

[27] D. L. Weiss, G. Seemann, F. B. Sachse, and O. Dössel, "Modelling of short QT syndrome in a heterogeneous model of the human ventricular wall," *EP Eur.*, vol. 7, no. s2, pp. S105–S117, Jan. 2005.

- [28] H. Zhang and J. C. Hancox, "In silico study of action potential and QT interval shortening due to loss of inactivation of the cardiac rapid delayed rectifier potassium current," *Biochem. Biophys. Res. Commun.*, vol. 322, no. 2, pp. 693–699, 2004.
- [29] I. Adeniran, M. J. McPate, H. J. Witchel, J. C. Hancox, and H. Zhang, "Increased vulnerability of human ventricle to re-entrant excitation in hERG-linked variant 1 short QT syndrome," *PLOS Comput. Biol.*, vol. 7, no. 12, p. e1002313, Dec. 2011.
- [30] E. Drouin, F. Charpentier, C. Gauthier, K. Laurent, and H. Le Marec, "Electrophysiologic characteristics of cells spanning the left ventricular wall of human heart: evidence for presence of M cells," *J. Am. Coll. Cardiol.*, vol. 26, no. 1, pp. 185–192, Jul. 1995.
- [31] A. V. Glukhov et al., "Transmural dispersion of repolarisation in failing and nonfailing human ventricle," *Circ. Res.*, vol. 106, no. 5, pp. 981–991, Mar. 2010.
- [32] R. Schimpf et al., "Electromechanical coupling in patients with the short QT syndrome: Further insights into the mechanoelectrical hypothesis of the U wave," *Heart Rhythm Off. J. Heart Rhythm Soc.*, vol. 5, no. 2, pp. 241–245, Feb. 2008.

Appendix A

AP	Action Potential
APD	Action Potential Duration (ms)
APD ₉₀	Action Potential Duration at 90% repolarisation
AF	Atrial Fibrillation
BCL	Basic Cycle Length (ms)
BSR	Anionic SR Binding Sites for Ca ²⁺ in Subspace
BSL	Anionic Sarcolemmal Binding Sites for Ca ²⁺ Buffer in Subspace
CDI	Ca ²⁺ Dependent Inactivation of L-type Ca ²⁺ Current
CICR	Calcium Induce Calcium Release
C _m	Total Membrane Capacitance, 1μF
CMDN	Calmodulin, Ca ²⁺ Buffer in Myoplasm
CSQN	Calsequestrin, Ca ²⁺ Buffer in JSR
CaMK	Ca ²⁺ / Calmodulin-Dependent Protein Kinase II/
DI	Diastolic Interval, Relative to APD ₉₀ (ms)
Diffusion flux	$J_{diff,Na^+}, J_{diff,Ca^{2+}}, J_{diff,K^+}$
ERP	Effective Refractory Period (ms)
EM Model	Electro-Mechanical Model
E _S	Reversal Potential for Ion S (mV)
ECG	Electrocardiogram
F	Faraday Constant, 96485 coul/mol
HH model	Hodking and Huxley Cell Model
I-V Curve	Current Voltage Relationship
I _{Ca_b}	Ca ²⁺ Background Current
I _{Ca_L}	Ca ²⁺ Current through the L-type Ca ²⁺ Channel
I _{Ca_{Na}}	Na ⁺ Current through the L-type Ca ²⁺ Channel
I _{Ca_K}	K ⁺ Current through the L-type Ca ²⁺ Channel
I _{K_b}	K ⁺ Background Current
I _{K_r}	Rapid Delayed Rectifier K ⁺ Current
I _{K_s}	Slow Delayed Rectifier K ⁺ Current
I _{K₁}	Inward Rectifier K ⁺ Current

I_{Na}	Na ⁺ current
I_{Nab}	Na ⁺ Background Current
I_{NaCa}	Total Na ⁺ /Ca ²⁺ Exchange Current
$I_{NaCa,i}$	Myoplasmic Component of Na ⁺ /Ca ²⁺ Exchange Current
$I_{NaCa,ss}$	Sub-Space Component of Na ⁺ /Ca ²⁺ Exchange Current
I_{pCa}	Sarcolemmal Ca ²⁺ Pump Current
I_{sac}	Stretch Activated Channel
I_{stim}	Stimulus Current ($\mu A/\mu F$)
I_{to}	Transient Outward K ⁺ Current
$J_{diff, Ca^{2+}}$	Diffusion of Ca ²⁺ from Sub-Space to Myoplasm
J_{diff, K^+}	Diffusion of K ⁺ from sub-space to myoplasm
J_{diff, Na^+}	Diffusion of Na ⁺ from Sub-Space to Myoplasm
J_{rel}	SR Calcium Release Flux via Ryanodine Receptor
J_{UP}	Calcium Uptake via SERCA Pump
J_{TR}	Calcium Translocation from NSR to JSR
JSR	Junctional SR Compartment
LVEPI	Left Ventricular Epicardial Cell
LVMCELL	Left Ventricular Myocardial Cell
LVENDO	Left Ventricular Endocardial Cell
MM model	Mechanical Model
NSR	Network SR Compartment
ORd model	O'Hara-Rudy Dynamic Human Ventricular Cell Model
PSD	Power Spectrum Distribution
RyR	Ryanodine Receptor
R	Gas Constant, 8314 J/kmol/K
SCD	Sudden Cardiac Death
SQTS	Short QT Syndrome
SI	Stimulus Interval
SS	Subspace compartment
SR	Sarcoplasmic Reticulum
T	Temperature, 310°K

TRPN	Troponin, Ca ²⁺ buffer in myoplasm
VF	Ventricular Fibrillation
VW	Vulnerable Window
VDI	Voltage Dependent Inactivation of L-type Ca ²⁺ Current
V, or V _m	Membrane Voltage (mV)

Appendix B

Amplitude	-80.0 $\mu\text{A}/\mu\text{F}$
BCL	1000ms
$[\text{Ca}^{2+}]_o$	1.8 Mm
$[\text{Ca}^{2+}]_i$	$8.54 \cdot 10^{-5}$ mM
$[\text{Ca}^{2+}]_{ss}$	$8.43 \cdot 10^{-5}$ mM
$[\text{Ca}^{2+}]_{nsr}$	1.61 mM
$[\text{Ca}^{2+}]_{jsr}$	1.56 mM
CaMK _{trap}	0.0124065
Duration	0.5 ms
j	0.69mM/ms
j _{CaMK}	0.692413mM/ms
J _{rel,NP}	2.5mM/ms
J _{rel,CaMK}	3.1mM/ms
J _{diff,Ca}	0.2ms
$[\text{K}^+]_i$	143.79 mM
$[\text{K}^+]_{ss}$	143.79 mM
$[\text{K}^+]_o$	5.4 mM
L	0.01cm
n_CDI+VDI	1
n_VDI	0
$[\text{Na}^+]_i$	7.23mM
$[\text{Na}^+]_{ss}$	7.23 mM
$[\text{Na}^+]_o$	140 mM
V _m	-87.84
V _{cell}	$38.10 \text{ e}^{-6} \mu\text{L}$
V _{nyo}	$25.54 \text{ e}^{-6} \mu\text{L}$
V _{nsr}	$2.098 \text{ e}^{-6} \mu\text{L}$
V _{jsr}	$0.182 \text{ e}^{-6} \mu\text{L}$

Appendix C








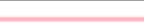











Voltage (mV)	Colour
50	
45	
40	
35	
30	
25	
20	
15	
10	
5	
0	
-5	
-10	
-15	
-20	
-25	
-30	
-35	
-40	
-45	
-50	

Table C1: Colour codes representing the change of voltage in Figure 5.1, the voltage range is between 50 and -50 mV with a voltage step of 5 mV.

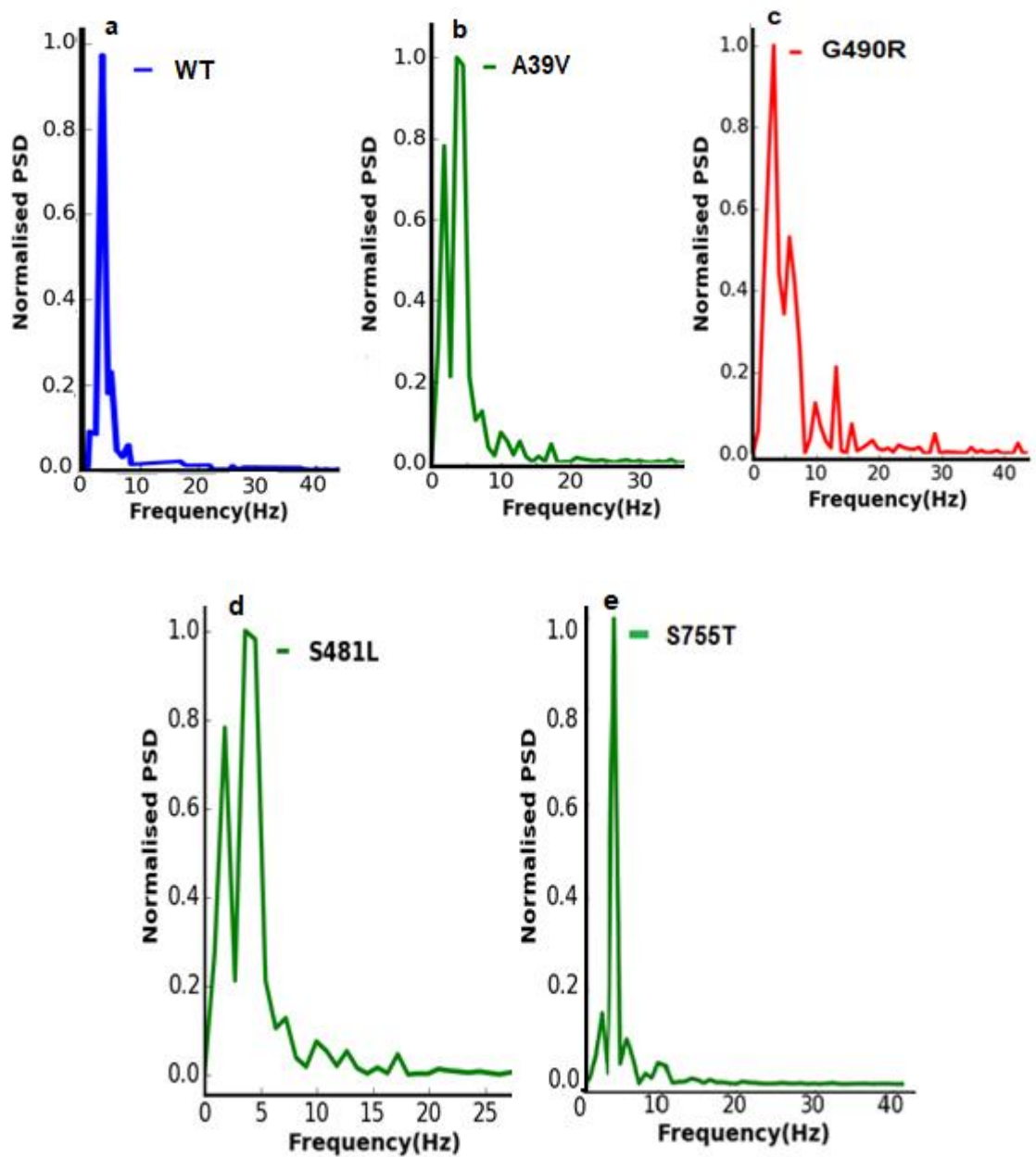


Figure C1: The power spectral distribution of the recorded local electrical activity of the WT, A39V, G490R, S481L and S755T models. Power spectral density (PSD) shows the strength of the electrical signal variation as a function of frequency.